# JOURNAL OF THE AERONAUTICAL SCIENCES

VOLUME 23 FEBRUARY, 1956 NUMBER 2


LIBRARY ST. LOUIS PUBLIC 1956 16 FEB

## CONTENTS


Transition Studies and Skin-Friction Measurements on an Insulated Flat Plate at a Mach Number of 5.8 ..... ROBERT H. KORKEGI 97

Fluid Dynamic Effects at Speeds from $M = 11$ to 15 ..... SEYMOUR M. BOGDONOFF AND ANDREW G. HAMMITT 108

Experimental Pressure Distributions on Oscillating Low Aspect Ratio Wings ..... WILLIAM R. LAIDLAW AND ROBERT L. HALFMAN 117

Viscous Flow Along a Flat Plate Moving at High Supersonic Speeds ..... Y. H. KUO 125

Equations for the Loading, Section Pitching-Moment Coefficient, and Center-of-Pressure Distributions on Triangular Wings Having Supersonic Leading and Trailing Edges for Various Basic Camber Distributions ..... JULIAN H. KAINER 137

On the Sonic Drag of a Slender Body ..... JOHN W. MILES 146

Response Matrix Method of Rotor Blade Analysis ..... ALEX BERMAN 155

Heat Transfer to an Incompressible Turbulent Boundary Layer and Estimation of Heat-Transfer Coefficients at Supersonic Nozzle Throats ..... MERWIN SIBULKIN 162

Stress Distribution, Instability, and Free Vibration of Beam Grid-Works on Elastic Foundations ..... HUGH L. COX AND PAUL H. DENKE 173

Readers' Forum ..... 177–192



*Published by*

INSTITUTE OF THE AERONAUTICAL SCIENCES, INC.

# JOURNAL OF THE AERONAUTICAL SCIENCES

*Editor:* W. R. SEARS
*Director, Graduate School of Aeronautical Engineering, Cornell University*

*Associate Editor:* ROBERT R. DEXTER *Managing Editor:* RITA J. TURINO
*Editorial Assistant:* CAROLINE TAYLOR

## Editorial Committee

**Aerodynamics and Fluid Mechanics**
Holt Ashley
H. Julian Allen
Dean R. Chapman
Francis H. Clauser
Hugh L. Dryden
John C. Evvard
Antonio Ferri
Alexander Flax
Wallace D. Hayes
R. T. Jones
Carl Kaplan
H. W. Liepmann
C. C. Lin
H. F. Ludloff
Harold Luskin
Clark B. Millikan
C. D. Perkins
H. J. E. Reid
George S. Schairer
G. B. Schubauer
John Stack
Theodore Theodorsen
Arthur N. Tifford
Th. von Karman

**Flight Testing**
R. R. Gilruth
Melvin N. Gough
W. L. Howland
W. F. Milliken, Jr.

**Rotating Wing Aircraft**
F. B. Gustafson
K. H. Hohenemser
Bartram Kelley
R. B. Maloy
Ralph McClarren
R. H. Miller
R. H. Prewitt
Igor I. Sikorsky

**Structures**
John E. Duberg
N. J. Hoff
Samuel Levy
J. F. McBrearty
W. Ramberg
E. E. Sechler
F. R. Shanley
C. R. Strang
S. Timoshenko

**Meteorology**
C. F. Brooks
D. M. Little
F. W. Reichelderfer
K. C. Spengler

**Vibration and Flutter**
Lee Arnold
M. A. Biot
R. L. Bisplinghoff
Harold A. Cheilek
I. E. Garrick
Martin Goland

**Aircraft Design**
W. E. Beall
E. H. Heinemann
Hall L. Hibbard
Richard Hutton
C. L. Johnson
A. A. Kartveli
E. G. Stout
F. K. Teichmann
Robert J. Woods

**Electronics**
Welcome W. Bender
K. C. Black
M. V. Kiebert, Jr.
David S. Little
S. B. Rogers
Paul Rosenberg
L. M. Sherer

**Physiologic Problems**
H. G. Armstrong
Louis H. Bauer
Robert J. Benford
W. Randolph Lovelace, II
Ross A. MacFarland

**Flight Propulsion**
William Bollay
George W. Brady
R. P. Kroon
Frank E. Marble
Abe Silverstein
Martin Summerfield
E. S. Taylor

**Instruments**
Allan G. Binnie
Charles H. Colvin
Frank R. Cook
C. S. Draper
S. G. Eskin
C. F. Savage
R. C. Sylvander

## SUBSCRIPTION RATES

JOURNAL OF THE AERONAUTICAL SCIENCES, Published Monthly.—United States and Possessions: 1 Year, $15.00; Single Copies, $1.50. Foreign Countries Including Canada (American Currency Rates): 1 Year, $16.00; Single Copies, $1.50.

AERONAUTICAL ENGINEERING REVIEW, Published Monthly.—United States and Possessions: 1 Year, $3.00; Single Copies, $0.50. Foreign Countries Including Canada (American Currency Rates): 1 Year, $3.50; Single Copies, $0.50.

Notices of change of address should be sent to the Institute at least 30 days prior to actual change of address.

Manuscripts for publication, proofs, and all correspondence should be addressed to the Editorial Office of the JOURNAL.

Correspondence regarding subscriptions may be addressed to the Editorial Office of the JOURNAL OF THE AERONAUTICAL SCIENCES, 2 East 64th Street, New York 21, N.Y., or to the Publication Office, 20th and Northampton Sts., Easton, Pa.

© *Copyright, 1956, by the Institute of the Aeronautical Sciences, Inc.*

Entered as Second Class Matter at the Post Office, Easton, Pa., May 1, 1937. Acceptance for mailing at a special rate of Postage provided for in the Act of August 24, 1912. Authorized April 29, 1937.

JOURNAL OF THE AERONAUTICAL SCIENCES

VOLUME 23 FEBRUARY, 1956 NUMBER 2

# Transition Studies and Skin-Friction Measurements on an Insulated Flat Plate at a Mach Number of 5.8*

ROBERT H. KORKEGI†

*California Institute of Technology*

SUMMARY

An investigation of transition and skin friction on an insulated flat plate, 5 by 26 in., was made in the GALCIT 5 by 5 in. Hypersonic Wind Tunnel at a nominal Mach Number of 5.8.

The phosphorescent lacquer technique was used for transition detection and was found to be in good agreement with total-head rake measurements along the plate surface and pitot boundary-layer surveys. It was found that the boundary layer was laminar at Reynolds Numbers of at least $5 \times 10^6$. Transverse contamination caused by the turbulent boundary layer on the tunnel sidewall originated far downstream of the flat plate leading edge at Reynolds Numbers of 1.5 to $2 \times 10^6$, and spread at a uniform angle of $5^1/_2°$ compared to $9^1/_2$ degree in low-speed flow.

The effect of two-dimensional and local disturbances was investigated. The technique of air injection into the boundary layer as a means of hastening transition was extensively used. Although the onset of transition occurred at Reynolds Numbers as low as $10^6$, a fully developed turbulent boundary layer was not obtained at Reynolds Numbers much below $2 \times 10^6$ regardless of the amount of air injected.

A qualitative discussion of these results is given with emphasis on the possibility of a greater stability of the laminar boundary layer in hypersonic flow than at lower speeds.

Direct skin-friction measurements were made by means of the floating element technique, over a range of Reynolds Numbers (based on distance from flat plate leading edge) from $10^6$ to $4 \times 10^6$. Without artificial tripping, the boundary layer was verified as being laminar over the complete range. With air injection, turbulent shear was obtained only for Reynolds Numbers greater than $2 \times 10^6$, this value being in good agreement with earlier results of this investigation. The turbulent skin-friction coefficient was found to be approximately 0.40 of that for incompressible flow for a constant value of $R_\theta$, and 0.46 for an effective Reynolds Number between 5 and $6 \times 10^6$.

Received November 29, 1954.

* The work described in this paper was undertaken in the Hypersonic Wind Tunnel Laboratory, Guggenheim Aeronautical Laboratory, California Institute of Technology, under joint sponsorship of Army Ordnance and Air Force on Contract No. DA-04-495-Ord-19.

† Formerly, Research Engineer. Now, Research Associate, Engineering Center, University of Southern California.

SYMBOLS

| | | |
|---|---|---|
| $C_f$ | = | local skin-friction coefficient, $\tau_w/q$ |
| $H$ | = | boundary-layer shape parameter, $\delta^*/\theta$ |
| $M$ | = | Mach Number |
| $M_a$ | = | mass flow of air jets per unit span (slugs/sec./in.) |
| $M_{\delta^*}$ | = | boundary-layer mass defect per unit span, $\rho_\infty U_\infty \delta^*$ (slugs/sec./in.) |
| $m$ | = | $100 \times M_a/M_{\delta^*}$ (per cent) |
| $p$ | = | pressure (lbs./sq.in.) |
| $Re$ | = | free stream Reynolds Number, $u_\infty x/\nu_\infty$ |
| $Re/\text{in.}$ | = | Reynolds Number per in., $u_\infty/\nu_\infty$ (1/in.) |
| $R_{\delta^*}$ | = | Reynolds Number based on displacement thickness, $u_\infty \delta^* \nu_\infty$ |
| $R_\theta$ | = | Reynolds Number based on momentum thickness, $u_\infty \theta/\nu_\infty$ |
| $T$ | = | temperature (°F. or °R.) |
| $u$ | = | $x$-component of velocity (ft./sec.) |
| $x$ | = | streamwise distance from flat plate leading edge (in.) |
| $y$ | = | vertical distance from plate surface (in.) |
| $\gamma$ | = | ratio of specific heats |
| $\delta$ | = | boundary-layer thickness (based on $u/u_\infty = 0.995$) (in.) |
| $\delta^*$ | = | boundary-layer displacement thickness (in.) |
| $\theta$ | = | boundary-layer momentum thickness (in.) |
| $\mu$ | = | absolute viscosity (lb. sec./sq.ft.) |
| $\nu$ | = | kinematic viscosity (sq.ft./sec.) |
| $\rho$ | = | density (slugs/cu. ft.) |
| $\tau$ | = | shear stress (lbs./sq.in.) |

*Subscripts*

| | | |
|---|---|---|
| $i$ | = | incompressible value |
| $0$ | = | stagnation or reservoir conditions |
| $w$ | = | conditions at wall (flat plate surface) |
| $\infty$ | = | free-stream conditions |

## (I) INTRODUCTION

TRANSITION AND SKIN FRICTION in the hypersonic regime are of great interest at present. Drag, performance, and heat-transfer rates depend on the location of transition on the surface of a body in flight.

While the effects of free-stream turbulence, pressure gradients, surface curvature, surface roughness, and heat transfer on transition are at least known qualitatively,[1] the effect of compressibility in the high Mach Number range is still subject to speculation. At low supersonic Mach Numbers various wind-tunnel tests indicate a general decrease of transition Reynolds Number with increasing Mach Number.[2, 3]

What causes transition from laminar to turbulent boundary layers to occur? Tollmien and Schlichting predicted that transition is caused by the selective amplification of small disturbances originating within the laminar boundary layer, and gave a limiting Reynolds Number ($Re_{crit.}$) below which no amplification occurs. Later, Taylor proposed that turbulence in the free stream produces pressure pulses which cause intermittent separation of the boundary layer and eventual transition. Subsequently, the latter was found to correspond to the case where large free-stream turbulence is present, while the former type of instability, verified experimentally by Schubauer and Skramstad,[4] was found to exist in flows with a very low turbulence level.[1, 5]

Lees and Lin[6, 7] contributed a revision and extension of the small disturbance theory to compressible flows. Van Driest[8] made calculations based on the Lees-Lin theory in the supersonic regime. His results indicate a substantial decrease in critical Reynolds Number with increasing Mach Number for a laminar boundary layer on an insulated flat plate. For example, at a Mach Number of 5, the critical Reynolds Number is less than 200, compared to a value of about 80,000 in low-speed flow. On this basis, one might conclude that compressibility has the effect of decreasing the stability of the boundary layer. It should be noted, however, that transition is also dependent upon the amplification rates and wave lengths of laminar disturbances, for which there are presently no calculations at high Mach Numbers.

The present transition studies were prompted by preliminary surveys on a flat plate at a Mach Number of 5.8, which indicated extensive laminar layers and the inability of induced disturbances to produce transition at low Reynolds Numbers.

The second part of this work deals with direct measurements of surface shear. Quantitatively, emphasis was placed on turbulent skin-friction measurements at a Mach Number of 5.8. Theoretically, the state of the art is well exemplified by the large scatter of predictions of turbulent skin friction on an insulated flat plate at high Mach Numbers.[9] In the hypersonic regime it is probable that fluctuations of the properties of state of air become as important as velocity fluctuations in a turbulent boundary layer. An extensive discussion of the theoretical literature on turbulent boundary layers is given by Coles.[10]

Experimentally, direct measurements of turbulent skin friction on insulated flat plates were made by Dhawan[11] in subsonic flow, by Hakkinen[12] in the transonic regime, and by Coles[10] in supersonic flow. Measurements on bodies of revolution in supersonic flow were made by Chapman and Kester,[9] and by Bradfield, DeCoursin, and Blumer.[13] The measurements of Coles which extend the range of knowledge of turbulent surface shear to a Mach Number of 4.5 are particularly significant.

The technique employed by the aforementioned investigators and the present writer makes use of a floating element which constitutes a portion of the working surface of the model. The shear force on the element is measured by a sensitive balance system. Developmental work of this technique applied to local measurements of aerodynamic friction was undertaken by Dhawan[11] under Liepmann. The present balance system is essentially a modification of Dhawan's with the addition of a nul-return device.

A comprehensive discussion of this work is reported by the writer in his thesis.[14]

The writer wishes to thank Profs. Henry T. Nagmatsu, Hans W. Liepmann, Lester Lees, and Donald E. Coles for many helpful suggestions and discussions throughout the course of the research described in this paper.

## (II) Experimental Equipment and Techniques

The research described in this paper was conducted in the GALCIT 5 by 5 in. Hypersonic Wind Tunnel at a nominal Mach Number of 5.8. All tests were made at a fixed reservoir temperature of 225°F., over a range of reservoir pressures from 35 to 110 lbs. per sq.in. absolute. The temperature was selected to yield the maximum Reynolds Number per in. at the highest pressure, while ensuring the absence of condensation of air components in the test section.[15] An extensive description of the experimental facilities is given in reference 16.

### (1) *Transition Survey Flat Plate*

The extensive laminar layers noted on flat plates at a Mach Number of 5.8 in the present tunnel pointed to the need for a very long model—i.e., high Reynolds Numbers—for transition studies. For this purpose, full advantage was taken of the large uniform flow rhombus at this high Mach Number, permitting model lengths of the order of 30 in. A practical limitation was imposed by waves emanating from the tunnel side walls near the nozzle throat and crossing the test section centerline approximately 13 in. downstream, where their strength resulted in a local 5 to 10 per cent rise in free-stream static pressure. An allowance for these waves would have demanded a reduction of the plate length beyond any usefulness for transition studies and subsequent turbulent skin-friction measurements, while the effect of their presence on the boundary layer on a long flat plate admittedly limited the quantitative interpretation of data in laminar regions. However, as is later shown, extensive laminar layers were observed to exist up to Reynolds Numbers of $5 \times 10^6$ in spite of these waves.

In the final analysis, it was decided to make the flat plate 26 in. long ($Re_{max}$ of the order of $6 \times 10^6$), and to locate the leading edge 6 in. downstream of the throat section, as shown in Fig. 1. The flat plate is equipped with 22 orifices for surface pressure measurements, 16 of which are evenly distributed along the centerline, with six copper-constantan thermocouples for surface temperatures, and with a spanwise row of small holes $1\frac{1}{2}$ in. behind the leading edge, for air injection into the boundary layer. The air jet holes have a 0.013-in. diameter and a spacing of 3/16 in., and lead to a common manifold fed by a line extending outside the tunnel to a flowmeter. Atmospheric air was used for the jets, and the flow rate was controlled by a needle valve and registered on the flowmeter.

#### (2) *Transition Detection Techniques*

Two techniques were used for transition detection: (1) a traversing total-head rake and (2) a luminescent lacquer. The total-head rake consists of seven tubes evenly spaced across one-half of the 5-in. span and 1/16 in. above the surface of the flat plate, as shown in Fig. 2. The vertical position of the tubes was chosen to yield a substantial increment in impact pressure between laminar and turbulent boundary layers which, over a large extent of the plate, were of the order of 1/5 to 1/2 in. thick.

The second technique for transition detection is dependent upon the more rapid drying of a lacquer compound in turbulent areas than in laminar ones.[17] Phosphor pigment in the lacquer gives it the property of fluorescing under ultra-violet irradiation when dry while remaining dark when wet, thus visually defining regions of turbulence. The lacquer was finely sprayed over the working surface of the plate by means of an air gun. The composition and drying times for the lacquer used in this work are given in reference 14.

#### (3) *Skin-Friction Instrument*

A floating surface element, 1 by 1/4 in., is located at $x = 15.5$ in., on the centerline of a second 26 by 5 in. flat plate. The plate is identical in geometry and similar in construction to that used for transition studies, and has a row of holes for air injection and seven pressure orifices in common with the latter. The basic design of the skin-friction instrument is essentially that of Dhawan,[11] with particular emphasis placed on compactness and temperature insensitivity. The floating element is fixed to a vertical frame suspended by two thin flexures to a $1\frac{3}{4}$ in. diameter circular disc which is provided with a rectangular slot for the element. The disc, when inserted into a cutout in the flat plate, becomes part of the working surface. The instrument is thus self-contained and can easily be removed from the flat plate without requiring disassembly of its component parts. An exploded view of the instrument is shown in Fig. 3.

Several parts of the instrument were made of Invar (low expansion alloy steel) in order to minimize differential expansion at high temperatures. Total depth of the instrument is less than $1\frac{1}{8}$ in. Its spring constant is 0.11 lbs. per in. and its natural frequency approximately 30 cycles per sec. The position of the floating element was determined to within a few microinches by means of a Schaevitz linear variable differential transformer.[18]

#### (4) *Chain-Loading Null System*

The main departure from the instrument developed by Dhawan is in the use of a null-return device. This device makes use of the weight of a jeweler's chain to balance the shear drag on the floating element. The principle is that of the chainomatic balance commonly used in chemical laboratories. It has the inherent advantages of simplicity, continuous force variation, adaptability to remote control, and a wide choice of ranges permitting accurate measurements of very small forces.

The use of chain-loading was dependent upon a frictionless means of converting a vertical force (chain weight) into a horizontal restoring force. This was accomplished with a symmetrical W-shaped linkage, the ends of which are fixed to the balance housing, and its center to the frame supporting the floating element, as shown in Fig. 4. The loading chain is suspended from the apices of the W-linkage (load transfer linkage) so that a variable differential force is obtained by progressively increasing the chain length on one side and decreasing it on the other.

The chain system was not only found to be insensitive to tunnel vibrations, but also to provide substantial damping of the instrument. This is due to the fact that the frequency spectrum of the chain is substantially different from that of the skin-friction instrument and that of the tunnel.

The effect of thermal expansion on the system is very small at the operating temperature used in the tests. The balance assembly shown in Fig. 4 illustrates the operation of the nulling device and the method of calibration. An extensive description of the skin-friction instrumentation and sources of error is given in reference 14.

### (III) Transition and Boundary-Layer Studies

#### (1) *Flat Plate Flow Characteristics*

The flat plate surface pressures are shown in Fig. 5 for representative reservoir pressures from 47 to 110 lbs. per sq.in. absolute, corresponding to a range of Reynolds Numbers per inch from 1.07 to $2.50 \times 10^5$. The positive pressure gradient over the downstream end of the plate is attributed to a fan of waves caused by the flat plate bow wave interaction with the boundary layer on the nozzle wall. Some attempts were made to eliminate it by reflecting the waves away from the plate surface. However, while this gradient was cancelled, other equally undesirable pressure nonuniformities resulted. The surface temperatures yield

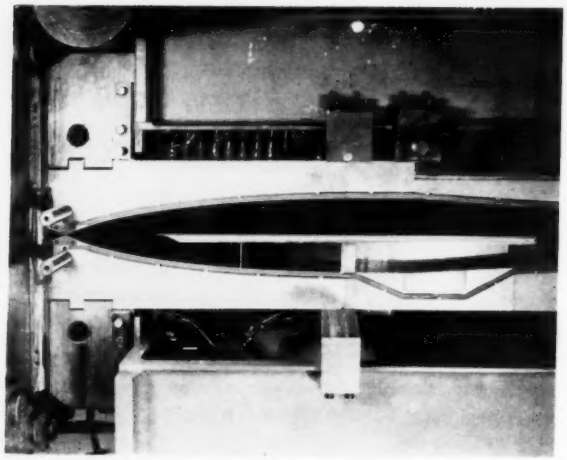

FIG. 1. Transition survey flat plate in hypersonic wind tunnel.

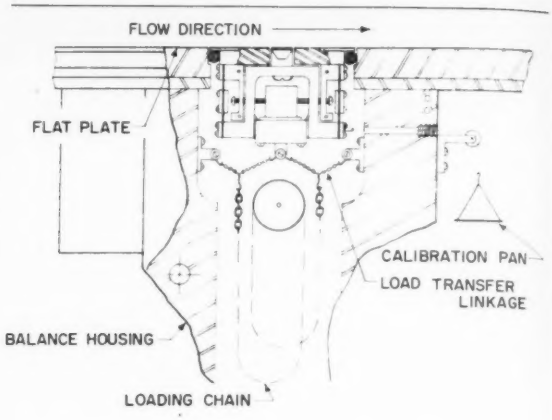


BALANCE ASSEMBLY
FIG. 4

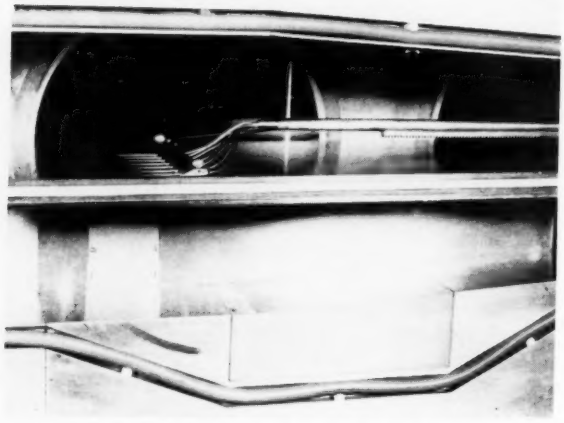

FIG. 2. Total head rake on the flat plate.

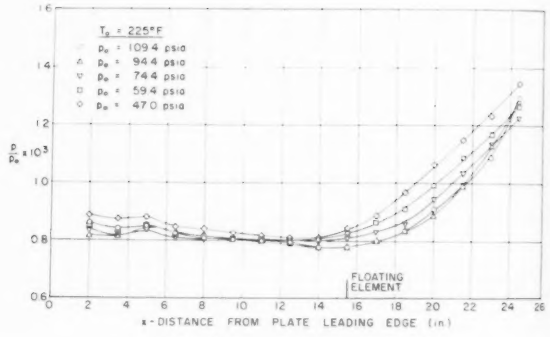
$T_o$ = 225°F
$p_o$ = 109.4 psia
$p_o$ = 94.4 psia
$p_o$ = 74.4 psia
$p_o$ = 59.4 psia
$p_o$ = 47.0 psia
$\frac{p}{p_o} \times 10^3$
FLOATING ELEMENT
x - DISTANCE FROM PLATE LEADING EDGE (in.)

FLAT PLATE SURFACE PRESSURES
FIG. 5

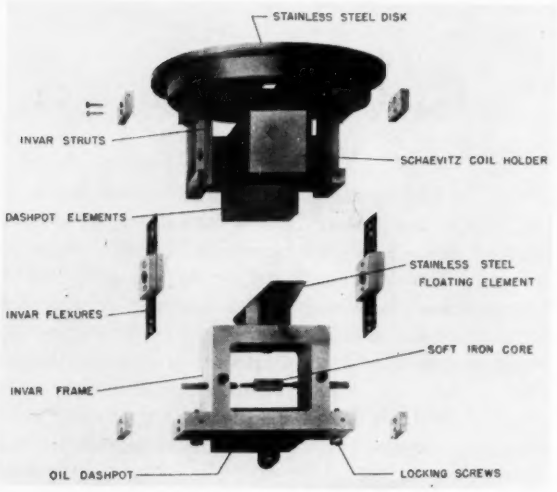


FIG. 3 Exploded view of balance system.

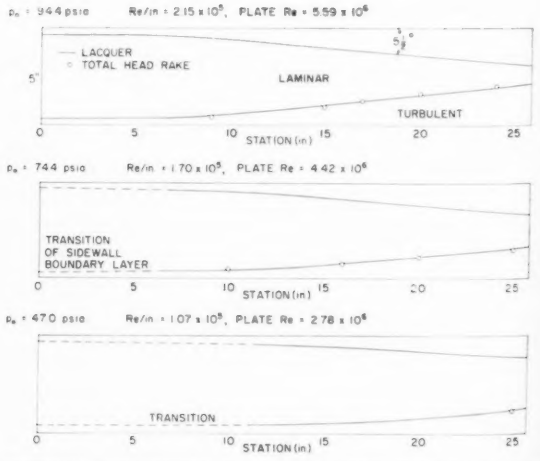
$p_o$ = 94.4 psia Re/in = 2.15 x $10^5$, PLATE Re = 5.59 x $10^6$
LACQUER
TOTAL HEAD RAKE
LAMINAR
TURBULENT
STATION (in.)
$p_o$ = 74.4 psia Re/in = 1.70 x $10^5$, PLATE Re = 4.42 x $10^6$
TRANSITION OF SIDEWALL BOUNDARY LAYER
STATION (in.)
$p_o$ = 47.0 psia Re/in = 1.07 x $10^5$, PLATE Re = 2.78 x $10^6$
TRANSITION
STATION (in.)

TRANSVERSE CONTAMINATION AND SIDEWALL BOUNDARY LAYER ON FLAT PLATE AT DIFFERENT REYNOLDS NUMBERS
FIG. 6

recovery factors of 0.86 to 0.88, thus indicating an essentially insulated model.[19]

The effect of the throat waves mentioned earlier is that of thickening the laminar boundary layer downstream of the interaction, thus leading to a higher effective Reynolds Number than that measured from the flat plate leading edge. Boundary-layer velocity profiles upstream and downstream of this interaction are similar, thus indicating that local distortions of the flow are rapidly damped. In the following sections the discussion is based on plate (or uncorrected) Reynolds Number since the effective *Re* is unknown; however, this factor imposes no severe restrictions in view of the qualitative nature of most of the laminar results.

#### (2) *Transition by Transverse Contamination*

Transition by transverse contamination due to the mixing of the turbulent sidewall boundary layer with the laminar boundary layer on a flat plate was first noted by Charters[20] in 1939. His experiments performed in low-speed flow showed that contamination spread from the plate leading edge at a uniform angle of $9^1/_2°$ independent of speed in the 20 to 60 m.p.h. range. That this phenomenon can be considered a mixing process was suggested by Liepmann in an Appendix to reference 20. In more recent experimental research in compressible flow, Liepmann, Roshko, and Dhawan[21] incidentally noted transverse contamination which spread from the leading edge of a flat plate at an angle of approximately 9° at $M = 1.4$.

The present experiments at $M = 5.8$ yielded two important results: (1) transverse contamination spread at a uniform angle of $5^1/_2°$, and (2) it originated far downstream of the leading edge of the flat plate at Reynolds Numbers of approximately 1.5 to $2 \times 10^6$.

While the boundary layer on the tunnel sidewall was partially laminar at lower reservoir pressures, the origin of transverse contamination on the flat plate always occurred at a substantial distance downstream of transition on the sidewall. This fact, coupled with the results of later findings, appears to indicate greater stability of the laminar boundary layer. Fig. 6 illustrates the growth of the sidewall boundary layer and eventual spread of transverse contamination for *Re*/in. of 2.15, 1.70, and $1.07 \times 10^5$. As is shown, agreement between the lacquer and the total-head rake results is quite good.

The smaller angle of spread of transverse contamination compared with that for low-speed flow is attributed to the large temperature extremes present in the thermal layer in hypersonic flow. This argument is substantiated by theoretical and experimental work on the effect of temperature variations on the mixing and divergence of free jets. In a theoretical treatise on two-dimensional jet mixing of a compressible fluid, Pai[22] predicts greater divergence of the mixing when the jet temperature is higher than that of the surrounding medium, and lesser divergence for lower jet temperatures. Experimental evidence of the more rapid spread of a turbulent jet as its temperature is raised above that of the receiving medium is supplied by the work of Corrsin and Uberoi.[23]

For the present case, the static temperature throughout most of the turbulent boundary layer is close to that of the free stream, or cold (cf. Fig. 11), whereas through most of the laminar boundary layer, the temperature is close to that of the wall, or hot (cf. Fig. 10). The ratio of wall to free-stream temperature at $M = 5.8$ is approximately seven. Thus the present case corresponds to a cooled turbulent jet exhausting into a hot surrounding medium, and, therefore, the angle of spread is smaller.

For the case of $M = 1.4$,[21] no measurable effect of compressibility on the angle of spread was noted, most probably because the effective temperature difference between the laminar and the turbulent boundary layers is small, being only 30 or 40 per cent.

#### (3) *Induced Transition*

The results of the investigation of transverse contamination also revealed the conspicuous absence of natural transition at Reynolds Numbers in excess of $5 \times 10^6$. Means of tripping transition artificially were investigated in order to study the effects of disturbances on the flow and the properties of the turbulent boundary layer. Particular emphasis was placed on the method of injecting small amounts of air into the boundary layer through surface holes in the plate. This technique was explored by Fage and Sargent[24] as a means of fixing transition by adjusting the rate of injection, and recently used by Coles[10] who presents a discussion of the local effect of the jets on the boundary layer.

*Local Disturbances*—Air was injected into the boundary layer through single orifices along the plate centerline over a range of Reynolds Numbers from $10^6$ to $3 \times 10^6$. The luminescent lacquer revealed what is interpreted as two spiral vortices generated on either side of the air jet, each individually leading to transverse contamination of the boundary layer at a substantial distance downstream of the jet. The distance between the jet and the beginning of contamination decreased as the Reynolds Number of the point of injection was increased; however, contamination never started at the point of injection over the range investigated. The corresponding Reynolds Number increment varied from approximately $1.3 \times 10^6$ to $0.65 \times 10^6$ as the jet was displaced from a Reynolds Number of $1.1 \times 10^6$ to $3 \times 10^6$, and the included angle of spread of contamination was approximately 10°. From these results immediate contamination from the jets may not be expected at *Re* below 4 or $5 \times 10^6$.

Small rods 0.25 in. long and 0.028 in. in diameter were mounted normal to the surface of the flat plate at *Re* of $1.1 \times 10^6$ and $1.7 \times 10^6$, respectively. These proved ineffective in producing transition. The wake of the rods was traced downstream with no sign of transverse contamination of the boundary layer.

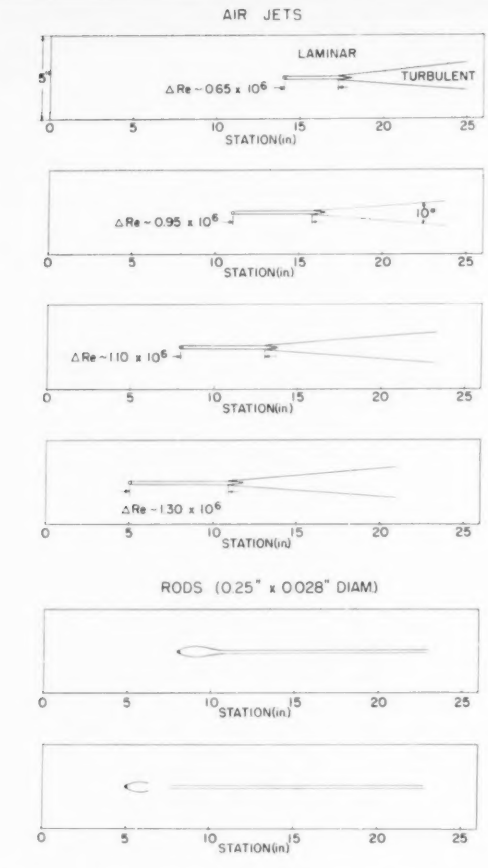


CONTAMINATION ON FLAT PLATE DUE TO LOCAL DISTURBANCES
$p_o$ = 94.4 psia, Re/in = 2.15 x $10^5$, PLATE Re = 5.59 x $10^6$

FIG. 7

In Fig. 7 is sketched the wake and transverse contamination induced by the air jets, and the wake with the absence of transverse contamination behind the rods.

*Two-Dimensional Disturbances*—Variable rates of air were injected into the boundary layer through the row of surface holes $1^1/_2$ in. behind the leading edge of the plate. Transition was observed to move gradually upstream as the mass flow injected was increased to 2 per cent of the boundary-layer mass defect ($m = 2$). A further increase in the rate of injection did not measurably decrease the transition Reynolds Number below $2 \times 10^6$. At the higher reservoir pressures it was also possible to detect transition from local rises in the surface pressures along the flat plate, as shown in Fig. 8. The pressure peaks are associated with the end of the transition region. In his measurements on a flat plate, Coles[10] found that these peaks occur slightly downstream of the point of maximum surface shear. Fig. 8 shows that, for a $Re$/in. of $2.5 \times 10^5$, there is already no appreciable change in the pressure rise, and hence $Re_t$, as $m$ is increased from 1.3 to 1.9.

Distributed surface roughness and single wire trips proved ineffective in hastening transition. In particular, the only effect of a wide, coarse sandstrip (50 grit emery paper) on the tunnel sidewall at a $p^0$ of 47 lbs. per sq.in. absolute was to thicken the laminar boundary layer.

### (4) *Boundary-Layer Characteristics*

What are the characteristics of the boundary layer at a Mach Number of 5.8? The profiles presented below are considered typical of the laminar and turbulent boundary layers at $M = 5.8$.

Measurements of impact pressure, static pressure, and total temperature—i.e., total energy—distributions in the boundary layer completely determine the velocity profile. The present surveys were made with a pitot probe. Sample static pressure surveys through the boundary layer indicated a maximum variation only slightly greater than 1 per cent, thus verifying the near constancy of the pressure. Hence, the surface pressure on the plate was taken as that prevailing throughout the boundary layer. In lieu of total temperature measurements, the conservation of energy equation was used with a Prandtl Number correction ($Pr = 3/4$) whereby conditions in the free stream and on the plate surface ($T_w$) were satisfied. Actually, the profiles thus obtained varied little from those resulting from the assumption of $Pr = 1$ (constant total enthalpy).

Typical impact pressure distributions in a laminar and a turbulent boundary layer at $M = 5.8$ are shown in Fig. 9.

*Laminar Boundary Layer*—Profiles of velocity, Mach Number, density, and temperature for a typical laminar boundary layer on an insulated flat plate are given in Fig. 10. The conventional dimensionless parameter $(y/x)\sqrt{Re}$ was not used since the actual $Re$ is unknown. $\delta$, $\delta^*$, and $\theta$ are much larger than the theoretical values based on Reynolds Number measured from the leading edge. This fact is due to the interaction of the throat waves with the boundary layer on the flat plate, as discussed earlier. It was, hence, necessary to define the profiles in terms of the local properties of the boundary layer. The choice of $y/\theta$ was made because $(\theta/x)\sqrt{Re}$ varies little with Mach Number and is of order unity. The wall slope of the velocity profile was obtained from local surface shear measurements discussed later.

The velocity profile is almost linear as originally predicted by von Karman and Tsien.[25] That the hypersonic boundary layer is so clearly defined physically can be partly explained from consideration of the viscous dissipation $\mu(\partial u/\partial y)^2$. While the viscous dissipation becomes small near the edge of the boundary layer, a large velocity gradient $\partial u/\partial y$ can be sustained since the viscosity (or temperature) drops rapidly to its relatively low free-stream value. The viscosity drops by almost a factor of ten from the wall to the edge of the boundary layer. The theoretical boundary-layer Mach Number distribution given by Van Driest[26] for a free-stream Mach Number of 6, when converted

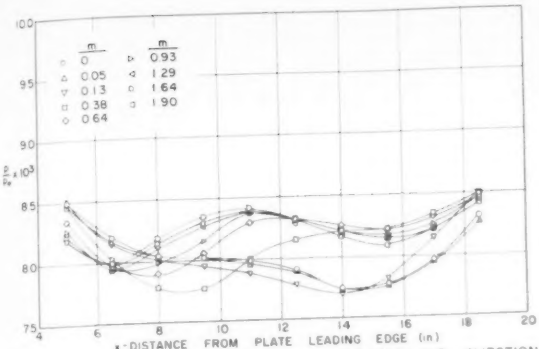


FLAT PLATE SURFACE PRESSURES WITH VARIABLE AIR INJECTION
$p_o$ = 109.4 psia, $T_o$ = 225°F, Re/in = 2.50 x $10^5$
FIG. 8

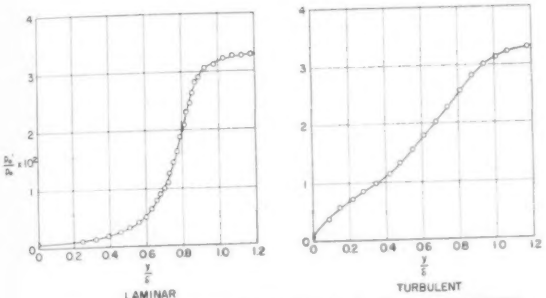


TYPICAL IMPACT PRESSURE DISTRIBUTION IN THE BOUNDARY LAYER AT M = 5.8
FIG. 9

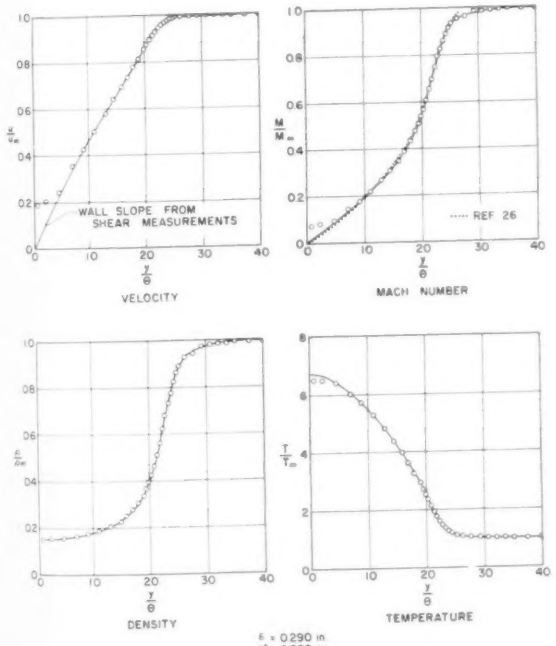


δ = 0.290 in.
δ* = 0.209 in.
θ = 0.0102 in.
$R_\theta$ = 2190
$p_o$ = 94.4 psia, $T_o$ = 225°F

DISTRIBUTION OF FLOW VARIABLES IN A TYPICAL LAMINAR BOUNDARY LAYER AT M = 5.8
FIG. 10

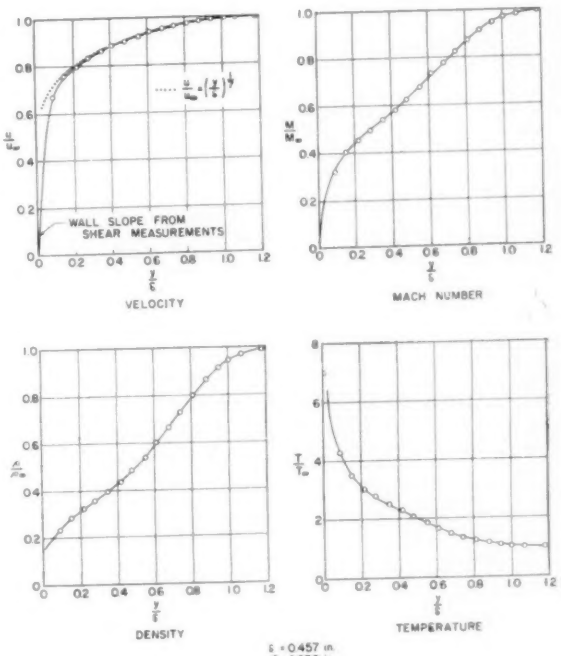


δ = 0.457 in.
δ* = 0.256 in.
θ = 0.0162 in.
$R_\theta$ = 4040
$p_o$ = 109.4 psia, $T_o$ = 225°F

DISTRIBUTION OF FLOW VARIABLES IN A TYPICAL TURBULENT BOUNDARY LAYER AT M = 5.8
FIG. 11

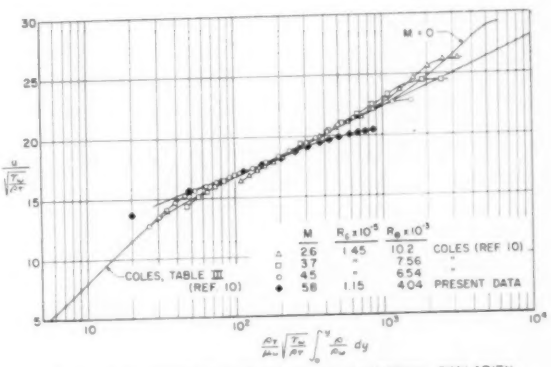


TURBULENT PROFILES ACCORDING TO FUNCTIONAL SIMILARITY
FIG. 12

TABLE 1
Laminar Boundary Layer Parameters

$M = 5.8$; $P_0 = 94.4$ psia; $T_0 = 225°$F.; $Re$/in. $= 2.15 \times 10^6$; $T_\infty = 88°$R.

| $\theta$ (in.) | $\delta^*$ (in.) | $H$ | $\delta^*/\delta$† | $R_\theta$ | $C_f \times 10^{-4}$ |
|---|---|---|---|---|---|
| 0.00377 | 0.0801 | 21.2 | 0.728 | 810 | |
| 0.00448 | 0.0841 | 19.8 | 0.697 | 964 | |
| 0.00839 | 0.1777 | 21.1 | 0.787 | 1800 | |
| 0.01018 | 0.2088 | 20.5 | 0.720 | 2190 | 2.5 |
| Young & Janssen (reference 27) $M = 5.8$; $T_\infty = 100°$R. | | 24.5 | 0.810 | | |

† Based on $u/u_\infty = 0.995$ for both measurements and reference 27.

from $(y/x)\sqrt{Re}$ to $y/\theta$,† is in excellent agreement with the present experimental results. Van Driest utilizes the Crocco method of solution of the boundary-layer equations assuming a Prandtl Number of 3/4 and the Sutherland formula for viscosity. The large density gradient near the edge of the laminar boundary layer (cf. Fig. 10) appears as a narrow dark line over the model surface through schlieren visualization.

The characteristic parameters of the laminar boundary layer are listed in Table 1. It is to be noted that the displacement thickness is almost 3/4 of the boundary-layer thickness due to the very low mass flow in the laminar layer.

An extensive survey of theoretical literature on the compressible laminar boundary layer is given by Kuerti[28] and also by Bradfield, DeCoursin, and Blumer.[13]

*Turbulent Boundary Layer*—Profiles of velocity, Mach Number, density, and temperature for a typical turbulent boundary layer on an insulated flat plate at $M = 5.8$ are given in Fig. 11. The turbulent boundary layer is characterized by an almost linear density profile which appears as a region of uniform light intensity through schlieren visualization. The velocity profile follows very closely the one-seventh power law as was also noted for a turbulent velocity profile at a Mach Number of 7 by Wegener, Winkler, and Sibulkin at NOL.[29]

Fig. 12 compares a velocity profile at $M = 5.8$ with profiles obtained by Coles at Mach Numbers of 2.6, 3.7, and 4.5, in a coordinate system based on a formulation of similarity in compressible turbulent boundary layers proposed by Coles.[10, 30] The parameter $\rho_\tau$, or friction density, in Fig. 12 is chosen arbitrarily to give agreement with incompressible data. The value of $\rho_\tau/\rho_w$ is 1.81 for the velocity profile at $M = 5.8$.

In Table 2 is given a list of experimentally obtained turbulent boundary-layer parameters at $M = 5.8$ and the corresponding calculated values for one-fifth and one-seventh power profiles.[31] The agreement between the experimental parameters for $R_\theta$ of 3,430 and 4,040 with those obtained from the one-seventh power law is noteworthy. The skin-friction results given in Table 2 are discussed below.

A good review and comparison of the theoretical literature on the compressible turbulent boundary layer is presented in reference 10. Literature surveys are also given in references 13 and 32.

### (5) *Discussion*

While experimental data from many supersonic wind tunnels indicate a general decrease of transition Reynolds Number with increasing Mach Number, the present experiments at a Mach Number of 5.8 show a surprisingly high value. Natural transition did not occur below a Reynolds Number of at least $5 \times 10^6$, whereas the value at lower supersonic speeds is of the order of $2 \times 10^6$. Another important result is the inability of artificial disturbances and the sidewall boundary layer to induce transition at Reynolds Numbers much below $2 \times 10^6$.

Of the factors affecting transition, the level of turbulence in the free stream is a very important one in low-speed wind tunnels. Although there are presently no measurements of turbulent fluctuations at supersonic speeds, it is reasonable to assume that these are very small at high Mach Numbers due in part to the large damping effect of the throat of the nozzle on the incoming flow.[33] However, while the free-stream turbulence level is probably low enough so that it has no effect on transition, the boundary layer was found to remain laminar far downstream of induced disturbances. In some cases, such as with the rods, no trace of the disturbance is noted downstream. The disturbance appears to be completely damped, thus tending to indicate a greater stability of the laminar boundary layer at hypersonic Mach Numbers than at lower

† For $M = 6$ and $T_\infty = 100°$ (present experimental value, 88°), $\theta/x\sqrt{Re} = 0.66$.[27]

TABLE 2
Turbulent Boundary-Layer Parameters†

$M = 5.8$; $T_0 = 225°$F.

| $P_0$ (psia) | $M$ | $Re$/in. $\times 10^{-5}$ ($\text{in.}^{-1}$) | $\theta$ (in.) | $R_\theta$ | $\delta^*$ (in.) | $\theta/\delta$ | $\delta^*/\delta$ | $H$ | $C_f \times 10^{-4}$ | $C_f/C_{fi}$‡ | $C_f/C_{fi}$** |
|---|---|---|---|---|---|---|---|---|---|---|---|
| 64.4 | 5.787 | 1.468 | 0.01688 | 2,477 | 0.2380 | 0.0375 | 0.529 | 14.10 | 13.16 | 0.403 | 0.467 |
| 74.4 | 5.770 | 1.695 | 0.01638 | 2,780 | 0.2356 | 0.0361 | 0.519 | 14.38 | 12.75 | 0.400 | 0.463 |
| 94.4 | 5.792 | 2.151 | 0.01594 | 3,429 | 0.2500 | 0.0357 | 0.561 | 15.68 | 12.23 | 0.400 | 0.463 |
| 109.4 | 5.805 | 2.489 | 0.01623 | 4,040 | 0.2562 | 0.0355 | 0.561 | 15.79 | 11.79 | 0.397 | 0.462 |
| | 5.80 | | | | | 0.0340 | 0.546 | 16.08 | — 1/7th Power Law[31] | | |
| | 5.80 | | | | | 0.0365 | 0.610 | 16.70 | — 1/5th Power Law[31] | | |

† Turbulent boundary layer obtained with air jets ($m = 2.8$).
‡ For $R_\theta = R_{\theta i}$ and $C_{fi}$ from Table 1, reference 10.
** For $C_f/C_{fi}$ $R_\theta/R_{\theta i}$ from Table 1, reference 10.

speeds. Similar protuberances in a boundary layer at low speeds would produce almost immediate contamination. With the air jets, contamination does occur, but only at a large distance downstream of the point of injection. This suggests that the rate of amplification of induced velocity fluctuations may be very low. Also, the wave length of propagation of small disturbances in the laminar layer may become very much larger at high Mach Numbers than at low speeds ($\lambda \sim \delta \sim M^2$). Since a finite number of wave lengths is required for these disturbances to become large enough to cause the breakdown of laminar motion, a substantial delay might be expected before transition occurs.† Van Driest's calculations based on the Lees-Lin theory show a progressively decreasing critical Reynolds Number with increasing Mach Number on an insulated flat plate (cf. Introduction). But since transition is also dependent on wave lengths and amplification rates for which there are presently no calculations, no conclusive verification of these analytical results can be made. It should be noted, however, that the Lees-Lin theory is not strictly valid at high Mach Numbers.

The trend of transition with Mach Number is shown in Fig. 13. The data for Mach Numbers from 2 to 4.5 were obtained in the JPL 20-in. wind tunnel.[10] The transition region is defined by curves representing respectively a minimum and a maximum in surface shear. While quantitatively the transition Reynolds Number (upper curve) is dependent upon the effects of the given wind tunnel, qualitatively it is significant that the transition region increases to higher Reynolds Numbers in the higher supersonic regime. The present results and those of Coles[10] indicate that artificial disturbances become progressively less effective in stimulating transition as the Mach Number is increased. In particular, the small effect of surface roughness at high Mach Numbers suggests that a smooth surface is not as essential as in low-speed flow for the existence of extensive laminar layers. Of the various artificial disturbances, air injection proved to be the most effective transition tripping device. It also offers the advantage of control. This feature was fully exploited in the skin-friction investigation discussed below.

## (IV) Skin-Friction Measurements

The flow characteristics over the flat plate are essentially the same as those for the transition studies. The shear measurements in the transition region and in a fully developed turbulent boundary layer were obtained by inducing transition with air injection.

While slight streamwise pressure gradients were present over the element at low reservoir pressures, the flow was relatively uniform at the higher reservoir pressures which were required to obtain a fully developed turbulent boundary layer at $x = 15.5$ in.

† This argument was suggested to the writer by Prof. L. Lees.

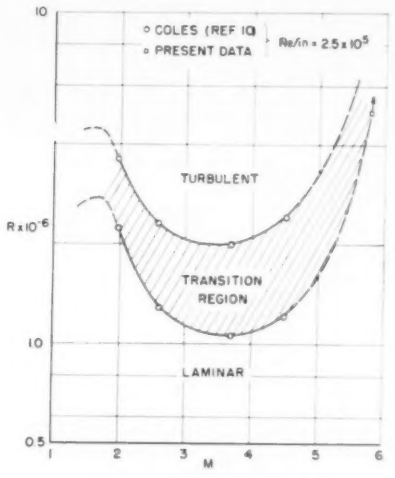


TRANSITION – MACH NUMBER TREND

FIG 13

The Reynolds Number (uncorrected) at the surface element was varied from approximately $10^6$ to $4 \times 10^6$ by proportionately varying the reservoir pressure.

### (1) *Effect of Variable Air Injection on Shear*

Surface shear measurements were made for variable rates of air injection through the row of surface holes near the leading edge. The results are shown in Fig. 14 where each curve represents a fixed Reynolds Number at the element station—i.e., a fixed reservoir pressure. For each condition transition was progressively moved upstream across the element by increasing the intensity of the air jets. The jet mass flow is expressed as a percentage of the mass defect in the boundary layer ($m$).

The measurements for $m = 0$ (no induced disturbance) indicate laminar shear over the whole range of Reynolds Numbers. The finite amount of injection ($m = 0.065$) required to bring the onset of transition over the element at $Re$ of $3.9 \times 10^6$ shows that natural transition must occur at a substantial distance downstream of this point in support of results discussed above. It is also shown in Fig. 14 that, in spite of large rates of air injection, a fully developed turbulent

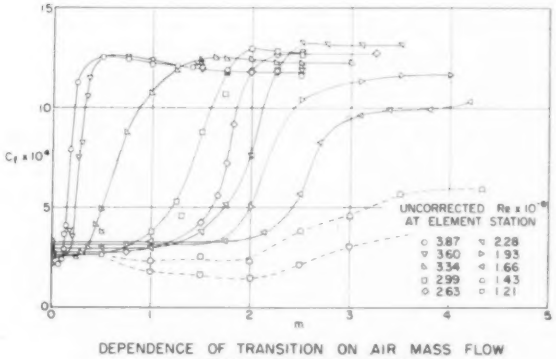


DEPENDENCE OF TRANSITION ON AIR MASS FLOW AT VARIOUS REYNOLDS NUMBERS

FIG 14

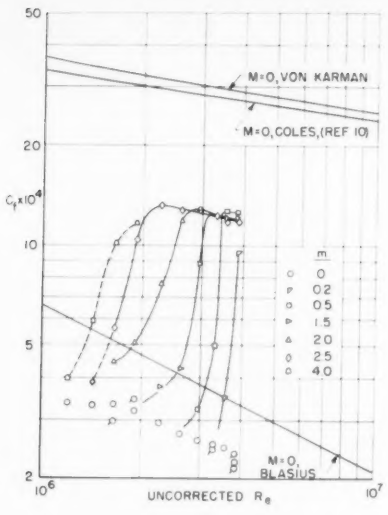


LOCAL SKIN FRICTION AT M = 5.8
FIG. 15

boundary layer is not obtained at Reynolds Numbers below $2 \times 10^6$. The lower four curves ($Re$ 1.2 to 1.9 $\times$ $10^6$) show an almost random rise in surface shear with no indication of eventual flattening as is in the case for the upper curves ($Re > 2 \times 10^6$). It is interesting to note that air injection has no measurable effect on surface shear until the onset of transition, with the exception of the lower two curves in Fig. 14 ($Re$ 1.2 and 1.4 $\times$ $10^6$) where the initial decrease in surface shear is indicative of extensive separation behind the jets, followed by laminar reattachment.

The rapidly increasing rate of air injection required to trip transition as the Reynolds Number is reduced below $4 \times 10^6$ indicates that the mechanism of transition is essentially the same as in low-speed flow. The intensity of the induced disturbance must be substantially magnified in order to accelerate instability of laminar waves.

In Fig. 15 is shown the variation of skin-friction coefficient with Reynolds Number. The transition curves shown correspond to different rates of air injection; however, they are not true transition curves since the data for each Reynolds Number were obtained under different operating conditions ($x$ fixed, $Re$/in. variable). Here it is clearly shown that fully turbulent shear is not obtained below a Reynolds Number of $2.3 \times 10^6$ with $m \geq 2.5$. While the effective Reynolds Numbers of the experimental data are unknown, Fig. 15 offers some measure of comparison with the incompressible predictions of von Karman[34] and Coles.[10]

The consistently low values of laminar skin friction compared with measurements at lower speeds and reasonable theoretical predictions[26, 35, etc.] are indicative of a higher effective Reynolds Number than that measured from the leading edge of the flat plate (uncorrected $Re$). This is in agreement with the results of boundary-layer surveys discussed above. The scatter in the laminar measurements as shown in Fig. 15 is relatively large and hence, with the additional uncertainty of the effective Reynolds Number, the laminar data are of qualitative interest only. By contrast, the turbulent measurements were repeatable within a few per cent. This illustrates the difficulty, also noted by other investigators, in obtaining reliable shear measurements in the laminar boundary layer.

### (2) *Local Turbulent Skin Friction*

While an element of uncertainty enters the determination of the effective free-stream Reynolds Number associated with turbulent skin-friction measurements, the local shear for a fully developed turbulent boundary layer may be uniquely described in terms of local flow properties, in particular the Reynolds Number based on momentum thickness, $R_\theta$. A full discussion of the interpretation of turbulent shear data is given by Coles.[10, 36]

In Fig. 16 are presented turbulent skin-friction data ($m = 2.8$) at $M = 5.8$ in terms of $R_\theta$. The corresponding boundary-layer parameters are given in Table 2. The measurements of Coles[10] and Hakkinen[12] on a flat plate and Chapman and Kester[9] on a cylinder serve to illustrate the effect of Mach Number on turbulent skin friction. No correction for cylinder curvature was applied to the data of Chapman and Kester since it is estimated to be very small. The incompressible reference chosen for Fig. 16 is that of Coles[10] since it offers very good agreement with low-speed experimental data for $Re > 10^6$ (cf. Fig. 8 of reference 12 and Figs. 1 and 2 of reference 10).

As shown in Figs. 14 and 15, the maximum value of $C_f$ observed was approximately 0.00130. Values of $C_f$ at Reynolds Numbers below $2.3 \times 10^6$ (or $R_\theta <$ 2,500 in Fig. 16) were lower. Hence, in the present measurements at $M = 5.8$ turbulent shear was not obtained below an $R_\theta$ of approximately 2,500. The lower limit observed by Coles in supersonic flow was 2,000, and the turbulent shear measurements of Hakkinen at $M = 1.5$ extended to values of $R_\theta$ down to 1,600. This clearly illustrates the trend of turbulent boundary-layer development toward larger values of $R_\theta$ with in-

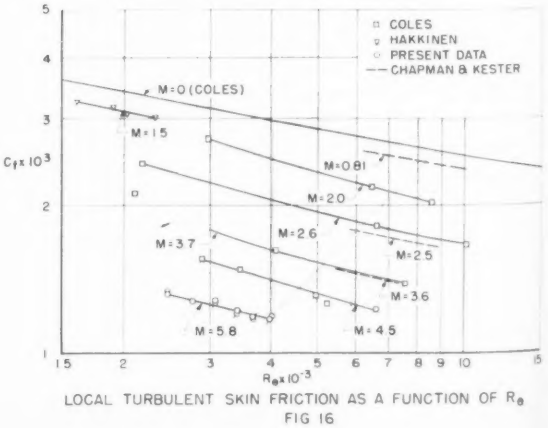


LOCAL TURBULENT SKIN FRICTION AS A FUNCTION OF $R_\theta$
FIG 16

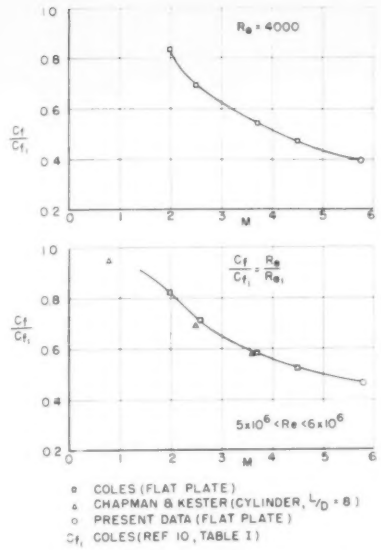


VARIATION OF LOCAL TURBULENT SKIN FRICTION WITH MACH NUMBER

FIG 17

creasing Mach Number, as was first noted and discussed by Coles.[36]

The variation of experimental local turbulent skin friction with Mach Number is shown in Fig. 17 for $R_\theta$ = 4,000 and for $C_f/C_{fi} = R_\theta/R_{\theta i}$, respectively. The latter case corresponds closely to a constant Reynolds Number, which, from the incompressible reference and the data of Coles and Chapman and Kester, is estimated to lie between 5 and 6 × $10^6$. Measurements in high-speed flow of other investigators[12, 13, 37] are not included in Fig. 17 because either $R_\theta$ could not be deduced, or their data are not within the $R_\theta$ range of the present results. In particular, the skin-friction values of Lobb, Winkler, and Persh,[37] deduced from boundary-layer surveys and measurements of heat-transfer rates at $M$ = 5, 6.8, and 7.7, cover a higher range of values of $R_\theta$ than the present measurements.

Finally, it is shown that, over the $R_\theta$ range presently investigated, $C_f/C_{fi}$ is relatively constant, being approximately 0.40 for constant $R_\theta$, and 0.46 for $C_f/R_\theta$ constant (cf. Table 2).

## (V) Conclusion

The results of the transition and skin-friction investigation on an insulated flat plate at a Mach Number of 5.8 indicate the following:

(1) A very high transition Reynolds Number (in excess of 5 × $10^6$) and the inability of various disturbances to trip transition at low Reynolds Numbers, which appears to indicate greater stability of the laminar boundary layer in hypersonic flow than at lower speeds.

(2) A delay in the origin of transverse contamination triggered by the sidewall boundary layer, and a $5^1/_2°$ angle of spread (compared with contamination originating at the leading edge and spreading at an angle of $9^1/_2°$ in low-speed flow).

(3) Evidence that air injection into the boundary layer is a more effective means of tripping transition at hypersonic speeds than the conventional devices used in low-speed flow (wire and fence trips, surface roughness, etc.).

(4) Direct measurement of turbulent skin friction at a Mach Number of 5.8 indicates a continued decrease of coefficient with increasing Mach Number.

## References

[1] Gazely, Carl, Jr., *Boundary Layer Stability and Transition in Subsonic and Supersonic Flow*," Journal of the Aeronautical Sciences, Vol. 20, No. 1, pp. 19–28, January, 1953.

[2] Czarneki, K. R., and Sinclair, A. R., *Factors Affecting Transition at Supersonic Speeds*, NACA RM L53I18a, November, 1953.

[3] Lange, A. H., Gieseler, L. P., and Lee, R. E., *Variation of Transition Reynolds Number with Mach Number*, Readers' Forum, Journal of the Aeronautical Sciences, Vol. 20, No. 10, p. 718, October, 1953.

[4] Schubauer, G. B., and Skramstad, H. K., *Laminar Boundary Layer Oscillations and Transition on a Flat Plate*, NACA WTR W-8, ACR, April, 1943.

[5] Dryden, H. L., *Some Recent Contributions to the Study of Transition and Turbulent Boundary Layers*, NACA TN 1168, April, 1947.

[6] Lees, L., and Lin, C. C., *Investigation of the Stability of the Laminar Boundary Layer in a Compressible Fluid*, NACA TN 1115, September, 1946.

[7] Lees, L., *The Stability of the Laminar Boundary Layer in a Compressible Fluid*, NACA TN 1360, 1947.

[8] Van Driest, E. R., *Calculation of the Stability of the Laminar Boundary Layer in a Compressible Fluid on a Flat Plate with Heat Transfer*, North American Aviation Report No. AL-1334, September, 1951; also Journal of the Aeronautical Sciences, Vol. 19, No. 12, pp. 801–812, 828, December, 1952.

[9] Chapman, D. R., and Kester, R. H., *Measurements of Turbulent Skin Friction on Cylinders in Axial Flow at Subsonic and Supersonic Velocities*, Journal of the Aeronautical Sciences, Vol. 20, No. 7, pp. 441–448, July, 1953.

[10] Coles, D., *Measurements in the Boundary Layer on a Smooth Flat Plate in Supersonic Flow*, GALCIT, Ph.D. Thesis, June, 1953; also JPL Reports No. 20–69, 20–70, and 20–71 (in press).

[11] Dhawan, S., *Direct Measurements of Skin Friction*, GALCIT, Ph.D. Thesis, June, 1951; also NACA TN 2567, January, 1952.

[12] Hakkinen, R. J., *Measurements of Skin Friction in Turbulent Boundary Layers at Transonic Speeds*, GALCIT, Ph.D. Thesis, June, 1954.

[13] Bradfield, W. S., DeCoursin, D. G., and Blumer, C. B., *Characteristics of Laminar and Turbulent Boundary Layers at Supersonic Velocity*, University of Minnesota, Research Report 83, July, 1952.

[14] Korkegi, R. H., *Transition Studies and Skin Friction Measurements on an Insulated Flat Plate at a Hypersonic Mach Number*, GALCIT, Ph.D. Thesis, June, 1954; also Hypersonic Wind Tunnel Memorandum No. 17, California Institute of Technology.

[15] Buhler, R. D., *Condensation of Air Components in Hypersonic Wind Tunnels—Theoretical Calculations and Comparison with Experiment*, Contract No. DA-04-495-Ord-19, Hypersonic Wind Tunnel Memorandum No. 13, California Institute of Technology, December 1, 1952.

[16] Eimer, M., *Direct Measurement of Laminar Skin Friction at Hypersonic Speeds*, GALCIT, Ph.D. Thesis, June, 1953; also Hypersonic Wind Tunnel Memorandum No. 16, California Institute of Technology.

(*Continued on page 192*)

# Fluid Dynamic Effects at Speeds From $M = 11$ to 15*

SEYMOUR M. BOGDONOFF† AND ANDREW G. HAMMITT‡
*Princeton University*

SUMMARY

The phenomena of viscous-inviscid interaction effects at very high speeds over the fore part of bodies have been studied at speeds considerably higher than those previously investigated. A tunnel, using helium as a working fluid, has been developed for these studies and has been operated at speeds up to $M = 15$. Increases in the speed up to $M = 20$ seem quite possible with further development. Pressure distributions have been obtained over the fore part of some simple bodies; a flat plate, two wedges, and a cone. In addition, schlieren and interferometric photographs have been taken. The results show that extremely high pressures, as high as ten times the values predicted by inviscid theories, are obtained over the region close to the nose of the body. Although some aspects of theoretical work on this problem appear to be correct, the numerical values of the pressures obtained are considerably different than predicted—on the order of two to three times as large. This difference may be explained by the influence of the leading edge and some preliminary results on this effect are presented.

## INTRODUCTION

THE PROBLEM OF FLIGHT at very high speeds is complicated by a complex interaction of fluid mechanical or viscous and inviscid effects and the chemical or dissociation and ionization effects. Of these two interacting effects, there is considerable knowledge and background of only one—the fluid mechanical effects. A large amount of fluid mechanics work has been done in the supersonic and subsonic fields. Although there are few complete solutions, in many cases engineering solutions are available neglecting effects which are known to be small in these ranges. The problems of dissociation and ionization are, on the other hand, relatively unknown in the usual aerodynamic problems. The change in gas characteristics caused by these phenomena are not experienced except perhaps in rocket or combustion chambers since in subsonic and supersonic flows the temperatures reached are not sufficiently high.

The extension of the known results on fluid mechanical effects and dissociation and ionization to the problem of flight at very high speeds is extremely difficult, especially with the almost complete lack of any accurate experimental results. Experimental studies could indicate the factors which are important and, at least, give indications as to a tentative method of approach which would correspond to the actual physical problem.

This paper describes some experimental equipment designed to obtain data on part of this problem at speeds considerably higher than previously investigated. A wind tunnel, using helium as a working fluid, has been developed to study the purely fluid mechanical effects at speeds in the range of $M = 15$. The tunnel is of the high pressure blowdown-type so that the aerodynamic results obtained are well within the "continuum" regime and significant Reynolds Numbers are obtained over the models tested at these very high speeds. The work herein reported covers the major part of a complete aerodynamic study of the flow over the fore part of several simple bodies over a range of Reynolds Numbers and at Mach Numbers from 11 to 15. Pressure distributions and optical data have been obtained. An analysis of the results and comparison with the available theories provides a picture of the present state of the knowledge of fluid mechanical effects in this speed range. A more complete discussion of the details of the tunnel construction and some of the aerodynamic results are presented in references 1 and 2.

## SYMBOLS

$C$ = linear viscosity coefficient in relation $(\mu_w/\mu_1) = C(T_w/T_1)$
$d_b$ = boundary-layer parameter depending on surface temperature
$F$ = theoretical factor to account for geometry of wedge and cone
$M$ = Mach Number
$P$ = pressure
$T$ = temperature
(static conditions unless other indicated)
$x$ = distance from leading edge
$Re$ = Reynolds Number
$\beta$ = geometric leading-edge half angle
$\gamma$ = specific heat ratio
$\delta$ = shock deflection angle
$\Delta p$ = induced static pressure increment
$\theta$ = angle of boundary-layer displacement thickness with respect to undisturbed stream
$\mu$ = coefficient of viscosity
$\chi$ = theoretical hypersonic interaction parameter $(M^3\sqrt{C})/\sqrt{Re_x}$
$\omega$ = power law viscosity exponent in relation $(\mu_w/\mu_1) = (T_w/T_1)^\omega$

*Sub cripts*

$l$ = condition far from leading edge outside the boundary layer of the body
$W$ = condition on wall
$0$ = stagnation
$\infty$ = condition in free stream ahead of all disturbances
$x$ = parameter based on distance from leading edge

Presented at the Aerodynamics Session, Twenty-Third Annual Meeting, IAS, New York, January 24–27, 1955.

* This work was sponsored by the United States Air Force, Aeronautical Research Laboratory, Wright Air Development Center, Wright-Patterson Air Force Base, under Contracts Numbers AF 33(038)-250 and AF 33(616)-2547.

† Associate Professor, Gas Dynamics Laboratory.

‡ Research Associate, Gas Dynamics Laboratory.

## Preliminary Considerations

Most aerodynamic studies have been carried out in wind tunnels. A simple basic model may be easily modified to study effects of many variables, and the time available for testing is almost infinitely higher than provided by free flight techniques Conditions in the tunnel can be kept constant for long periods while detailed studies of the forces and the flows are carried out. An error in the design simply means another test with a modified model, as contrasted to the loss of the entire model in the free flight work. For most supersonic speeds, one can simulate all of the steady state flight conditions with the exception of stagnation temperatures. This has, however, no significant effect at low Mach Numbers since the temperature levels are below that at which the gas constants change significantly. The conventional wind tunnel has several important limitations with regard to hypersonic speeds: (1) It is well known that expansion of air at room temperature will cause condensation of the components of air when Mach Numbers in excess of about 5 are attained. For higher Mach Numbers, the air must be heated, and *just on the basis of preventing condensation*, temperatures of the order of 1,300° to 1,500°F. are needed to obtain Mach Numbers of 10. (2) Although the wind tunnel may simulate the Mach and Reynolds Numbers of flight, the stagnation temperature cannot be simulated. At a Mach Number of 10, this temperature is several thousand degrees, far above the limits set by the metals of the settling chamber and nozzle. Therefore, the conventional wind tunnel may be used to reach Mach Numbers of the order of 10 but cannot hope to simulate complete flight conditions. The temperatures which can now be attained will just about provide noncondensing air in which to make a test and thus can really only be used to study the purely fluid mechanical phenomenon without the interacting effect of dissociation or ionization. These considerations apply to the conventional tunnel where the testing time may extend over many minutes. At the same time, even the "hypersonic fluid mechanical effects" may not be predominant or even large unless the Mach Number is quite high. At low Mach Numbers, the tests must be of very high precision to obtain results of sufficient accuracy to verify or build a theory. At very high Mach Numbers, relatively simple tests with relatively crude instrumentation could yield major results and provide a much better basis of critical comparison with theory or for the construction of a basic model. Several models have been used for the hypersonic viscous theories now in existence,[3–12] but little data are available on which to base any critical evaluation of them.

Since present wind tunnels at Mach Numbers up to 10 do not simulate flight, but only provide a noncondensing medium, the obvious solution to get higher Mach Numbers and at the same time eliminate the mechanical problem of heating, is to use a gas which has a very low condensation temperature. Since fluid mechanical theory—if correct—would predict such effects in any gas, the particular test medium is not vital as long as the gas does not change characteristics within the tunnel. The gases with sufficiently low condensation temperatures to permit the attainment of Mach Numbers of the order of 15 without any heating are hydrogen and helium. Hydrogen has the advantage of a specific heat ratio about the same as air and would lend itself more to matching experiments in air. However, hydrogen is difficult and dangerous to handle and, for this reason, was not used in the hypersonic tunnel. Helium seemed to be the best choice for our purposes; it has a very low condensation point, an almost constant specific heat, and is not dangerous. Helium can be obtained in the quantities required to operate a small experimental wind tunnel with only 0.1 per cent impurities, mostly hydrogen. This makes no important change in the characteristics of the gas which are well known to very low temperatures.[13,14]

It has already been pointed out that a helium wind tunnel will not completely simulate flight conditions. It can be used to provide hypersonic flows which contain the same viscous phenomena as those obtained in air tunnels with stagnation temperatures below the temperatures for internal changes of the gas molecules. Either gas can be used to study the fluid mechanical hypersonic flow phenomena.

The relation of the various quantities to be compared, as a function of specific heat ratio, must be known in order to compare data from flows in helium and air. This relation may be obtained from either a theoretical understanding of the problem or by data gathered for different values of specific heat ratio. Without information of this type, the *data* for helium and air cannot be *directly* compared.

In any consideration of high Mach Number-low Reynolds Number flow, we must consider the possibilities of slip flow and other deviations from the usual flow consideration. The range in which slip flow can be expected is for $M^2/Re > 0.1$. For $M = 15$ and $Re = 6(10^5)$ per in., which are the most critical conditions which have been achieved in this tunnel, this criterion indicates that slip is unimportant for dimensions larger than about 0.004 in. Since the major dimensions of the bodies tested were much larger than this, possible slip flows will be restricted to a very limited region close to the leading edge. Another effect which must be considered at high $M/Re$ ratios is the change in reading of total head tubes caused by the viscous effect at the front of the tube. The magnitude of this effect has been studied and is described in reference 15. For $M/Re < 0.015$, a deviation of less than 1 per cent from the high density case was observed on total head tubes. For $M = 15$ and $Re$ of $6(10^5)$ per in., this restriction says that total head tubes of greater diameter than 0.002 in. will be free of this viscous effect.

## The Helium Hypersonic Tunnel

The hypersonic wind tunnel is of the blowdown type using helium as the test fluid and is described in detail in

reference 1. The helium is obtained in tank semi-trailers—which are used as a high pressure storage system—and piped through a regulating valve to the settling chamber. The tunnel may be run at stagnation pressures up to 1,500 lbs. per sq.in. for periods up to 10 min. To obtain the high pressure ratios which are needed, an air operated ejector, using air at 1,500 lbs. per sq.in. from a second high pressure storage system, is used downstream of the hypersonic diffuser. A general layout of the piping and tunnel is shown in Figs. 1 and 2. The first nozzle, shown in Fig. 3, is an axial symmetric conical nozzle with no windows and a maximum diameter of approximately 3 in. The models and probes are supported in the test section by means of the sting and spider shown. This nozzle was used for all the tests reported herein, except the optical studies. The second nozzle, shown in Fig. 4, is similar to the first one except that it has been cut open and windows installed. The disturbances from the windows do not effect the central core in the region of interest.

The Mach Number-Reynolds Number range of operation, which is obtained with the diffuser arrangement shown in previous figures, is shown in Fig. 5. The nozzle-diffuser configuration used in these tests is not the result of an extensive development program. This configuration was satisfactory for the original set of tests, but higher Mach Numbers and a wider Reynolds Number range could be obtained with further development. The Mach Number distribution along the axis of the nozzle is shown in Fig. 6. The effect of the gradient on the test results is discussed later in this paper.

## Brief Review of Theories

In flow of a real fluid over any body, the fluid in contract with the body is retarded because of the viscosity of the fluid. The retarded layer is generally referred to as the boundary layer. Since the mass flux in the boundary layer is not as large as the free stream, there is a boundary-layer displacement thickness which represents the amount which the outside flow is forced away from the body. Because of this viscous layer, the essentially inviscid or external flow sees a body which is represented by the physical body plus the displacement thickness. The effective change in shape of the body changes the pressure about the body, which, in turn, changes the viscous layer. While this condition exists at all speeds, not until hypersonic speeds are reached ($M \gg 1$), does this effect become of primary importance because the thickness of the boundary layer and the pressure rise associated with the change in direction increase rapidly with Mach Number. The problem then becomes a simultaneous solution of the boundary-layer and external flow relations. Also, because of the high Mach Number, a shock wave lies close to the surface of the body. This means that, near the leading edge, the shock wave lies very close to the edge of the boundary layer and the region in which inviscid flow may exist behind the shock wave is very limited.

Several attempts have been made to analyze and solve this problem of hypersonic viscous-inviscid interaction. There have been two distinct approaches used in the theoretical treatment of this problem. One assumes that the region behind the shock wave consists of a viscous boundary layer and an inviscid region between the shock and boundary layer (Fig. 7a). The boundary layer equations are applied to the boundary-layer region and some approximation to the inviscid flow is applied between the shock and the boundary layer. The other approach assumes that the whole region below the shock can be treated by the boundary-layer equations. In this case, the edge of the boundary layer and the shock wave are made to coincide (Fig. 7b). This treatment can only be appropriate near the leading edge where the shock is near the surface.

The original work on this problem was carried out at the Langley NACA Laboratory.[3] The first approach mentioned above was used. The pressure on the front part of a flat plate was predicted by calculating the boundary-layer thickness on a plate under the assumption of zero pressure gradient. The pressure distribution about a body whose shape was the flat plate plus the boundary-layer displacement thickness was then calculated. A more complete treatment using the same basic method is given in reference 4. The method was applied to flat plates and wedges, and with some modifications, to circular arc airfoils. It is essentially a numerical method for calculating the pressure and Mach Number distribution and does not give rise to any important parameters.

The work done at Princeton by Lees and Probstein is given in references 7–11. The work was based on the first model presented—that is, a boundary layer separated from the shock by an inviscid layer. The region far from the leading edge, where the induced pressure effects were small, was treated first. The technique used here was to take the zero pressure gradient boundary layer as the first approximation, to find the pressure distribution caused by this boundary layer, to use this in calculating the next boundary-layer approximation and to continue to iterate. This solution was accomplished by an analytic method which brought out the important parameters of the flow. For a flat plate, a wedge, and a cone, the surface pressures can be expressed as $(P/P_1) = 1 + \gamma d_b F \bar{\chi} + \ldots$ where $d_b$ is a parameter depending on the surface temperature, $F$ is a factor depending on body geometry and is equal to one for a flat plate,[2] and $\bar{\chi}$ is the viscous hypersonic parameter.

This whole technique is limited to the regions in which the interaction effect is weak. $\bar{\chi}$ must be small if the series relations are to be rapidly convergent and $(P - P_1)/P \gg 1$ if the linearized solution of the second-order boundary-layer solution is to be used. For these reasons, this type of solution is restricted to regions well away from the leading edge.

In treating the interaction near the leading edge, where it was much stronger, the inviscid flow was rep-

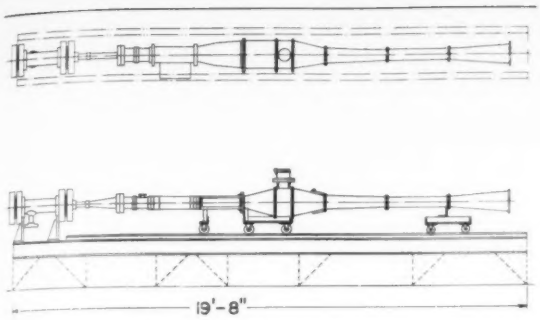


FIG. 1. Assembly layout of Princeton University helium hypersonic wind tunnel.

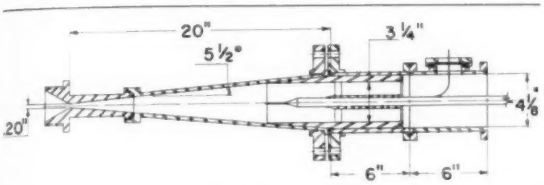


FIG. 3. Cross section of axial symmetric nozzle and diffuser.

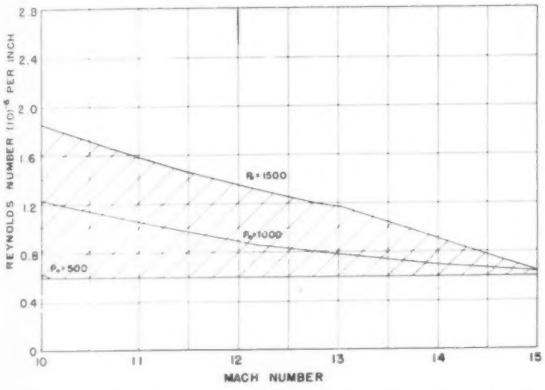


FIG. 5. Reynolds Number–Mach Number range for the helium hypersonic wind tunnel with present ejector-diffuser configuration.

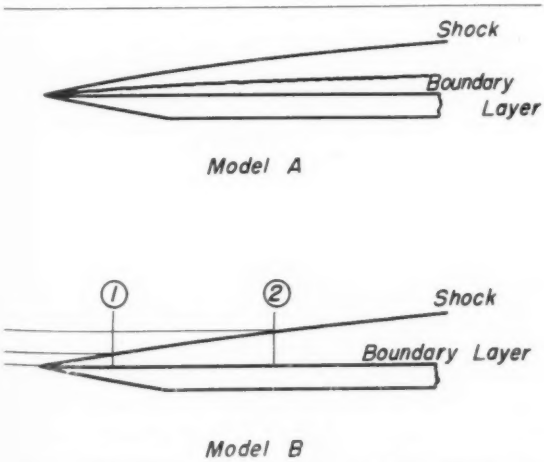


FIG. 7. Theoretical models for viscous-inviscid interaction.

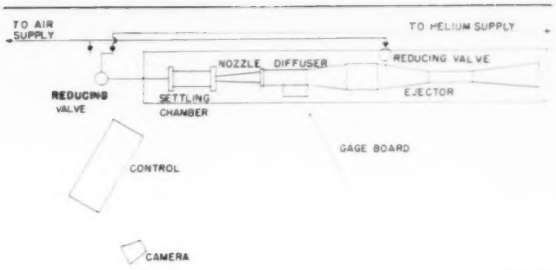


FIG. 2. Piping and control system for the helium hypersonic wind tunnel.

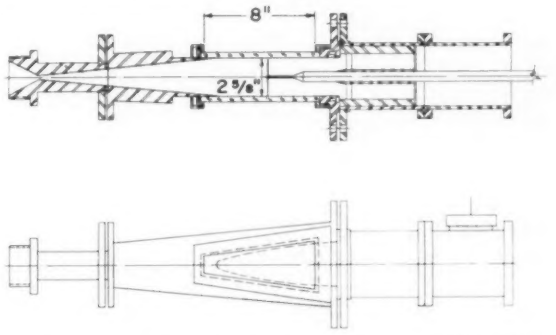


FIG. 4. Window installation in the axial symmetric nozzle.

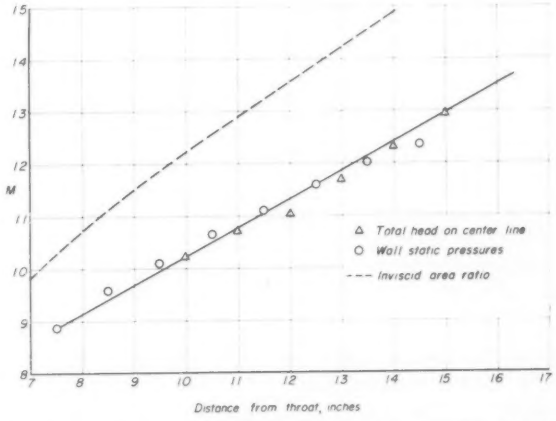


FIG. 6. Mach Number distribution along the centerline of axial symmetric nozzle.

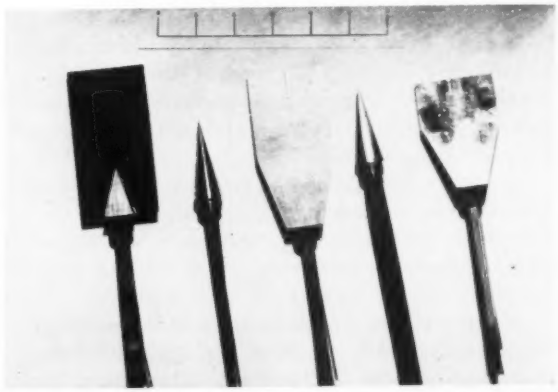

FIG. 8. Test models: flat-plate, 5° wedge, 10° wedge, and two 10° cones.

resented by the tangent wedge relations. In this case, for large angles, $M\theta \gg 1$, it may be expanded in the parameter $1/M\theta$ and only the first few terms retained. By an order of magnitude analysis, it was shown that when the viscous forces are of the same order of magnitude as the pressure gradient forces, then, to a first approximation, the pressure may be represented by an expression of the type $p/p_1 = p_0\bar{\chi}$ where $p_0$ is a constant to be determined. In this case, $\bar{\chi} \gg 1$, so an expansion in inverse powers of $\bar{\chi}$ was appropriate. Using a pressure gradient of this type and suitable transformation of variables, the boundary-layer equations for the insulated case were reduced to the Falkner Skan equation to which solutions are available. These solutions determine the constant, $p_0$. The first-order solution for this case was worked out and the way in which the higher order solutions might be calculated was indicated.

This solution does not connect to the weak interaction solution, but there is an intermediate range where neither method is appropriate. However, both solutions seem to exhibit the same trends and seem to be mutually consistent.

The strong interaction solution was extended to the case of the wedge. In this case, the geometric wedge angle is a correction on the slope of the boundary layer, since $\theta/\beta \gg 1$ for this theory to apply. The numerical results for this theory have not been presented, so it cannot be directly compared to other work.

The second approach to the hypersonic viscous interaction problem has been taken by Shen[10] and later elaborated by Li and Nagamatsu.[11] This approach was to apply the boundary-layer equation in the whole region between the body and the shock wave (Fig. 7b). A momentum integral technique was then applied to the boundary layer, and the outer boundary conditions were taken as those behind an oblique shock of slope equal to the rate of boundary-layer growth. By this technique, it was possible to simultaneously satisfy both the shock wave and boundary-layer relations without an iteration scheme.

Both of these authors arrive at a solution for a flat plate with insulated wall of the form $(p/p_1) = 1 + (M_\infty{}^{2+\omega}/\sqrt{Re_{\chi\infty}})$ where $\omega$ is defined by $(\mu_w/\mu_\infty) = (T_w/T_\infty)^\omega$.

This is very similar to the parameter of Lees and Probstein and, in most cases, numerically equivalent. The difference seems to be caused by the different form of the viscosity temperature relation assumed. If viscosity is taken directly proportional to temperature, the two become identical.

All of the theories discussed treat the problem a finite distance from the leading edge. They neglect the details of the flow in the immediate region of the leading edge and therefore they must ignore the history of the flow and base the results on local conditions. Since the theories do not consider the effects of finite leading-edge thickness, they should only be applied to the case of an infinitely thin leading edge. The error or effects caused by finite leading-edge thickness cannot be predicted by any of these theories. Recently Lees has modified his strong interaction theory in an attempt to account for the effect of shock wave "heating" and vorticity on the boundary layer.[16] The results show that the effect of the "history" of the air entering the boundary layer has an appreciable effect on the pressure distribution. Bertram[17] has also postulated a model of the flow over a leading edge of finite thickness. These results are discussed further in the following section.

## Experimental Studies

A test program was undertaken to study the flow of a real fluid over several simple bodies at speeds significantly higher than previously studied. These tests provided experimental data to which theoretical work done on this problem could be compared. Tests were made over a range of Mach Numbers and Reynolds Numbers so that a critical evaluation of the effects of these parameters could be made. Some typical results are presented herein, complete studies are presented in reference 2.

Pressures were measured on several models; a flat plate, a 5° wedge, a 10° wedge, and a 10° cone. A photograph of these models is shown in Fig. 8. Pressure measurements were made at Mach Numbers between 10.75 and 13.6 and Reynolds Numbers between 50,000 and 4,500,000 based on distance from the model leading edge. The Mach Number was varied by testing at several different positions in the axial symmetric nozzle. The reference Mach Number is that at the leading edge. The significant Reynolds Number parameter has been taken as the Reynolds Number based on flow conditions far back on the body and the distance from the leading edge. The variation in Reynolds Number was achieved by measuring pressures at different distances from the leading edge and at different stagnation pressures. Most models have been run at nominal stagnation pressures of 800, 1,000, and 1,400 lbs. per sq.in. and have had a leading-edge thickness of 0.001 in. Some typical results are presented in Figs. 9–14 for the flat plate and the 5° wedge.

The pressure distributions were plotted in two ways: first, as the measured pressures over stagnation pressure as a function of distance from the leading edge and, second, as the pressures increment above the theoretical inviscid pressure as a function of $1/\sqrt{Re}$ based on distance from the leading edge. The inviscid pressure was calculated by taking the tunnel empty, conditions at the location being considered, and calculating the conditions behind a shock corresponding to the geometric shape of the body. This gave the pressure and Mach Number gradient shown in the plots.

The Mach Number gradient in the nozzle caused some questions about the pressure distributions. The method used to calculate the inviscid pressures seemed to be the fairest, and the fact that the extended straight line sections of the $1/\sqrt{Re}$ plots passed close to the origin lent support to this method. Other assumptions on the inviscid pressure did not change the order of the in-

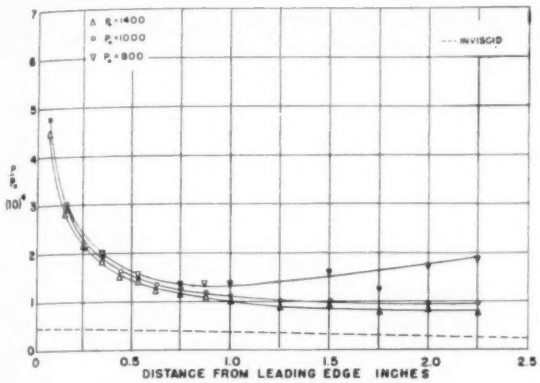


FIG. 9. Static pressure ratio versus distance along the flat-plate model at $M = 11.8$.

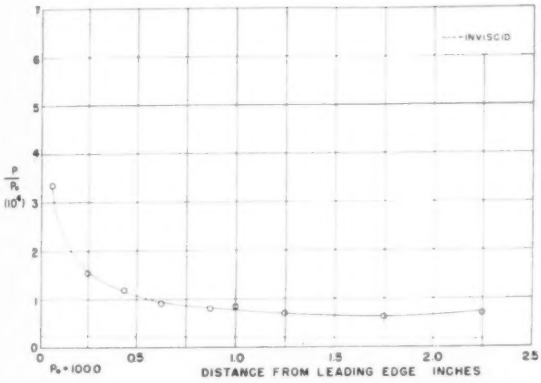


FIG. 10. Static pressure ratio versus distance along the flat-plate model at $M = 13.8$.

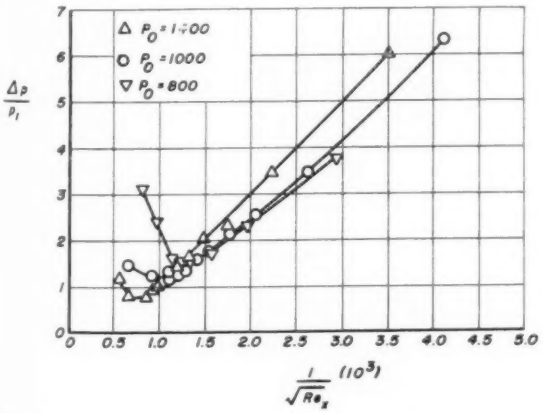


FIG. 11. Static pressure ratio increment versus $1/\sqrt{Re}$ for the flat-plate model at $M = 11.8$.

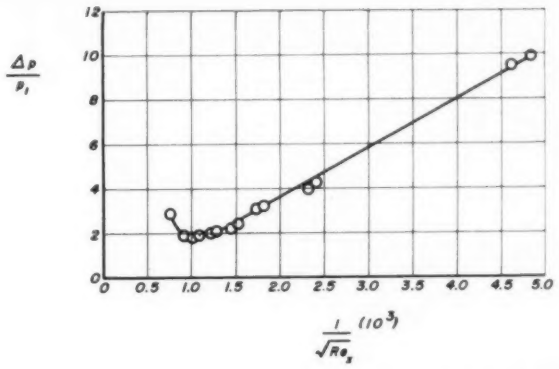

FIG. 12. Static pressure ratio increment versus $1/\sqrt{Re}$ for the flat-plate model at $M = 13.8$ and $p_0 = 1{,}000$ lbs. per sq. in.

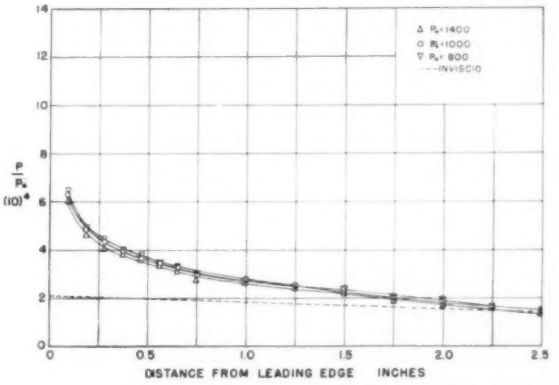


FIG. 13. Static pressure ratio versus distance along a 5° wedge model at $M = 11.8$.

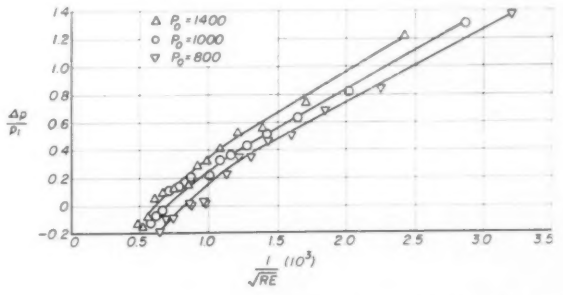

FIG. 14. Static pressure ratio increment versus $1/\sqrt{Re}$ for a 5° wedge model at $M = 11.8$.

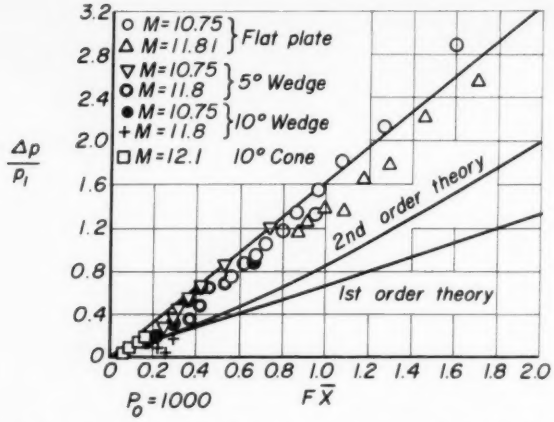


FIG. 15. Static pressure ratio increment versus $F\sqrt{\chi}$ for flat plate, 5° wedge, 10° wedge, 10° cone at $M$ between 10.75 and 12.1 compared to Lees-Probstein theory for $\gamma = 5/3$.

duced pressure rise but did prevent the extrapolated values of the induced pressure from approaching zero at infinity. The gradient itself must have had some influence on the induced pressure, but since the tunnel empty gradient was much less than the induced gradient over most of the region of interest, it should not have made a major change. Tests in a constant Mach Number region are needed to definitely determine this effect.

On the basis of the theoretical studies, the surface temperature of the model would be expected to effect the pressure distribution. No effect on the pressures with time was observed on runs up to 7 min. in length. Temperatures have also been measured on a model similar to the pressure models and equilibrium was established after a run of about 1 min. The data presented herein were obtained after the tunnel was in operation for 1 min., so the results are for the adiabatic or no heat transfer case.

## Discussion of Data

The plots of $1/\sqrt{Re}$ bring out several significant results. The pressures near the leading edge are of the order of ten times higher than would be predicted by inviscid theory. The various stagnation pressures are brought into fairly good agreement by the use of $Re$ based on distance from the leading edge. The part of the plots representing pressure near the leading edge form fairly straight lines which, when extrapolated, pass almost through the origin. The fact that the induced pressures approach zero as Reynolds Number approaches infinity helps justify the way in which the inviscid pressures were calculated (as previously pointed out). The data from the rear section of the models fall above this line for the flat plate and below for wedges and cones. The effect of the trailing-edge disturbances, propagating forward through the boundary layer would account for these deviations. A check of this explanation was obtained by running a longer plate, which increased the length of the straight line portion of the curve.

While plotting against $Re$ based on distance from the leading edge correlates the data fairly well, there is still a systematic variation with stagnation pressure. This could be caused by a small change in Mach Number in the tunnel with change in stagnation pressure or perhaps by a change in Reynolds Number based on leading edge thickness. However, the variation in Mach Number with stagnation pressure, as measured by total head surveys, is slight and insufficient to account for this change.

## Correlation of Data and Theory

The theoretical work[7–11] indicates that the flat-plate induced pressures should be a function of $\bar{\chi}$ and should correlate on this parameter in both the weak and strong interaction range. For the weak interaction, the flat plate, wedge, and cone data should correlate, to a first approximation, by the use of the $F\bar{\chi}$ parameter. Since $F$ is 1 for a flat plate and all the wedge and cone data are out of the strong interaction range, all of the induced pressures should fall on a continuous curve, if plotted against $F\bar{\chi}$. Such a plot is shown in Figs. 15 and 16. In order to avoid the confusion caused by the small variations with stagnation pressure, only data at $P_0 = 1{,}000$ lbs. per sq.in. have been used for these correlation plots. The sections of the curves which show effects from the rear of the body are also left out. The induced pressures for the flat plate, wedges, and cones at several Mach Numbers all form a continuous band. It is interesting to note that the induced pressure seems to form a straight line relation with $F\bar{\chi}$ over the entire range.

In attempting to compare these results with the existing theoretical work, there are difficulties in accounting for the effect of $\gamma$. Since most of the theoretical work has been done for $\gamma = 1.4$, and because it appears in a complicated way in the numerical calculations, it is hard to make any direct comparisons. Only references 7–11 explicitly show the $\gamma$ dependence so it may easily

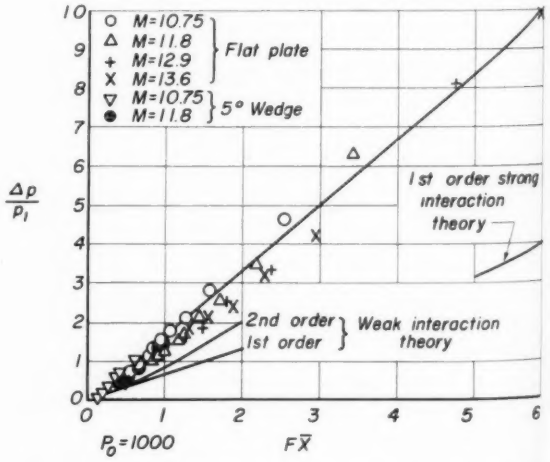


FIG. 16. Static pressure increment versus $F\chi$ for flat plate and 5° wedge at $M$ between 10.75 and 13.8 compared to the Lees-Probstein theory for $\gamma = 5/3$.

be compared to the helium data for $\gamma = 5/3$. For this reason, only this theory has been shown on Figs. 15 and 16.

The first-order Lees-Probstein theory for both the weak and strong interaction are straight lines. While these lines do not connect, they are close enough so that it is not hard to fair a connection between them to form an approximately straight line. The second-order weak interaction theory is also shown. The shape of this curve does not agree with the experimental curve and the joining with the strong interaction becomes more difficult. If the weak interaction curve is cut off when $[(p - p_1)/p] \ll 1$ the conditions which is assumed in the second-order boundary-layer solution, then the effect of the second-order term is negligible and an effective straight line relation exists.

The only way to compare the results of all of the theories is on a basis of $\gamma = 1.4$, and Fig. 17 is a plot of the various theoretical solutions previously mentioned. The $\bar{\chi}$ parameter used here is taken as the parameter found by Lees and Probstein and also as that found by Shen and Li and Nagamatsu since they are numerically approximately equivalent. Since all the authors have not rigidly defined the range in which they expect their solutions to hold, it is somewhat difficult to know how to do so. This plot represents the best compromise consistent with showing all the theories on one plot.

In addition to the experimental work done at Princeton, similar work at lower Mach Numbers has been done elsewhere. These other data are given in references 4, 12, and 17. All these data are for air and so may be plotted directly on the $\gamma = 1.4$ plot. The helium data presented in this report is also shown, but reduced to $\gamma = 1.4$ by use of the $\gamma$ dependence given in the Lees-Probstein theory. The accuracy of this conversion seems very open to question since the theory does not match the experiments, but, at present, there is no other way to make the comparison. This plot shows that there is no overall agreement between the various theories. The experimental data exhibit a slope greater than any of the theories. The various data

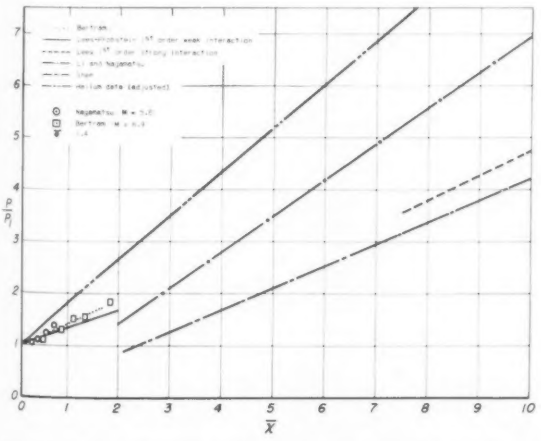

FIG. 17. Static pressure ratio increment versus $\bar{\chi}$ for various theories and experiments.

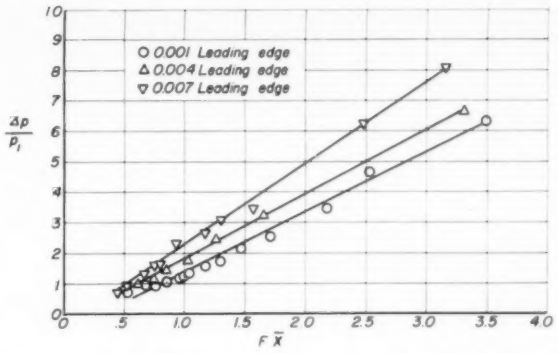


FIG. 18. Static pressure ratio versus $F\bar{\chi}$ for three leading-edge thicknesses on a flat plate at $M = 10.75$ and 11.8.

taken for air are fairly consistent and the reduced helium data have a greater slope than the air data. The air experiments presented are for fairly low Mach Numbers so that the induced pressures are not large. When the air data are extrapolated, they do not seem to approach free stream pressure far from the leading edge, so this fact should be considered when judging the slope of these data.

## Leading-Edge Effects

The most obvious explanation for the large discrepancy between theory and experiments is the finite leading edge of the test model. The theories mentioned above all start with the assumption of an infinitely thin leading edge—probably approached experimentally only if the leading-edge dimension becomes a fraction of a mean free path. Some preliminary results have been obtained on the effect of the leading-edge thickness both by pressure distribution measurements and optical techniques. In Fig. 18 the reduced pressure distributions for three leading-edge thicknesses are presented. Because of the thin leading edge, pressure orifices are restricted to the region some distance downstream and are thus at relatively low values of $\bar{\chi}$. Nevertheless, significant effects are found. The thinnest leading edge, 0.001 in., was still on the order of 25 mean free paths based on conditions ahead of the model. The mechanical complications of the pressure distribution installation precludes any thinner leading edge.

In an attempt to get some indication of the effect of even wider variations of leading-edge thickness, a special model with no pressure orifices, has been tested using only optical observation. Because the end and wall effects could not be determined, the interferograms obtained cannot be directly evaluated but only used to determine shock wave shapes and to indicate general regions. Tests have been made at leading-edge thicknesses varying from 0.00017 to 0.0595 in. (approximately 4 to 300 mean free paths) and a few typical interferograms are presented in Fig. 19. Several important observations can be made on the basis of the preliminary optical studies but they must be considered speculative until more detailed pressure distribution results have been obtained.

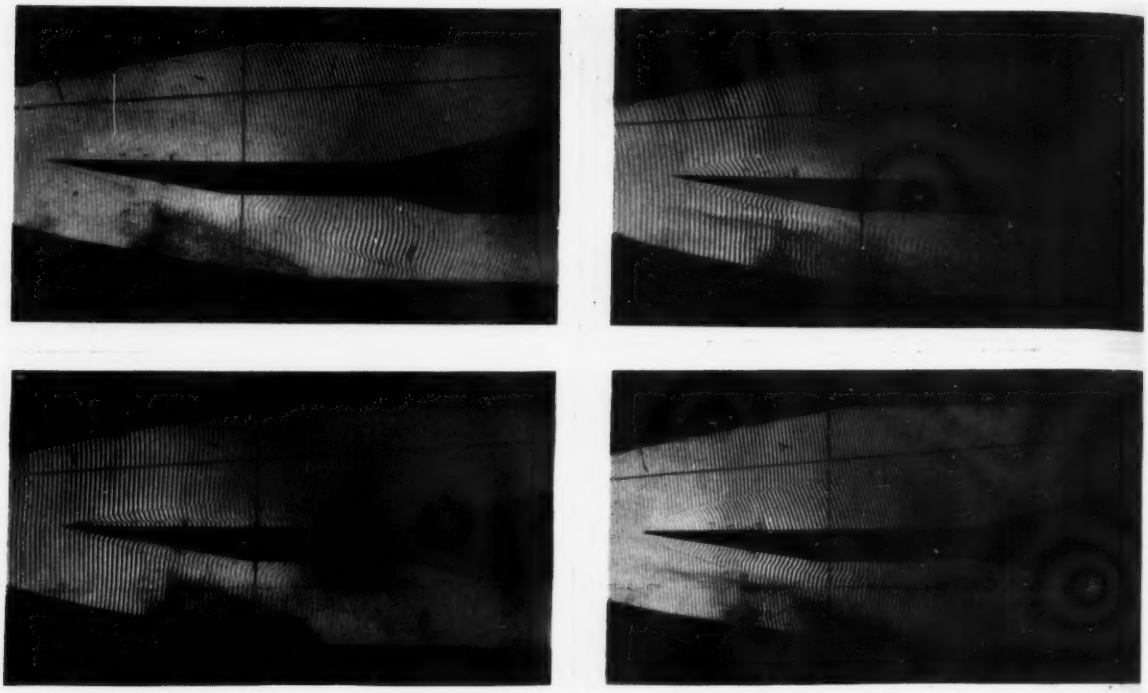

FIG. 19. Interferogram of a flat plate with various leading-edge thicknesses; $M = 12.7$, stagnation pressure approximately 1,200 lbs. per sq. in. The leading-edge thicknesses equal, respectively: upper left, 0.00017 in.; lower left, 0.00128 in.; upper right 0.00400 in.; lower right, 0.01456 in.

(1) The results of the preliminary tests seem to indicate that the shock shape does not correlate on the basis of leading-edge Reynolds Number.

(2) Even though leading-edge thicknesses down to approximately 4 mean free paths have been tested, the shock shape is still changing.

(3) There is some indication that the detailed flow near the leading edge changes at about 50 mean free paths and slip flow may be important at the smallest leading-edge thickness.

(4) Below a leading-edge thickness of approximately 50 mean free paths, the region between the plate and the shock wave appears to be separated into a boundary-layer viscous region and a variable entropy external field.

(5) Above a leading-edge thickness of approximately 50 mean free paths, separation of a viscous and an external field is not possible. The entire field is a strong entropy gradient caused by the highly curved leading-edge shock wave, and skin friction does not appear to have an important effect within the dimensions of the test model.

It appears from the preliminary tests that the flow field over the plate is determined primarily by the condition at the leading edge and an understanding of this region (with its associated highly curved shock waves) is necessary before a complete solution for the entire plate is possible. Changes of the leading-edge thickness, as defined by changing the mean free path (wide altitude changes) or by physical changes (such as burning off of the leading edge) will result in pressure changes which can easily approach a ratio of 50 to 1.

## CONCLUSIONS

On the basis of the results presented herein, the following conclusions can be drawn:

(1) The helium hypersonic tunnel provides a relatively simple tool to study purely fluid mechanical effects at Mach Numbers considerably higher than previously investigated.

(2) The pressure distribution results obtained indicate that, although some aspects of the theoretical work appear to be correct, the actual pressures were underestimated by a factor of 2 to 3.

(3) Some preliminary results on the effect of leading-edge thickness indicates the primary importance of the leading-edge region with its associated highly curved shock wave.

## REFERENCES

[1] Bogdonoff, S. M., and Hammitt, A. G., *The Princeton Helium Hypersonic Tunnel and Preliminary Results Above M = 11*, Princeton Univ. Aero. Eng'g. Dept. Rpt. 260, June, 1954. Also WADC Technical Report 54-124.

[2] Hammitt, A. G., and Bogdonoff, S. M., *A Study of the Flow About Simple Bodies at Mach Numbers from 11 to 15*, Princeton Univ. Aero. Eng'g. Dept. Rpt. 277, September, 1954. Also WADC Technical Report 54-257.

[3] Becker, J. V., *Results in Recent Hypersonic and Unsteady Flow Research at the Langley Aeronautical Laboratory*, J. of Appl. Phys., Vol. 21, No. 7, particularly pp. 622–624, July, 1950.

[4] Bertram, M. H., *An Approximate Method for Determining the Displacement Effects and Viscous Drag of Laminar Boundary Layers in Two-Dimensional Hypersonic Flow*, NACA TN 2773, September, 1952.

(*Continued on page 145*)

# Experimental Pressure Distributions on Oscillating Low Aspect Ratio Wings*

WILLIAM R. LAIDLAW† AND ROBERT L. HALFMAN‡

*Massachusetts Institute of Technology*

SUMMARY

The distribution of lifting pressure over the surface of low aspect ratio wings oscillating in an incompressible flow has been measured, and the results have led to a number of important conclusions regarding the relative status of existing lifting surface theories. Rectangular, sweptback, and delta plan forms were tested as well as a wing-tip tank configuration. Measurements were made both in the wind tunnel and in still air. The pressures were determined by means of a small lightweight barium titanate pressure transducer while the wings performed simple harmonic pitching and vertical translation motions. The pressures so obtained were then integrated numerically to yield lift and pitching moment distributions and total lift and pitching moment coefficients. Wherever possible, the final results were compared with theoretical aerodynamic data. The following general conclusions resulted from these comparisons.

(i) The high aspect ratio theory of Reissner[1] which is relatively simple to use, should be sufficiently accurate for aeroelastic and dynamic stability calculations in the aspect ratio range above two.

(ii) The low aspect ratio pressure distribution theory developed by one of the authors[2] is in excellent agreement with the experimental measurements taken on the rectangular wings.

(iii) Chordwise lift distributions and total lift and pitching moment coefficients as computed by the Lawrence and Gerber[3] low aspect ratio theory agree very well with the test data taken on the rectangular and delta wings. The method is at a disadvantage, however, since it is incapable of predicting the pressure distributions.

(iv) The very low aspect ratio theory for delta wings as developed by Garrick[4] and Voss[5] is definitely unsuitable for aspect ratios above one. The method may be modified empirically, however, to give excellent results for delta wings of aspect ratios as high as three.

(v) The high aspect ratio sweptback wing theory of Ashley[6] may not be used in the low aspect ratio range. This is due primarily to the fact that conditions at the wing center section are not adequately accounted for by the mathematical representation of the flow. The present tests have indicated that the lower limit on aspect ratio is about four, but it may be possible to use the method for wings of still lower aspect ratio when a fuselage is present.

(vi) The experiments have shown that the "end-plate" effect of wing-tip tanks produces higher pressure amplitudes (particularly near the wing tips), but that the phase angles are essentially the same as for the wing without the tanks.

## SYMBOLS

$b$ = semichord ($c/2$)

$c$ = chord

$c_0$ = root chord

$g$ = acceleration of gravity

$k$ = reduced frequency = $\omega b/U$

$\Delta p_a$ = amplitude of lift per unit area at a point (positive upwards)

$S$ = wing area

$sb$ = semispan (normal to air stream)

$U$ = air speed

$x$ = chordwise coordinate (positive downstream from most forward point)

$y$ = spanwise coordinate

$h$ = amplitude of vertical translation motion (dimensional)

$\alpha_a$ = amplitude of pitching motion

$\rho$ = air density

$\chi$ = motion amplitude—i.e., $h_a = (h/b)$ for translation, $\alpha_a$ for pitching

$\omega$ = circular frequency of oscillation

$\beta$ = local nondimensional semispan (delta wings)

$\bar{C}_i$ = complex coefficient ($C_i e^{i\phi_i}$)

$C_i$ = amplitude of the coefficient representing the quantity $i$

$\phi_i$ = phase angle by which the quantity $i$ leads the motion

$C_p$ = pressure amplitude coefficient $[\Delta p_a/(1/2)\rho U^2\chi]$

$\bar{C}_l$ = section lift coefficient $\left[\int_0^1 \bar{C}_p d\left(\frac{x}{c}\right)\right]$ positive upwards

$\bar{C}_m$ = section moment coefficient $\left[\int_0^1 \left(\frac{1}{2} - \frac{x}{c}\right) \bar{C}_p d\left(\frac{x}{c}\right)\right]$ positive nose up

$\bar{C}_{l_c}$ = chordwise sectional lift coefficient $\left[\int_{-\beta(x)}^{\beta(x)} \bar{C}_p d\left(\frac{y}{sb}\right)\right]$

$C_L^{(0)}$ = total zero air-speed lift coefficient $[L^{(0)}/2\rho\omega^2 b^3(sb)\chi]$

$C_M^{(0)}$ = total zero air-speed moment coefficient $[M_{1/2}^{(0)}/2\rho\omega^2 b^4(sb)\chi]$

$\bar{C}_L$ = total lift coefficient $\{[L/(1/2)\rho U^2 S\chi]$ given by $\int_0^1 \bar{C}_l d\left(\frac{y}{sb}\right)$ for straight and swept wings and $\int_0^1 \bar{C}_{l_c} d\left(\frac{x}{c}\right)$ for delta wings$\}$

$\bar{C}_M$ = total mid-chord moment coefficient $\{[\bar{M}_{1/2}/(1/2)\rho^2 U S c_0 \chi]$ given by $\int_0^1 \bar{C}_m d\left(\frac{y}{sb}\right)$ for straight and swept wings and $\int_0^1 \left(\frac{1}{2} - \frac{x}{c}\right) \bar{C}_{l_c} d\left(\frac{x}{c}\right)$ for delta wings$\}$

Presented at the Aeroelasticity Session, Twenty-Third Annual Meeting, IAS, New York, Jan. 24–27, 1955.

* The results presented in this paper were obtained in the course of research sponsored by the Bureau of Aeronautics under Contract NOas 52-576-c.

† Formerly Research Engineer, Aeroelastic and Structures Research Laboratory. Now, Group Leader, Dynamics Section, North American Aviation, Inc., Columbus, Ohio.

‡ Associate Professor of Aeronautical Engineering.

## Introduction

THE LOW ASPECT RATIO WING has been acquiring an ever increasing popularity in the past few years for use on aircraft designed to operate near and above the speed of sound. This has resulted, quite naturally, in a demand for further information concerning the aerodynamic properties of such wings—and it has been the purpose of the present investigation to study this problem for the particular case of incompressible flow.

Although the main interest is in compressible flow, a number of factors have led to carrying out the initial work at low speeds. Of primary importance is the relative ease with which low speed, and therefore low frequency, pressure measurement techniques could be developed. Also of importance is the fact that most existing low aspect ratio theories are primarily applicable to incompressible flow and that they have not been verified experimentally nor checked as to range of validity. Other considerations are related to design problems such as the take-off and landing, low speed stability and control, aeroelastic and gust analyses, and the determination of critical structural loads during low-speed maneuvers. The techniques developed under this program have already been applied to a preliminary investigation of oscillatory pressure distributions in transonic flow.[7] A similar program is planned for the supersonic flow regime.

Even though the present work has been devoted primarily to the experimental determination of the pressure distributions on oscillating wings of low aspect ratio, this emphasis on the unsteady flow does not indicate a neglect of the steady flow. On the contrary, unsteady flow studies are more general in nature and yield the steady state situation for the particular case of zero frequency. Interest in the pressure distribution itself rather than any of its integrated forms such as the spanwise (or chordwise) lift distribution, the spanwise pitching moment distribution, or the total lift and pitching moment arises for two reasons. The first, and most obvious, of these is that the fundamental loading on the wing occurs in the form of distributed pressures, which, if known, permit the ready calculation of all other aerodynamic quantities necessary to the solution of a given problem. Many of the current day lifting surface theories, both steady and unsteady, do not permit calculation of this important load distribution and consequently further studies and extensions are definitely warranted.

The second reason for the present interest in pressure distributions is a consequence of the simultaneous interest in low aspect ratio wings. (For present purposes, the term "low aspect ratio" will be taken to apply to any wing the aspect ratio of which lies in the range of one half to three. Wings of aspect ratio less than one half will be referred to as "very low aspect ratio," whereas wings in the aspect ratio range above three will be designated by "high aspect ratio.") The modern trend from wings of high aspect ratio to wings in the low aspect ratio range has brought about much revision of the structural configuration as well as the aerodynamic form. These changes have taken the form of multispar or thick skin construction with the result that the low aspect ratio wing has tended to become more "platelike" in its behavior under the action of applied loads. This is in contrast to the characteristic "beam-rod" deformations of high aspect ratio wings where the stiffness of the wing in the chordwise direction is normally much greater than that in the spanwise direction. The structural and aeroelastic analysis of the low aspect ratio wing therefore requires that the applied loads be presented in the form of surface pressure distributions rather than spanwise distributions of section lift and pitching moment.

The purpose of the present experimental program has been to investigate the nature of the unsteady airloads on wings of finite span oscillating sinusoidally in pitch and vertical translation. The present work differs from previous experimental investigations[6,8–13] in two main respects:

(1) It is restricted primarily to wings of low aspect ratio for which most existing theoretical methods of analysis are invalid.

(2) Pressure distributions over the surface of each wing are measured rather than the total lift and pitching moment.

The pressure measurement program was divided into two phases, the first of which was devoted to the determination of pressures depending on air speed, and the second to those pressures which are independent of air speed—i.e., the so-called "virtual mass" pressures. This division was advantageous since it permitted the individual components of the pressure distribution to be determined separately, and this made possible a more detailed check on the theoretical expressions. The results of this program may be put to use in two ways:

(1) The pressure distributions themselves provide us with a store of physical knowledge which may be called upon to substantiate future theoretical developments in the low aspect ratio range.

(2) The necessary chordwise and spanwise integrations may be performed numerically on the pressure distribution data to yield appropriate lift and pitching moment distributions and the resultant total lift and pitching moment. It is then possible to check the validity of a large number of current theoretical methods when they are applied to the calculation of the aerodynamic forces on wings of low aspect ratio. Since the majority of these theories are not strictly valid for wings in the present aspect ratio range, we are in a position to evaluate the resultant errors—and to recommend methods of correction. Furthermore, the total lift and pitching moment data serve as a basis of comparison with the results of previous experimental studies, where only the total forces and moments were measured.

## Pressure Pickup

The basic item in both phases of the pressure measurement program described above, was a small crystal-

type pressure pickup developed at Massachusetts Institute of Technology by Y. T. Li of the Instrumentation Laboratory. The sensitive element of this pickup is a thin layer of barium titanite, arranged as shown in Fig. 1. Barium titanate, quartz, rochelle salt, and several other crystalline compounds possess piezo-electric properties—i.e., when the crystal is loaded or stressed, an electric potential proportional to the stress appears between opposing plane faces. A reversal of the stress will cause a reversal of the electric charges on the crystal faces. The sensitivity of the crystal may be greatly increased by initial polarization of the opposite faces thus causing a permanent potential to exist between them even in the unstressed state. In this application, the crystal is bonded to a thin circular steel diaphragm which is secured firmly to a circumferential stiffening ring. When pressure (or suction) is applied to the outer surface of the diaphragm it deforms at any cross section in a manner similar to that of a beam built in at its ends (see Fig. 1). Since the incremental piezo-electric voltage of the crystal is linearly related to its stress, and since the bending stresses of the diaphragm are linear with pressure for small deflections, a straight line relationship exists between applied pressure and pickup output.

Although the pressure pickup described here has proved itself to be an excellent instrument for the detection of extremely small pressure fluctuations, it is not without its disadvantages. The first major problem which presented itself in connection with the circuit design resulted from the extremely high impedance of the pickup. The effect of this was to cause large spurious signals when any part of the lead connecting the pickup and the amplifier was moved. This difficulty was attributed to relative motion between the shield and central conductor giving rise to a "separation of charges," and it was largely overcome by careful design and selection of the connecting cable. This phenomena and methods of overcoming it are described fully by Perls.[14]

The second disadvantage of the piezo-electric pressure pickup used in these tests was its inability to generate a constant voltage as a result of a steadily applied pressure. This came about through the fact that the barium titanite crystal is not a perfect insulator, and additional potentials created by stresses in the crystal tended to decay to zero in a period of about one second. This characteristic, although it constitutes no distortion problem for pressures varying periodically at frequencies above 5 cycles per sec. gives rise to major calibration difficulties, since it becomes necessary for quantitative pressure measurements to calibrate the system against a known time varying pressure, rather than a more easily applied constant pressure.

The final problem concerning the pressure pickup installation was a consequence of its sensitivity to linear accelerations. This sensitivity, although slight by conventional standards, constituted a serious consideration in the present investigation in which the working pressures were of the order of 0.01 lb. per sq.in. or less. Due to the very high natural frequency of the pickup (about 5000 cycles per sec.), the output was found to be directly proportional to the applied acceleration for the frequencies of interest. In terms of equivalent pressure, this sensitivity amounted to approximately 0.002 lb. per sq.in./$g$. Since in the wind-tunnel tests, the pickup was flush-mounted on the surface of the oscillating wing, it is readily seen that the output resulting from the wing's acceleration could easily obscure any output due to a pressure fluctuation. Furthermore, since the acceleration depends on the amplitude of the motion and the square of the frequency the situation becomes progressively worse as the frequency is increased. In order to overcome this obstacle, it was necessary to design an acceleration compensating circuit consisting of a "dummy" pressure pickup subjected to the same sinusoidal motion as the "active" pickup. The output of the "dummy" pickup was adjusted during still air vibration to null the output of the "active" pickup. This procedure also resulted in the nulling of the signal due to the noncirculatory or virtual-mass pressures which are not a function of airspeed. In order to obtain these noncirculatory forces, which were previously balanced out, the second phase of the program consisted of determining the "still air" pressure distributions very close to the surface of the oscillating wing by means of a probe arrangement. This installation permitted a pressure pickup mounting which was stationary and thus free of acceleration effects.

## Wind-Tunnel Tests

As the first phase of the experimental program, the purpose of the wind-tunnel tests was to determine the distributions of pressure amplitude and phase angle over the surface of several wings of low aspect ratio when oscillating in a moving air stream. The following wing plan forms were selected since they represent configurations which are of current interest to the aeronautical profession, and, at the same time, they are related to plan forms in the more extreme aspect ratio ranges for which theories are currently available.

(i) Aspect ratio one rectangular wing.
(ii) Aspect ratio two rectangular wing.
(iii) Aspect ratio two constant chord wing with 45° sweepback.
(iv) Delta wing with 60° leading edge sweepback (aspect ratio = 2.31).
(v) Delta wing with 75° leading edge sweepback (aspect ratio = 1.07).
(vi) Aspect ratio two rectangular wing fitted with wing-tip tanks of circular cross section, fineness ratio 11.1, and a length to wing chord ratio of 2.0.

The tests were performed in the M.I.T. 5 by 7½ ft. low-speed Flutter Wind Tunnel at a constant air speed of 90 m.p.h. The models were mounted on the M.I.T.-NACA airfoil oscillator which is a mechanical device capable of shaking a wing in sinusoidal motions at

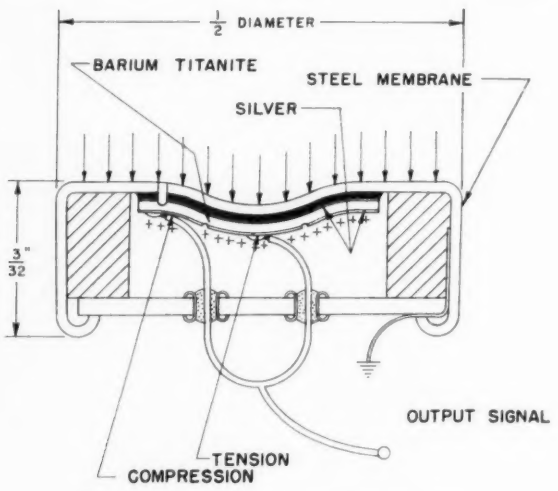


FIG. 1. Barium titanate pressure transducer.

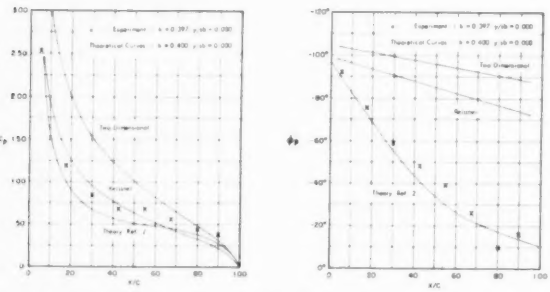

FIG. 2. Pressure amplitude and phase angle, aspect ratio 1.00 rectangular wing, vertical translation motion.

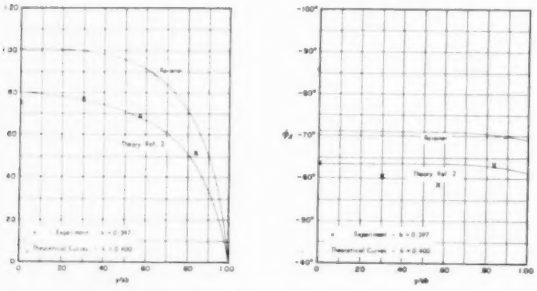

FIG. 3. Section lift amplitude and phase angle, aspect ratio 1.00 rectangular wing, vertical translation motion.

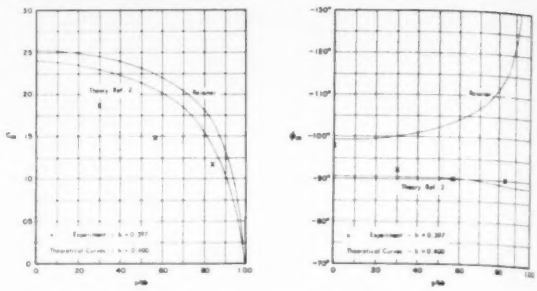

FIG. 4. Section mid-chord pitching moment amplitude and phase angle, aspect ratio 1.00 rectangular wing, vertical translation motion.

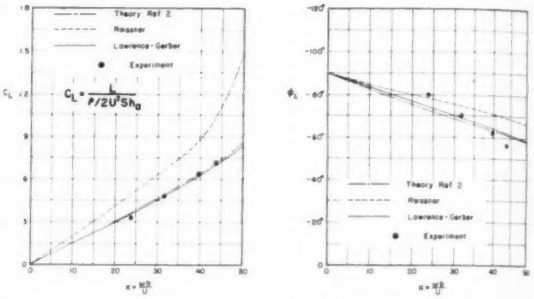

FIG. 5. Total lift amplitude and phase angle, aspect ratio 1.00 rectangular wing, vertical translation motion.

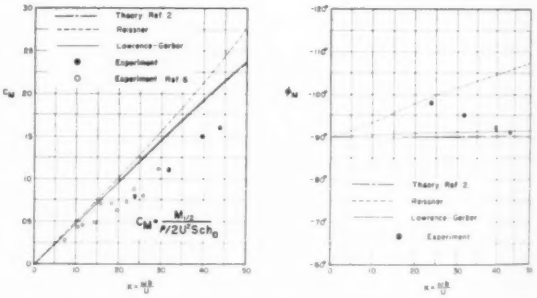

FIG. 6. Total mid-chord pitching moment amplitude and phase angle, aspect ratio 1.00 rectangular wing, vertical translation motion.

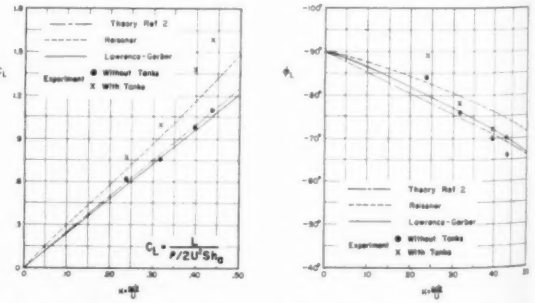

FIG. 7. Total lift amplitude and phase angle, aspect ratio 2.00 rectangular wing, vertical translation motion.

frequencies of from 2 to 15 cycles per sec. Two basic motions were used in all tests:

(1) Rigid body vertical translation with a mean angle of attack of 0°.

(2) Rigid body pitching about a spanwise axis located at the mid-chord point for the rectangular and delta wings; and the 70 per cent root chord point for the 45° sweptback wing. The mean angle of attack in both cases was 0°.

The reduced frequencies for the rectangular wings and the 45° sweptback wing were in the range $0.20 < k < 0.45$ at a test Reynolds Number of 1,400,000, whereas for the two delta wings the reduced frequency range was $0.30 < k < 0.60$ at a Reynolds Number based on a root chord of 2,100,000.

Pressure measurements were made at about 30 points on the half span of each wing for both the pitching and vertical translation motions. An individual "pressure measurement" at a given point on the wing consisted of recording (a) the amplified alternating voltage output of the pressure pickup mounted at the point in question, and (b) the phase angle between this alternating voltage (or "pressure") and the wing motion. The magnitude of the pickup output voltage was read on a suitable r.m.s. voltmeter, while the phase angle was indicated directly on a Technology Instrument Corporation Phasemeter. The reference voltage for the phase angle measurement was supplied to the phasemeter from a covered pressure pickup mounted on the frame of the oscillator and moving in phase with the wing. This second pickup served then essentially as an accelerometer.

It should be noted that the alternating voltage signal produced by the pressure pickup mounted at any point on the upper surface of the oscillating wing is directly proportional to the unsteady (or fluctuating) component of the pressure, and that according to thin airfoil theory this pressure amounts to one half of the total unsteady lift per unit area at the point. Previous experimental investigations have established the validity of the thin airfoil theory assumptions regarding profile shape, thickness, amplitude of motion, and mean angle of attack for wing motions which do not approach the stall range and for which the Reynolds Number of the flow is above approximately 300,000. Since motions in the present tests are restricted to small amplitudes and since the Reynolds Numbers are well over 1,000,000, it is therefore assumed that the effects of profile and thickness are negligible and that equal pressure fluctuations occur on the upper and lower surfaces of the wing at a given point.

## Still Air Tests

The second and final phase of the investigation was directed toward the determination of those pressures which act on a wing as a result of its oscillatory motion in still air. The results of this phase of the work provide considerable insight into a problem which heretofore has been somewhat neglected; and, at the same time, they combine with the results of the first phase to give the complete airload distribution as it would actually occur on a wing in a moving air stream.

Since the results of this study were intended to amplify those of the first phase, the same wing plan form shapes were again chosen, omitting however, the sweptback wing and the tip-tank configuration. (The zero air-speed pressures for these wings were estimated by a method outlined in reference 2.) An additional set of "two-dimensional" tests was made by operating the aspect ratio two rectangular wing in the presence of vertical "end plates." The models used in these tests were constructed of $^1/_4$ in. steel plate and mounted in the laboratory on three electro-magnetic shakers. As in the wind-tunnel tests, the two basic rigid body motions of vertical translation and mid-chord pitching were used.

Pressures were measured over the surface of the oscillating wing by means of a pressure pickup similar to that used in the wind-tunnel program. In this case, however, the pickup was not mounted on the surface of the wing, but rather it was built into a pressure probe unit which was carried above the wing on a moving carriage. The probe extended downward from the pressure capsule to a point very near the upper surface of the wing. The end of the probe could be located above any desired point on the oscillating wing by appropriate movement of the carriage and pressure unit. The pressure pickup produced a voltage output proportional to the amplitude of the pressure fluctuation at the end of the measuring probe. It may be shown by means of two dimensional theory[2] that this pressure is very nearly equal to the "lifting pressure" on the wing surface directly under the probe.

Tests were conducted in all cases at a frequency of 35 cycles per sec., and the output of the pressure pickup was observed on a Ballantyne voltmeter. No phase angle measurements were taken since the success of the zero air-speed balance system employed in the wind-tunnel program definitely established the fact that the required pressures occurred in phase with the local accelerations of the wing.

## Presentation of Results

Typical experimental results are given in Figs. 2–13, and a complete presentation of the findings appears in reference 2. For purposes of brevity the discussion here will be limited only to the vertical translation motion; although, in general, the same observations and conclusions are also true for the pitching case. The data of Figs. 2–13 include both the air speed and zero air-speed contributions to the aerodynamic forces, suitably combined by vectorial addition.

Chordwise distributions of pressure coefficient amplitude and phase angle at the center section of the aspect ratio one rectangular wing are shown in Fig. 2 for $k = 0.397$. The corresponding theoretical distributions were obtained from (i) strip theory, (ii) Reissner high aspect ratio theory,[1] and, (iii) the low aspect ratio

theory of reference 2 for a reduced frequency of 0.400. It will be observed that the low aspect ratio theory gives good agreement with experiment; whereas the Reissner theory although reasonably close in regard to pressure amplitudes, gives phase angles which are at a considerable variance with the test results. The strip theory (or infinite aspect ratio) result is obviously unsuitable and gives large errors both in magnitude and phase angle. These errors increase rapidly as the wing tip is approached. The effects of spanwise position are illustrated quite well by the plots of section lift and mid-chord pitching moment (Figs. 3 and 4). Again the low aspect ratio theory gives satisfactory results; but the Reissner theory is in surprisingly good agreement with experiment—a remarkable circumstance considering the restrictive aspect ratio assumptions involved in the theory.

The effect of reduced frequency on the total lift and mid-chord pitching moment coefficients is shown in the curves of Figs. 5 and 6. In addition to the theoretical comparisons used above, the results of calculations by the method of Lawrence and Gerber[3] are also shown. The most significant fact which appears is that the two low aspect ratio theories give results which are practically identical. These are in excellent agreement with the experimental lift magnitudes and phase angles, but the moment data show definite discrepancies with the test results as obtained in the present experiments and in the experiments of reference 6. This can no doubt be attributed to the effects of Reynolds Number, nose curvature, and thickness which are not accounted for in the thin airfoil theory.

Figs. 7 and 8 give the total lift and moment coefficients for the aspect ratio two rectangular wing—with and without the tip tanks. The same general conclusions regarding the low aspect ratio theories may be drawn; and, for this wing, the high aspect ratio theory of Reissner is noticeably closer to the test points. The wing-tip tanks cause an increase of about 25 per cent in the magnitudes of both the lift and pitching moment but leave the phase angles unaltered. This latter behavior indicates that the flow is "more two dimensional" only insofar as the spanwise distributions of section lift and moment magnitudes are concerned.

Sweepback effects may be deduced by a comparison of Figs. 7 and 8 with Figs. 9 and 10. Experimentally, there appears to be very little difference in the total lift measurements, whereas the moment phase angles for the straight and swept wings are roughly 180° apart. This is due to the fact that the swept wing center of pressure is located behind the moment axis (mid-chord of root section) whereas for the straight wing it was ahead of this axis. The swept-wing theory of reference 6 is used in Figs. 9 and 10 for purposes of comparison. The lift and moment magnitudes are predicted very well, but large phase errors exist. It was found that for the pitching motion the theoretical data involved errors in both magnitude and phase, and that for both motions large discrepancies occurred in the pressure distributions. This was particularly true near the center section and can no doubt be attributed to the inadequacy of the theoretical assumptions in this region.

The chordwise lift distribution—i.e., lift per ft. in the chordwise direction—is given for the aspect ratio 2.31 delta wing in Fig. 11 for a reduced frequency of 0.476. The pressure distributions have been omitted, but it may be stated that the shape of the spanwise pressure amplitude plots at all chordwise stations were in qualitative agreement with the predictions of Garrick[4] and Voss.[5] The phase angles agreed not only in magnitude but also in distribution. The chordwise lift distributions are adequate, therefore, to illustrate the shortcomings of this slender wing theory. It is certainly clear from Fig. 11 that the main criticism concerns the failure of the method to provide for the Kutta condition at the trailing edge ($x/c = 1.0$). The Lawrence and Gerber theory,[3] on the other hand, appears satisfactory in this respect and gives results which are reasonably close to experiment. It will be noted that both theories predict phase angles with about the same degree of accuracy. This fact is interesting since the slender wing theory of Garrick and Voss takes no account of the unsteady wake behind the oscillating wing, whereas the Lawrence and Gerber theory takes the wake vorticity into account. From this we may make two significant conclusions:

(1) The unsteady wake is less important for the low aspect ratio oscillating wing than it is for the high aspect ratio case.

(2) It may be possible to apply a corrective function to the lift amplitudes of the slender wing theory in order to allow empirically for the Kutta condition. This would be advantageous since the inherent simplicity of the slender wing theory would be retained and, at the same time, a closer agreement with experiment would result. For this purpose, the lift amplitudes of the Garrick-Voss theory have been multiplied by the chordwise function $\sqrt{1 - (x/c)^2}$ with the excellent results shown in Fig. 11. This behavior was observed in all cases for both delta wings. The use of this function permits the retention of the spanwise pressure distribution shape but incorporates the necessary "scale" correction.

The total lift and pitching moment data of Figs. 12 and 13 show the comparisons between the experimental points, the slender wing theory, and the low aspect ratio theory of Lawrence and Gerber. Again the practical value of the modified slender wing theory is evident.

The results of the zero air-speed (or "virtual mass") tests are presented briefly in Table 1 as comparisons between the experimental and theoretical total forces and moments. The theoretical rectangular wing coefficients were computed from strip theory considerations, whereas infinite "sheared" wing theory was used for the sweptback wing. The unmodified slender wing theory was used in the case of the delta wings. In all instances, appreciable corrections for the effects of finite aspect ratio are indicated.

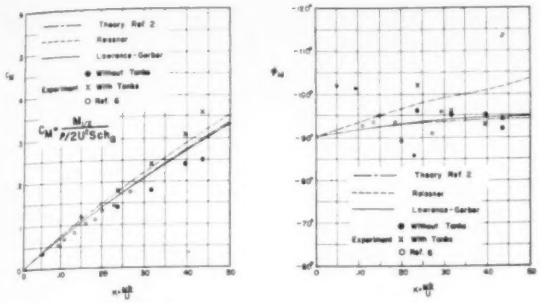


FIG. 8. Total mid-chord pitching moment amplitude and phase angle, aspect ratio 2.00 rectangular wing, vertical translation motion.

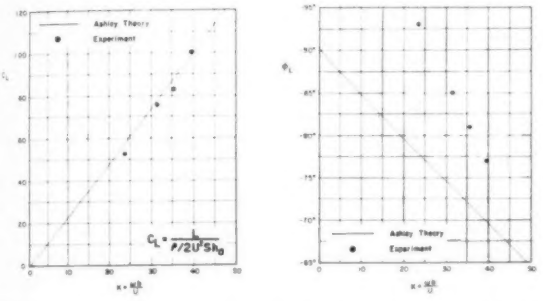


FIG. 9. Total lift amplitude and phase angle, aspect ratio 2.00, 45° sweptback wing, vertical translation motion.

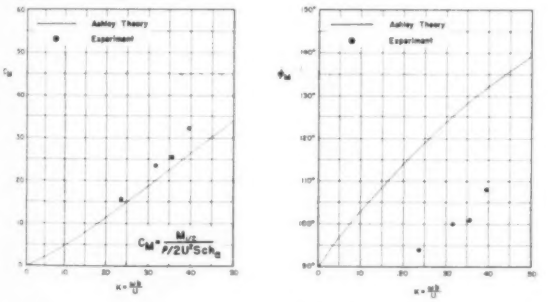


FIG. 10. Total root mid-chord pitching moment amplitude and phase angle, aspect ratio 2.00, 45° sweptback wing, vertical translation motion.

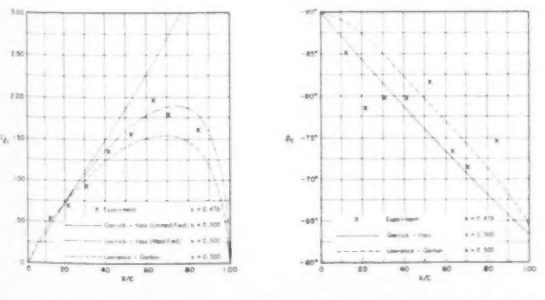

FIG. 11. Chordwise lift amplitude and phase angle, aspect ratio 2.31 delta wing, vertical translation motion.

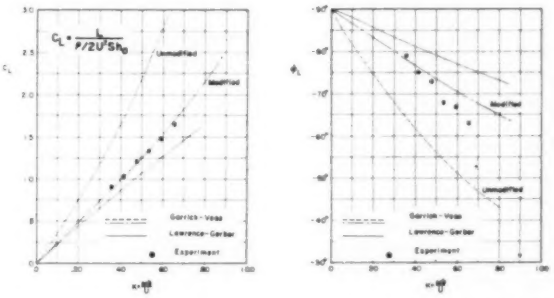


FIG. 12. Total lift amplitude and phase angle, aspect ratio 2.31, delta wing, vertical translation motion.

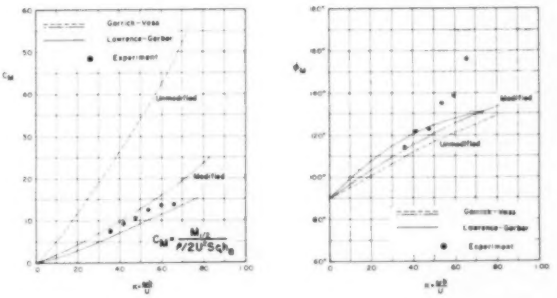


FIG. 13. Total root mid-chord pitching moment amplitude and phase angle, aspect ratio 2.31, delta wing, vertical translation motion.

TABLE I
Total Lift and Pitching Moment at Zero Air-Speed, Vertical Translation Motion

| WING | ASPECT RATIO | $C_L^{(0)}$ | | $C_M^{(0)}$ | |
|---|---|---|---|---|---|
| | | EXPERIMENT | THEORY | EXPERIMENT | THEORY |
| RECT. | 1.00 | 2.08 | 3.142 | 0 | 0 |
| RECT. | 2.00 | 2.51 | 3.142 | 0 | 0 |
| RECT. and TANKS | 2.00 | 3.14* | 3.142 | 0* | 0 |
| 45° SWEPT | 2.00 | 1.77* | 2.220 | -0.764* | -2.220 |
| DELTA | 1.07 | 0.370 | 0.561 | -0.132 | -0.281 |
| DELTA | 2.31 | 0.760 | 1.210 | -0.240 | -0.605 |

* Estimated.

## Conclusions

The theoretical and experimental comparisons of the present investigation have led to several important conclusions regarding the status of existing lifting surface theories. They have also pointed the way to future theoretical extensions in order that ultimately more general lifting surface problems may be handled.

The major conclusions of the present research program may be summarized briefly as follows:

(a) The two-dimensional thin airfoil theory, although offering simplicity not found elsewhere, has no place in low aspect ratio calculations. This theory permits a determination of the chordwise pressure distribution, but since it takes no account of tip effects it must be restricted to use on wings of very high aspect ratio where the wing tips are of secondary importance. Such wings are usually of a structural configuration which may be analyzed without recourse to the pressure distribution hence the two dimensional pressure distribution theory although of interest as a limiting case has very little value as a practical tool.

(b) The high aspect ratio theory of Reissner is a direct extension of the two dimensional theory and consequently is still subject to many of its limitations. In the past, the Reissner theory has proved itself to be a very useful instrument in high aspect ratio flutter and dynamic stability calculations. The present experiments have shown that this method could probably be used for finite wings of aspect ratio as low as two without serious error, but that beyond this point it is inadequate.

(c) The low aspect ratio theory of Lawrence and Gerber has been found to give very good results both for chordwise lift distribution and for total lift and pitching moments The method has the facility of handling a variety of plan forms in the low aspect ratio range, but unfortunately it is incapable of yielding pressure distributions for wings where these distributions are of primary interest.

(d) The very low aspect ratio theory of Garrick and Voss when applied to delta wings of low aspect ratio is at a tremendous disadvantage because it is unable to account for the trailing edge condition of zero pressure difference. This shows up in the integrated data and gives rise to very large errors in the total lift and pitching moment. In all other respects, however, this theory must be judged favorably since the spanwise shape of the pressure distributions, the chordwise lift distribution near the nose, and the pressure phase angles over the whole wing are generally in very good agreement with experiment. An empirical modification of the pressure amplitudes near the trailing edge, in order to satisfy the Kutta condition, has produced results which in all cases check the test measurements very well; and it is thought that, in its modified form, the Garrick-Voss theory will probably become widely used as a method for predicting the aerodynamic characteristics of delta wings.

(e) The high aspect ratio swept-wing theory of Ashley[6] is not sufficiently accurate for analysis in the low aspect ratio range, as was the equivalent straight wing theory of Reissner. This is due to the strong three-dimensional flow near the center section of a swept wing which the theory is incapable of handling with any degree of precision. For a high aspect ratio wing, these effects are confined to a relatively small portion of the total wing span and hence the theoretical approximations near the center section probably have very little effect on the overall result. This theory does however show promise from the standpoint of obtaining total lift and pitching moment data providing some empirical modifications are incorporated which would permit its extension into the low aspect ratio range.

(f) The low aspect ratio theory of reference 2 enables predictions of the pressure distributions on rectangular wings in a range of aspect ratio excluded by the great majority of existing lifting surface theories. These distributions, and all integrals of them, appear to agree very well with the experimental evidence now on hand.

(g) The present tests have included only one wing-tip tank configuration, and much more extensive testing would be required before any general conclusion could be drawn. However, when wing-tip tanks are added to a rectangular wing of aspect ratio two, the spanwise distributions of section lift and pitching moment assume a nearly two dimensional form—i.e., practically constant in the spanwise direction. The total lift and pitching moment amplitudes are both increased by the same factor while the phase angles remain unaltered. This amplitude factor, which is apparently independent of the reduced frequency, is very nearly equal to the ratio of the steady state lift curve slope of the wing with tanks to that of the same wing without tanks.

## References

[1] Reissner, E., *Effect of Finite Span on the Airload Distributions for Oscillating Wings: I—Aerodynamic Theory of Oscillating Wings of Finite Span*, NACA Technical Note 1194, 1947.

[2] Laidlaw, W. R., *Theoretical and Experimental Pressure Distributions on Oscillating Low Aspect Ratio Wings*, Sc. D. Thesis, Massachusetts Institute of Technology, May, 1954.

[3] Lawrence, H. R., and Gerber, E. H., *The Aerodynamic Forces on Low Aspect Ratio Wings Oscillating in an Incompressible Flow*, Journal of the Aeronautical Sciences, Vol. 19, No. 11, Nov., 1952.

[4] Garrick, I. E., *Some Research on High Speed Flutter*, Proceedings of the Third Anglo-American Aeronautical Conference, Appendix B., RAeS-IAS, 1951.

[5] Voss, H. M., *Flutter of Low Aspect Ratio Lifting Surfaces*, S. M. Thesis, Massachusetts Institute of Technology, May, 1951.

[6] Ashley, H., Zartarian, G., and Neilson, D. O., *Investigation of Certain Unsteady Aerodynamic Effects in Longitudinal Dynamic Stability*, USAF Technical Report 5986, Dec., 1951.

[7] Mollo-Christensen, E. L., *An Exploratory Experimental and Theoretical Investigation of Unsteady Transonic Flow*, Sc.D. Thesis, Massachusetts Institute of Technology, May, 1954.

[8] Bratt, J. B., and Scruton, C., *Measurements of Pitching Moment Derivatives for an Airfoil Oscillating about the Half-Chord*

*(Continued on page 176)*

# Viscous Flow Along a Flat Plate Moving at High Supersonic Speeds*

Y. H. KUO†
*Cornell University*

SUMMARY

By the distortion of coordinates, it is shown that, in the case of supersonic viscous flow past a flat plate, the boundary-layer and simple wave theories can be combined to give a complete representation of the velocity and pressure fields. Consistent first-order solutions are considered. An expression for the induced pressure on the plate, correct to the second order, is obtained. At high Mach Numbers the important parameter satisfies the hypersonic similarity law; and for arbitrary Mach and Reynolds Numbers and for different gases, the theoretical curve correlates closely the experimental data. Asymptotic shock curve and skin-friction coefficient are also deduced, but the experimental verifications are yet to be made.

SYMBOLS

| | |
|---|---|
| $Re$ | $= \rho_\infty UL/\mu_\infty$ |
| $\beta$ | $= \sqrt{M^2 - 1}$ |
| Physical variables defined in Eqs. (2.1) and (3.1) | |
| $T_w, \omega$ | defined in Eq. (2.7) |
| $v_e$ | defined in Eq. (3.3) |
| $\epsilon, v_0$ | defined in Eq. (3.4) |
| $J$ | defined in Eq. (3.5) |
| $f_1, g_1$ | defined in Eq. (4.1) |
| $p^{(2)}$ | defined in Eq. (4.10) |
| $C_2$ | defined in Eq. (8.3) |
| $\theta$ | defined in Eq. (9.1) |
| $K, \chi$ | defined in Eq. (10.4) |
| Superscripts indicate order of approximation | |
| Subscripts indicate partial differentiation | |
| Primes indicate total differentiation | |

## (1) INTRODUCTION

WHEN A SEMI-INFINITE FLAT PLATE moves edgewise through a gas of infinite extent with a constant flight speed, the gas close to the plate will be brought into motion by the action of viscosity of the gas. If the gas is incompressible, the flow is mainly a diffusion phenomenon and, consequently, can be conveniently described by a variable following the law of molecular diffusion, as has been done by Blasius.

As the flight speed increases, the simple hypothesis of incompressibility of gases is no longer valid and the effect of compressibility has to be considered. Because of the motion of the plate, the forward propagating family of waves generated by the viscous displacement of the flow tends to collect and form a shock with strength varying with flight Mach Number as well as with the distance from the leading edge of the plate. After a shock is formed, the pressure waves, which would have disappeared into infinity, are caught by the shock; and being a poor reflector, the shock will deflect more and more of the flow, which will, in turn, generate stronger waves. This interplay of two dominant effects, viscosity and compressibility, eventually reaches a permanent state, for a given Mach Number, as observed in high-speed flight or in the wind tunnel.

Distinct from the incompressible case, the induced quantities, such as the viscous deflection of streamlines and the pressure, are not small. At flight Mach Number 6, say, the shock strength near the plate becomes as high as 5 atmospheres. Furthermore, their order of magnitude changes as the distance from the leading edge varies. This, in essence, is the reason why simple mathematical descriptions, such as in the Blasius problem, are not possible. Of course, one might attempt to find a solution by iteration with boundary-layer theory at one's disposal. But the difficulty one will face is that if the Blasius solution is chosen as the basic approximation, it will lead to a second-order deflection infinitely large at infinity and a strong singularity near the leading-edge shock. The process of iteration thus diverges. If, on the other hand, the flow is assumed to follow the law of similarity, as Lees has proposed,[1] simple solutions can be found but, from experimental evidence, their range of application is very limited.

In the light of these difficulties, it is believed that in dealing with problems of this nature only solutions that bear a resemblance to exact ones can be useful. This requires that the analytic behavior of the solution should closely follow the character of the exact solution, if not every detail. In other words, near the plate, where the boundary-layer approximation is valid, the solution should agree with the predictions of boundary-layer theory. When the distance from the plate is large—namely, at the edge of the boundary layer—it should merge smoothly with the inviscid field. Thus, at any section of the plate, the solution gradually shifts from the character of the boundary-layer solution to that of the inviscid field, which is what the exact solution does. If such a solution were available, it would, at least, give the most outstanding features of the high-speed viscous flow. In what follows, in the hope of attaining this goal, an attempt, based on an extension of the idea of Lighthill,[2] has been made. The results are not entirely without interest even though there are still points that have not yet been clarified. It will

Received December 10, 1954. Revised and received July 23, 1955.

* This work was carried out at the Daniel and Florence Guggenheim Jet Propulsion Center, California Institute of Technology, while the author was on leave of absence from Cornell University. The continued interests of, and the frequent discussions with, Prof. H. S. Tsien were invaluable for a clearer understanding of the problem.

† Professor, Graduate School of Aeronautical Engineering.

serve a useful purpose if further interests are stimulated.

As a trial, the first-order problem will be treated first. To this order—i.e., to the order of viscous displacement of streamlines—the solution is made uniformly valid at the edge of the boundary layer and is singular only at the leading edge. In this sense, the solution obtained below is asymptotic and can be regarded as the counterpart of the Blasius solution for low-speed flow.

The most fundamental hypothesis in this paper is that the fluid dealt with is a continuum. This means that the Navier-Stokes equations as well as the nonslip condition at the surface of the plate are assumed to be valid. There is no question that on the whole this is acceptable. It is debatable, however, whether it would give a true physical picture near the leading edge in the range of Mach Number considered, aside from objections on purely pedagogical grounds. Nevertheless, from all indications, classical hydrodynamics does provide a correct order of magnitude for all the practically interesting quantities and, at this stage, should be of great value to engineers.

In the following, the problem will be subdivided into four sections. Sections (I) and (II) are devoted, as a preparation, to methods of solution for the viscous and inviscid fields. Section (III) deals with the main problem of interaction between these two fields of flow, which constitute the foundation of the entire problem. The remarkable result in Section (III) is that the two distinct fields of flow are made to overlap, which is conceptually much broader than the usual notion of "smooth joining." Finally, Section (IV) contains the results deduced from solutions in Section (III). One of the conclusions is that, due to the interaction of the leading-edge shock with the boundary layer, the shear stress on the plate first increases, reaches a maximum, and then asymptotically follows the classical law of friction, with increasing distance from the leading edge of the plate. Thus, the question whether this phenomenon is primarily caused by slip-flow or by the presence of shock can easily be settled by experiments.

## (I) Viscous Field

### (2) Boundary-Layer Equations

Suppose a uniform stream of viscous gas flows at high supersonic speeds past a semi-infinite flat plate at no angle of attack. The motion around the plate is considered to be two-dimensional and steady. Near the surface of the plate, the flow problem can be dealt with by boundary-layer theory according to Shen[3] and Lees[1] under suitable restrictions of Reynolds and Mach Numbers. However, if the whole flow field is to be considered, the boundary-layer equations have to be modified.

In a Cartesian system, let the velocity components $\bar{u}$ and $\bar{v}$ be parallel respectively to $\bar{x}$ and $\bar{y}$-axes, and let the plate be defined by $\bar{y} = 0$ and $0 \leq \bar{x}$. If the density $\bar{\rho}$, temperature $\bar{T}$, pressure $\bar{p}$, and viscosity $\bar{\mu}$ are respectively $\rho_\infty$, $T_\infty$, $p_\infty$, and $\mu_\infty$ at infinity, the following nondimensional variables are introduced:

$$\left.\begin{aligned} u &= \bar{u}/U \\ V &= (Re/C)^{1/2}\bar{v}/U = (Re/C)^{1/2}v \\ p &= \bar{p}/p_\infty \\ x &= \bar{x}/L \\ Y &= (Re/C)^{1/2}\bar{y}/L = (Re/C)^{1/2}y \\ \rho &= \bar{\rho}/\rho_\infty \\ T &= \bar{T}/T_\infty \\ \mu &= \bar{\mu}/\mu_\infty \end{aligned}\right\} \tag{2.1}$$

where $Re$ denotes the Reynolds Number $\rho_\infty UL/\mu_\infty$, $U$ and $L$ are the flight speed and a measure of the length of plate, respectively; and $C$ is a constant to be defined below. Since $L$ is not a characteristic length of the problem, it will drop out from the final results.

In terms of these variables and using the subscript notation for partial differentiation, the modified boundary-layer equations can be written as

$$\begin{aligned} &\Psi_Y\left(\frac{1}{\rho}\Psi_Y\right)_x - \Psi_x\left(\frac{1}{\rho}\Psi_Y\right)_Y = \\ &\qquad -\frac{1}{\gamma M^2}p_x + \left[\frac{\mu}{C}\left(\frac{1}{\rho}\Psi_Y\right)_Y\right]_Y \\ &-\frac{1}{\gamma M^2}p_Y + \frac{C}{Re}\left\{\Psi_Y\left(\frac{1}{\rho}\Psi_x\right)_x - \Psi_x\left(\frac{1}{\rho}\Psi_x\right)_Y - \right. \\ &\qquad \frac{4}{3}\left[\frac{\mu}{C}\left(\frac{1}{\rho}\Psi_x\right)_Y\right]_Y - \frac{2}{3}\left[\frac{\mu}{C}\left(\frac{1}{\rho}\Psi_Y\right)_x\right]_Y + \\ &\qquad \left.\left[\frac{\mu}{C}\left(\frac{1}{\rho}\Psi_Y\right)_Y\right]_x\right\} = 0 \end{aligned} \tag{2.2}$$

and for a perfect gas the equation of state:

$$p = \rho T \tag{2.3}$$

Here $\Psi(x, Y)$ denotes the stream function defined by

$$\rho u = \Psi_Y, \quad \rho V = -\Psi_x \tag{2.4}$$

$\gamma$ is the ratio of the specific heats, and $M$ is the free-stream Mach Number $U/(\gamma p_\infty/\rho_\infty)^{1/2}$. In the case where the plate is thermally insulated and the Prandtl Number is unity, the energy equation admits a relation between temperature and velocity:

$$T = 1 + [(\gamma - 1)/2]M^2(1 - u^2) \tag{2.5}$$

It was noticed by Howarth[4] that if $\mu$ varies linearly with temperature, the differential equations [Eqs. (2.2)] can be considerably simplified by a transformation of $Y$. This approximation, however, was found to underestimate the compressibility effects at high Mach Numbers. To improve its accuracy, a form due to Chapman and Rubesin[5] has been adopted—namely,

$$\mu = CT \tag{2.6}$$

where the constant $C$ will be so chosen as to give the

best fit in the important temperature range with the measured viscosity coefficient. As the high temperature region usually occurs in the neighborhood of the wall, it is customary to make the fit at the wall. If the viscosity obeys the power law $T^{\omega}$ where $\omega$ is 0.76 for air and 0.75 for helium, it follows from Eqs. (2.5) and (2.6) that

$$C = T_w^{\omega-1} = \{1 + [(\gamma - 1)/2]M^2\}^{\omega-1} \quad (2.7)$$

where $T_w$ denotes the temperature at the plate. This relation will be consistently used in the subsequent deductions.

## (3) Method of Solution

From Eqs. (2.2), it is seen that the determination of the function $\Psi$, within the limitations of the boundary-layer approximation, is possible when the pressure in the main stream is prescribed. In the present problem, however, the pressure, which is a result of the mutual interaction of the viscous and compressible effects of the gas in the presence of a solid boundary, is at first unknown. In what follows, a process of iteration will be developed by which ultimately both the velocity and pressure fields can be calculated.

In view of the fact that the pressure in the case of a flat plate moving at high supersonic speeds is a first-order quantity, it seems possible to begin the iteration by taking the pressure to be constant. The zero-order solution is then the classical case treated by von Kármán and Tsien[6] and, by means of Howarth's transformation, reduces to that of Blasius. Due to the boundary-layer approximation, which neglects the curvature effect of the streamlines, this perturbation, if carried out, would lead, however, to a second-order velocity which diverges at infinity, besides the singularity at the leading edge. This difficulty can be avoided by modifying the method of perturbation according to a concept of Lighthill.[2] Namely, by writing

$$\begin{aligned} \Psi &= \sqrt{p}\,\psi \\ \psi &= \psi^{(0)}(\xi,\eta) + \epsilon\psi^{(1)}(\xi,\eta) + \dots \\ p &= 1 + \epsilon p^{(1)}(\xi,\eta) + \epsilon^2 p^{(2)}(\xi,\eta) + \dots \\ T &= T^{(0)}(\xi,\eta) + \epsilon\, T^{(1)}(\xi,\eta) + \dots \\ x &= \xi + \epsilon\, x^{(1)}(\xi,\eta) + \dots \end{aligned} \quad (3.1)$$

and, as a measure of simplification, Howarth's transformation is also incorporated:

$$Y = \frac{1}{\sqrt{p}} \int_0^{\eta} T dz \quad (3.2)$$

Here $\xi$, $\eta$ may be considered as new parameters related to the old variables $x$ and $Y$ by Eqs. (3.1) and (3.2). The perturbation parameter $\epsilon$ can be interpreted as the lateral displacement of a streamline because, to the first order, the pressure, as will be shown in Section (II) is proportional to the velocity $v_e$ at the edge of the boundary layer, which according to Howarth's approximation is

$$V_e = \sqrt{C/Re}[0.860 + 0.596(\gamma - 1)M^2]\,(1/\sqrt{x}) \quad (3.3)$$

Without loss of generality, let the parameter $\epsilon$ and the constant $v_0$ be defined by

$$\left.\begin{aligned} \epsilon &= \sqrt{C/Re} \\ v_0 &= 0.860 + 0.596\,(\gamma - 1)M^2 \end{aligned}\right\} \quad (3.4)$$

Following the transformation [Eqs. (3.1) and (3.2)], the derivatives $\partial/\partial x$ and $\partial/\partial Y$ in Eqs. (2.2) are replaced by, respectively,

$$\left.\begin{aligned} \frac{\partial}{\partial x} &= \frac{\partial}{\partial \xi} - \frac{\sqrt{p}}{T} Y_{\xi} \frac{\partial}{\partial \eta} + \epsilon\,(J x_{\eta}^{(1)} - x_{\xi}^{(1)}) \times \\ &\qquad \left(\frac{\partial}{\partial \xi} - J\,\frac{\partial}{\partial \eta}\right) + \dots \\ \frac{\partial}{\partial Y} &= \frac{\sqrt{p}}{T}\left[\frac{\partial}{\partial \eta} + \epsilon\, x_{\eta}^{(1)}\left(J\,\frac{\partial}{\partial \eta} - \frac{\partial}{\partial \xi}\right) + \dots\right] \end{aligned}\right\} \quad (3.5)$$

where $J$ is defined by $(1/T^{(0)}) \int_0^{\eta} T_{\xi}^{(0)} dz$. Eqs. (3.2) and (3.5), although not strictly expansions in powers of $\epsilon$, are preferable because of the fact that the simplification brought by Howarth's transformation will be preserved. After the transformation is completed, the expansion can then be carried out. If $\Psi$, $p$, and $T$ are now substituted from Eqs. (3.1) in the transformed equations, the zero-order equations resulting from the vanishing of the coefficient of $\epsilon^0$ of both equations lead to the conclusions that $\psi^{(0)}$ has the same form as the famous Blasius solution for the case of incompressible fluid and that $p^{(1)}$ can be a function of $\xi$ alone. Furthermore, the vanishing of the coefficient of $\epsilon$ of the first equation and that of $\epsilon^2$ of the second equation yields the system:

$$\begin{aligned} &L(\psi_{\eta}^{(1)}) = \psi_{\eta\eta\eta}^{(0)} x_{\xi}^{(1)} + [L(\psi_{\xi}^{(0)}) - 2\psi_{\xi\eta\eta}^{(0)} + \\ &J\psi_{\eta\eta\eta}^{(0)} - J_{\xi}\,\psi_{\eta}^{(0)2} + J_{\eta}(\psi_{\xi}^{(0)}\psi_{\eta}^{(0)} + 3\psi_{\eta\eta}^{(0)}) + \\ &J_{\eta\eta}\psi_{\eta}^{(0)}]\, x_{\eta}^{(1)} + (\psi_{\xi}^{(0)} - J\psi_{\eta}^{(0)})\psi_{\eta}^{(0)} x_{\xi\eta}^{(1)} - \\ &[3\psi_{\xi\eta}^{(0)} + \psi_{\xi}^{(0)2} - 2J_{\eta}\,\psi_{\eta}^{(0)} - J(\psi_{\xi}^{(0)}\psi_{\eta}^{(0)} + \\ &3\psi_{\eta\eta}^{(0)})]x_{\eta\eta}^{(1)} - (\psi_{\xi}^{(0)} - J\psi_{\eta}^{(0)})\, x_{\eta\eta\eta}^{(1)} + \\ &\frac{1}{2}p_{\xi}^{(1)}\left[\psi^{(0)}\psi_{\eta\eta}^{(0)} - \frac{\gamma - 1}{\gamma}(1 - \psi_{\eta}^{(0)2}) - \frac{2}{\gamma M^2}\right] \end{aligned} \quad (3.6)$$

$$\begin{aligned} &-\frac{1}{\gamma M^2}\,(p_{\eta}^{(2)} - x_{\eta}^{(1)}\, p_{\xi}^{(1)}) = -T^{(0)}L(\psi_{\xi}^{(0)}) - T_{\xi}^{(0)} \times \\ &\left(2\psi_{\xi}^{(0)}\psi_{\eta}^{(0)} + \frac{10}{3}\,\psi_{\eta\eta}^{(0)}\right) + T_{\eta}^{(0)}\left(\psi_{\xi}^{(0)2} + \frac{10}{3}\,\psi_{\xi\eta}^{(0)}\right) + \\ &\frac{4}{3}\,(T_{\eta\eta}^{(0)}\,\psi_{\xi}^{(0)} - T_{\xi\eta}^{(0)}\,\psi_{\eta}^{(0)}) + \psi_{\eta}^{(0)2} Y_{\xi\xi}^{(0)} \end{aligned} \quad (3.7)$$

where $L(\psi_{\eta}^{(1)})$ and $L(\psi_{\xi}^{(0)})$ are defined by

$$\left.\begin{aligned} L(x_{\eta}^{(1)}) &\equiv \psi_{\eta}^{(0)}\psi_{\xi\eta}^{(1)} + \psi_{\xi\eta}^{(0)}\psi_{\eta}^{(1)} - \\ &\qquad \psi_{\xi}^{(0)}\psi_{\eta\eta}^{(1)} - \psi_{\eta\eta}^{(0)}\psi_{\xi}^{(1)} - \psi_{\eta\eta\eta}^{(1)} \\ L(\psi_{\xi}^{(0)}) &\equiv \psi_{\eta}^{(0)}\psi_{\xi\xi}^{(0)} - \psi_{\xi}^{(0)}\psi_{\xi\eta}^{(0)} - \psi_{\eta\eta\xi}^{(0)} \end{aligned}\right\} \quad (3.8)$$

As concluded above, $\psi^{(0)} = \sqrt{\xi}\, f_0(\zeta)$ and $\zeta = \eta/\sqrt{\xi}$ according to Blasius. The properties of the function $f_0(\zeta)$ which satisfies a total differential equation are well known. With $\psi^{(0)}$ so chosen, the velocities, to the first approximation, can be calculated by the rules of transformation (3.5); and from $u^{(0)}$, $T^{(0)}$ is known by Eq. (2.5). It can be verified that the velocities $u^{(0)}$ and $\epsilon v^{(1)}$ vanish on the wall and approach, respectively, the asymptotic values 1 and $v_2$ in Eq. (3.3) when $\zeta$ becomes infinite. Because of this asymptotic value of $v_2$, there induces in the external field a pressure $p^{(1)}$ equal to $\gamma M^2 v_0/\beta\sqrt{\xi}$, $\beta$ being $\sqrt{M^2 - 1}$, as will be shown in Section (II). Consequently, in Eqs. (3.6) and (3.7) there are left three functions $\psi^{(1)}$, $x^{(1)}$, and $p^{(2)}$ to be determined.

## (4) Coordinate Distortion in the Viscous Field

The forms of $\psi^{(0)}$ and $p^{(1)}$ together with the differential equation [Eq. (3.6)] demands that

$$\psi^{(1)} = (v_0/\beta) f_1(\zeta), \quad x^{(1)} = (v_0/\beta)\sqrt{\xi}\, g_1(\zeta) \tag{4.1}$$

From Eqs. (2.4), (2.5), and (3.5) it follows that the velocities and temperature in the boundary layer are, respectively,

$$u = f_0' + \frac{v_0\epsilon}{\beta\sqrt{\xi}}\left(f_1' + \frac{v_1}{T^{(0)}}\, g_1'\right) + \ldots \tag{4.2}$$

$$v = \frac{\epsilon v_1}{\sqrt{\xi}} + \frac{v_0\epsilon^2}{2\beta\xi}\left\{\left(f_1' + \frac{v_1}{T^{(0)}}\, g_1'\right) \times \left[(\gamma - 1)M^2 f_0 f_0' + \int_0^\zeta T^{(0)} d\zeta\right] + \frac{\gamma M^2}{2}\,(2f_0 T^{(0)} - v_1 g_1)\right\} + \ldots \tag{4.3}$$

$$T = T^{(0)} - \frac{(\gamma - 1)M^2 v_0\epsilon}{\beta\sqrt{\xi}}\, f_0'\left(f_1' + \frac{v_1}{T^{(0)}}\, g_1'\right) + \ldots \tag{4.4}$$

where the prime denotes total differentiation with respect to $\zeta$ and $v_1$ and $T^{(0)}$ are defined by

$$\left.\begin{aligned} v_1 &= \frac{1}{2}\,(\zeta f_0' - f_0)T^{(0)} - \frac{1}{2} f_0' \int_0^\zeta \zeta \frac{dT^{(0)}}{d\zeta}\, d\zeta \\ T^{(0)} &= 1 + [(\gamma - 1)/2]M^2(1 - f_0'^2) \end{aligned}\right\} \tag{4.5}$$

It will be shown in Section (II) that with the first-order $v$ and $p$ in the external field defined above there will associate a first-order $u$ equal to $-v_0/\beta\sqrt{\xi}$. In order that the velocity joins smoothly at the edge of the boundary layer, the following condition must be satisfied

$$f_1' + (v_1/T^{(0)})g_1' = -1, \quad \zeta = \infty \tag{4.6}$$

Moreover, the condition of no-slip together with the fact that $\Psi = 0$ on the wall lead to

$$f_1 = f_1' + (v_1/T^{(0)})g_1' = 0, \quad \zeta = 0 \tag{4.7}$$

By substituting $\psi^{(1)}$ and $x^{(1)}$ from Eqs. (4.1) in Eq. (3.6) and eliminating simultaneously $\psi^{(0)}$ and $p^{(1)}$, there results a total differential equation of the third order for $f_1$ and $g_1$. This equation can be twice integrated, and by using the second of the conditions (4.7), the result can be written as

$$f_1' + \frac{v_1}{T^{(0)}}\, g_1' = -\frac{1}{2}\,\zeta f_0'' g_1 + \frac{f_0''}{2}\int_0^\zeta \frac{g_1'}{T^{(0)}} \times \left(\int_0^\zeta \zeta \frac{dT^{(0)}}{d\zeta}\, d\zeta\right) d\zeta - \frac{\gamma M^2}{2}\left(\zeta f_0'' - \frac{\gamma - 1}{\gamma} f_0' + \frac{T_w}{\gamma M^2} f_0'' \int_0^\zeta \frac{\zeta d\zeta}{f_0''}\right) + C_1 f_0'' \int_0^\zeta \frac{d\zeta}{f_0''} \tag{4.8}$$

where $C_1$ is a constant of integration. From the properties of $f_0$, it can be shown that the product $f_0'' \int_0^\zeta d\zeta/f_0''$ tends to zero when $\zeta$ is infinite. It appears that $C_1$ might be indeterminate. It is noted, however, that for large $\zeta$ this product is of the order $(1/\zeta)$. This would make the solution [Eq. (4.8)] approach the boundary value [Eq. (4.6)] very much slower than does $f_0'$, which is contrary to the character of the boundary-layer solutions. In order that both $f_1''$ and $g_1''$ tend to zero exponentially at infinity, it is necessary to cancel the slowly varying terms by choosing $C_1$:

$$C_1 = 0.860\, T_w \tag{4.9}$$

Now, since $f_0'' \int_0^\zeta (\zeta - 1.720)d\zeta/f_0''$ approaches the asymptotic value 2 at infinity, the condition (4.6) is, as a consequence, fulfilled.

The solution [Eq. (4.8)] now contains two functions, $f_1$ and $g_1$. In an attempt to eliminate this indeterminacy, the asymptotic behavior of the second-order velocity $v^{(2)}$ and pressure $p^{(2)}$ are examined. In Eq. (3.7) if $\psi^{(0)}$, $x^{(1)}$, $p^{(1)}$ are substituted by their similarity solutions and if $p^{(2)}$ is replaced by

$$p^{(2)} = [(\gamma M^2 v_0^2)/(\beta^2\xi)]p_2(\zeta) \tag{4.10}$$

the resulting total differential equation can again be integrated to give the solution:

$$g_1 + 2p_2 = \frac{\beta^2}{v_0^2}\left\{\frac{f_0}{2}\,(\zeta f_0' - f_0) + \zeta f_0'' + \frac{\gamma - 1}{4}\, M^2 \times \left[f_0(\zeta f_0' - f_0) + 0.664(f_0 f_0' + 2f_0'') + 2\zeta f_0'' - 4f_0'^2 + \frac{4}{3} f_0 f_0' f_0''\right]\right\} + C_2 \tag{4.11}$$

where $C_2$ is an integration constant. At the edge of the boundary layer $\zeta \to \infty$, the asymptotic properties of $f_0$ lead to the result

$$g_1 + 2p_2 \sim [(\beta^2/v_0)\zeta] + \text{constant} + 0(e^{-\zeta^2}) \tag{4.12}$$

Eq. (4.12) shows that if the coordinate-distortion function $g_1$ were absent, then the second-order pressure would be infinite at infinity. It might be argued that at the physical edge of the boundary layer $\zeta$ is

really not infinite. Nevertheless, if $\zeta$ were eliminated in terms of $x$ and $y$ according to Eqs. (2.1) and (3.2), $\epsilon^2 p^{(2)}$ would give a first-order term $\gamma M^2 v_0 \epsilon y / 2x^{3/2}$ which would make the overlap of pressure fields for arbitrarily large $y$ impossible. A more reasonable solution would be to require the second-order pressure to remain finite across the boundary layer. Then at the edge of the boundary layer, $\zeta \to \infty$

$$g_1 \sim [(\beta^2/v_0)\zeta] + \text{constant} + 0(e^{-\zeta^2}) \quad (4.13)$$

Thus, by causing the second-order pressure $p^{(2)}$ to behave satisfactorily at the edge of the boundary layer, the coordinate-distortion function is fixed in that region.

With the asymptotic form of $g_1$ specified by (4.13), the second-order velocity $v^{(2)}$ as calculated from Eq. (4.3) is finite for $\zeta \to \infty$. This very satisfactory result is radically different from the previous classical perturbation analysis without coordinate distortion carried out by Maslen.[7] Maslen's $v^{(2)}$ is infinite for infinite $\zeta$. Although Maslen did not compute $p^{(2)}$, it is certain that had he computed it, $p^{(2)}$ would also be found infinite as $\zeta \to \infty$. Such anomalies of the classical perturbation calculation are objectionable not only from the point of view of physical reality but also on the ground of leading to divergent successive iterations. By introducing the coordinate-distortion function $g_1$ as specified by (4.13), these difficulties are resolved and the boundary-layer solution is rendered uniformly valid for all $\zeta$. However, as yet $g_1$ is not determined for the complete range of from $\zeta = 0$ to infinity. To do this, the question of joining the solutions with those of the inviscid field has to be considered.

## (II) Inviscid Field

### (5) Differential Equations of Steady Isoenergetic Flow

Outside the boundary-layer region where the viscous shear stresses become unimportant, the motion is governed by the system:

$$\left.\begin{aligned} \rho u u_x + \rho v u_y &= -[1/(\gamma M^2)]p_x \\ \rho u v_x + \rho v v_y &= -[1/(\gamma M^2)]p_y \\ (\rho u)_x + (\rho v)_y &= 0 \end{aligned}\right\} \quad (5.1)$$

and for perfect gas

$$p = \rho T$$

By virtue of the conservation of energy, the temperature can be expressed in terms of velocity:

$$T = 1 + [(\gamma - 1)/2]M^2(1 - u^2 - v^2) \quad (5.2)$$

Since the flow in the external field is produced mainly by the viscous deflection of the streamlines, the velocity component $v$ at large $\zeta$ as given by Eq. (3.3) can be considered as the boundary value of the inviscid field. In view of the fact that the Reynolds Number is large, $v$ will stay small even though the Mach Number may be in the hypersonic range. For this reason, a fact that is not enjoyed by the flow around a solid body with a nonzero thickness, the present problem can be linearized by expanding:

$$\left.\begin{aligned} u &= 1 + \epsilon u^{(1)} + \epsilon^2 u^{(2)} + \dots \\ v &= \epsilon v^{(1)} + \epsilon^2 v^{(2)} + \dots \\ p &= 1 + \epsilon p^{(1)} + \epsilon^2 p^{(2)} + \dots \\ \rho &= 1 + \epsilon \rho^{(1)} + \epsilon^2 \rho^{(2)} + \dots \\ T &= 1 + \epsilon T^{(1)} + \epsilon^2 T^{(2)} + \dots \end{aligned}\right\} \quad (5.3)$$

provided $u^{(n)}$, $v^{(n)}$, $M^{-2}p^{(n)}$, $M^{-2}\rho^{(n)}$ are not large where $\epsilon$ is the same parameter as defined by Eq. (3.4). Because of the boundary value of $v^{(1)}$ as described by Eq. (3.3), the first-order quantities must vanish at infinity. Consequently, the zero-order shock must be a Mach wave.

It must be recalled, however, that as $v^{(1)}$ satisfies a boundary value [Eq. (3.3)] which is singular at the leading edge, in a supersonic field this singularity must be propagated along the whole Mach line through the leading edge. As a result, all first-order quantities are singular there. Moreover, if the perturbation is pushed to high orders, the singularity of all high-order solutions will progressively become stronger, and the approximation, consequently, is poor as the leading edge is approached. In order to prevent the unnecessarily high-order singularity of the second- or higher-order quantities from appearing, the coordinate $x$ will be expanded once again:

$$\left.\begin{aligned} x &= \xi + \epsilon x^{(1)}(\xi, \eta) + \dots \\ y &= \eta \end{aligned}\right\} \quad (5.4)$$

Taking into account the transformation (5.4), the substitution of $u$, $v$, $p$, $\rho$, $T$, from Eqs. (5.4) in Eqs. (5.1) yields, for order $\epsilon$, the system:

$$\left.\begin{aligned} u_\xi^{(1)} &= -[1/(\gamma M^2)]p_\xi^{(1)} \\ v_\xi^{(1)} &= -1/\gamma M^2\, p_\eta^{(1)} \\ (u^{(1)} + \rho^{(1)})_\xi + v_\eta^{(1)} &= 0 \\ p^{(1)} &= \rho^{(1)} - (\gamma - 1)M^2 u^{(1)} \end{aligned}\right\} \quad (5.5)$$

and, by making use of Eq. (5.2),

$$T^{(1)} = -(\gamma - 1)M^2 u^{(1)} \quad (5.6)$$

For order $\epsilon^2$, one has

$$\left.\begin{aligned} u_\xi^{(2)} + [1/(\gamma M^2)]p_\xi^{(2)} &= \\ &\quad -(u^{(1)} + \rho^{(1)})u_\xi^{(1)} - v^{(1)}u_\eta^{(1)} \\ v_\xi^{(2)} + [1/(\gamma M^2)]p_\eta^{(2)} &= -(u^{(1)} + \rho^{(1)})v_\xi^{(1)} - \\ &\quad v^{(1)}v_\eta^{(1)} + v_\xi^{(1)}x_\xi^{(1)} + [1/(\gamma M^2)]p_\xi^{(1)}x_\eta^{(1)} \\ (u^{(2)} + \rho^{(2)})_\xi + v_\eta^{(2)} &= -(\rho^{(1)}u^{(1)})_\xi - \\ &\quad (\rho^{(1)}v^{(1)})_\eta + (u^{(1)} + \rho^{(1)})_\xi x_\xi^{(1)} + v_\xi^{(1)}x_\eta^{(1)} \\ p^{(2)} &= \rho^{(2)} - (\gamma - 1)M^2 u^{(2)} - \\ &\quad (\gamma - 1)M^2[\rho^{(1)}u^{(1)} + (1/2)(u^{(1)^2} + v^{(1)^2})] \end{aligned}\right\} \quad (5.7)$$

and from the energy equation

$$T^{(2)} = -(\gamma - 1)M^2[u^{(2)} + (1/2)\,(u^{(1)^2} + v^{(1)^2})] \quad (5.8)$$

### (6) First-Order Solution

The elimination of $\zeta^{(1)}$ between the last two of Eqs. (5.5) gives a relation connecting the derivatives of $u^{(1)}$, $p^{(1)}$, and $v^{(1)}$ which, on combining with the first of Eqs. (5.5), can express $v_\eta^{(1)}$ in terms of $p_\xi^{(1)}$. Thus, for the first-order problem the fundamental system can be expressed as:

$$\left.\begin{aligned} v_\xi^{(1)} &= -[1/(\gamma M^2)]p_\eta^{(1)} \\ v_\eta^{(1)} &= -[\beta^2/(\gamma M^2)]p_\xi^{(1)} \end{aligned}\right\} \quad (6.1)$$

The advantage of this system is that even if the flow is rotational the potential character of the mathematical problem is preserved.

For a given problem, after $v^{(1)}$ and $p^{(1)}$ are determined by solving Eqs. (6.1) subject to a prescribed boundary condition, such as being described by Eq. (3.3) for $\eta = 0$, $u^{(1)}$ can be obtained by partial integration of the first of Eqs. (5.5). If the flow is rotational, the arbitrary function of $\eta$ will serve to determine the vorticity from the shock conditions. In case the leading-edge shock, to the zero order, is a Mach wave $\xi - \beta\eta = 0$, the vorticity will be of high order and, consequently, the reflected waves are absent. If $F(\xi - \beta\eta)$ represents a simple wave, the complete solutions of the first-order problem are given below:

$$\left.\begin{aligned} &v^{(1)} = F(\xi - \beta\eta), \quad u^{(1)} = -(1/\beta)F(\xi - \beta\eta) \\ &p^{(1)} = \\ &(\gamma M^2/\beta)F(\xi - \beta\eta), \quad \rho^{(1)} = (M^2/\beta)F(\xi - \beta\eta) \end{aligned}\right\} \quad (6.2)$$

which are the well-known Ackeret's formulas.

This shows that for a given problem if any one quantity such as $v^{(1)}$ is described, the rest are all defined. For instance, if $v^{(1)}$ takes on the value given by Eq. (3.3) on $\eta = 0$, it follows immediately from Eqs. (6.2) that

$$F = v_0/\sqrt{\xi - \beta\eta} \quad (6.3)$$

The singularity of the first-order solution at the leading-edge Mach line is, consequently, $(\xi - \beta\eta)^{-1/2}$. This implies that there must be a rapid change of flow properties in the neighborhood of this limiting Mach line, and the order of magnitude as defined by Eqs. (5.3) may very likely alter. This problem will be investigated in detail in Section (III).

### (7) Determination of the Coordinate Distortion Function

After the elimination of $u^{(2)}$ from the first of Eqs. (5.7), the fundamental system of the second-order problem will read:

$$\left.\begin{aligned} v_\xi^{(2)} + [1/(\gamma M^2)]p_\eta^{(2)} &= q_1 \\ v_\eta^{(2)} + [\beta^2/(\gamma M^2)]p_\xi^{(2)} &= q_2 \end{aligned}\right\} \quad (7.1)$$

where $q_1$ and $q_2$ are known functions of the first-order quantities such as $u^{(1)}$, $v^{(1)}$, $x^{(1)}$, . . . , etc. If the first-order solutions are simple waves as given by Eqs. (6.2), $q_1$ and $q_2$ are simplified to

$$\left.\begin{aligned} q_1 &= (\beta^{-1}x_\eta^{(1)} + x_\xi^{(1)})F' \\ q_2 &= (\gamma + 1)\,(M^4/\beta^2)FF' + (\beta x_\xi^{(1)} + x_\eta^{(1)})F' \end{aligned}\right\} \quad (7.2)$$

If the integration of the system [Eqs. (7.1)] were carried out, because of its inhomogeneity, the second-order solution would contain a singular term such as $(\xi + \beta\eta)\,(\xi - \beta\eta)^{-2}$. It is clear that due to this strong singularity, the second-order solution would not give better accuracy than the first-order solution, particularly in the neighborhood of $\xi - \beta\eta = 0$. The process of perturbation then actually diverges. This singular term disappears only if $x^{(1)}$ satisfies

$$F'(\beta^2 x_{\xi\xi}^{(1)} - x_{\eta\eta}^{(1)}) + 2\beta F''(\beta x_\xi^{(1)} + x_\eta^{(1)}) + (\gamma + 1)\,(M^4/\beta)\,(F'^2 + FF'') = 0 \quad (7.3)$$

whereupon $v^{(2)}$ will satisfy a homogeneous equation

$$\beta^2 v_{\xi\xi}^{(2)} - v_{\eta\eta}^{(2)} = 0 \quad (7.4)$$

For a given problem, if $v^{(2)}$ is obtained by solving Eq. (7.4) satisfying prescribed conditions, then the integration of Eqs. (7.1) leads to

$$p^{(2)} = \frac{\gamma M^2}{\beta}\left(v^{(2)} + \frac{\gamma + 1}{4}\,\frac{M^4}{\beta^3}\,\frac{v_0^2}{\xi - \beta\eta}\right) \quad (7.5)$$

Let the characteristic parameters be introduced:

$$s = \xi - \beta\eta, \quad t = \xi + \beta\eta$$

Eq. (7.3) can then be integrated with the result:

$$x^{(1)} = -\frac{(\gamma + 1)}{4}\,\frac{M^4}{\beta^3}\,\frac{v_0 t}{\sqrt{s}} + A(s) + s^{3/2}B(t) \quad (7.6)$$

where $A$ and $B$ are, respectively, functions of $s$ and $t$. $x^{(1)}$, in this general form, ensures only the analytic behavior of the solutions near the leading-edge shock. The determination of $A$ and $B$ again cannot be done until the mutual relationship between the two fields of flow is considered.

## (III) Interaction Between Viscous and Inviscid Fields

### (8) Determination of the Transformation

As shown in Section (4), the choice of $g_1$ [Eq. (4.13)] at large $\zeta$ guarantees the rapid approach to constant values of second-order normal velocity $v^{(2)}$ and pressure $p^{(2)}$ at the edge of boundary layer. These constant values of velocity and pressure are otherwise unspecified. A moment's reflection on the method of solution adopted here shows that the iteration procedure starts with $v^{(1)}$. From $v^{(1)}$, $p^{(1)}$ is determined. From $p^{(1)}$, $v^{(2)}$ is computed. Then $p^{(2)}$ is computed. This process can be carried on and on; with each additional step there is an improvement of the accuracy. However, with emphasis on the pressure along the plate, it is important to have an exact expression for this quantity even if other quantities have to be computed by iteration. This can be accomplished by choosing the

coordinate such that $p^{(2)} \equiv 0$ throughout the field. Then the pressure is *exactly* $1 + \epsilon p^{(1)}$. Now within the boundary layer, since $p^{(1)}$ is only a function of $\xi$, the exact pressure is also a function of $\xi$ only. This then gives a physical meaning to the independent variable $\xi$: Lines of constant $\xi$ are lines of constant pressure within the boundary layer. The meaning of the independent variable $\eta$ is obtained through $\zeta = \eta/\sqrt{\xi}$: $\zeta$ is the similarity parameter of the solution.

The fact that the pressure is constant for constant values of $\xi$ does not imply that pressure is constant for constant $x$. Actually, along constant $x$ in the boundary layer, the pressure changes are of the $0(\epsilon^2)$. This is the correct order of magnitude.

With $p^{(2)} \equiv 0$, Eq. (4.11) gives the coordinate distortion function $g_1$ in the boundary layer,

$$g_1 = \frac{\beta^2}{v_0^2}\left\{\frac{1}{2} f_0(\zeta f_0' - f_0) + \zeta f_0'' + \frac{\gamma - 1}{4} M^2\left[f_0(\zeta f_0' - f_0) + 0.664\,(f_0 f_0' + 2f_0'') + 2\zeta f_0''' - 4f_0''^2 + \frac{4}{3} f_0 f_0' f_0''\right]\right\} + C_2 \quad (8.1)$$

With $g_1$ fixed, $f_1$ can be determined by using Eqs. (4.8) and (4.9).

In the inviscid field, the vanishing of $p^{(2)}$ leads to $u^{(2)} = 0$ and determines $v^{(2)}$ according to Eq. (7.5). Thus

$$v^{(2)} = -[(\gamma + 1)/4]\,(M^4/\beta^3)\,(v_0^2/s) \quad (8.2)$$

This form of second-order normal velocity in the inviscid region must now join smoothly to the asymptotic value of $v^{(2)}$ in Eq. (4.3) at the edge of the boundary layer. At the edge of the boundary layer, $s \simeq \xi$. Then the continuity of $v^{(2)}$ at $\zeta \to \infty$ determines the constant

$$C_2 = [(\gamma + 1)/2]\,(M^4/\beta^2) - 2 \quad (8.3)$$

The solution within the boundary layer is now completely determined. It is interesting to note that the second-order normal velocity $v^{(2)}$ at the edge of the boundary layer is negative. This actually is accompanied by a decrease of temperature and density.

It remains to determine the functions $A(s)$ and $B(t)$ in the coordinate-distortion function [Eq. (7.6)] of the inviscid field. To do this, consider again the junction of functions at the edge of the boundary layer. From Eqs. (2.1) and (3.2), together with Eqs. (4.5) and (4.8), $y$ in the boundary layer can be calculated as a function of $\xi$ and $\zeta$. Thus

$$y = \epsilon\sqrt{\frac{\xi}{p}}\int_0^\zeta T d\zeta = \epsilon\sqrt{\frac{\xi}{p}}\left[y_1(\zeta) + \frac{\epsilon}{\sqrt{\xi}}\, y_2(\zeta) + \ldots\right] \quad (8.5)$$

where

$$y_1 = T_w\zeta - [(\gamma - 1)/2]M^2(f_0 f_0' + 2f_0'' - 0.664)$$
$$y_2 = \{[(\gamma - 1)M^2 v_0]/\beta\}\,[\zeta + I(\zeta)] \quad (8.6)$$

The function $I(\zeta)$ has the properties that $I = 0(\zeta)$ if $\zeta$ is small and tends asymptotically to a constant at infinity. Thus, when $\zeta$ is large, $y$ as a function of $\xi$ and $\zeta$ reduces to

$$y = \epsilon\sqrt{\frac{\xi}{p}}\left[1 + \frac{(\gamma - 1)M^2 v_0 \epsilon}{\beta\sqrt{\xi}}\right]\zeta + 1.19(\gamma - 1)M^2\,\epsilon\sqrt{\frac{\xi}{p}} + 0(\epsilon^2) \quad (8.7)$$

On the other hand, the coordinate $x$, according to Eqs. (3.1), and (8.1), for large $\zeta$ is

$$x = \xi + \frac{v_0\epsilon}{\beta}\left(\frac{\beta^2}{v_0}\,\zeta + C_2 - 1.72\,\frac{\beta^2}{v_0}\right)\sqrt{\xi} + \ldots \quad (8.8)$$

The elimination of $\zeta\sqrt{\xi}$ between Eqs. (8.7) and (8.8) leads to a relation expressing $\xi$ as a function of $x$ and $y$—viz.,

$$\xi^{3/2} + \frac{v_0\epsilon}{\beta} M^2\left(\frac{\gamma + 1}{2}\frac{M^2}{\beta^2} - 2\right)\xi - (x - \beta y)\xi^{1/2} + \frac{(2 - \gamma)M^2 v_0 \epsilon\, y}{2} = 0 \quad (8.9)$$

It is interesting to note that $\xi$, and so the velocity at large $\zeta$, is constant on straight lines in $x$, $y$-plane. It will be shown later that these straight lines are the outgoing Mach waves. This point will be further amplified below.

By comparing Eq. (8.9) with Eqs. (5.4) and (7.6), the arbitrary function $B(t)$ must be zero, and $A(s)$ is equal to $v_0 c_2\sqrt{s}/\beta$. The transformation equation for the inviscid field can then be written as

$$s^{3/2} + \frac{v_0\epsilon}{\beta}\left(c_3 - \frac{\gamma + 1}{4}\frac{M^4}{\beta^2}\right)s - (x - \beta y)s^{1/2} - \frac{(\gamma + 1)M^4 v_0 \epsilon y}{2\beta^2} = 0 \quad (8.10)$$

As the velocities in the viscous field at $\zeta \to \infty$ are functions of $\xi$ and those of the inviscid field are functions of $s$ by Eqs. (4.6) and (6.2), the velocity field will agree at a point $(x, y)$ only when their arguments agree. To the first approximation, this condition is fulfilled if

$$c_3 = -[(5 - 3\gamma)M^2 - 8]M^2/4\beta^2$$

as in the region of overlapping $y$ is of the order $\epsilon$. In order to make the joining accurate to $0(\epsilon^2)$, the second-order term $\epsilon^2\psi^{(2)}$ in Eq. (3.1) will have to be considered.

This completes the problem of continuation of the viscous solution into the external inviscid field. What has been done here is essentially the restoration of the correct analytic behavior at the edge of the boundary layer to the first-order velocities and the suppression of the second-order pressure in the whole field. Moreover, by means of coordinate distortion the viscous and inviscid solutions are made to overlap in a region rather than along a line, and consequently a smooth transition from viscous to inviscid field has been achieved.

### (9) Properties of the Transformation

The analytic behavior of the transformation determined in the preceding section can now be investigated. From Eq. (8.10) it is clear that the inverse transformation of Eq. (5.4) will be three-sheeted. The branch-point is given by

$$x_s = 0$$

which corresponds also to the vanishing of the Jacobian of the transformation. As the flow behind the shock is regular, the Jacobian is expected to be finite and non-vanishing.

It can be proved very simply from Eq. (8.10) that the branch $\sqrt{s} > 0$ covers the whole right half $(x, y)$ plane singly but folds three times in the left half plane. The envelope begins to form at negative infinity ($\sqrt{s} = \infty$, $x = y = -\infty$) and moves forward to a point $x = -0(\epsilon^2)$, $y = 0(\epsilon^2)$, $[\sqrt{s} = 0(\epsilon)]$ where it has cusp and turns abruptly toward the origin ($\sqrt{s} = 0$) with a horizontal tangent. Therefore, in the physical domain $x \geq 0$ and $y \geq 0$ and $0\ (\epsilon) < \sqrt{s}$, the transformation is regular.

The relationship between the parameter $s$ and $(x, y)$ as expressed by Eq. (8.10) has a very simple geometrical interpretation. $s$ = constant are parallel straight lines in the $\xi, \eta$-plane, which belong to the out-going family of Mach waves by the linearized theory. Now, if $s$ is held constant in Eq. (8.10), there results a linear relation between $x$ and $y$. The equation of this straight line can be written as

$$\left[1 - \frac{(\gamma + 1)}{2}\frac{M^4}{\beta^3}\theta(s)\right] y = \frac{x}{\beta} - \frac{s}{\beta}\left\{1 - \frac{[(3 - \gamma)M^2 - 4]M^2}{2\beta^3}\theta(s)\right\} \quad (9.1)$$

where $\theta(s) = \epsilon v_0/\sqrt{s}$. It can be readily verified that this equation, to the first order, represents just the out-going family of Mach waves in the $x, y$-plane if $\theta$ is interpreted as the local deflection of the flow. Thus, the original parallel straight Mach waves in the $\xi, \eta$-plane become a family of straight waves in the $x, y$-plane, whose slope increases toward the leading edge.

These conclusions, in part, cover also the transformations (3.1) and (3.2), for as $\zeta$ is large they tend to merge and, consequently, must share the same property. When $\zeta$ is not large, a separate study has to be made. The Jacobian of the transformations (3.1) and (3.2), to the first order, is proportional to

$$1 + [(\epsilon v_0)/(2\beta\sqrt{\xi})]\,[C_2 + 0(\zeta^3)] > 0$$

when $\zeta$ is small and $g_1 \simeq C_2 + 0(\zeta)$. Therefore, the transformations (3.1) and (3.2) can be singular only at the origin $\xi = 0$ for small $\zeta$. By increasing $\zeta$, the factor in the bracket will first change sign and then gradually tends to the asymptotic value of the inviscid case. Since both $g_1$ and $T^{(0)}$ are regular functions of $\zeta$, the above argument is sufficient to establish the regularity of the transformations (3.1) and (3.2).

The relationship between the pair of variables $(\xi, \eta)$ and $(x, y)$ can be ascertained by study, to the first order, of the equations:

$$\left.\begin{aligned} x &= \xi + [(v_0\epsilon)/\beta]\, g_1\sqrt{\xi} + 0(\epsilon^2) \\ y &= \epsilon\sqrt{\xi/p}\, y_1 + 0(\epsilon^2) \end{aligned}\right\} \quad (9.2)$$

where $g_1$ and $y_1$ are defined respectively in Eqs. (8.1) and (8.6). If this transformation is considered exact, it would follow that $\xi = 0$ is transformed to the origin of the $x, y$-plane. To any $\xi$ = const. $\neq 0$ there corresponds a curve that begins at the wall with a positive slope and approaches asymptotically a straight line at infinity. On the other hand, $\zeta$ = const. lines, which are parabolas with vertices at the origin, correspond to lines in the $x, y$-plane

$$y = \frac{\epsilon}{\sqrt{p}}\, y_1\left(-\frac{1}{2}\tilde{g} + \sqrt{x + \frac{1}{4}\tilde{g}^2}\right), \qquad \sqrt{\xi} > 0 \quad (9.3)$$

where $\tilde{g} = v_0\epsilon g_1/\beta$. Since $y_1 \geq 0$ for $\zeta \geq 0$, $y = 0$ when $x = 0$; and $y \equiv 0$ when $\zeta = 0$. It follows that all curves pass through the origin.

This shows that without considering high-order effects, the viscous region remains in the region $x \geq 0$ and $y \geq 0$, as in the Blasius problem. The boundary-layer thickness, however, grows as $x^{3/2}$ near the leading edge, instead of as $\sqrt{x}$, according to the Blasius solution. The constant of proportionality is approximately $1/(\epsilon v_0 M^2)$ at high Mach Number (a factor depending on $\gamma$ has been left out). When $x$ is large, according to Eq. (9.3), the boundary-layer thickness asymptotically tends to $\epsilon y_1[\sqrt{x} - (1/2)\tilde{g}]$.

It might be of interest to point out that previously Schaaf,[8] by a simple consideration that takes into account slip effect but neglects pressure, had reached the conclusion that the boundary layer initially grows linearly with $x$, which can also be deduced from Eq. (9.3) by putting $p = 1$. From this it follows also that the initial slope of the boundary-layer thickness is $2/(\gamma + 1)M$, being independent of Reynolds Number. The difference between these two results is large and should serve as a crucial test for the two different assumptions. The implications of the new result will be further discussed in connection with the shock pattern near the leading edge.

## (IV) Results and Conclusions

### (10) Pressure on the Plate

According to the method adopted in Sections (6) and (7), the induced pressure is determined, by the knowledge of the maximum viscous displacement of a streamline, in terms of a characteristic parameter—namely, the out-going Mach waves. By continuation of the velocity and pressure fields as established in Section (8), it is shown that the pressure in the boundary layer reads

$$p = 1 + [(\gamma M^2 v_0\epsilon)/(\beta\sqrt{\xi})] + 0(\epsilon^3) \quad (10.1)$$

As $\xi$ is a function of both $x$ and $y$, the pressure in the

boundary layer, consequently, varies in both directions $x$ and $y$.

On the plate where $y$ vanishes, $g_1$ reduces to $C_2$, and the equation governing $\xi$ and $x$ becomes

$$\xi + [(v_0 C_2 \epsilon)/\beta] \sqrt{\xi} - x = 0 \tag{10.2}$$

or

$$\sqrt{\xi} = -\frac{v_0\epsilon}{2\beta}\left(\frac{\gamma+1}{2}\frac{M^4}{\beta^2} - 2\right) + \sqrt{x + \frac{v_0^2\epsilon^2}{4\beta^2}\left(\frac{\gamma+1}{2}\frac{M^4}{\beta^2} - 2\right)^2}$$

The elimination of $\xi$ between Eqs. (10.2) and (10.1) leads to the expression:

$$p = 1 + \frac{\gamma M^2 v_0 \epsilon}{\beta\sqrt{x}}\left[\frac{v_0\epsilon}{2\beta\sqrt{x}}\left(\frac{\gamma+1}{2}\frac{M^4}{\beta^2} - 2\right) + \sqrt{1 + \frac{v_0^2\epsilon^2}{4\beta^2 x}\left(\frac{\gamma+1}{2}\frac{M^4}{\beta^2} - 2\right)^2}\right] \tag{10.3}$$

By defining two parameters $K$ and $\chi$:

$$K = \gamma M^2 \Big/ \left(\frac{\gamma+1}{2}\frac{M^4}{\beta^2} - 2\right), \qquad \chi = \frac{v_0\epsilon}{\beta\sqrt{x}}\left(\frac{\gamma+1}{2}\frac{M^4}{\beta^2} - 2\right) \tag{10.4}$$

the pressure given in Eq. (10.3) can be expressed as

$$\frac{p-1}{K} = \chi\left(\frac{1}{2}\chi + \sqrt{1 + \frac{1}{4}\chi^2}\right) \tag{10.5}$$

It is interesting to remark that as for large $x$, $v_0\epsilon/\sqrt{x}$ is approximately the deflection $\theta$ of the flow at the edge of the boundary layer, the parameter $\chi$ at hypersonic Mach Numbers reduces to $(\gamma+1)M\theta/2$ and the pressure given in Eq. (10.5) becomes identical to the pressure on a wedge airfoil, deduced first by Linnell.[9] In the present case, however, as the surface deflection is not uniform, it implies that Linnell's formula, although derived for the case of uniform flow, can be applied to calculate the pressure on a curved surface. This has been also independently verified by Probstein* at Princeton, and good agreement with the characteristics method has been obtained. It is also of interest to note that, using the shock-expansion theory Lighthill[10] has shown that for small $\theta$ the pressure given by Eq. (10.3) is accurate to $0(\theta^3)$.

The universal form for the pressure on the plate in Eq. (10.5) is plotted in Fig. 1. In view of the fact discussed above, the available experimental data† at different Reynolds and Mach Numbers and for different gases have been converted on the same graph by Eq. (10.5). As $\chi$ is directly proportional to $M^{2+\omega}$ and inversely to $\sqrt{Rex}$, the increase of $\chi$ may either mean

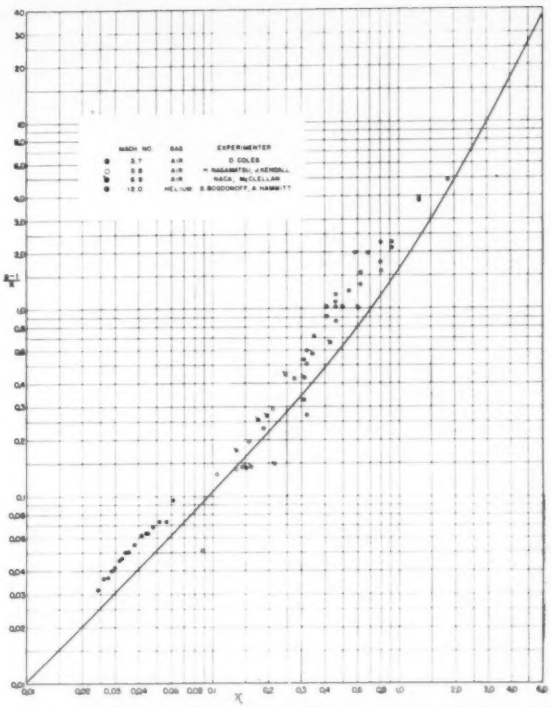


FIG. 1. Pressure distribution along the plate. The solid curve represents Eq. (10.5). Points denote experimental data by Coles,[13] Nagamatsu and Kendall,[14] Bertram,[15] and Bogdonoff and Hammitt.[16] *Correction:* "McClellan" appearing within the drawing should read "Bertram."

increase of Mach Number or decrease of $x$. Thus, in the weak interaction zone, the curve is nearly linear. It tends to be quadratic in the strong interaction zone. At present stage, the experimental accuracy is still difficult to assess, but within the range of experimental scattering the theoretical curve does seem to give a consistent correlation. In order to establish this formula firmly, more experimental data are, of course, urgently needed.

## (11) Velocity Field

The formulas for the velocities in the boundary layer are already given by Eqs. (4.2) and (4.3). These formulas together with the function $g_1$ in Eq. (8.1) describe the velocity distribution in the boundary layer. In this preliminary study, however, detailed numerical calculations will not be made. A simple qualitative discussion will be given below.

First, for small $\zeta$, the pair of transformation equations can be approximated by

$$\left.\begin{aligned} x &= \xi + \frac{v_0\epsilon}{\beta}\left(C_2 + \frac{0.32\beta^2 T_w}{v_0}\zeta\right)\sqrt{\xi} + 0(\zeta^3) \\ y &= (\epsilon T_w/\sqrt{\bar{p}})\zeta\sqrt{\xi} + 0(\zeta^2) \end{aligned}\right\} \tag{11.1}$$

where $\bar{p}$ is the pressure on the plate given by Eq. (10.3). To the same approximation, the velocities $u$ and $v$ are

$$\left.\begin{aligned} u &= 0.332\,\zeta + \ldots \\ v &= [(0.332\,T_w\epsilon)/(4\sqrt{\bar{p}})]\,(\zeta^2/\sqrt{\xi}) + \ldots \end{aligned}\right\} \tag{11.2}$$

* Unpublished.

† The author is indebted to Prof. Lester Lees of the California Institute of Technology for supplying him with the assembled experimental data.

Since $p$ is singular at the leading edge and by Eq. (10.3) $\sqrt{p} \sim v_0 M\epsilon/\sqrt{x}$ for $\sqrt{x} << \epsilon v_0 c_2/2\beta$, the transformation equations yield

$$\sqrt{\xi} \sim [\beta/(\epsilon v_0 c_2)]x[1 - \alpha M^2\epsilon(y/x^{3/2})]$$

where $\alpha = 0.332\sqrt{\gamma(\gamma + 1)/2}$. Within the boundary layer and for small $\zeta$, the quantity in the second set of brackets is never zero. Therefore, in a small neighborhood at the leading edge, $u = \tilde{u}(y/x^{3/2})$ and $v = x^{-1/2}\tilde{v}(y/x^{3/2})$. The existence of the parameter $y/x^{3/2}$ is in agreement with the behavior of the boundary-layer thickness near the leading edge. The fact that the velocity field exhibits such a singularity at $x = 0$ indicates that the solutions will not be valid for $x < 0(M^6\epsilon^2)$.

When $x = 0(M^6\epsilon^2)$ but $\chi < 1$, it follows that $p$ is proportional to $1/\sqrt{x}$, $u = \tilde{u}(y/x^{3/4})$, and $v = x^{-1/4}\tilde{v}(y/x^{3/4})$ approximately. These are essentially the forms deduced by the similarity hypothesis. In view of the fact that in this range of $x$ the parameter $\chi$ is almost unity, the approximation of the pressure Eq. (10.3) by the leading term $K\chi$, as in the case of the similarity solutions, is clearly difficult to justify. This might be the reason why the validity of the similarity solutions is restricted.

If $x$ is large, the effect of the coordinate distortion will be small. $x$ then will be approximately $\xi$, and $p$ is almost unity. In other words, in the weak interaction zone the flow in the boundary layer will have much the same characteristics as that under constant pressure.

On the other hand, for arbitrary $x$ as $\zeta$ is large, the velocities Eqs. (4.2) and (4.3) reduce to

$$\left.\begin{aligned} u &= 1 - [(\epsilon v_0)/(\beta\sqrt{\xi})] + 0(\epsilon^3) \\ v &= [(\epsilon v_0)/\sqrt{\xi}] - \{[\epsilon^2 v_0^2(\gamma + 1)M^4]/(4\beta^3\xi)\} + 0(\epsilon^3) \end{aligned}\right\} \quad (11.3)$$

From Eqs. (8.9) and (8.10) $\xi$ approaches asymptotically $s$ as $\zeta$ becomes infinite, $u$ and $v$ then merge smoothly with the external field described by Eqs. (5.3) and (6.2). As pointed out previously—$s$ = constant lines are out-going Mach lines in the $x$, $y$-plane—the velocity field in the boundary layer then approaches the values described by the simple wave theory.

## (12) Determination of Shock Strength

Let the shock curve be represented by $y_s = y_s(x)$. Then, the shock strength $p - 1$, according to the Rankine-Hugoniot relations, is given by

$$p - 1 = [(2\gamma)/(\gamma + 1)]\{[(M^2 y_s'^2)/(1 + y_s'^2)] - 1\} \quad (12.1)$$

where the prime denotes differentiation with respect to $x$. From Eqs. (5.3) and (6.2), $y_s'$ can be solved in terms of $\theta(s)$:

$$y_s'^2 = \frac{1}{\beta^2}\left\{\left[1 + \frac{\gamma + 1}{2}\frac{M^2}{\beta}\theta(s)\right] \div \left[1 - \frac{\gamma + 1}{2}\frac{M^2}{\beta^3}\theta(s)\right]\right\} \quad (12.2)$$

where $s$ as function of $x$ and $y$ is given by Eq. (8.10).

Since the deflection of the flow $\theta(s)$ increases with decreasing $s$, the denominator of Eq. (12.2) will diminish toward the leading edge. Accordingly, the slope of the shock curve will increase as one proceeds along the shock from infinity and becomes infinite when the denominator vanishes. This critical point at large Mach Number is found to be $\sqrt{s} = 0(M\epsilon)$. However, the smallest value that $\sqrt{s}$ is allowed to reach is, from Section (9), $0(M^3\epsilon)$, where the Mach line will be parallel to the $y$-axis. Therefore, infinite slope cannot occur in a physically realizable region, and, as a consequence, the shock can be assumed to begin at the leading edge where $\sqrt{s} = \sqrt{s_0} = [(\gamma + 1)/(2\beta^3)]M\epsilon v_0$ by Eq. (9.1).

Since the largest value of $(\gamma + 1)M^2\theta(s)/2\beta^3$ in the denominator of Eq. (12.2) is $0(1/M^2)$, Eq. (12.2) can be simplified by writing:

$$\dot{y}_s = (1/\beta)\{1 + [(\gamma + 1)/2](M^4/\beta^3)\theta(s)\}^{1/2}\dot{x} \quad (12.3)$$

where $(\dot{})$ denotes differentiation with respect to $s$. From Eq. (8.10), on the other hand, $y$ can be expressed in terms of both $x$ and $s$—namely,

$$\beta y_s = [1 - (2\epsilon\sigma/\sqrt{s})]^{-1}(x - s + 2\epsilon\sigma m\sqrt{s}) \quad (12.4)$$

where $\sigma = (\gamma + 1)M^4 v_0/4\beta^3$ and $m = [(3 - \gamma)M^2 - 4]/(\gamma + 1)M^2$. By differentiating Eq. (12.4) with respect to $s$ along the shock, there will result a new relationship between $\dot{x}$ and $\dot{y}_s$. This relation, together with Eq. (12.3), then yields

$$\dot{x} - P(s)x = Q(s) \quad (12.5)$$

where

$$P(s) = \epsilon\sigma s^{-3/2}\left(1 - \frac{2\epsilon\sigma}{\sqrt{s}}\right)^{-1} \times \left[1 - \left(1 - \frac{2\epsilon\sigma}{\sqrt{s}}\right)\left(1 + \frac{2\epsilon\sigma}{\sqrt{s}}\right)^{1/2}\right]^{-1}$$

$$Q(s) = \left[1 - \left(1 - \frac{2\epsilon\sigma}{\sqrt{s}}\right)\left(1 + \frac{2\epsilon\sigma}{\sqrt{s}}\right)^{1/2}\right]^{-1} \times \left(1 - \frac{\epsilon\sigma m}{\sqrt{s}} - \left\{\left[\epsilon\sigma\left(1 - \frac{2\epsilon\sigma m}{\sqrt{s}}\right)\right] \div \left[\sqrt{s}\left(1 - \frac{2\epsilon\sigma}{\sqrt{s}}\right)\right]\right\}\right)$$

From the initial condition that when $s = s_0$, $x(s_0) = 0$, there follows the solution:

$$x = e^{\int_{s_0}^{s} P\,ds}\int_{s_0}^{s} Q\, e^{-\int_{s_0}^{s} P\,ds}\, ds \quad (12.6)$$

which together with Eq. (12.4) gives a parametric representation of the shock curve.

When $s$ is large, $P \sim 1/s$ and $Q \sim \sqrt{s}/\epsilon\sigma$. Eq. (12.6) then gives

$$x \sim [2/(\epsilon\sigma)]s^{2/3} + 0(s)$$

From Eq. (12.4), the shock curve asymptotically tends to

$$\beta y_s \sim x + (3/2^{2/3})(\epsilon\sigma x)^{2/3}, x >> 1 \quad (12.7)$$

When $x$ is small, $s \sim s_0$. From Eqs. (11.9) and (12.3)

$$y_s \sim \sqrt{2}(x/M) \quad (12.8)$$

The shock curve according to Eqs. (12.7) and (12.8), together with the Mach waves Eq. (11.8), is illustrated in Fig. 2. It shows that the shock begins at the leading edge and increases linearly with $x$ with a slope twice as large as that of the boundary-layer thickness in that region. The fact that the character of the shock near the leading edge does not depend on the viscous effect may indicate either the breakdown of the no-slip hypothesis for $\sqrt{x} < \epsilon\sigma$ or that the flow near the leading edge is dominated mainly by compressibility effects. Neither case, however, supports the view that near the leading edge the shock and the boundary-layer thickness coincide.

With the asymptotic shock curve Eq. (12.7), it can be deduced that the shock strength decays asymptotically according to

$$p - 1 \sim [\gamma/(\gamma + 1)](\sqrt{2}\,\sigma\epsilon)^{2/3}x^{-1/3}, x \gg 1 \quad (12.9)$$

That is, the shock strength falls off with a rate much slower than the decay of pressure along the plate. This is consistent with the fact that for large $x$ the shock is nearly parallel to the Mach waves, along which the flow properties are constant.

## (13) Skin Friction

Following the definitions of Eqs. (2.1), (2.4), and (3.1), the shear stress on the wall can be calculated by

$$\bar{\mu}_w(\partial\bar{u}/\partial\bar{y})_w = (U\mu_\infty/L)C\epsilon^{-1}p^{1/2}(\psi_{YY})_w$$

where $p$ is the pressure given by Eq. (10.3). If the skin-friction coefficient $c_f$ is introduced, then

$$c_f = \bar{\mu}_w(\partial\bar{u}/\partial\bar{y})_w/(1/2)\rho_\infty U^2 = 2\epsilon p^{1/2}(\psi_{YY})_w \quad (13.1)$$

From the transformation (3.5)

$$(\psi_{YY})_w = (0.322/\sqrt{\xi}) - [(\epsilon v_0\alpha_1)/(\beta\xi)] + \ldots$$

The substitution in Eq. (13.1) gives

$$c_f = 2\epsilon p^{1/2}\{(0.332/\sqrt{\xi}) - [(\epsilon v_0\alpha_1)/(\beta\xi)] + \ldots\} \quad (13.2)$$

where $\alpha_1 = (0.332/2)(C_2 + M^2) - 0.860T_w$ and $\sqrt{\xi}$ is defined in Eq. (10.2).

Thus, the skin friction on the plate is determined by two opposing effects: the second term in the braces, which represents the contribution by the shock, tends to diminish the friction, while the induced pressure tends to increase it. Shock decreases the velocity outside of the boundary layer, and hence the slope of the velocity profile is reduced, resulting in smaller skin friction. Pressure increases the density of the fluid and contracts the boundary layer; it thus tends to increase the slope of the velocity profile and the skin friction. In the weak interaction zone, the effect of the coordinate contraction is strong, and the shear is in excess of the value deduced by the von Kármán and Tsien theory. In the strong interaction zone, however, the effect of the shock is dominant; the shear increases at a slower rate than according to the classical law and falls off after a maximum has been reached (Fig. 3). A simple calculation shows that the shear vanishes at $\sqrt{\xi} = \epsilon v_0\alpha_1/0.332\beta$. In the case of air at $M = 10$, $\epsilon = 10^{-3}$ this corresponds to $x$ approximately 0.01 cm.

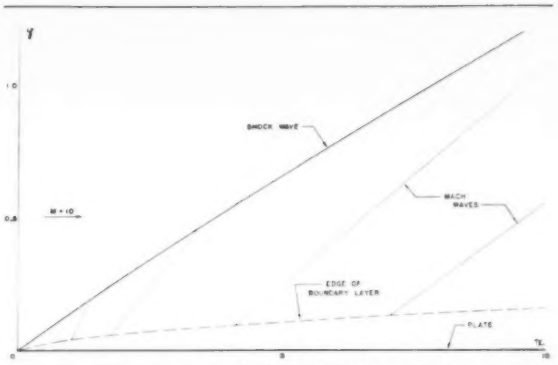


FIG. 2. Wave system in the inviscid field outside the boundary layer for $\gamma = 1.40$, $\epsilon = 10^{-3}$, and $M = 10$. In the figure the scale of the ordinate has been magnified by a factor of ten.

This shows that the combined effects of interaction produce near the leading edge a phenomenon that is similar to ordinary boundary-layer flow under favorable pressure gradient, for which the shear continually increases in the direction of the flow. In the case of high-speed flow, this has customarily been attributed to the slip effect, but this conjecture has not been borne out by the present investigation. It is believed that with proper accuracy the Navier-Stokes equations can still give a correct physical picture without the necessity of introducing new hypotheses.

## (14) Conclusions and Discussions

To summarize, it can be concluded that at high supersonic speeds, the flow past a flat plate can still be subdivided into viscous and nonviscous fields. In the outer, inviscid field, the flow is irrotational and can be described, to at least second order, by Friedrichs' simple waves,[11] which are shown by Lighthill[12] to be correct to this order. In the inner, viscous field, the flow is of the boundary-layer type, but the problem has to be dealt with by a combination of the boundary-layer theory and Lighthill's method of straining the coordinates. Concrete results concerning the flow are as follows:

(1) The leading-edge shock is attached, with an initial shock strength $2\gamma/(\gamma + 1)$ for $M \gg 1$ and an initial slope $\sqrt{2}/M$. Far away from the leading edge it approaches the Mach wave with a rate proportional to $(\epsilon\sigma)^{2/3}x^{-1/3}$, according to which its strength decays.

(2) The pressure along the plate can be expressed in a form in which the parameter can be interpreted as the

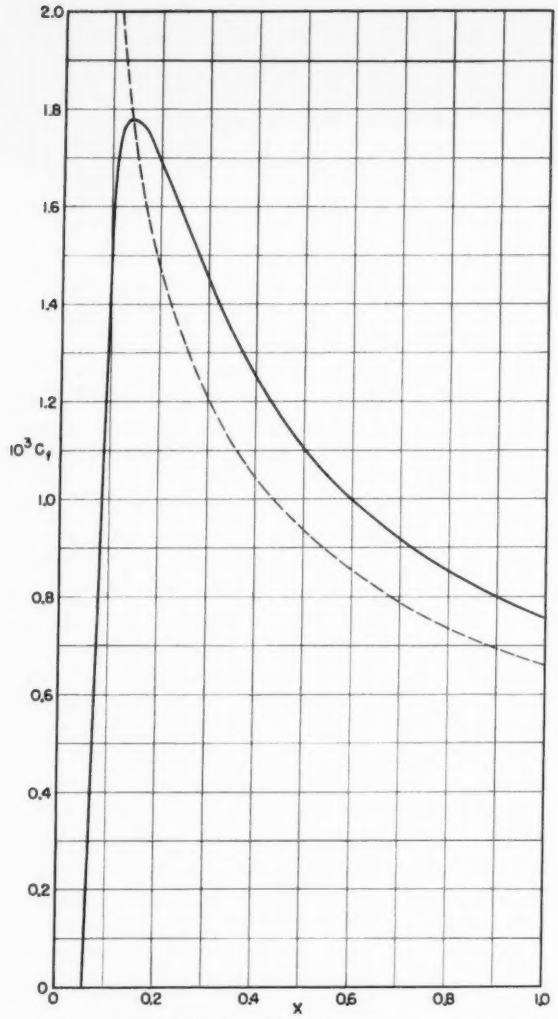


FIG. 3. Local skin friction along the plate for $\gamma = 1.40$, $\epsilon = 10^{-3}$, and $M = 10$. The dashed curve shows the skin friction when the shock wave is absent.

local deflection of a streamline. In the hypersonic range the pressure formula reduces to the same form as that on a wedge airfoil. In fact, for both the viscous and the inviscid fields, the solutions depend on a parameter that corresponds to Tsien's hypersonic parameter—i.e., $Mv_e \sim M^{2+\omega}/\sqrt{Rex}$. This is in full agreement with Lees' hypothesis.[1]

(3) The second-order vertical velocity component is directed inward, and, consequently, there results a reduction of boundary-layer thickness, as compared with the case of a shock-free flow.

(4) The boundary-layer thickness grows like $x^{3/2}$ near the leading edge due to the singularity of the pressure. If the pressure were regular at the leading edge, the boundary layer would grow linearly with $x$. When $x$ is large, it assumes the behavior of the ordinary boundary layer.

(5) The skin friction on the plate is larger than for the case in which the pressure is constant, when $x$ is large. As $x$ decreases toward the leading edge, the skin friction increases gradually and falls off after it reaches a maximum. If the singularity were shifted toward the other side of the flow field, the skin friction would be finite at the leading edge.

In view of the fact that the shock is initially independent of the viscous effects, it must be concluded that the initial behavior of the boundary-layer thickness cannot be proportional to $x^{3/2}$. For this would imply that the flow would follow concave streamlines and would be compressive but continuous; then the viscous effects would have a strong influence on the shock and Mach waves. This seems to indicate that the solution cannot be valid when $x$ is less than $0(m^6\epsilon^2)$.

The deficiency of the first-order theory can be seen also from Eqs. (8.9) and (8.10) in connection with the continuation of the solutions from one to the other field. If in the transformation (3.1) a term $\epsilon^2 x^{(2)}$ were added, then it would be possible to make Eqs. (8.9) and (8.10) agree to the order $\epsilon^2$. In that event, when $\sqrt{\xi}$ is $0(M^3\epsilon)$, the transformation equation [Eq. (3.1)] would likely cease to converge, and a different approach near the leading edge would have to be contemplated.

## REFERENCES


[1] Lees, L., *On Boundary-Layer Equations in Hypersonic Flow and Their Approximate Solutions*, Journal of the Aeronautical Sciences, Vol. 20, pp. 143–145, 1953.

[2] Lighthill, M. J., *A Technique for Rendering Approximate Solutions to Physical Problems Uniformly Valid*, Phil. Mag., Vol. 40, pp. 1179–1201, 1949.

[3] Shen, S. F., *An Estimate of Viscosity Effect on the Hypersonic Flow over an Insulated Wedge*, J. of Mathematics and Physics, Vol. 31, pp. 192–205, 1952.

[4] Howarth, L., *Concerning the Effect of Compressibility on Laminar Boundary Layers and Their Separation*, Proc. Roy. Soc., A 194, pp. 16–42, 1948.

[5] Chapman, D. R., and Rubesin, M. W., *Temperature and Velocity Profiles in Compressible Laminar Boundary Layer with Arbitrary Distribution of Surface Temperature*, Journal of the Aeronautical Sciences, Vol. 16, pp. 547–565, 1949.

[6] von Kármán, Th., and Tsien, H. S., *Boundary Layer in Compressible Fluids*, Journal of the Aeronautical Sciences, Vol. 5, pp. 227–232, 1938.

[7] Maslen, S. H., *Second Approximation to Laminar Compressible Boundary Layer on Flat Plate in Slip Flow*, NACA TN 2818, 1952.

[8] Schaaf, S. A., *A Note on the Flat Plate Drag Coefficient*, Univ. of California, Engineering Research Report No. HE-150-66, February, 1950.

[9] Linnell, R. D., *Two-dimensional Airfoil in Hypersonic Flows*, Journal of the Aeronautical Sciences, Vol. 16, pp. 22–30, 1949.

[10] Lighthill, M. J., *High-speed Aerodynamics and Jet Propulsion*, Vol. VI, Sec. E, Princeton University Press, p. 387, 1954.

[11] Friedrichs, K. O., *Formation and Decay of Shock Waves*, Communications on Pure and Applied Math., Vol. 1, pp. 211–245, 1948.

[12] Lighthill, M. J., *The Energy Distribution Behind Decaying Shocks*, Phil. Mag., Vol. 41, No. 7, pp. 1101–1128, 1950.

[13] Coles, D., *Measurements in the Boundary Layer on a Smooth Flat Plate in Supersonic Flow*, Ph.D. thesis, California Institute of Technology, 1953.

[14] Nagamatsu, H., and Kendall, J., Guggenheim Aeronautical Laboratory, California Institute of Technology, Preliminary data, Unpublished.

[15] Bertram, M. H., *An Approximate Method for Determining the Displacement Effects and Viscous Drag of Laminar Boundary Layers in Two-Dimensional Hypersonic Flow*, NACA TN 2773, September, 1952.

[16] Bogdonoff, S. M., and Hammitt, A. G., Department of Aeronautical Engineering, Princeton University, Preliminary data, unpublished, 1954.

# Equations for the Loading, Section Pitching-Moment Coefficient, and Center-of-Pressure Distributions on Triangular Wings Having Supersonic Leading and Trailing Edges for Various Basic Camber Distributions

JULIAN H. KAINER*

*Ryan Aeronautical Company*

## (1) Summary

The linearized supersonic flow theory has been applied to obtain generalized equations in closed form for the potential, pressure, span-load distributions, section pitching-moment coefficient distributions, and the section center-of-pressure distributions for various camber distributions for triangular wings having supersonic leading and trailing edges. In addition, these quantities are presented graphically for constant, linear, parabolic, and cubic camber distributions.

The results herein may be used to account for the presence of a body, geometric warp, and aerolastic effects in the fashion prescribed for the effects of twist.[1, 2, 3]

## (2) Symbols

***Free-Stream Conditions***

| | |
|---|---|
| $V$ | = velocity |
| $M$ | = Mach Number |
| $\beta$ | = $\sqrt{M^2 - 1}$ |
| $\mu$ | = Mach angle, arc sin $(1/M)$ |
| $\rho$ | = mass density of air |
| $q$ | = dynamic pressure, $(1/2)\rho V^2$ |

***Wing Geometry***

| | |
|---|---|
| $b/2$ | = semispan |
| $c_0$ | = root chord |
| $c_{av.}$ | = average chord |
| $\bar{c}$ | = mean aerodynamic chord, $(2/3)c_0$ |
| $\epsilon$ | = half apex angle degree |
| $\delta$ | = angle between trailing edge and axis of symmetry, degree |
| $m$ | = $\beta \tan \epsilon$ |
| $m_0$ | = $\beta \tan \delta$ |
| $S$ | = wing area |
| $x, y, z$ | = Cartesian coordinates of system of axes with origin at leading edge of root chord |
| $\xi, \eta, \zeta$ | = integration variables |
| $\alpha(\zeta, \eta)$ | = angle of attack in the stream direction, rad. |

***Analysis Parameters***

| | |
|---|---|
| $\phi$ | = velocity potential |
| $\phi_x$ | = horizontal perturbation velocity |
| $\phi_{xx}, \phi_{yy}, \phi_{zz}$ | = second partial derivatives of the velocity potential with respect to $x$, $y$, $z$, respectively |
| $\mathfrak{v}$ | = elementary solution to linearized equation of motion |
| $\sigma(\xi, \eta)$ | = source-strength per unit area upwash |
| $w$ | = upwash |
| $f(\xi, \eta, \zeta)$ | = $1/\sqrt{(x-\zeta)^2 - \beta^2(y-\eta)^2 - \beta^2(z-\zeta)^2}$ |
| $\gamma$ | = an arbitrary characteristic dimension |
| $S'$ | = area of integration |
| $\iota$ | = $\beta y/x$ |
| $\theta_1$ | = arc cos $[(1 - m\iota)/(m - \iota)]$ |
| $\theta_2$ | = arc cos $[(1 + m\iota)/(m + \iota)]$ |
| $(x')_{T.E.}$ | = $x/c_0$ evaluated at the trailing edge |
| $\Delta p/q$ | = lifting pressure coefficient |
| $a_i, b_i$ | = coefficients of spanwise and chordwise power series expansion for the angle of attack, respectively |
| $x_{c.p.}$ | = section center-of-pressure |
| $\bar{x}_{c.p.}$ | = wing longitudinal center-of-pressure |
| $\bar{y}_{c.p.}$ | = wing lateral center-of-pressure |
| $C_n$ | = section normal-force-coefficient per rad. |
| $C_m$ | = section pitching-moment coefficient per rad. |
| $C_{mb}$ | = section bending-moment coefficient per rad. |
| $L, \bar{M}, \overline{M}$ | = wing lift, pitching and bending moments, respectively, per rad. |
| $C_N$ | = wing normal force coefficient per rad., $(N/qS)$ |
| $C_M$ | = wing pitching-moment coefficient per rad., $(\bar{M}/qS\bar{c})$ |
| $C_{M_b}$ | = wing bending-moment coefficient per rad., $(\overline{M}/qSb/2)$ |
| $E_i(t)$ | = conical functions from which the potential and normal force coefficients for basic camber distributions are determined for triangular wings |
| $F_i(t)$ | = conical functions from which the horizontal perturbation velocities for basic camber distributions are determined for triangular wings |
| $\bar{E}_i(t)$ | = conical functions from which the potential and normal-force coefficients for basic camber distributions are determined for unswept wings |
| $\bar{F}_i(t)$ | = conical functions from which the horizontal perturbation velocities for basic camber distributions are determined for unswept wings |
| $\tau_i(t)$ | = conical functions from which the section centers-of-pressure for basic camber distributions are determined for triangular wings |
| $\bar{\tau}_i(t)$ | = conical functions from which the section centers-of-pressure for basic camber distributions are determined for unswept wings |

***Superscripts***

| | |
|---|---|
| * | = represents multiplication by $\beta$—i.e., $C_L^* = \beta C_L$, is read as the "effective" lift coefficient. |
| $i$ | = index of power series, 0, 1, 2, 3 . . . . |
| $'$ | = primed $(x, y)$ quantities are nondimensionalized by $(c_0, b/2)$, respectively. |

***Subscripts***

| | |
|---|---|
| $i$ | = index, representing degree of camber (or twist) |

Received November 8, 1954.

* Aerodynamics Engineer.

The author acknowledges the assistance of Mrs. H. Grijalva for her contribution of the calculations.

## (3) Introduction

It was previously indicated[3] that an empirical correlation[4] between span-load distributions based on linearized theory and some supersonic wind-tunnel data was sufficiently encouraging to warrant further consideration of the entities which have a substantial effect on the air loads carried on the wings. In accordance with this theme, several investigations[1, 2, 3] have been carried out to determine the loading distributions due to various basic twist distributions induced by either body upwash,[5] geometric warp, or the effects of aerolasticity. The effects of the body upwash and geometric warp on the loading is a direct problem wherein the source-strength is known. The inverse problem of developing an aerolastic analysis is described by the noniterative procedure of Brown, Holtby, and Martin[6] for which the main ingredients are the wing structural matrix and the aerodynamic loading properties of the wing for basic twist and camber distributions.

The effects of various basic twist distributions on the spanwise variations in section pitching-moment coefficient and center-of-pressure were presented[3] as a means of proportioning the loading distributions[1, 2] to the control-points of the structural matrix for triangular wings having supersonic leading and trailing edges. The wing pitching and bending-moment coefficients and the corresponding centers-of-pressure were obtained graphically; however, the corresponding results in the form of generalized equations in closed form and design charts are in preparation and will be reported on at a later date. The purpose of the present paper is to report on the effects of various basic camber distributions on the spanwise and chordwise loading functions, the section pitching-moment coefficients and the section centers-of-pressure for this class of wings. The corresponding results will subsequently be extended to include triangular wings having subsonic leading edges.

## (4) Analysis

### *General Background*

The chordwise and spanwise parameters will be shown to be quasi-conical in the fashion previously established.[1, 2, 3] The general derivation will be briefly reviewed to furnish a basis for the new developments below.

$$\beta^2\phi_{xx} - \phi_{yy} - \phi_{zz} = 0 \tag{4.1}$$

a solution of which is[7]

$$\Phi = c(\xi, \eta, \zeta)f(\xi, \eta, \zeta) \tag{4.2}$$

where

$$f(\xi, \eta, \zeta) = 1/\sqrt{(x - \xi)^2 - \beta^2(y - \eta)^2 - \beta^2(z - \xi)^2}\dagger \tag{4.3}$$

and $c(\xi, \eta, \zeta)$ is the source-strength per unit volume, which may be reduced to a source-strength per unit area since the considerations are in the plane of the wing, where

$$c(\xi, \eta) = w/\pi = (V/\pi)\alpha(\xi, \eta) \tag{4.4}$$

Due to the linearity of the equation of motion, it is assumed that the composite upwash may be obtained by superposition of the separate upwashes due to twist, $\alpha(\eta)$, and camber, $\alpha(\xi)$. From geometric considerations

$$\alpha(\xi, \eta) \sim \alpha(\eta) + \alpha(\xi) \tag{4.5}$$

is valid only for small angles, but by the same token it is recalled that the theory was derived specifically for small angles, or small disturbances. Hence, for small angles of attack, Eq. (4.5) is justified without consideration of the cross-products in $(\xi, \eta)$.

It was pointed out previously[4] that the prime value of linearized theory is in predicting qualitative trends and, in particular, the increments due to such higher order effects as geometric warp, body interference, and aeroelasticity rather than the absolute magnitudes of the desired quantities. This consideration is most practical when some means is available for accurately predicting the desired quantity in the absence of these higher order effects. The increments in loading and/or in loads due to these effects is usually a small fraction of the basic quantity. For the first order, it should be quite acceptable to neglect the cross-product terms in the series expansion [as in Eq. (4.5)] at high angles of attack with the knowledge that the additional error which remains after correcting the theoretical incremental loading and/or loads by a correction factor[1] will be of higher order than the actual effects under consideration.

The additional fact that the leading edge is swept does not inconvenience the method of analysis. The source-strength is expanded in terms of a coordinate about the wing apex, $\xi$, rather than a coordinate about the leading edge, $\xi - (\beta y/m)$. This merely implies a displacement of the vertical position of the leading edge. The composite loading for any basic degree of camber, $i$, will then depend upon all the preceding basic degrees of camber—i.e., if $i = 2$, then the composite $\alpha(\xi)$ is

$$\alpha = b_i(\xi - \beta y/m)^2 = b_i[\xi^2 - 2\beta y/m\xi + (\beta y/m)^2] \tag{4.6}$$

which is of the form

$$\alpha = b_0 + b_1\xi + b_2\xi^2 \tag{4.7}$$

This additional step may be neglected if it is not required that $z$ equal zero at the leading edge.

The analysis for the effects of camber on the loading may now proceed in the same manner as the corresponding analysis for the effects of twist.[2]

The slope of the camber distribution is expanded in a power series about the $y$ or $\eta$ axis

$$\alpha(\xi) = \sum_{i=0}^{\infty} b_i \left(\frac{\xi}{\gamma}\right)^i \tag{4.8}$$

where the coordinate at the leading edge is $\xi = \beta y/m$.

† Hereafter the term $\beta^2(z - \zeta)^2$ is not considered inasmuch as the solution is satisfied in the plane of the wing.

### *Velocity Potential*

The velocity potential at a point $P(x, y)$, Fig. 1, is the integrated effect of the elementary sources distributed within the fore-cone of $P$; hence, from Eqs. (4.2) and (4.4), it follows that

$$\phi = R.P.\left[\frac{V}{\pi}\int_{S'}\int \alpha(\xi)f(\xi,\eta)d\xi d\eta\right]^{\dagger} \quad (4.9)$$

where $R.P.$ means the real part of the expression.

The analysis now takes the same direction as previously outlined for the case of basic twist distributions,[2]

$$\phi = b_0(\phi/b)_0 + b_1(\phi/b)_1 + b_2(\phi/b)_2 + \ldots \quad (4.10)$$

or

$$\phi = \sum_{i=0}^{\infty} b_i\left(\frac{\phi}{b}\right)_i \quad (4.11)$$

Eqs. (4.10) and (4.11) follow as a result of the absolute convergence of the integrand of Eq. (4.9).

The potential for any basic camber distribution is

$$\left(\frac{\phi}{b}\right)_i = \frac{V}{\pi\gamma^i}\int_{S'}\int \xi^i f(\xi,\eta)d\xi\, d\eta \quad (4.12)$$

integration of which leads to results of the form

$$(\pi/V)[(\beta^i\gamma^i)/x^{1+i}](\phi/b)_i^* = E_i(t) \quad (4.13)$$

$E_i(t)$ is presented in the Appendix for values of $i = 0$, 1, 2, and 3.

### *Pressure Distribution*

The lifting pressure distribution is

$$\frac{\Delta p}{q} = \frac{4}{V}\sum_{i=0}^{\infty} b_i\frac{\partial}{\partial x}\left(\frac{\phi}{b}\right)_i \quad (4.14)$$

and the horizontal perturbation velocity parameter may be obtained from the potential parameter of Eq. (4.13), where $\gamma$ is assigned the value $c_0$.

$$\frac{\pi}{V}\left(\frac{\beta}{x'}\right)^i\left(\frac{\phi_c}{b}\right)_i^* = (1+i)E_i(t) - t\frac{\partial}{\partial t}[E_i(t)] \quad (4.15)$$

$$\equiv F_i(t) \quad (4.16)$$

$F_i(t)$ is presented in the Appendix for values of $i = 0$, 1, 2, and 3.

### *Span-Load Distribution*

The span-load distribution, or section normal-force coefficient, $C_n$ is defined as

$$C_n = \frac{1}{c}\int_{x_{L.E.}}^{x_{T.E.}}\frac{\Delta p}{q}\,dx \quad (4.17)$$

Substituting Eq. (4.14) in Eq. (4.17) results in

† In all subsequent formulas involving potential, pressure, span-loading, section pitching-moment coefficient, and center-of-pressure, the real part will be implied but the symbol $R.P.$ will be deleted.

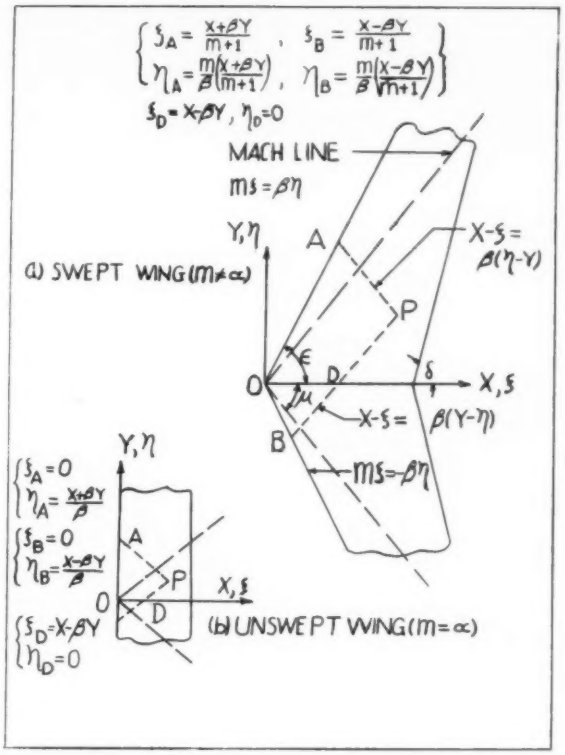


FIG. 1. Details and limits of integration.

$$C_n c = \frac{4}{V}\int_{x_{L.E.}}^{x_{T.E.}}\sum_{i=0}^{\infty} b_i\frac{\partial}{\partial x}\left(\frac{\phi}{b}\right)_i dx \quad (4.18)$$

Since the integrand is absolutely convergent,

$$C_n c = \frac{4}{V}\sum_{i=0}^{\infty} b_i\left(\frac{\phi}{b}\right)_i \quad (4.19)$$

The quantity $(\phi/b)_i$, is evaluated at the trailing edge because the potential vanishes at the leading edge. The characteristic dimension, $\gamma$, from Eq. (4.13) is arbitrarily assumed equal to the wing semispan, $b/2$.

The span-loading parameter may be written as

$$\frac{\pi}{8}\left(\frac{mm_0}{m_0-m}\right)^i\left(\frac{1}{x'}\right)_{T.E.}^{1+i}\left(\frac{C_n}{b}\right)_i^*\left(\frac{c}{c_{av.}}\right) = E_i(t) \quad (4.20)$$

where $t$ and $x_{T.E.}$ are evaluated at the trailing edge, and $E_i(t)$ may be found in the Appendix.

### *Section Pitching-Moment Coefficient*

The section pitching-moment coefficient about the leading edge of the root chord is

$$C_m = \frac{1}{c^2}\int_{x_{L.E.}}^{x_{T.E.}} x\frac{\Delta p}{q}\,dx \quad (4.21)$$

or

$$C_m(c/c_{av.})^2 = 2x_{c.p.}'C_n(c/c_{av.}) \quad (4.22)$$

substituting Eq. (4.20) into Eq. (4.22)

$$\frac{\pi}{16}\left(\frac{mm_0}{m_0-m}\right)^i\left(\frac{1}{x'}\right)_{T.E.}^{2+i}\left(\frac{C_m}{b}\right)_i^*\left(\frac{c}{c_{av.}}\right)^2 = E_i(t)\tau_i(t) \quad (4.23)$$

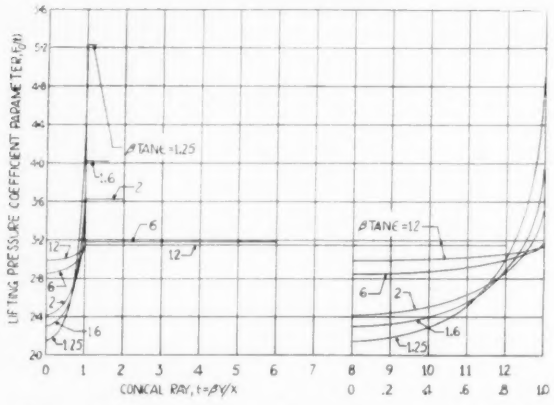


FIG. 2. Lifting pressure coefficient parameter, $F_0(t)$, against conical ray, $t$, for several families of $\beta$ tan $\epsilon$ and for all families of $\beta$ tan $\delta$ for constant camber distribution.

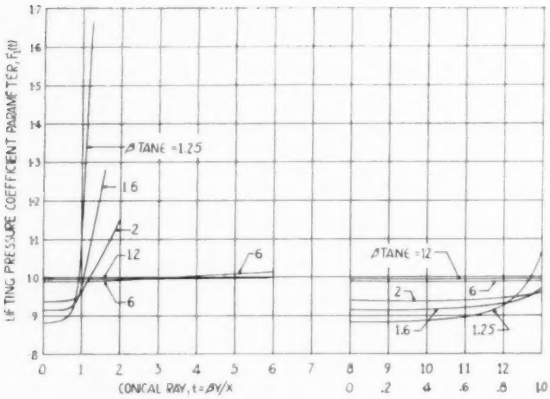


FIG. 3. Lifting pressure coefficient parameter, $F_1(t)$, against conical ray, $t$, for several families of $\beta$ tan $\epsilon$ and for all families of $\beta$ tan $\delta$ for linear camber distribution.

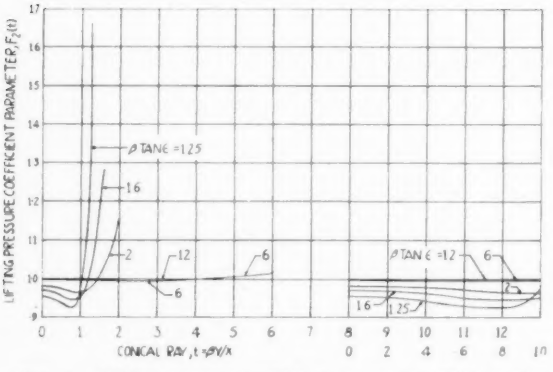


FIG. 4. Lifting pressure coefficient parameter, $F_2(t)$, against conical ray, $t$, for several families of $\beta$ tan $\epsilon$ and for all families of $\beta$ tan $\delta$ for parabolic camber distribution.

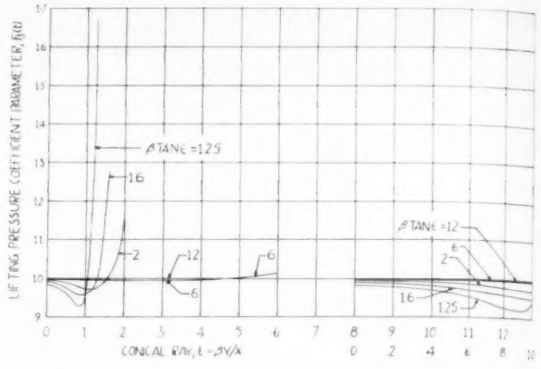


FIG. 5. Lifting pressure coefficient parameter, $F_3(t)$, against conical ray, $t$, for several families of $\beta$ tan $\epsilon$ and for all families of $\beta$ tan $\delta$ for cubic camber distribution.

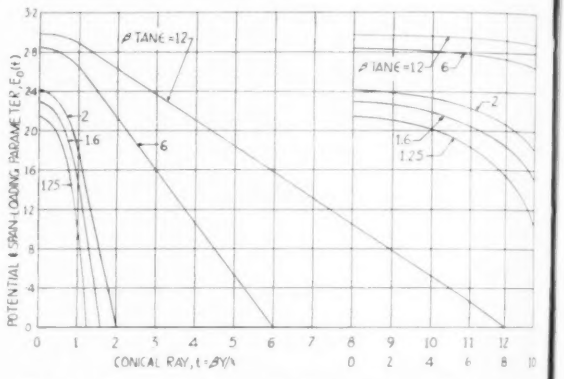


FIG. 6. Potential and span-loading parameter, $E_0(t)$, against conical ray, $t$, for several families of $\beta$ tan $\epsilon$ and for all families of $\beta$ tan $\delta$ for constant camber distribution.

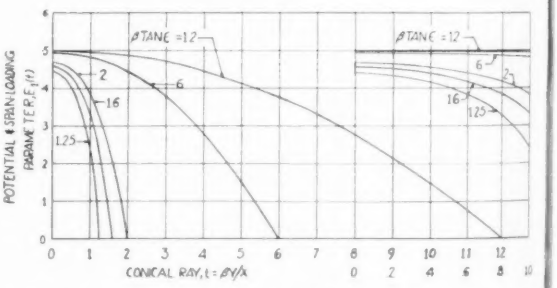


FIG. 7. Potential and span-loading parameter, $E_1(t)$, against conical ray, $t$, for several families of $\beta$ tan $\epsilon$ and for all families of $\beta$ tan $\delta$ for linear camber distribution.

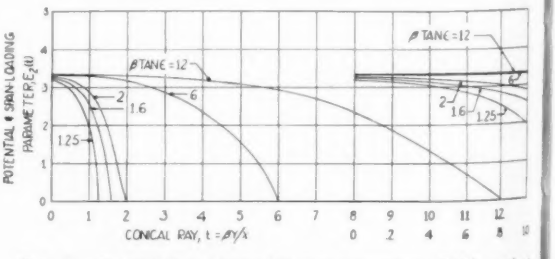


FIG. 8. Potential and span-loading parameter, $E_2(t)$, against conical ray, $t$, for several families of $\beta$ tan $\epsilon$ and for all families of $\beta$ tan $\delta$ for parabolic camber distribution.

where $$x_{c.p.}' \equiv (x')_{T.E.}\tau_i(t) \tag{4.24}$$

such that $$0 < \tau_i(t) \leq 1.0$$

The resultant section pitching-moment coefficient parameter is

$$C_m^* \left(\frac{c}{c_{av.}}\right)^2 = \sum_{i=0}^{\infty} b_i \left(\frac{C_m}{b}\right)_i^* \left(\frac{c}{c_{av.}}\right)^2 \tag{4.25}$$

$$= 2(x')_{T.E.} \sum_{i=0}^{\infty} b_i \left(\frac{C_n}{b}\right)_i^* \left(\frac{c}{c_{av.}}\right) \tau_i(t) \tag{4.26}$$

***Section Center-of-Pressure***

By definition

$$x_{c.p.}' = \frac{1}{c_0} \frac{\text{section pitching-moment}}{\text{section normal-force}} \tag{4.27}$$

$$= \frac{1}{c_0} \frac{\int_{x_{L.E.}}^{x_{T.E.}} x \frac{\Delta p}{q} dx}{\int_{x_{L.E.}}^{x_{T.E.}} \frac{\Delta p}{q} dx} \tag{4.28}$$

$$= \frac{1}{c_0} \frac{x_{T.E.}\phi_{T.E.} - \int^{x_{T.E.}} \phi dx}{\phi_{T.E.}} \tag{4.29}$$

(lower limit is not considered in the integral above since the potential vanishes at a supersonic leading edge).

Substituting Eq. (4.20) into Eq. (4.29)

$$\frac{x_{c.p.}'}{(x')_{T.E.}} = 1 - \frac{\int^{x_{T.E.}} x^{1+i} E_i(t)\, dx}{(x)_{T.E.}^{2+i} E_i(t)} \tag{4.30}$$

$$\equiv \tau_i(t) \tag{4.31}$$

$\tau_i(t)$ is presented in the Appendix for values of $i = 0$, 1, 2, and 3.

***Wing Force, Moment, and Center-of-Pressure Characteristics***

The following results are not available yet in analytic form, hence, graphical means may be used.

*Wing Normal-Force Coefficient Parameter*

$$C_N \equiv \int_0^1 C_n \frac{c}{c_{av.}} dy' \tag{4.32}$$

and from Eq. 4.20 it follows that

$$\frac{\pi}{8m_0^2} \left(\frac{m}{m_0 - m}\right)^i \left(\frac{C_N}{b}\right)_i^* = \int_0^m (m_0 - t)^{-(3+i)} E_i(t) dt \tag{4.33}$$

The total normal force coefficient is

$$C_N^* = \sum_{i=0}^{\infty} b_i \left(\frac{C_N}{b}\right)_i^* \tag{4.34}$$

*Wing Pitching-Moment Coefficient Parameter*

$$C_M \equiv \frac{3}{4} \int_0^1 C_m \left(\frac{c}{c_{av.}}\right)^2 dy' \tag{4.35}$$

and from Eq. (4.23) it follows that

$$\frac{\pi}{12m_0^3} \left(\frac{m}{m_0 - m}\right)^{1+i} \left(\frac{C_M}{b}\right)_i^* = \int_0^m (m_0 - t)^{-(4+i)} E_i(t)\tau_i(t) dt \tag{4.36}$$

The total pitching-moment coefficient is

$$C_M^* = \sum_{i=0}^{\infty} b_i \left(\frac{C_M}{b}\right)_i^* \tag{4.37}$$

*Wing Longitudinal Center-of-Pressure*

$$\bar{x}_{c.p.} = \frac{1}{2} \frac{\int_0^1 C_m \left(\frac{c}{c_{av.}}\right)^2 dy'}{\int_0^1 C_n \left(\frac{c}{c_{av.}}\right) dy'} \tag{4.38}$$

$$(\bar{x}_{c.p.}')_i = m_0 \frac{\int_0^m (m_0 - t)^{-(4+i)} E_i(t)\tau_i(t) dt}{\int_0^m (m_0 - t)^{-(3+i)} E_i(t) dt} \tag{4.39}$$

*Wing Lateral Center-of-Pressure*

$$\bar{y}_{c.p.} = \frac{\int_0^1 y' C_n \left(\frac{c}{c_{av.}}\right) dy'}{\int_0^1 C_n \left(\frac{c}{c_{av.}}\right) dy'} \tag{4.40}$$

$$(\bar{y}_{c.p.}')_i = \left(\frac{m_0}{m} - 1\right) \frac{\int_0^m t(m_0 - t)^{-(4+i)} E_i(t) dt}{\int_0^m (m_0 - t)^{-(3+i)} E_i(t) dt} \tag{4.41}$$

***Swept Wings***

It is quite expedient in the theoretical treatment of wings having nonpointed tips to separate[1] the study of the loading in the tip Mach cone region from that in the root Mach cone region. Thus, the functions given herein are also applicable to the regions outside the tip Mach cones of swept wings. Inasmuch as there are no available calculations within the tip Mach cone for the longitudinal center-of-pressure distributions corresponding to twist and camber distributions, one of the purposes of this section is to suggest a reliable approximation. At the tip chord the potential is known due to twist[8] and may easily be determined for camber for various values of the index $i$.

Since these loadings may be written as

$$\phi = kx^{1+i} \tag{4.42}$$

where $k$ is a simple function of the wing plan form, the center-of-pressure may be deduced from Eq. (4.30) as

$$x_{c.p.}'/(x')_{T.E.} = [(1 + i)/(2 + i)] \tag{4.43}$$

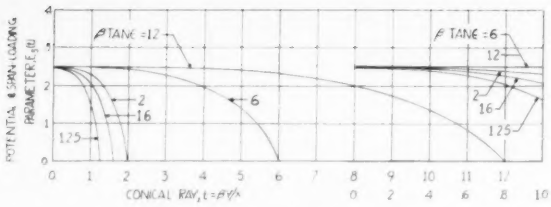


FIG. 9. Potential and span-loading parameter, $E_0(t)$, against conical ray, $t$, for several families of $\beta$ tan $\epsilon$ and for all families of $\beta$ tan $\delta$ for cubic camber distribution.

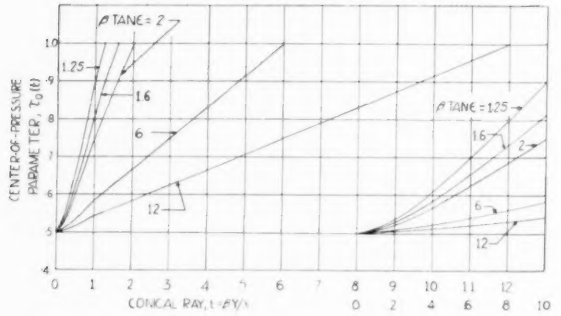


FIG. 10. Section center-of-pressure parameter, $\tau_0(t)$, against conical ray, $t$, for several families of $\beta$ tan $\epsilon$ and for all families of $\beta$ tan $\delta$ for constant camber distribution.

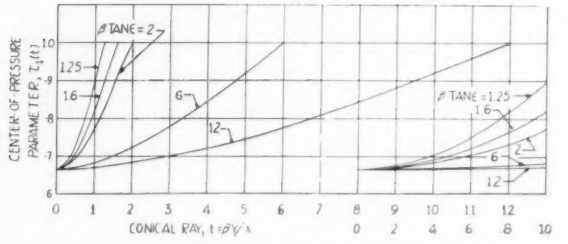


FIG. 11. Section center-of-pressure parameter, $\tau_1(t)$, against conical ray, $t$, for several families of $\beta$ tan $\epsilon$ and for all families of $\beta$ tan $\delta$ for linear camber distribution.

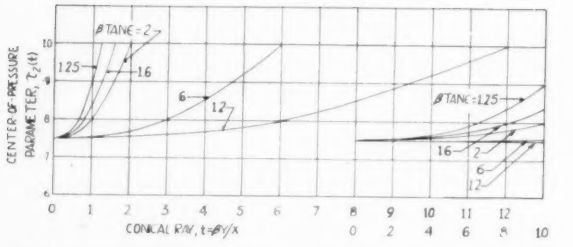


FIG. 12. Section center-of-pressure parameter, $\tau_2(t)$, against conical ray, $t$, for several families of $\beta$ tan $\epsilon$ and for all families of $\beta$ tan $\delta$ for parabolic camber distribution.

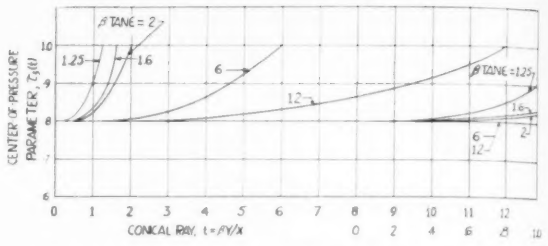


FIG. 13. Section center-of-pressure parameter, $\tau_3(t)$, against conical ray, $t$, for several families of $\beta$ tan $\epsilon$ and for all families of $\beta$ tan $\delta$ for cubic camber distribution.

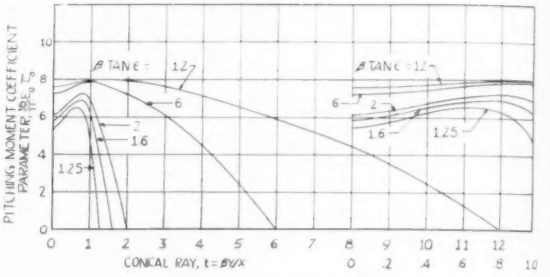


FIG. 14. Section pitching-moment coefficient parameter, $(16/\pi)E_0(t)\tau_0(t)$, against conical ray, $t$, for several families of $\beta$ tan $\epsilon$ and for all families of $\beta$ tan $\delta$ for constant camber distribution.

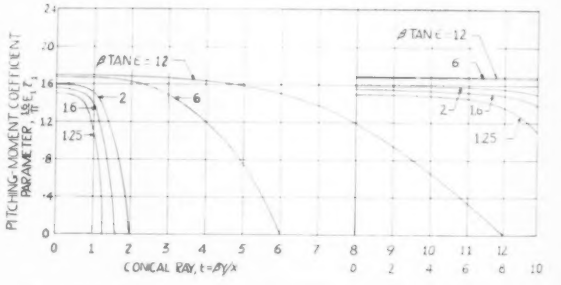


FIG. 15. Section pitching-moment coefficient parameter, $(16/\pi)E_1(t)\tau_1(t)$, against conical ray, $t$, for several families of $\beta$ tan $\epsilon$ and for all families of $\beta$ tan $\delta$ for linear camber distribution.

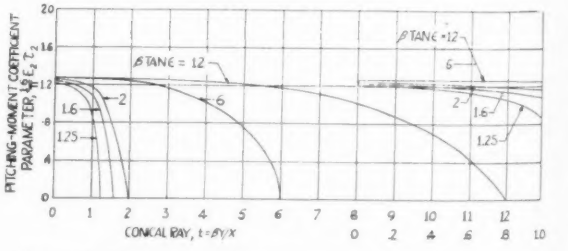


FIG. 16. Section pitching-moment coefficient parameter, $(16/\pi)E_2(t)\tau_2(t)$, against conical ray, $t$, for several families of $\beta$ tan $\epsilon$ and for all families of $\beta$ tan $\delta$ for parabolic camber distribution.

The spanwise variation in the center-of-pressure may be plotted from the root chord to the root-chord Mach line (from the results herein for camber and from the previously published results for twist),[1, 2, 3] and the center-of-pressure distribution may be completed by fairing from this spanwise position to the known value at the tip chord, Eq. (4.43).

The complete variation of the section pitching-moment coefficient for both twist and camber may then be obtained from the known results within the root-chord Mach cone and the faired center-of-pressures within the tip Mach cone with the aid of Eq. (4.22).

### *Unswept Wings*

The results of the preceding sections may be used to construct the desired quantities for unswept wings. These limiting cases are obtained from the conical functions $E_i(t)$, $F_i(t)$, and $\tau_i(t)$ when $m = \infty$. The limiting results are designated by the barred quantities $\bar{E}_i(t)$, $\bar{F}_i(t)$, and $\bar{\tau}_i(t)$, respectively, and are tabulated in the Appendix for values of $i = 0, 1, 2$, and 3.

From the latter results it is noted that such wings are two-dimensional in the Ackeret sense except within the tip region, unlike the corresponding results for twisted wings. This follows from the fact that unswept cambered wings have no geometric discontinuity in slope at the wing apex or center line.

## (5) Discussion

The results of the analysis for the pressures, potentials, section normal force coefficients, section pitching-moment coefficients and section centers-of-pressure are presented in the form of generalized equations in closed form and as design charts in parametric form.

For basic camber distributions, $i = 0, 1, 2, 3$, the pressure distribution parameters, $F_i(t)$, are presented in Figs. 2–5; the span-loading and potential parameters, $E_i(t)$, are presented in Figs. 6–9; the section centers-of-pressure parameters, $\tau_i(t)$, are presented in Figs. 10–13; and the section pitching-moment parameters, $(16/\pi)E_i(t)\tau_i(t)$, are presented in Figs. 14–17. The results are plotted for several values of the leading edge—Mach Number parameters, $\beta \tan \epsilon$, against the conical ray, $t$, evaluated at the trailing edge. The solutions are valid for all supersonic values of the trailing edge—Mach Number parameter, $\beta \tan \delta$.

Unpublished results† indicate that for a delta wing, the wing normal force coefficients, wing longitudinal centers-of-pressure, and the wing pitching-moment coefficients for camber reduce to the same functions determined for the corresponding twisted wings.

$$\frac{C_N{}^*}{b_0} = 4 + \frac{4}{3}\frac{b_1}{b_0} + \frac{2}{3}\frac{b_2}{b_0} + \frac{2}{5}\frac{b_3}{b_0} \qquad (4.44)$$

$$\left(\frac{x_{c.p.}{}'}{x_{T.E.}{}'}\right)_t = \frac{2}{3}, \frac{3}{4}, \frac{4}{5}, \frac{5}{6} \qquad (4.45)$$

† To be presented at a later date.

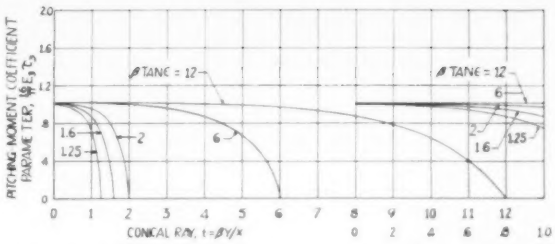


FIG. 17. Section pitching-moment coefficient parameter, $(16/\pi)E_3(t)\tau_3(t)$, against conical ray, $t$, for several families of $\beta$ tan $\epsilon$ and for all families of $\beta$ tan $\delta$ for cubic camber distribution.

$$\frac{C_M{}^*}{b_0} = 4 + \frac{3}{2}\frac{b_1}{b_0} + \frac{4}{5}\frac{b_2}{b_0} + \frac{1}{2}\frac{b_3}{b_0} \qquad (4.46)$$

## (6) Concluding Remarks

An analysis was carried out by means of linearized theory to determine the distributions of the potential, pressure, span-loading, section pitching-moment coefficient, and section center-of-pressure for triangular wings having various basic camber distributions. The results were presented as generalized equations in closed form and in the form of design charts for the rapid estimation of the subject material. The solutions are valid for configurations having supersonic leading and trailing edges.

Preliminary analysis indicated that for a delta wing, the wing normal force coefficient, wing pitching-moment coefficients, and longitudinal center-of-pressure for camber reduced to the same functions predicted for the corresponding twisted wings.

Unswept cambered wings are two-dimensional in the Ackeret sense except within the tip Mach cones (it is recalled that this is also true for wings having even degrees of twist since there is no geometric discontinuity in slope at the wing apex).

## (7) References

[1] Kainer, Julian H., *A Simplified Method to Obtain the Load Distribution Corresponding to the Ackeret Region for Wings Having Arbitrary Source Distribution at Supersonic Speeds*, Journal of the Aeronautical Sciences, Vol. 20, No. 11, p. 749, November, 1953.

[2] Kainer, Julian H., *Equations for the Loading on Triangular Wings Having Supersonic Leading and Trailing Edges Due to Various Basic Twist Distributions*, Journal of the Aeronautical Sciences, Vol. 20, No. 7, p. 469, July, 1953.

[3] Kainer, Julian H., *Spanwise Variations in the Pitching-Moment Coefficient and the Center-of-Pressure Due to Various Basic Twist Distributions on Triangular Wings Having Supersonic Leading and Trailing Edges*, Ryan Aeronautical Company Report No. G-20-94, August, 1953, Journal of the Aeronautical Sciences, Vol. 22, No. 9, p. 598, September, 1955.

[4] Kainer, Julian H., *On the Empirical Use of Linearized Theory for the Supersonic Characteristics and Loading Distributions on Delta Wings with Special Reference to Twist and Camber, Aeroelasticity, and Wing-Body Interference*, Ryan Aeronautical Company Report No. G-20-95, January, 1954.

[5] Beskin, L., *Determination of Upwash Around a Body of Revolution at Supersonic Velocities*, Convair, CVAC-DEVF Memo BB-6; May 27, 1946.

[6] Brown, R. B., Holtby, K. F., and Martin, H. C., *A Superposition Method for Calculating the Aeroelastic Behavior of Swept*

*Wings*, Journal of the Aeronautical Sciences, Vol. 18, No. 8, p. 531, August, 1951.

[7] Puckett, Allen E., *Supersonic Wave Drag of Thin Airfoils*, Journal of the Aeronautical Sciences, Vol. 13, No. 9, p. 475, September, 1946.

[8] Kazan, Elliott, and Kainer, Julian H., *Theoretical Spanwise Loading and Pressure Coefficients in the Tip Region of a Supersonic Leading Edge Swept Back Wing Having Various Spanwise Twist Distributions*, Republic Aviation Corporation Report No. EAR 356.

## (8) Appendix

### *General Triangular Wings (Including Application to Swept Wings)*

*Potential and Span-Loading Functions, $E_i(t)$*

$$E_0(t) = (1/\sqrt{m^2-1})[(m-t)\theta_1 + (m+t)\theta_2] \tag{8.1}$$

$$E_1(t) = \{1/[2(m^2-1)^{3/2}]\}[2m\sqrt{m^2-1}\sqrt{1-t^2} + (m-t)(m^2-2+mt)\theta_1 + (m+t)(m^2-2-mt)\theta_2] \tag{8.2}$$

$$E_2(t) = \{1/[6(m^2-1)^{5/2}]\}\{[m(2m^4-5m^2+6) - 3(m^2+2)t + 9mt^2 - (2m^2+1)t^3]\theta_1 + [m(2m^4-5m^2+6) + 3(m^2+2)t + 9mt^2 + (2m^2+1)t^3]\theta_2 + 2m\sqrt{m^2-1}(2m^2-5-3t^2)\sqrt{1-t^2}\} \tag{8.3}$$

$$E_3(t) = \{1/[24(m^2-1)^{7/2}]\}\{3[m(2m^6-7m^4+8m^2-8) + 4(3m^2+2)t - 6m(m^2+4)t^2 + 4(4m^2+1)t^3 - m(2m^2+3)t^4]\theta_1 + 3[m(2m^6-7m^4+8m^2-8) - 4(3m^2+2)t - 6m(m^2+4)t^2 - 4(4m^2+1)t^3 - m(2m^2+3)t^4]\theta_2 + 2m\sqrt{m^2-1}[(6m^4-17m^2+26) + (2m^2+43)t^2]\sqrt{1-t^2}\} \tag{8.4}$$

*Pressure Functions, $F_i(t)$*

$$F_0(t) = (m/\sqrt{m^2-1})(\theta_1+\theta_2) \tag{8.5}$$

$$F_1(t) = [1/(m^2-1)^{3/2}]\{[m(3m^2-4) - (m^2-2)t]\theta_1 + [m(3m^2-4) + (m^2-2)t]\theta_2 + 2m\sqrt{m^2-1}\sqrt{1-t^2}\} \tag{8.6}$$

$$F_2(t) = \{1/[2(m^2-1)^{5/2}]\}\{[m(2m^4-5m^2+6) - 2(m^2+2)t + 3mt^2]\theta_1 + [m(2m^4-5m^2+6) + 2(m^2+2) + t3mt^2]\theta_2 + 2m(2m^2-5)\sqrt{m^2-1}\sqrt{1-t^2}\} \tag{8.7}$$

$$F_3(t) = \{1/[6(m^2-1)^{7/2}]\}\{3[m(2m^6-7m^4+8m^2-8) + 3(3m^2+2)t - 3m(m^2+4)t^2 + (4m^2+1)t^3]\theta_1 + 3[m(2m^6-7m^4+8m^2-8) - 3(3m^2+2)t - 3m(m^2+4)t^2 - (4m^2+1)t^3]\theta_2 + 2m\sqrt{m^2-1}[(6m^4-17m^2+26) + (2m^2+13)t^2]\sqrt{1-t^2}\} \tag{8.8}$$

*Center-of-Pressure Functions, $\tau_i(t)$*

$$\tau_0(t) = \left\{1 - \frac{1}{2m}\left[\frac{(m^2-t^2)(\theta_1+\theta_2) - 2t(m-t)\theta_1 + 2t(m+t)\theta_2 - 2\sqrt{m^2-1}\,t^2\cosh^{-1}(1/t)}{(m-t)\theta_1 + (m+t)\theta_2}\right]\right\} \tag{8.9}$$

$$\tau_1(t) = \left(1 - \frac{1}{3m^2}\left\{\frac{[m^3(m^2-2) + 3m^2t - 3m^3t^2 + (2m^2-1)t^3]\theta_1 + \dots}{2(m^2-1)[(m-t)\theta_1 + (m+t)\theta_2] + \dots} \right.\right.$$
$$\left.\left.\frac{+ \dots [m^3(m^2-2) - 3m^2t - 3m^3t^2 - (2m^2-1)t^3]\theta_2 + 2m\sqrt{m^2-1}(m^2+t^2)\sqrt{1-t^2}}{+ \dots 2m\sqrt{m^2-1}\sqrt{1-t^2}}\right\}\right) \tag{8.10}$$

$$\tau_2(t) = \left(1 - \frac{1}{4m^3}\left\{\frac{(m-t)[m^3(2m^4-5m^2+6) + m^2(2m^4-9m^2-2)t + \dots}{[m(2m^4-5m^2+6) - 3(m^2+2)t + \dots}\right.\right.$$
$$\frac{+ \dots m(2m^4+9m^2-2)t^2 - (6m^4-5m^2+2)t^3]\theta_1 + (m+t)[m^3(2m^4-5m^2+6) + \dots}{+ 9mt^2 - (2m^2+1)t^3]\theta_1 + [m(2m^4-5m^2+6) + \dots}$$
$$\frac{+ \dots - m^2(2m^4-9m^2-2)t + m(2m^4+9m^2-2)t^2 + (6m^4-5m^2+2)t^3]\theta_2 + \dots}{+ \dots 3(m^2+2)t + 9mt^2 + (2m^2+1)t^3]\theta_2 + \dots}$$
$$\left.\left.\frac{-4(m^2-1)^{5/2}t^4\cosh^{-1}(1/t) + 2m^2\sqrt{m^2-1}[m^2(2m^2-5) - (8m^2+1)t^2]\sqrt{1-t^2}}{+ \dots 2m\sqrt{m^2-1}(2m^2-5-3t^2)\sqrt{1-t^2}}\right\}\right) \tag{8.11}$$

$$\tau_3(t) = \left(1 - \frac{1}{15m^4}\left\{\frac{9(m-t)[m^4(2m^6 - 7m^4 + 8m^2 - 8) + m^3(2m^6 - 7m^4 + 23m^2 + 2)t + \ldots}{3[m(2m^6 - 7m^4 + 8m^2 - 8) + 4(3m^2 + 2)t + \ldots}\right.\right.$$
$$\frac{+ \ldots + m^2(2m^6 - 17m^4 - 17m^2 + 2)t^2 + m(2m^6 + 23m^4 - 7m^2 + 2)t^3 - (8m^6 - 8m^4 + 7m^2 - 2)t^4]\theta_1 + \ldots}{+ \ldots - 6m(m^2 + 4)t^2 + 4(4m^2 + 1)t^3 - m(2m^2 + 3)t^4]\theta_1 + \ldots}$$
$$+ \ldots \frac{9(m+t)[m^4(2m^6 - 7m^4 + 8m^2 - 8) - m^3(2m^6 - 7m^4 + 23m^2 + 2)t + m^2(2m^6 - 17m^4 - 17m^2 + 2)t^2 + \ldots}{+ \ldots 3[m(2m^6 - 7m^4 + 8m^2 - 8) - 4(3m^2 + 2)t - 6m(m^2 + 4)t^2 + \ldots}$$
$$+ \ldots \frac{-m(2m^6 + 23m^4 - 7m^2 + 2)t^3 - (8m^6 - 8m^4 + 7m^2 - 2)t^4]\theta_2 + 9m\sqrt{m^2 - 1}\,[m^2(2m^6 - 7m^4 + 23m^2 + 2) + \ldots}{+ \ldots - 4(4m^2 + 1)t^3 - m(2m^2 + 3)t^4]\theta_2 + \ldots}$$
$$+ \ldots \frac{(2m^8 - 3m^6 + 69m^4 - 12m^2 + 4)t^2]t^2\sqrt{1 - t^2} + m^3\sqrt{m^2 - 1}[6m^2(6m^4 - 17m^2 + 26 + \ldots}{+ \ldots 2m\sqrt{m^2 - 1}[(6m^4 - 17m^2 + 26) + (2m^2 + 43)t^2]\sqrt{1 - t^2} + \ldots}$$
$$\left.\left.\frac{+ \ldots 3(6m^6 - 9m^4 + 155m^2 - 2)t^2](1 - t^2)^{3/2}\}}{+ \ldots}\right) \tag{8.12}$$

***Unswept Wings***

*Potential and Span-Loading Functions, $\bar{E}_i(t)$*

$$\bar{E}_0(t) = \pi \tag{8.13}$$
$$\bar{E}_1(t) = \pi/2 \tag{8.14}$$
$$\bar{E}_2(t) = \pi/3 \tag{8.15}$$
$$\bar{E}_3(t) = \pi/4 \tag{8.16}$$

*Pressure Functions, $\bar{F}_i(t)$*

$$\bar{F}_0(t) = \pi \tag{8.17}$$
$$\bar{F}_1(t) = \pi \tag{8.18}$$
$$\bar{F}_2(t) = \pi \tag{8.19}$$
$$\bar{F}_3(t) = \pi \tag{8.20}$$

*Center-of-Pressure Functions, $\bar{\tau}_i(t)$*

$$\bar{\tau}_0(t) = 1/2 \tag{8.21}$$
$$\bar{\tau}_1(t) = 2/3 \tag{8.22}$$
$$\bar{\tau}_2(t) = 3/4 \tag{8.23}$$
$$\bar{\tau}_3(t) = 4/5 \tag{8.24}$$

## Fluid Dynamic Effects . . .

(*Continued from page 116*)


[5] Lees, L., and Probstein, R. F., *Hypersonic Viscous Flow Over a Flat Plate*, Princeton Univ. Aero. Eng'g. Dept. Rpt. 195, April 20, 1952.

[6] Lees, L., *On the Boundary Layer Equations in Hypersonic Flow and Their Approximate Solutions*, Princeton Univ. Aero. Eng'g. Dept. Rpt. 212, September 20, 1952.

[7] Lees, L., and Probstein, R. F., *Hypersonic Flows of a Viscous Fluid*, Princeton Univ. Aero. Eng'g. Dept., 1953 (unpublished).

[8] Lees, L., *Hypersonic Viscous Flow Over an Inclined Wedge*, Journal of the Aeronautical Sciences, Readers' Forum, Vol. 20, No. 11, pp. 794–796, November, 1954.

[9] Lee, L., *Note on the Hypersonic Similarity Law for an Unyawed Cone*, Journal of the Aeronautical Sciences, Vol. 18, No. 10, pp. 700–702, October, 1951.

[10] Shen, S. F., *An Estimate of Viscosity Effect in Hypersonic Flow Over an Insulated Wedge*, J. of Math. and Phys., Vol. 31, No. 3, pp. 192–305, October, 1952.

[11] Li, Ting-Yi, and Nagamatsu, H., *Shock Wave Effects on the Laminar Skin Friction of an Insulated Flat Plate at Hypersonic Speeds*, Journal of the Aeronautical Sciences, Vol. 20, No. 5 pp. 345–355, May, 1953.

[12] Nagamatsu, H., and Kendall, J., Preliminary data (unpublished), Guggenheim Aeronautical Laboratory, California Institute of Technology.

[13] Akin, S. W., *The Thermodynamic Properties of Helium*, ASME Transactions, Vol. 72, No. 6, pp. 751–759, August, 1950.

[14] Keyes, F. G., *The Heat Conductivity, Viscosity, Specific Heat and Prandtl Number for Thirteen Gases*, Massachusetts Institute of Technology, Project Squid Report 37, April 1, 1952.

[15] Kane, E. D., and Maslach, G. J., *Impact-Pressure Interpretation in a Rarefied Gas at Supersonic Speeds*, NACA TN 2210, October, 1950.

[16] Lees, L., *Influence of the Leading-Edge Shock Wave on the Laminar Boundary Layer at Hypersonic Speeds*, California Institute of Technology, Guggenheim Aeronautical Laboratory, Technical Report No. 1.

[17] Bertram, M. H., *Viscous and Leading-Edge Thickness Effects on the Pressures on the Surface of a Flat Plate in Hypersonic Flows*, Journal of the Aeronautical Sciences, Readers' Forum, Vol. 21, No. 5, pp. 430–431, June, 1954.

# On the Sonic Drag of a Slender Body

JOHN W. MILES*

*University of California at Los Angeles*

SUMMARY

The wave drag on a slender body in sonic flight is evaluated by matching linearized theory with the asymptotic solution of Guderley and Yoshihara along the sonic line. The result exhibits satisfactory agreement with Yoshihara's analysis of a cone-cylinder and, on this evidence, appears to furnish a reliable approximation to the head drag on any slender body of revolution terminating in a sharp shoulder; moreover, for this class of bodies the result can be extended to free-stream Mach Numbers slightly different than unity. If the body is smooth and terminates either in a cylindrical section or in a pointed end, the result assumes a particularly simple form and depends only on the cross-sectional distribution (and, therefore, is not restricted to a body of revolution). The reliability of the result for the latter class of bodies is less certain (especially for the converging portion of the body) and awaits further data for comparison. However, it appears that the sonic drag of a sharp shouldered body is of the same order of magnitude as its supersonic drag, whereas the sonic drag of a smooth body is only a very small fraction of its supersonic drag.

NOTATION

Note that dimensionless coordinates, referred to the body length, are used throughout most of the analysis.

$C$ = see Eq. (4.19)
$C_D$ = drag coefficient (referred to base area)
$C_{D_0}$ = $C_D$ at $M = 1$
$D$ = drag
$M$ = free-stream Mach Number
$R$ = body radius
$R^*$ = body radius at sonic point
$S$ = body cross-sectional area
$a$, $a_0$ = $S'(x)/2\pi$
$b$, $b_0$ = see Eqs. (3.1) and (1.2)
$c^*$ = sonic velocity
$f$ = similarity solution [see Section (4)]
$k$ = transonic similarity parameter [see Eq. (5.9)]
$p$ = pressure
$p^*$ = pressure at sonic speed
$q$ = free-stream dynamic pressure ($q = (1/2)\rho^* c^{*2}$ at $M = 1$)
$r$ = cylindrical polar radius
$r^*$ = radius of sonic surface
$r_1$ = radius at which slender body and asymptotic solutions are matched [see Eq. (4.13)]
$u$, $v$ = axial and radial perturbation velocity components, respectively
$v^*$ = $v$ at sonic surface
$\mathbf{w}$ = total, vector velocity
$x$ = axial coordinate, measured from body nose
$x^*$ = $x$ at sonic point on body
$x_1$ = $x$ at intersection of limiting Mach wave with body
$\gamma$ = specific heat ratio
$\delta$ = parameter measuring fineness of body [used in different ways in Sections (5) and (6)]
$\zeta$ = similarity coordinate [see Eq. (4.7)]
$\theta$ = azimuthal angle
$\lambda$ = similarity parameter [see Eq. (4.14)]
$\xi$ = apparent location of singularity representing asymptotic solution [see Section (4)]
$\rho^*$ = mass density of medium at sonic velocity
$\phi$ = perturbation velocity potential (dimensionless)

Received November 12, 1954.
* Department of Engineering.

## (1) INTRODUCTION

IT CAN BE SHOWN by an order analysis[1, 2] that linearized theory gives an adequate approximation to the equations of transonic flow in the neighborhood of a sufficiently slender body, even though there is always some other neighborhood in which nonlinear effects are decisive (at least for the determination of the drag). It follows that to produce a solution satisfying the boundary conditions imposed on the body is not difficult; but, in general, it cannot be supposed that this solution will exhibit the proper behavior at infinity. This shortcoming may not be important in the determination of the transverse forces, but it usually must be decisive for the drag force.

Let $M$ denote the Mach Number of the free stream and $\epsilon$ the order of magnitude of the perturbation velocity (resulting from the presence of the body) relative to the free-stream velocity; the transonic regime then is defined by

$$|M - 1| = 0(\epsilon) \tag{1.1}$$

which is to say that the difference between the free-stream and sonic velocities is of the same order as the perturbation velocity. Within this approximation the perturbation velocity potential *in the neighborhood of the body* satisfies Laplace's equation in planes transverse to the flow ("slender body" approximation) and can be expressed in the dimensionless form[3] [cf. reference 3, Eq. (10)]

$$\phi(x, r, \theta) = a_0(x) \ln r + b_0(x) + Rl \sum_{n=1}^{\infty} a_n(x) r^{-n} e^{-in\theta} \tag{1.2}$$

where $(x, r, \theta)$ is a set of cylindrical polar coordinates with $x$ measured in the free-stream direction from the most upstream point of the body. The units of velocity and length, to which all dimensions are referred, are the free-stream velocity and the body length.

The coefficients $a_n(x)$, which may be complex, are determined by the boundary conditions at the body; in particular, the source strength is given by [reference 3, Eq. (26)]

$$a_0(x) = [1/(2\pi)]S'(x) \tag{1.3}$$

where $S(x)$ is the transverse area of the body at $x$. The determination of the coefficient $b_0(x)$, on the other

hand, also rests on the requirements imposed on the solution at large distances from the body. However, it may be inferred from the form of the expansion [Eq. (1.2)] or directly from physical considerations that the dominant term in the solution at large distances is axially symmetric, so that it must be possible to express $b_0$ solely in terms of the source strength distribution $a_0$ and, therefore, the distribution of transverse area of the body. In purely supersonic flow the solution for $b_0$ has been given by Ward [reference 3, Eq. (27)], but, as implied by the foregoing discussion, its determination in transonic flow depends on the solution of the nonlinear, transonic equations.†

Recently, Guderley and Yoshihara[4, 5] have obtained an axially symmetric solution to the transonic equations which represents the flow at large distances from a body of revolution (and, on the basis of the foregoing arguments, any slender body) for the special case where the free-stream velocity is exactly sonic ($M = 1$). It therefore suggests itself to attempt an approximate solution for the drag on a slender body in a sonic free stream by joining the slender-body and asymptotic approximations in an appropriate manner, and it is toward this end that the following analysis is primarily directed. It appears that a reasonable approximation can be obtained for the drag on that part of the body forward of the sonic line and probably also for the entire body forward of the maximum cross section, but not for the converging portion of the body.

While the asymptotic solution obtained by Guderley and Yoshihara is developed initially only for a free-stream Mach Number of unity, it has been argued by Liepmann and Eryson[6] that the flow pattern forward of the sonic line is essentially stationary with respect to first-order changes of this Mach Number. Accordingly, *at least if the position of the sonic line is fixed*, the $M = 1$ results for "head drag" [Section (5)] can be extended to values of $M$ for which $M - 1$ is sufficiently small. ["Sufficiently small" implies $|M - 1| << \delta^2$ rather than $|M - 1| << 1$; see Section (5), especially Eq. (5.12) et seq.] The extension over a somewhat wider range of $M$ has been considered by Guderley,[7] but his results are not sufficiently complete for specific application except insofar as they reduce to the result obtained by Liepmann and Bryson.

## (2) The Drag Integral

The flow over a body in a sonic free stream will be divided into subsonic (fore) and supersonic (aft) regions by a surface over which sonic conditions prevail (velocity = $c^*$, pressure = $p^*$, density = $\rho^*$). This sonic surface can be prescribed by one parameter in the asymptotic solution [Section (4)], and the flow conditions are particularly simple there, so that it seems the most convenient location at which to attempt a match between the slender-body and asymptotic

† Cf. Eq. (4.1).

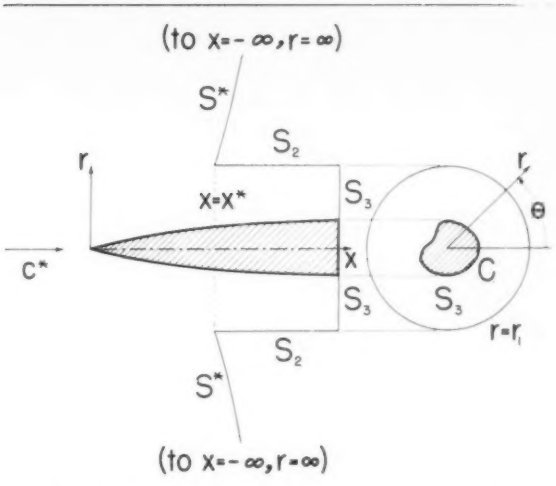


FIG. 1. The control surface for the drag evaluation.

solutions. In the slender-body approximation [see Section (3)] the sonic surface must be normal to the free stream and therefore is specified by a particular value of $x$, say $x^*$, while in the asymptotic approximation [see Section (4)] it must be inclined downstream; accordingly, matching solutions on the sonic surface precludes the prediction of the pressure distribution on the body forward of $x^*$. However, the total drag resulting from this pressure distribution can be placed in a particularly simple form by integrating the axial momentum transport over part or all of the sonic surface.

Consider a slender body (*not necessarily axially symmetric*) that is placed with its nose at the origin of the cylindrical polar coordinates $(x, r, \theta)$ in the otherwise undisturbed, uniform flow of sonic velocity $c^*$, as shown in Fig. 1. The total velocity $\mathbf{w}$ at any point will be expressed in terms of the dimensionless perturbation velocity potential $\phi$ according to

$$\mathbf{w} = c^*[1 + \phi_x, \phi_r, (1/r)\phi_\theta] = c^*(1 + \nabla\phi) \quad (2.1)$$

At large distances from the body $\phi_x$, $\phi_r$, and $\phi_\theta$ must vanish with sufficient rapidity to ensure the evanescence of the perturbation fluxes of mass and momentum through any control surface all parts of which are at an infinite distance from the $x$ axis,‡ and the pressure, density, and velocity approach the free-stream values $p^*$, $\rho^*$, and $c^*$.

Now consider a control surface consisting of that part ($S^*$) of the sonic surface lying outside of $r = r_1$ and closing upstream at infinity, that part ($S_2$) of the

‡ The condition that the perturbation mass flux vanishes perhaps should be stated as a hypothesis. The writer regards it as physically necessary for an *exact* solution, but it might not be possible to satisfy it within the limitations imposed by the *approximation* of small perturbations; inasmuch as the latter assumption is made subsequently to the imposition of the mass condition in Eq. (2.3), such a shortcoming would be of no consequence in the following analysis. *Cf.* footnote following Eq. (4.3).

cylindrical surface $r = r_1$ lying in $x^* \leq x \leq 1$, and the annular area ($S_3$) bounded externally by $r = r_1$ and internally by the contour $C$ around the base of the body. The radius $r_1$ is to be determined by the requirement that the slender-body and asymptotic approximations exhibit an appropriate agreement [cf. sections (3) and (4)] on the circle defined by $x = x^*$ and $r = r_1$. That $S^*$ approaches a surface of revolution outside of $r = r_1$ follows from the axial symmetry of the far field [see Section (1)].

The drag on the body now can be calculated by a pressure-momentum survey over this surface. Replacing the pressure by the perturbation pressure (which, by definition, vanishes over $S^*$) *and thereby excluding the base drag from the calculation*, this survey yields

$$D + \iint_{S^*} \rho^* c^* (1 + \phi_x) w_n dS^* + \iint_{S_2} \rho_2 c^{*2} (1 + \phi_x) \phi_r dS_2 + \iint_{S_3} [(p_3 - p^*) + \rho_3 c^{*2} (1 + \phi_x)^2] dS_3 = 0 \quad (2.2)$$

where $w_n$ is the *total* (as opposed to *perturbation*) velocity component normal to $S^*$. Moreover, the net mass flux through this control surface must vanish, so that

$$\iint_{S^*} \rho^* w_n dS^* + \iint_{S_2} \rho_2 c^* \phi_r dS_2 + \iint_{S_3} \rho_3 c^* (1 + \phi_x) dS_3 = 0 \quad (2.3)$$

and Eq. (2.2) reduces to

$$D = - \iint_{S^*} \rho^* c^* \phi_x w_n dS^* - \iint_{S_2} \rho_2 c^{*2} \phi_x \phi_r dS_2 - \iint_{S_3} [(p_3 - p^*) + \rho_3 c^{*2} \phi_x (1 + \phi_x)] dS_3 \quad (2.4)$$

The integral (2.4) can be further simplified by invoking the small perturbation approximation. First, it may be noted that the requirement that the velocity be sonic on $S^*$ yields

$$(1 + \phi_x)^2 + \phi_r^2 + (1/r^2)\phi_\theta^2 = 1 \quad (2.5a)$$

whence (to the required approximation)†

$$\phi_x \doteq -(1/2)[\phi_r^2 + (1/r^2)\phi_\theta^2] \quad (2.5b)$$

Further, since the sonic surface is everywhere almost normal to the free stream [cf. Section (3)] and since $w_n$ multiplies a quantity that, by virtue of Eq. (2.5b), is already quadratic in the disturbance amplitude, $w_n$ may be replaced by its undisturbed value $c^*$, and the first integral in Eq. (2.4) may be approximated according to

$$- \iint_{S^*} \rho^* c^* \phi_x w_n dS^* \doteq \frac{1}{2} \rho^* c^{*2} \iint_{S^*} \left( \phi_r^2 + \frac{1}{r^2} \phi_\theta^2 \right) dS^* \quad (2.6)$$

In the second and third integrals in Eq. (2.4), $\rho_2$ and $\rho_3$ may be replaced by $\rho^*$ and the term in $\phi_x^2$ may be neglected compared with $\phi_x$ and $(p_3 - p^*)/\rho^* c^{*2}$, while the approximate Bernoulli equation yields

$$p_3 - p^* \doteq -\rho^* c^{*2} \{\phi_x + (1/2)[\phi_r^2 + (1/r^2)\phi_\theta^2]\} \quad (2.7)$$

Introducing these approximations in Eq. (2.4) and dividing by the free-stream dynamic pressure yields

$$\frac{D}{q} = \iint_{S^*} \left( \phi_r^2 + \frac{1}{r^2} \phi_\theta^2 \right) dS^* - 2 \iint_{S_2} \phi_r \phi_r dS_2 + \iint_{S_3} \left( \phi_r^2 + \frac{1}{r^2} \phi_\theta^2 \right) dS_3 \quad (2.8)$$

where

$$q = (1/2)\rho^* c^{*2} \quad (2.9)$$

The result [Eq. (2.8)] may be further simplified as follows. First, the asymptotic solution is axially symmetric over $S^*$, so that the term in $\phi_\theta^2$ can be dropped and the $\theta$ integration carried out; thus

$$\iint_{S^*} \left( \phi_r^2 + \frac{1}{r^2} \phi_\theta^2 \right) dS^* = 2\pi \int_{r_1}^{\infty} \phi_r^2 \Big|_{r = r^*(x)} r^* dr^* \quad (2.10)$$

Secondly, if $\phi_x$ and $\phi_r$ are substituted from Eq. (1.2) in the second integral (since, by hypothesis, slender-body theory is valid inside the sonic surface) and $r_1$ assumed sufficiently large, only the axially symmetric terms contribute to the end result, which reads

$$\begin{aligned} \iint_{S_2} \phi_x \phi_r dS_2 &= \int_{x^*}^{1} dx \int_0^{2\pi} (\phi_x \phi_r)_{r = r_1} r_1 d\theta \\ &= 2\pi \int_{x^*}^{1} [a_0'(x) \ln r_1 + b_0'(x)] a_0(x) dx - \pi \sum_{n=1}^{\infty} n r_1^{-n} |a_n|^2 \Big|_{x^*}^{1} \\ &= 2\pi \int_{x^*}^{1} a_0(x) b_0'(x) dx + \pi [a_0^2(1) - a_0^2(x^*)] \ln r_1 + 0(r_1^{-1}) \end{aligned} \quad (2.11)$$

† This result also could be inferred from Bernoulli's equation and the requirement $p = p^*$ on $S^*$; cf. Eq. (2.7) infra.

Thirdly, since $\phi$ satisfies Laplace's equation on $S_3$, the third integral in Eq. (2.8) can be transformed into a line integral with the aid of Green's theorem—viz.,

$$\iint_{S_3} \left(\phi_r^2 + \frac{1}{r^2}\phi_\theta^2\right) dS_3 = \int_0^{2\pi} (\phi\phi_r)_{r=r_1} r_1 d\theta - \int_C (\phi\phi_n)_{x=1} dl = 2\pi a_0(1)[a_0(1) \ln r_1 + b_0(1)] - \int_C (\phi\phi_n)_{x=1} dl \tag{2.12}$$

where $n$ denotes the outwardly drawn normal to the base contour $C$ and $dl$ an element of arc on this contour (which is to be traversed counterclockwise). Substituting Eqs. (2.10)–(2.12) in Eq. (2.8) yields

$$\frac{D}{q} = 2\pi \int_{r_1}^{\infty} v^{*2} r dr + 2\pi a^2(x^*) \ln r_1 - 4\pi \int_{x^*}^{1} a_0(x) b_0'(x) dx + 2\pi a_0(1) b_0(1) - \int_C (\phi\phi_n)_{x=1} dl \tag{2.13}$$

where $v^*$ stands for $(\phi_r)_{r=r^*}$.

The result [Eq. (2.13)] can be further simplified for various special cases. Perhaps the most important of these is defined by the requirement that the last integral vanish. This will be the case if either (cf. reference 3, p. 83): (a) the body is pointed at the base ($x = 1$) or (b) the body has a cylindrical surface at the base, the generators of which are parallel to the free stream. If either of these conditions is satisfied each of the last two terms in Eq. (2.13) vanish, and the result reduces to

$$\frac{D}{q} = 2\pi \int_{r_1}^{\infty} v^{*2} r dr + 2\pi a^2(x^*) \ln r_1 - 4\pi \int_{x^*}^{1} a_0(x) b_0'(x) dx \tag{2.14}$$

Then, since both $a_0$ and $b_0$ depend only on the distribution of transverse area $S$, the transonic drag of a slender body satisfying (a) or (b) may be calculated for an equivalent body of revolution—i.e., one having the same distribution of $S(x)$.

If the body is axially symmetric (so that $\phi_n = R'$ on the body) but does not satisfy either (a) or (b) above, the line integral may be evaluated according to

$$\int_C (\phi\phi_n)_{x=1} dl = \int_0^{2\pi} (\phi R' R)_{z=1} d\theta = 2\pi a_0(1)[a_0(1) \ln R(1) + b_0(1)] \tag{2.15}$$

and Eq. (2.13) reduces to

$$\frac{D}{q} = 2\pi \int_{r_1}^{\infty} v^{*2} r dr + 2\pi[a_0^2(x^*) \ln r_1 - a_0^2(1) \ln R(1)] - 4\pi \int_{x^*}^{1} a_0(x) b_0'(x) dx \tag{2.16}$$

This result evidently includes Eq. (2.14) as a special case ($a_0(1) = 0$).

If $x^* = 1$—i.e., if the sonic surface meets the body at the base—or, alternatively, if only that part of the drag acting forward of the sonic line is calculated, $S_3$ coincides with $S^*$ along $r = r_1$, $x^* = 1$, and $S_2$ vanishes. If it is further assumed that the body is axially symmetric Eq. (2.8) then reduces to

$$\frac{D}{q} = 2\pi \int_{R(1)}^{\infty} v^{*2} r dr \tag{2.17}$$

It should be remarked that the slender-body approximation (as contrasted with the small perturbation approximation) has not yet been invoked in this last result.

## (3) Solution Near Body

The subsequent analysis will be restricted to bodies of revolution *or to bodies that can be treated as such in the calculation of total drag.* Then the slender-body solution [Eq. (1.2)] reduces to

$$\phi = a(x) \ln r + b(x) \tag{3.1}$$

where the zero subscripts on $a$ and $b$ have been dropped. The corresponding perturbation velocity components are

$$u = \phi_x = a'(x) \ln r + b'(x) \tag{3.2}$$

$$v = \phi_r = a(x) r^{-1} \tag{3.3}$$

These are assumed to be valid for $r < r^*$, where $r^*(x)$ specifies the sonic line.

The unknown function $b'$ now may be determined by the requirement that, in the present approximation, $u$ must vanish along the sonic line, whence Eq. (3.2) yields

$$b'(x) = -a'(x) \ln [r^*(x)] \tag{3.4}$$

Substituting this result in the last integral in Eq. (2.16) and integrating by parts then yields

$$\left.\begin{aligned} -\int_{x^*}^{1} ab' dx &= \int_{x^*}^{1} aa' \ln r^* dx \\ &= \frac{1}{2}[a^2(1) \ln r^*(1) - \\ &\quad a^2(x^*) \ln r_1] - \frac{1}{2}\int_{x^*}^{1} a^2 \frac{r^{*\prime}}{r^*} dx \end{aligned}\right\} \tag{3.5}$$

Substituting Eq. (3.5) in Eq. (2.16) then reduces the drag integral to

$$\frac{D}{2\pi q} = \int_{r_1}^{\infty} v^{*2} r dr - \int_{x^*}^{1} a^2 \frac{r^{*\prime}}{r^*} dx + a^2(1) \ln [r^*(1)/R(1)] \tag{3.6}$$

It might be thought that the foregoing calculation of $b'(x)$ could be improved by iteration—viz., substituting the solution $u = a' \ln (r/r^*)$ in the nonlinear term on the right-hand side of Eq. (4.1) and integrating the result subject to the boundary conditions that $\phi_r$ behave like $ar^{-1}$ as $r \to 0$ and that $\phi_x$ vanish at $r = r^*$, etc. However, an investigation of this process reveals that it is not necessarily convergent, so that it will not be attempted here. (A similar procedure has been applied to a cone with *attached* shock by Cole and Solomon,[8] the "distant" boundary condition being applied at the shock. In this application the results are favorable, as evidenced by comparison with the known, exact result.)

## (4) Asymptotic Solution

The differential equation satisfied by the dimensionless, perturbation velocity potential produced by a slender body of revolution in an otherwise uniform free stream of Mach Number unity is

$$\phi_{rr} + (1/r)\phi_r = (\gamma + 1)\phi_x\phi_{xx} \tag{4.1}$$

where $\gamma$ is the usual specific heat ratio. Guderley and Yoshihara[4] have shown that an appropriate solution to this equation at large distances (either radial or axial, but only forward of the limiting Mach wave) from the body is given by

$$\phi = r^{3n-2}f(\zeta) \tag{4.2}$$

where

$$\zeta = (\gamma + 1)^{-1/3}\, x\, r^{-n} \tag{4.3a}$$

$$(n^2\zeta^2 - f')f'' - n(5n - 4)\zeta f' + (3n - 2)^2 f = 0 \tag{4.3b}$$

On considering the behavior of this solution in the neighborhood of the singularities of the differential equation [Eq. (4.3b)], they conclude that the parameter $n$ must have the (approximate) value $4/7$ if the solution is to be physically admissible.†

In order to generalize the solution [Eq. (4.2)], the transformations under which Eq. (4.1) is invariant may be considered. Two such transformations are translation of $x$ and a scale transformation of $\phi$ and $r$—viz.,‡

$$x = x' + \xi \tag{4.4}$$

$$\phi = \lambda\phi', \quad r = \lambda^{-1/2}r' \tag{4.5}$$

While there exist other transformations under which Eq. (4.1) remains invariant, a two-parametric generalization of the similarity solution (4.2) evidently is the most general possible, and Eqs. (4.4) and (4.5) therefore are sufficient for the required extension. In the actual application of the scale transformation, however, it is convenient to replace $\lambda$ by $\lambda^{2/3n}$, whence the generalized, asymptotic solution reads

$$\phi \sim \lambda r^{3n-2}f(\zeta) \tag{4.6}$$

$$\zeta = \lambda^{-1/3}(\gamma + 1)^{-1/3}(x - \xi)r^{-n} \tag{4.7}$$

In the evaluation of the drag integral of Eq. (3.6), all that is required is the evaluation of the $r$ derivative of Eq. (4.6) along the sonic line (surface) and the location of this surface. The latter is specified (in first approximation) by $\phi_x = 0$ or, equivalently,

$$f'(\zeta^*) = 0 \tag{4.8}$$

whence, from Eq. (4.7),

$$r^*(x) = [(x - \xi)/(\gamma + 1)^{1/3}\lambda^{1/3}\zeta^*]^{1/n} \tag{4.9}$$

Evaluating $\phi_r$ at $\zeta^*$ and invoking Eq. (4.8) gives

$$v^* \sim (3n - 2)\lambda f^* r^{3n-3} \tag{4.10}$$

where $f^*$ stands for $f(\zeta^*)$.

In order that the asymptotic solution agree with the slender-body approximation at $r = r_1$, it is required (insofar as the evaluation of the drag integral is concerned) that both $r^*$ and $v^*$ be continuous there, whence

$$x^* = \xi + (\gamma + 1)^{1/3}\lambda^{1/3}\zeta^* r_1^{\,n} \tag{4.11}$$

$$a^* r_1^{-1} = (3n - 2)\lambda f^* r_1^{3n-3} \tag{4.12}$$

Solving these equations for $\lambda$ and $r_1$ yields

$$r_1 = \{[(3n - 2)f^*]/[(\gamma + 1)a^*]\}^{1/2}[(x^* - \xi)/\zeta^*]^{3/2} \tag{4.13}$$

$$\lambda = (\gamma + 1)^{-1}[(x^* - \xi)/\zeta^*]^3\, r_1^{-3n} \tag{4.14}$$

In the evaluation of the drag integral (3.6), it is convenient to write $v^*$ in the form [substituting Eqs. (4.13) and (4.14) in Eq. (4.10)]

$$v^* \sim a^* r_1^{-1}(r/r_1)^{3n-3} \tag{4.15}$$

where $a^*$ stands for $a(x^*)$. Substituting this expression in the first integral in Eq. (3.6) yields

$$\int_{r_1}^{\infty} v^{*2} r dr = (4 - 6n)^{-1} a^{*2} = \frac{7}{4}\, a^{*2} \tag{4.16}$$

The second integral in Eq. (3.6) simplifies to

$$\int_{x^*}^{1} a^2\, \frac{r^{*\prime}}{r^*}\, dx = n^{-1} \int_{x^*}^{1} \frac{a^2 dx}{(x - \xi)} = \frac{7}{4} \int_{x^*}^{1} \frac{a^2 dx}{(x - \xi)} \tag{4.17}$$

upon substitution of Eq. (4.9).

In the reduction of the third term in Eq. (3.6), it is convenient to write, using Eqs. (4.9) and (4.13) and setting $n = 4/7$,

† Professor Cole has pointed out that this choice of $n$ actually leads to a divergent integral for the total mass flux through a surface that tends to infinity. This shortcoming is not believed to be serious in the present application in virtue of the imposition of Eq. (2.3) in the formulation of the drag integral. The remaining integrals, being quadratic in the perturbation velocity components, converge in a satisfactory manner; see, e.g., Eq. (4.16) infra.

‡ The referee has pointed out that the transformations (4.4) and (4.5) follow directly from the transonic similarity law.

$$r^{*2}(1) = r_1^2[(1-\xi)/(x^* - \xi)]^{2/n} = C(\gamma + 1)^{-1}a^{*-1}(x^* - \xi)^{-1/2}(1-\xi)^{7/2} \quad (4.18)$$

where the parameter $C$ is defined by

$$C = (3n - 2)f^*\zeta^{*-3} = -(2/7)f^*\zeta^{*-3} \quad (4.19)$$

and is determined entirely by the asymptotic solution to the differential equation, subject to the condition (4.8). From reference 5, it is found that

$$\zeta^* = 0.7513$$
$$f^* = -2.651$$
$$C = 1.786$$

Substituting the results (4.16)–(4.18) in Eq. (3.6) yields

$$\frac{D}{q} = \frac{7\pi}{2}\left[a^{*2} - \int_{x^*}^{1} \frac{a^2(x)dx}{(x - \xi)}\right] + \pi a^2(1) \ln\left[\frac{C(x^* - \xi)^{-1/2}(1 - \xi)^{7/2}}{(\gamma + 1)a^*R^2(1)}\right] \quad (4.20)$$

It remains to determine the parameters $x^*$ and $\xi$, locating the sonic point on the body and the *apparent* position of the singularity that represents the asymptotic solution. Indeed, for the special class of bodies defined by $a(1) = 0$ these parameters contain *all* of the information required from the asymptotic solution except for the value of the exponent $n$, which is the only parameter that has been introduced from the asymptotic solution in the first two terms in Eq. (4.20).

## (5) Bodies of Revolution with Sharp Shoulders

If a body possesses a sharp shoulder (discontinuity in the slope of the curve intercepted by a meridian section) the sonic point must be located there,[5, 6] and, in the immediate neighborhood of the shoulder, the transition to supersonic flow will take place through an expansion fan of the Prandtl-Meyer type. Moreover, the limiting Mach wave (the flow downstream of which can have no effect on the subsonic flow) also must intersect the body at the shoulder. A discontinuity such as that presented by a sharp shoulder evidently is not compatible with the slender-body approximation, but this shortcoming is not crucial in that the flow downstream of the limiting Mach wave may be determined by the method of characteristics, utilizing the fact that the flow is locally of a Prandtl-Meyer type to start the solution from the shoulder. The present section will be devoted to the determination of the ("head") drag on that part of the body forward of the shoulder.

The formula for the head drag can be obtained by setting $x^* = 1$ in Eq. (4.20):

$$D = \pi q a^{*2}(\ln\{[C(x^* - \xi)^3]/[(\gamma + 1)a^*R^{*2}]\} + (7/2)) \quad (5.1)$$

Since $a^*$ (if not rendered dimensionless) has the dimensions of a length, this result is dimensionally correct as it stands and need not be referred to a particular characteristic length. It is for this reason that $x^*$ has not actually been replaced by 1 in Eq. (5.1).

It remains to determine the parameter $\xi$. On the basis of the asymptotic behavior of an aggregate of sources in linearized, potential theory, it appears reasonable to choose $\xi$ as the centroid of the subsonic portion of the linear source distribution at the body. (Sources aft of the limiting Mach wave are not included in the calculation since, by definition, they cannot influence the subsonic flow. In this connection, it should be recalled that Guderley and Yoshihara's asymptotic solution represents only the flow upstream of the limiting Mach wave.) Adopting this hypothesis,

$$\xi = \int_0^{x^*} xa\,dx \Big/ \int_0^{x^*} a\,dx \quad (5.2)$$

Substituting $a$ from Eq. (1.3), carrying out the integration in the denominator, and integrating the numerator by parts yields

$$\xi = x^* - (V^*/S^*) \quad (5.3)$$

where $V^*$ denotes the volume of that part of the body forward of the sonic point and $S^*$ denotes the cross section at this point. Substituting Eq. (5.3) in Eq. (5.1) and also substituting the numerical value of $C$ from Section (4) yields

$$D = \pi q a^{*2}\left\{\ln\left[\frac{1}{(\gamma + 1)a^*R^{*2}}\right] + 3\ln\left(\frac{V^*}{S^*}\right) + 4.080\right\} \quad (5.4)$$

In the special case of a conical head of semi-apex angle† $\delta$ and unit length ($x^* = 1$) $a^* = \delta^2$ and $(V^*/S^*) = 1/3$; substituting these values, together with $\gamma = 1.4$, in Eq. (5.4) yields the drag coefficient (referred to the base area)

$$C_D = D/(\pi\delta^2 q) = \delta^2[4 \ln(1/\delta) - 0.091] \quad (5.5)$$

For a cone having a semi-apex angle of 5° ($\delta = 5/57.3$), Eq. (5.5) gives $C_D = 0.074$, which is to be compared with the value of 0.076 obtained by Yoshihara (Simpson's rule integration of Fig. 7, reference 9) on the basis of numerical integration of the nonlinear transonic equation [Eq. (4.1)].

In order to extend the result (5.4) to free-stream Mach Numbers close to unity, Liepmann and Bryson's result that[5]

$$\frac{\partial}{\partial(M^2 - 1)}\left(\frac{p - p_0}{q}\right)\Bigg|_{M=1} = \frac{2}{(\gamma + 1)} \quad (5.6)$$

where $q$ and $M$ are the free-stream dynamic pressure and Mach Number, respectively, may be applied.‡

† Note that in this example $\delta$ is one-half the usual "fineness ratio"; in Section (6) $\delta$ is the fineness ratio.

‡ The result (5.6) also may be regarded as arising from the sonic line condition $U^2[(1 + u)^2 + v^2] = c^{*2}$. In first approximation, this implies $u^* = (1 - M^2)/(\gamma + 1)M^2$, which leads to Eq. (5.6) in the neighborhood of $M = 1$. It also should be remarked that Eq. (5.6) is not applicable to a body having a contracting cross section.

Since Eq. (5.6) implies a constant pressure increment over the body due to small changes in free-stream Mach Number, it applies directly to the drag coefficient. It follows that, if $C_{D_0}$ denotes the sonic free-stream result,

$$C_D \doteq C_{D_0} + 2[(M^2 - 1)/(\gamma + 1)] \tag{5.7}$$

for sufficiently small $|M^2 - 1|$. It should be emphasized that $C_D$ is referred to the actual $q$ and not (except at $M = 1$) the special value given by Eq. (2.9).

It is of interest to cast the result (5.7) in similarity form. Toward this end, let $R^*$ be replaced by $\delta$ and write

$$a(x) = \delta^2 \bar{a}(x) \tag{5.8}$$

$$k = (M^2 - 1)/(\gamma + 1)\delta^2 \tag{5.9}$$

$$\bar{C}_D = C_D/\delta^2 = D/\pi\delta^4 q \tag{5.10}$$

Substituting these in Eqs. (5.1) and (5.7) yields

$$\bar{C}_D = \bar{a}^{*2}\left\{\ln\left[\frac{1}{(\gamma + 1)\delta^4}\right] + \ln\left[\frac{C(x^* - \xi)^3}{\bar{a}^*}\right] + \frac{7}{2}\right\} + 2k \tag{5.11}$$

Transposing the first term on the right yields

$$\bar{C}_D + \bar{a}^{*2}\ln[(\gamma + 1)\delta^4] = \bar{a}^{*2}(\ln\{[C(x^* - \xi)^3/\bar{a}^*]\} + (7/2)) + 2k \tag{5.12}$$

Since $\bar{a}^*$, $x^*$, and $\xi$ remain invariant under a scale change, the right-hand side of Eq. (5.12) depends only on the transonic similarity parameter $k$ for a given geometry, and the result satisfies† the general similarity rule derived by Oswatitsch and Berndt.[10] Moreover, Eq. (5.12) may be regarded as giving the first two terms in a power series in $k$ and therefore would appear to be valid only if $k << 1$ ($|M^2 - 1| << \delta^2$) rather than for the less restrictive inequality $|M^2 - 1| << 1$.

## (6) Smooth Closed Bodies

The bodies of principal interest in aeronautical (as opposed to ballistic) application are smooth (and therefore do not possess sharp shoulders) and are "closed" in the sense that $a(1) = 0$, so that Eq. (4.20) reduces to

$$D = \frac{\pi}{2} q\left[a^{*2} - \int_{x^*}^{1} \frac{a^2(x)dx}{(x - \xi)}\right] \tag{6.1}$$

It should be recalled that this result, unlike Eq. (5.1), is not restricted to a body of revolution.

In order to approximate $x^*$ it may be observed that in the neighborhood of the sonic point $(x^*, r^*)$ $u$ has the form [cf. Eqs. (3.2) and (3.4)]

$$u = a'(x) \ln [r/r^*(x)] \tag{6.2}$$

Then, at the sonic point,

$$u_x\big|_{x=x^*,\ r=r^*} = -a'(x^*)\{[r^{*\prime}(x)]/[r^*(x)]\} \tag{6.3}$$

Now it may be inferred from Eqs. (4.9), (4.12), and (4.14) that, if $\delta$ is the fineness ratio of the body, so that $a^* = 0(\delta^2)$, $r^*(x)$ is $0(\delta^{-1})$ except very close to $x = x^*$, where $r^* = 0(\delta)$; moreover, $r^{*\prime}$ must be $0(\delta^{-1})$ everywhere. It follows that in the neighborhood of $x = x^*$ on the body $u_x$ exceeds its values elsewhere along the body by a factor of $0(\delta^{-2})$, unless $a'(x^*)$ is very small (compared with its values elsewhere) there. On the other hand, an examination of experimental data, as well as physical intuition, gives no reason to suppose that $u_x$ does experience such an order of magnitude of increase near the sonic point (even though it may be very large in the expansion zone following the sonic point or in the neighborhood of the shock closing this expansion zone) of a smooth body. Accordingly, within the slender-body approximation, it appears that a *necessary* condition at the sonic point on the body is‡

$$a'(x^*) = 0 \tag{6.4}$$

In general, it may be expected that the sonic point on a smooth body will be located at the most upstream point at which Eq. (6.4) is satisfied, but, if this point is too close to the nose (where there is a stagnation point) and another such point exists further downstream, the latter may be the sonic point; moreover, it is conceivable that the initial conditions and associated transient flow may be important in determining the sonic point among two or more possibilities (cf.—e.g., a one-dimensional nozzle with two or more throats). Again, if the body has a sharp shoulder, the sonic point usually would be located there, although this might not be true if Eq. (6.4) were satisfied sufficiently downstream of the nose but sufficiently upstream of the shoulder, and it almost certainly would not be true if the shoulder were downstream of the maximum cross section. (But, in any event, the sonic point could never be located downstream of a sharp shoulder.)

The source location parameter $\xi$ may be assumed to be at the linear source centroid, but $x^*$ must be re-

† In a previous note[11] it was found that this law was violated (with respect to variations of $\gamma$) when it was assumed that the sonic surface intersected the upstream body surface normally. While this certainly must be true if the flow is to be locally Prandtl-Meyer, Professor Cole has advanced the criticism that "normal to the body" and "normal to the axis" cannot be distinguished in the slender-body approximation. This argument carries considerable force, and it is difficult, on the one hand, to justify the assumption in any consistent manner, or, on the other hand, to understand the excellent agreement with Yoshihara's more exact analysis of a cone-cylinder. However, since the approximation in question did not satisfy the usual transonic similarity law with respect to variations of the specific heat ratio $\gamma$, it is at least open to question, and it may be that the agreement with Yoshihara's result is largely fortuitous. (But it may be remarked that the slender-body, transonic similarity law is not completely consistent with a Prandtl-Meyer expansion at the shoulder, and the essence of the question is the importance of the detailed nature of the flow near the shoulder as compared with the simple requirement that the velocity must be sonic there.)

‡ This condition was suggested to the writer by both J. D. Cole and E. W. Graham, after which the above argument suggested itself.

placed by $x_l$, the intersection of the limiting Mach wave with the body, in both Eqs. (5.2) and (5.3)—viz.,

$$\xi = \int_0^{x_l} x a dx \Big/ \int_0^{x_l} a dx = x_l - (V_l/S_l) \quad (6.5)$$

While it appears that the sonic point may be located without ambiguity by Eq. (6.4) for a large class of smooth bodies, the location of the intersection of the limiting Mach wave with the body offers greater difficulty, and the only thing that may be said with certainty is $x_l > x^*$. It is highly improbable, however, that $x_l$ could be downstream of the maximum cross section or even that it could be very far downstream of the sonic point on a slender body. The approximation adopted here will be $x_l = x^*$, but this must be regarded as much less reliable than the location of $x^*$ itself.

In connection with the approximation $x_l = x^*$, it may be deduced from Eqs. (6.1) and (6.5) that

$$\partial D/\partial x_l < 0 \quad \text{if} \quad S'(x_l) > 0 \quad (6.6)$$

It then follows, in virtue of the conclusions of the preceding paragraph (that $x_l$ lies between $x^*$ and the maximum cross section), that the approximation to the drag based on $x_l = x^*$ must be an upper bound to the value that would be obtained from Eqs. (6.1) and (6.5) on the basis of a more precise value of $x_l$.

The drag integral (6.1) can be placed in the alternative form

$$D = \frac{7\pi}{2} q \int_0^1 g(x) \frac{da^2(x)}{dx} dx \quad (6.7)$$

where

$$\begin{aligned} g(x) &= 1, && 0 \leq x < x^* \\ &= \ln [(x - \xi)/(x^* - \xi)], && x^* < x \leq 1 \end{aligned} \quad (6.8)$$

This result may be derived by integrating the second term of Eq. (6.1) by parts [using $a(1) = 0$] and replacing $a^{*2}$ by the integral of $(da^2/dx)$ between 0 and $x^*$. Still a third form is

$$D = \frac{7\pi}{2} q \int_{x^*}^1 \left[ \ln \left( \frac{x - \xi}{x^* - \xi} \right) - 1 \right] \frac{da^2(x)}{dx} dx \quad (6.9)$$

which follows from Eq. (6.7) in consequence of the requirement

$$\int_0^1 \frac{da^2}{dx} dx = a^2 \Big|_0^1 = 0 \quad (6.10)$$

As an example, consider a Kármán ogive[12] of base *diameter* $\delta$, for which (cf. Fig. 11, reference 12)

$$a_1(x) = (\delta^2/\pi) x^{1/2} (1 - x)^{1/2} \quad (6.11)$$

Setting $a'(x^*) = 0$ yields $x^* = 1/2$, and Eq. (6.5) gives $\xi = \{(1/2) - [2/(3\pi)]\}$ if $x_l$ is equated to $x^*$. Substituting these data in Eq. (6.1) and carrying out the integration yields

$$D_1 = q(\pi\delta^2/4)(0.029\delta^2) \quad (6.12)$$

The corresponding drag coefficient, referred to the base area $(\pi\delta^2/4)$, is $0.029\delta^2$, which is to be compared with the supersonic $(M^2 - 1 >> \delta^2)$ value $\delta^2$.[12]

As a second example, consider (cf. Fig. 12, reference 12) the parabolic *source* (not radius) distribution (normalized to base diameter $\delta$).

$$a_2(x) = (3/4)\delta^2 x(1 - x) \quad (6.13)$$

which is perhaps the simplest distribution satisfying $a(0) = a(1) = 0$. The corresponding values of $x^*$ and $\xi$ (assuming $x_l = x^*$) are $1/2$ and $5/16$, respectively, and the drag given by Eq. (6.1) is

$$D_2 = q(\pi\delta^2/4)(0.073\delta^2) \quad (6.14)$$

or approximately two and one-half times the drag on a Kármán ogive of the same base area. The supersonic drag coefficient corresponding to Eq. (6.13) is $1.125\ \delta^2$.

It appears from these two examples that the sonic drag on a smooth, "closed", expanding body is only a very small fraction of the supersonic drag. This is in marked contrast with the result for a sharp shouldered body, where the sonic drag is of the same order of magnitude as the supersonic drag [cf. Section (5), particularly Eq. (5.5)].

No examples will be given of bodies that have diminishing cross sections, although it is not difficult to find such bodies for which Eq. (6.1) predicts a negative drag. This is doubtless a result of the inadequacy of the approximation (3.4), which then must be regarded as unsatisfactory due to the fact that the distance of the sonic line form the body, measured in body radii, increases rapidly as the body cross section converges. Since the flow aft of the maximum cross section is purely supersonic and does not influence the subsonic flow, it could be computed alternatively by the method of characteristics. Even so, it may be questioned whether the result would be in sufficient accord with reality, since the overexpansion of the flow (in becoming supersonic) may lead to a shock somewhere on the rear part of the body.

## (7) Résumé of Results

On the basis of an approximate joining of the linearized[3] and asymptotic[4] solutions for the flow past a slender body of revolution in an otherwise undisturbed stream (along the $x$ axis) of sonic velocity, it is found that the drag is given by

$$D = \frac{7\pi}{2} q \left[ a^{*2} - \int_{x^*}^1 \frac{a^2 dx}{(x - \xi)} \right] + \pi q a^2(1) \ln \left[ \frac{1.786(x^* - \xi)^{-1/2}(1 - \xi)^{7/2}}{(\gamma + 1) a^* R^2(1)} \right] \quad (4.20)$$

where, in terms of the cross-sectional distribution $S(x)$,

$$a(x) = [1/(2\pi)] S'(x) \quad (1.3)$$

$x^*$ is the location of the sonic point on the body, $a^*$ is $a(x^*)$, $\xi$ is defined by

$$\xi = \int_0^{x_l} xadx \Big/ \int_0^{x_l} adx = x_l - (V_l/S_l) \quad (6.5)$$

$x_l$ denotes the intersection of the limiting Mach wave with the body, $S_l$ the cross section at $x_l$, $V_l$ the volume of that part of the body upstream of $x_l$, $R$ the body radius, $q$ the free-stream dynamic pressure, and $\gamma$ the usual specific heat ratio. All lengths are referred to the body length, so that the latter appears as unity in Eq. (4.20).

If the body possesses a sharp shoulder, then the sonic point ($x^*$) and limiting Mach wave intersection ($x_l$) must coincide there, and Eq. (4.20) gives for the drag forward of this shoulder

$$D = \pi q a^{*2}(\ln \{[1.786(x^* - \xi)^3]/[(\gamma + 1)a^* R^{*2}]\} + (7/2)) \quad (5.1)$$

where $\xi$ is obtained by equating $x_l$ to $x^*$ in Eq. (6.5). In this result, which is dimensionally correct as it stands, lengths are not necessarily referred to the body length.

As evidenced by comparison with the result of a more accurate analysis of a cone-cylinder,[9] it appears that the result (5.1) may be expected to furnish a reliable estimate of the sonic drag on that part of a body forward of a sharp shoulder. Moreover, if $C_{D_0}$ denotes the sonic drag coefficient corresponding to Eq. (5.1), the drag coefficient at Mach Numbers close to 1 (such that $|M^2 - 1| << R^2$) is given by[6]

$$C_D = C_{D_0} + 2[(M^2 - 1)/(\gamma + 1)] \quad (5.7)$$

The flow downstream of the shoulder may be constructed by the method of characteristics, taking advantage of the fact that the flow at the shoulder is locally of a Prandtl-Meyer type.

If the body is smooth (i.e., $R$, $R'$, and $R''$ continuous in $0 < x < 1$) and is "closed" in the sense that $S'(1) = 0$, Eq. (4.20) reduces to

$$D = \frac{7\pi}{2} q \left[ a^{*2} - \int_{x^*}^1 \frac{a^2(x)dx}{(z - \xi)} \right] \quad (6.1)$$

and the sonic point is located approximately at the point of maximum source strength—viz.,

$$2\pi a'(x^*) = S''(x^*) = 0 \quad (6.4)$$

*The results [Eqs. (6.1) and (6.4)] are valid for all slender bodies for which $S'(1) = 0$,* since then the drag depends only on the cross-sectional distribution—i.e., on $a(x)$. Unfortunately, it is no longer true that $x_l = x^*$, but this approximation (in lieu of information leading to a more precise value of $x_l$) does furnish an upper bound to the true value of the drag.

It is suggested that Eq. (6.1) *may* furnish a reasonable estimate of the drag on an expanding body terminating in a cylindrical section ($R' = 0$), although verification must await comparison with experiment (or more reliable theory). In any event, it appears unlikely that it could be valid for the drag on the contracting portion of a body in consequence of the probable failure of the linearized theory at the very large distances from the body implied in the approximation of Section (3) [in particular, Eq. (3.4)].

## References


[1] Miles, J. W., *Linearization of the Equations of Non-steady Flow in a Compressible Fluid*, Journal of Mathematics and Physics, Vol. 33, No. 2, pp. 135–143, July, 1954.

[2] Miles, J. W., *On Linearized Theory*, Journal of the Aeronautical Sciences, Vol. 20, No. 1, p. 64, January, 1953.

[3] Ward, G. N., *Supersonic Flow Past Slender Pointed Bodies*, Quarterly Journal of Mechanics and Applied Mathematics, Vol. 2, Part 1, pp. 75–97, March, 1949.

[4] Guderley, G., and Yoshihara, H., *An Axial-Symmetric Transonic Flow Pattern*, Quarterly of Applied Mathematics, Vol. 4, No. 4, pp. 333–339, April, 1951.

[5] Guderley, G., and Yoshihara, H., *Axial-Symmetric Transonic Flow Patterns*, AF Tech. Rep. 5797, USAF AMC, Dayton, Ohio, 1949.

[6] Liepmann, H. W., and Bryson, A. E., *Transonic Flow Past Wedge Sections*, Journal of the Aeronautical Sciences, Vol. 17, No. 12, pp. 745–755, December, 1950.

[7] Guderley, G., *Axial-Symmetric Flow Patterns at a Free Stream Mach Number Close to One*, AF Tech. Rep. 6285, USAF AMC, Dayton, Ohio, 1952.

[8] Solomon, G. E., *Transonic Flow Past Cone-Cylinders*, Thesis, Calif. Inst. of Tech., 1953; Cole, J. D., Solomon, G. E., and Wilmarth, W. W., *Transonic Flow Past Simple Bodies*, Journal of the Aeronautical Sciences, Vol. 20, No. 9, pp. 627–634, September, 1953.

[9] Yoshihara, H., *On the Flow Over a Cone-Cylinder Body at Mach Number One*, WADC Tech. Rep. 52-295, Dayton, Ohio, 1952.

[10] Oswatitsch, K., and Berndt, S., *Aerodynamic Similarity of Axisymmetric Transonic Flow around Slender Bodies*, KTH-Aero TN 15, Stockholm, 1950.

[11] Miles, J. W., *On the Transonic Drag of a Cone-Cylinder*, Journal of the Aeronautical Sciences, Vol. 20, No. 9, pp. 651–652, September, 1953.

[12] von Kármán, Th., *The Problem of Resistance in Compressible Fluids*, Reale Accademia D'Italia, Vol. 14, pp. 5–59, 1936; Proc. Fifth Volta Congress, 1935.

# Response Matrix Method of Rotor Blade Analysis

ALEX BERMAN*

*The Kaman Aircraft Corporation*

SUMMARY

A method of rotor blade analysis is presented which permits the calculation of the blade response—i.e., bending moment, curvature, slope, deflection—for any loading and harmonic without repeating solutions of the differential equation. The response is calculated by post-multiplying the appropriate "response matrix" by a column matrix representing the rigid blade load distribution. The response matrices for the zeroth harmonic are calculated directly by tabular means, and an approximate method for obtaining these matrices for any higher harmonic is developed using the natural frequencies and modes of the rotating beam. These frequencies and modes are themselves obtained using the response matrices for the zeroth harmonic which yield a secular equation in the natural frequencies.

SYMBOLS

$b_{n\eta}$ = loading coefficient, defined Eq. (14)
$b_{k\eta}$ = modal loading coefficient, defined Eq. (28)
det. = determinant of
$k$ = order of mode
$m$ = mass per unit length
$n$ = order of harmonic
$q_{n\eta k}$ = modal amplitude, defined Eq. (39)
$r$ = blade spanwise stations
$A$ = centrifugal shear coefficient, $\int_r^R mrdr$
$EI$ = bending rigidity
$H$ = number of spanwise intervals
$Im$ = imaginary part of
$L$ = rigid blade loading
$L_n$ = $n$th harmonic of rigid blade loading
$M_{nr}$ = $n$th harmonic bending moment at station $r_r$
$R$ = blade radius
$Re$ = real part of
$Z$ = blade deflection from plane of rotation
$Z_n$ = $n$th harmonic blade deflection
$Z_{n\eta}$ = $n$th harmonic blade deflection under loading of $\lambda_\eta$, defined Eq. (16)
$\mathfrak{L}_n$ = differential operator, Eq. (11)
$\boldsymbol{B}_k$ = modal loading matrix, Eq. (34)
$\boldsymbol{B}_n$ = loading matrix, defined Eqs. (26)
$\boldsymbol{I}$ = unit matrix
$\boldsymbol{M}_n$ = bending moment matrix, defined Eqs. (26)
$\boldsymbol{P}_n$ = deflection response matrix, defined Eqs. (26)
$\boldsymbol{P}_n'$ = slope response matrix, defined Eqs. (27)
$\boldsymbol{P}_n''$ = curvature response matrix, defined Eqs. (27)
$\boldsymbol{Q}_n$ = bending moment response matrix, defined Eqs. (27)
$\boldsymbol{R}_n$ = matrix, defined Eq. (34)
$\boldsymbol{Z}_n$ = deflection matrix, defined Eqs. (26)
$\boldsymbol{Z}_n'$ = slope matrix, defined Eqs. (26)
$\boldsymbol{Z}_n''$ = curvature matrix, defined Eqs. (26)
$\beta_b$ = built-in coning angle
$\Delta$ = discontinuity
$\eta$ = subscript referring to loading of $\lambda_\eta$
$\Theta$ = average aerodynamic damping coefficient, $-(1/2)\rho a_0 cr$
$\lambda_\eta$ = standard loading function, defined Eq. (15)
$\nu$ = subscript referring to spanwise station
$\xi$ = spanwise station of built-in coning angle
$\sigma_k$ = damping coefficient, defined Eq. (45)
$\phi_k$ = $k$th mode of rotating beam
$\psi$ = azimuth angle
$\omega_k$ = natural frequency of rotating beam
$\Omega$ = rotor angular velocity

Presented at the Helicopter Dynamics Session, Twenty-Third Annual Meeting, IAS, New York, January 24–27, 1955.

* Aerodynamicist.

## INTRODUCTION

THE MOST ACCURATE of the available methods of rotor blade bending analysis involve the tabular solution of the differential equation. Such methods have been presented by Flax and Goland[1] and Johnson and Mayne.[2] The major disadvantage of these methods is that they involve long and tedious calculation, especially in the case of harmonic loading. The usual method has been to obtain new solutions for each distribution of loading considered. When a number of different loadings are to be considered, a large amount of labor is involved.

Some of the properties of the equation of motion may be employed to help alleviate this situation. Since the equation is linear, the superposition principle applies. It is well known, for example, that if any linear combination of loadings is applied, the resulting bending moment is the same linear combination of the bending moments due to each of the loads applied separately. It is this principle that is used to derive the response matrix formulation. The process is simply to make tabular solutions for a set of standard loads. These solutions are then used to form the response matrices after which no further tabular solutions are required. The response to any loading is obtained by post-multiplying the response matrix by a matrix representing the loading.

Since even a small number of tabular solutions for harmonic loading are very tedious, it was considered desirable to find an approximate method for obtaining the harmonic response matrices. A modification of the amplification factor method of Flax and Goland[1] was used for this purpose using several modes rather than assuming that only one was important. This was made practical by a method developed in this paper for obtaining the rotating modes and natural frequencies using the response matrices for the zeroth harmonic.

## EQUATIONS OF MOTION

The partial differential equation for the uncoupled bending out of the plane of rotation of a rotor blade

under the small deflection assumption and including the average value of the aerodynamic damping has been developed elsewhere.[1] This equation may be written:

$$\frac{\partial^2}{\partial r^2}\left(EI\frac{\partial^2 Z}{\partial r^2}\right) - \Omega^2 A\frac{\partial^2 Z}{\partial r^2} + m\frac{\partial^2 Z}{\partial t^2} + \Omega^2 mr\frac{\partial Z}{\partial r} - \Omega\theta\frac{\partial Z}{\partial t} = L(r, t) \quad (1)$$

Now, since $\psi = \Omega t$, the equation may be written in terms of azimuthal derivatives:

$$\frac{\partial^2}{\partial r^2}\left(\frac{EI}{\Omega^2}\frac{\partial^2 Z}{\partial r^2}\right) - A\frac{\partial^2 Z}{\partial r^2} + m\frac{\partial^2 Z}{\partial \psi^2} + mr\frac{\partial Z}{\partial r} - \theta\frac{\partial Z}{\partial \psi} = \frac{1}{\Omega^2}L(r, \psi) \quad (2)$$

For an articulated rotor Eq. (2) must satisfy the following boundary conditions:

$$\left.\begin{aligned} &\frac{\partial^2}{\partial r^2}\left(\frac{EI}{\Omega^2}\frac{\partial^2 Z}{\partial r^2}\right) = \frac{\partial}{\partial r}\left(\frac{EI}{\Omega^2}\frac{\partial^2 Z}{\partial r^2}\right) = \frac{\partial^2 Z}{\partial r^2} = 0, \quad r = R \\ &\partial^2 Z/\partial r^2 = Z = 0, \qquad r = 0 \end{aligned}\right\} \quad (3)$$

For a teetering blade having a built-in coning angle of $\beta_b$ at $r = \xi$, Eq. (2) must satisfy these conditions:

$$\left.\begin{aligned} &\frac{\partial^2}{\partial r^2}\left(\frac{EI}{\Omega^2}\frac{\partial^2 Z}{\partial r^2}\right) = \frac{\partial}{\partial r}\left(\frac{EI}{\Omega^2}\frac{\partial^2 Z}{\partial r^2}\right) = \frac{\partial^2 Z}{\partial r^2} = 0, \quad r = R \\ &Z = 0, \quad r = 0 \\ &(\partial Z/\partial r)\ (r = -0) = (\partial Z/\partial r)\ (r = +0) \\ &(\partial^2 Z/\partial r^2)\ (r = -0) = (\partial^2 Z/\partial r^2)\ (r = +0) \\ &\Delta(\partial Z/\partial r) = \beta_b,\ r = \xi \end{aligned}\right\} \quad (4)$$

Only periodic responses to periodic forcing shall be considered—i.e., $L(r, \psi) = L(r, \psi + 2\pi)$ and $Z(r, \psi) = Z(r, \psi + 2\pi)$; thus both these functions may be expressed by Fourier series as follows:

$$\left.\begin{aligned} L(r, \psi) &= Re\sum_{n=0}^{\infty} L_n(r)\, e^{-in\psi} \\ Z(r, \psi) &= \mathrm{Re}\sum_{n=0}^{\infty} Z_n(r) e^{-in\psi} \end{aligned}\right\} \quad (5)$$

where $L_n(r)$ and $Z_n(r)$ are in general complex quantities, the real parts being the coefficients of cos $n\psi$ and the imaginary parts being the coefficients of sin $n\psi$. Substituting Eqs. (5) in Eq. (2) and making use of the orthogonality of the exponentials, the equation for any $n$ is:

$$\frac{d^2}{dr^2}\left(\frac{EI}{\Omega^2}\frac{d^2 Z_n}{dr^2}\right) - A\frac{d^2 Z_n}{dr^2} + mr\frac{dZ_n}{dr} - (n^2 m - in\theta)Z_n = \frac{1}{\Omega^2}L_n(r) \quad (6)$$

It is apparent that for an articulated blade Eq. (6) must satisfy;

$$\left.\begin{aligned} &\frac{d^2}{dr^2}\left(\frac{EI}{\Omega^2}\frac{d^2 Z_n}{dr^2}\right) = \frac{d}{dr}\left(\frac{EI}{\Omega^2}\frac{d^2 Z_n}{dr^2}\right) = \\ &\qquad \frac{d^2 Z_n}{dr^2} = 0, \ r = R \text{ for all } n \\ &\frac{d^2 Z_n}{dr^2} = Z_n = 0, \ r = 0 \text{ for all } n \end{aligned}\right\} \quad (7)$$

and for a teetering blade Eq. (6) must satisfy:

$$\left.\begin{aligned} &\frac{d^2}{dr^2}\left(\frac{EI}{\Omega^2}\frac{d^2 Z_n}{dr^2}\right) = \frac{d}{dr}\left(\frac{EI}{\Omega^2}\frac{d^2 Z_n}{dr^2}\right) = \\ &\qquad \frac{d^2 Z_n}{dr^2} = 0, \ r = R \text{ for all } n \\ &Z_n = 0 \text{ at } r = 0 \text{ for all } n \\ &(d^2 Z_n/dr^2) = 0 \text{ at } r = 0 \text{ for odd } n \\ &(dZ_n/dr) = 0 \text{ at } r = 0 \text{ for even } n \\ &\Delta(dZ_n/dr) = \beta_b \text{ at } r = \xi \text{ for } n = 0 \end{aligned}\right\} \quad (8)$$

It is Eq. (6) under the boundary conditions (7) and (8) which will be analyzed in this paper. The response matrices for $n = 0$ will be obtained directly from tabular solutions of Eq. (6). However, since tabular solutions for $n > 0$ are lengthy, an approximate method for calculating these response matrices will be developed making use of the natural modes and frequencies of the undamped rotating beam. These modes and frequencies may themselves be obtained by a method that is developed using the response matrices for $n = 0$.

Consider the complimentary form of Eq. (2) with $\theta$ set equal to zero:

$$\frac{\partial^2}{\partial r^2}\left(\frac{EI}{\Omega^2}\frac{\partial^2 Z}{\partial r^2}\right) - A\frac{\partial^2 Z}{\partial r^2} + mr\frac{\partial Z}{\partial r} + m\frac{\partial^2 Z}{\partial \psi^2} = 0 \quad (9)$$

If solutions of the following form are assumed:

$$Z(r, \psi) = \sum_{k=1}^{\infty} \phi_k(r) e^{-i\left(\frac{\omega_k}{\Omega}\right)\psi}$$

Eq. (9) yields for each $k$ the following equation:

$$\frac{d^2}{dr^2}\left(\frac{EI}{\Omega^2}\frac{d^2\phi_k}{dr^2}\right) - A\frac{d^2\phi_k}{dr^2} + mr\frac{d\phi_k}{dr} = \left(\frac{\omega_k}{\Omega}\right)^2 m\phi_k \quad (10)$$

which is the characteristic equation for the rotating beam, where $\varphi_k$ is the mode shape and $\omega_k$ is the natural frequency.

The linear differential operator, $\mathfrak{L}_n$, shall be defined as follows:

$$\mathfrak{L}_n(\alpha) = \frac{d^2}{dr^2}\left(\frac{EI}{\Omega^2}\frac{d^2\alpha}{dr^2}\right) - A\frac{d^2\alpha}{dr^2} + mr\frac{d\alpha}{dr} - (n^2 m - in\,\Theta)\alpha \quad (11)$$

Eq. (6) may then be written:

$$\mathfrak{L}_n(Z_n) = (1/\Omega^2)L_n \quad (12)$$

and the characteristic equation, Eq. (10), may be written in terms of the same operator for $n = 0$:

$$\mathfrak{L}_0(\phi_k) = (\omega_k/\Omega)^2 m\phi_k \tag{13}$$

## Solutions in Terms of Response Matrices

Each harmonic of the rigid blade loading shall be represented by the finite series:

$$L_n(r) = \sum_{\eta=1}^{H} b_{n\eta}\lambda_\eta(r) \tag{14}$$

where the $b_{n\eta}$ are complex constants (for $n > 0$) and the $\lambda_\eta$ are an arbitrary set of functions of $r$ of such a form that Eq. (14) is a good representation of the loading. The equation of motion, Eq. (12), may now be written

$$\mathfrak{L}_n(Z_n) = \frac{1}{\Omega^2}\sum_{\eta=1}^{H} b_{n\eta}\lambda_\eta(r) \tag{15}$$

If $Z_{n\eta}$ is defined as the solution of

$$\mathfrak{L}_n(Z_{n\eta}) = (1/\Omega^2)\lambda_\eta(r) \tag{16}$$

it is apparent, by superposition, that

$$Z_n = \sum_{\eta=1}^{H} Z_{n\eta}b_{n\eta} \tag{17}$$

for all cases where $Z_n$ satisfies homogeneous boundary conditions and where the $Z_{n\eta}$ each satisfy these same homogeneous boundary conditions.

For the teetering blade with a built-in coning there is a nonhomogeneous condition for $n = 0$. It may be shown that in this case

$$Z_0 = Z_0^* + \beta_b Z_b \tag{18}$$

where $Z_0^*$ is the solution for $\beta_b$ equal to zero and satisfies only the homogeneous boundary conditions and $Z_b$ is independent of the loading. Thus $Z_0$ may be written

$$Z_0 = \sum_{\eta=1}^{H} Z_{0\eta}b_{0\eta} + Z_b\beta_b \tag{19}$$

where $Z_{0\eta}$ satisfies the homogeneous boundary conditions. If, for convenience, one lets $b_{0,H+1} = \beta_b$, and $Z_{0,H+1} = Z_b$, Eq. (19) may be written:

$$Z_0 = \sum_{\eta=1}^{H+1} Z_{0\eta}b_{0\eta} \tag{20}$$

The subscript $\nu$ will be used to indicate the value of any function of $r$ at some discrete value of $r$: $r_\nu$. Thus, $f(r_\nu)$ will be written $f_\nu$. Eqs. (17) and (20) may be written

$$\left.\begin{aligned}
&Z_{n\nu} = \sum_\eta Z_{n\eta\nu}b_{n\eta}, \text{ also}\\
&\left(\frac{dZ_n}{dr}\right)_\nu = \sum_\eta \left(\frac{dZ_{n\eta}}{dr}\right)_\nu b_{n\eta}\\
&\left(\frac{d^2Z_n}{dr^2}\right)_\nu = \sum_\eta \left(\frac{d^2Z_{n\eta}}{dr^2}\right)_\nu b_{n\eta}\\
&M_{n\nu} = (EI)_\nu\left(\frac{d^2Z_n}{dr^2}\right)_\nu = \sum_\eta (EI)_\nu\left(\frac{d^2Z_{n\eta}}{dr^2}\right)_\nu b_{n\eta},\\
&\qquad\qquad \nu = 1, 2, 3 \ldots N
\end{aligned}\right\} \tag{21}$$

Eqs. (21) are the equations of matrix multiplications and may be written:

$$\boldsymbol{Z}_n = \boldsymbol{P}_n\boldsymbol{B}_n \tag{22}$$

$$\boldsymbol{Z}_n' = \boldsymbol{P}_n'\boldsymbol{B}_n \tag{23}$$

$$\boldsymbol{Z}_n'' = \boldsymbol{P}_n''\boldsymbol{B}_n \tag{24}$$

$$\boldsymbol{M}_n = \boldsymbol{Q}_n\boldsymbol{B}_n \tag{25}$$

where $\boldsymbol{Z}_n$, $\boldsymbol{Z}_n'$, $\boldsymbol{Z}_n''$, $\boldsymbol{M}_n$, $\boldsymbol{B}_n$ are column matrices whose $i$th elements are:

$$\left.\begin{aligned}
&(\boldsymbol{Z}_n)_i = Z_{ni}\\
&(\boldsymbol{Z}_n')_i = (dZ_n/dr)_i\\
&(\boldsymbol{Z}_n'')_i = (d^2Z_n/dr^2)_i\\
&(\boldsymbol{M}_n)_i = M_{ni} = (EI)_i(d^2Z_n/dr^2)_i,\\
&\qquad\qquad i = 1, 2, 3, \ldots, N\\
&(\boldsymbol{B}_n)_i = b_{ni}, \qquad i = 1, 2, 3, \ldots, H^*
\end{aligned}\right\} \tag{26}$$

and $\boldsymbol{P}_n$, $\boldsymbol{P}_n'$, $\boldsymbol{P}_n''$, $\boldsymbol{Q}_n$ are rectangular matrices whose $ij$th elements are:

$$\left.\begin{aligned}
&(\boldsymbol{P}_n)_{ij} = Z_{nji}\\
&(\boldsymbol{P}_n')_{ij} = (dZ_{nj}/dr)_i\\
&(\boldsymbol{P}_n'')_{ij} = (d^2Z_{nj}/dr)_i\\
&(\boldsymbol{Q}_n)_{ij} = (EI)_i\left(\frac{d^2Z_{nj}}{dr^2}\right)_i \begin{matrix} i = 1, 2, 3, \ldots, N \\ j = 1, 2, 3, \ldots, H\dagger \end{matrix}
\end{aligned}\right\} \tag{27}$$

The matrices $\boldsymbol{Z}_n$, $\boldsymbol{Z}_n'$, $\boldsymbol{Z}_n''$, $\boldsymbol{M}_n$ represent the $n$th harmonic response of the blade to any particular $n$th harmonic loading represented by $\boldsymbol{B}_n$. The matrices $\boldsymbol{P}_n$, $\boldsymbol{P}_n'$, $\boldsymbol{P}_n''$, $\boldsymbol{Q}_n$ are called "response matrices" and are independent of the loading, their elements being the solutions of Eq. (16). Thus, once the response matrices for a particular blade and rotor frequency have been calculated, the response to any loading may be obtained by the simple operations of matrix multiplication.

## The Form of $\lambda_\eta(r)$

For the purpose of obtaining the response matrices directly from tabular solutions of Eq. (16), $\lambda_\eta$ may be any convenient set of functions of $r$ which will well represent the loading, $L_\eta(r)$, in Eq. (14). A convenient form that will also satisfy the requirements of the next sections will now be described. Consider the blade span to be divided into $H$ uniform intervals, and let each $\lambda_\eta$ be unity over one of the intervals and zero elsewhere, there being one $\lambda_\eta$ for each of the intervals. $\eta = 1, 2, 3, \ldots, H$ starting at the most outboard interval. Then each element of $\boldsymbol{B}_n$ may be considered to be the average loading over one of the intervals. It

* $i = 1, 2, 3, \ldots, H + 1$ for $n = 0$ for teetering blade with built-in coning.

† $j = 1, 2, 3, \ldots, H + 1$ for $n = 0$ for teetering blade with built-in coning.

was this form of $\lambda_\eta$ which was used in the illustrative calculations.

### Use of the Response Matrices

The mass and stiffness distribution of a typical teetering type blade are shown in Fig. 1. The bending moment response matrices for $n = 0$ for both the teetering and articulated conditions have been calculated by tabular means and normalized on the last element of the first column of the first matrix. They are shown in Tables 1 and 2. Tables 3 and 4 give the matrices for $n = 1$ and $n = 2$ for the teetering blade. These have been calculated approximately by the method of the following sections and have been normalized in the same manner as Tables 1 and 2. For the purpose of illustration, a parabolic load was applied to the matrix of Table 1, and the resulting bending moment distribution is shown in Fig. 2. Similarly, a parabolic cosine load distribution was applied to the matrix of Table 4, the resulting bending moment distribution being shown in Fig. 3.

The matrices by themselves are of considerable physical interest. Each column represents the proportionality factors between the response of each blade station and loads applied at one of the blade intervals. Thus, by examining the matrices, it is possible to determine how the distribution of the loading will affect the blade response. Notice, for example, that Table 1 shows that the bending moment at the root is independent of the distribution of the load outboard of interval 7. It is possible, then, to ascertain the importance of the effects on blade response of theoretical refinements, such as the consideration of nonuniform inflow, which cause a redistribution of loading. It will be shown in the next sections that the approximate higher harmonic matrices are relatively easily obtained. Even though the high harmonic loads may not be known, these matrices will give an indication of their possible importance.

### Natural Frequencies and Modes

A method will now be developed for obtaining the natural frequencies and modes of the rotating beam using the response matrices for $n = 0$. It has been shown, see Eq. (13), that the characteristic equation may be written in terms of the operator $\mathfrak{L}_0$,

$$\mathfrak{L}_0(\phi_k) = (\omega_k/\Omega)^2 m\phi_k$$

Now the right-hand side of this equation will be expressed in a manner analogous to the loading representation of Eq. (14). Let

$$\omega_k{}^2 m\phi_k = \sum_{\eta=1}^{H} b_{k\eta}\lambda_\eta(r) \tag{28}$$

where $b_{k\eta}$ are unknown constants. Now Eq. (13) may be written

$$\mathfrak{L}_0(\phi_k) = \frac{1}{\Omega^2}\sum_{\eta=1}^{H} b_{k\eta}\lambda_\eta(r) \tag{29}$$

Since $Z_{0\eta}$ is the solution of

$$\mathfrak{L}_0(Z_{0\eta}) = (1/\Omega^2)\lambda_\eta(r) \tag{30}$$

it is apparent, by superposition, that

$$\phi_k = \sum_{\eta=1}^{H} Z_{0\eta} b_{k\eta} \tag{31}$$

Substituting Eq. (31) in Eq. (28), one gets:

$$\sum_{\eta=1}^{H}\left\{mZ_{0\eta} - \frac{1}{\omega_k{}^2}\lambda_\eta\right\} b_{k\eta} = 0 \tag{32}$$

or at $r_\nu$:

$$\sum_{\eta=1}^{H}\left\{m_\nu Z_{0\eta\nu} - \frac{1}{\omega_k{}^2}\lambda_{\eta\nu}\right\} b_{k\eta} = 0,$$

$$\nu = 1, 2, 3, \ldots, N \tag{33}$$

If the values of $r_\nu$ are chosen to coincide with the midpoints of the $H$ spanwise blade intervals, Eq. (33) is a set of $H$ homogeneous linear equations in $H$ variables. Writing Eq. (33) in matrix form one has:

$$\{\boldsymbol{R}_0 - (1/\omega_k{}^2)\boldsymbol{I}\}\boldsymbol{B}_k = 0 \tag{34}$$

where $\boldsymbol{R}_0$ is a square matrix formed by the rows of $\boldsymbol{P}_0$ that correspond to the midpoints of the blade intervals, each multiplied by $m_\nu$, and $\boldsymbol{I}$ is a unit matrix. The condition on $\omega_k$ is that $\boldsymbol{B}_k$ be nontrivial or

$$\det.\ \{\boldsymbol{R}_0 - (1/\omega_k{}^2)\boldsymbol{I}\} = 0 \tag{35}$$

which is the familiar secular determinant. There are several convenient methods for obtaining the secular equation from Eq. (35) suitable for hand calculation[3] or automatic calculating machines.[4] The solutions of the secular equation, Eq. (35), are the natural frequencies of the rotating beam. Substituting each $\omega_k$ in Eq. (34), the corresponding $\boldsymbol{B}_k$ may be obtained in terms of one of the $b_{k\eta}$ by Crout's method. Now the normalized mode shape is given by Eq. (31), which may be written in matrix form,

$$\Phi_k = \{1/[\phi_k(r = R)]\}\boldsymbol{P}_0\boldsymbol{B}_k \tag{36}$$

where $\Phi_k$ is the column matrix of the $\phi_{k\nu}$ and $\boldsymbol{P}_0$ is the deflection response matrix for $n = 0$. The bending moment of each mode is similarly given by

$$\boldsymbol{M}_k = \{1/[\phi_k(r = R)]\}\boldsymbol{Q}_0\boldsymbol{B}_k \tag{37}$$

The modes and frequencies satisfying various homogeneous boundary conditions are obtained by using response matrices that satisfy the same boundary conditions.

The first four symmetric and antisymmetric modes of the blade were calculated by the above method and are shown in Figs. 4 and 5.

### Response Matrices for $n > 0$

The response matrices for $n > 0$ may be obtained by an approximate method.* Eq. (16) may be written:

* The following development is similar to that of the amplification factor method of reference 1.

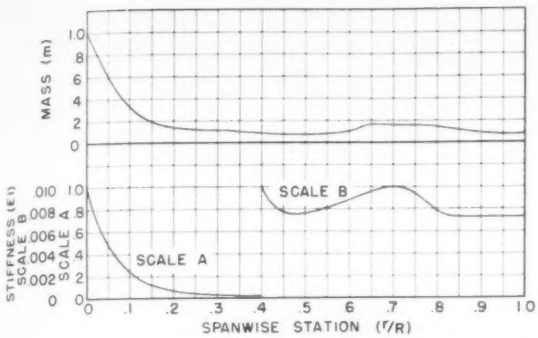


FIG. 1. Mass and stiffness distribution of typical teetering-type blade.

TABLE 1
Bending Moment Response Matrix—Teetering Blade, $n = 0$

| r/R | $\eta=1$ | $\eta=2$ | $\eta=3$ | $\eta=4$ | $\eta=5$ | $\eta=6$ | $\eta=7$ | $\eta=8$ | $\eta=9$ |
|---|---|---|---|---|---|---|---|---|---|
| 1.00 | 0 | 0 | 0 | 0 | 0 | 0 | 0 | 0 | 0 |
| .90 | .072 | -.050 | -.009 | -.001 | 0 | 0 | 0 | 0 | 0 |
| .85 | .115 | -.066 | -.023 | -.003 | -.001 | 0 | 0 | 0 | 0 |
| .80 | .114 | -.070 | -.057 | -.009 | -.001 | 0 | 0 | 0 | 0 |
| .75 | .096 | .028 | -.076 | -.021 | -.002 | 0 | 0 | 0 | 0 |
| .70 | .072 | .042 | -.038 | -.036 | -.005 | -.001 | 0 | 0 | 0 |
| .65 | .052 | .040 | .007 | -.074 | -.015 | -.001 | 0 | 0 | 0 |
| .60 | .039 | .025 | .013 | -.043 | -.046 | -.003 | 0 | 0 | 0 |
| .55 | .027 | .015 | .012 | -.006 | -.067 | -.011 | -.001 | 0 | 0 |
| .50 | .020 | .010 | .009 | .004 | -.038 | -.040 | -.004 | -.001 | 0 |
| .45 | .010 | .010 | .010 | .009 | -.003 | -.06 | -.015 | -.002 | 0 |
| .40 | .017 | .017 | .01 | .017 | .013 | -.01 | -.031 | -.008 | -.001 |
| .35 | .035 | .035 | .035 | .035 | .034 | .01 | -.074 | -.023 | -.00 |
| .30 | .070 | .070 | .070 | .070 | .070 | .060 | -.020 | -.056 | -.005 |
| .25 | .131 | .131 | .131 | .131 | .131 | .126 | .074 | -.050 | -.010 |
| .20 | .232 | .232 | .232 | .232 | .231 | .228 | .196 | .063 | -.019 |
| .10 | .555 | .555 | .555 | .555 | .555 | .552 | .532 | .444 | .081 |
| 0 | 1.000 | 1.000 | 1.000 | 1.000 | 1.000 | 1.000 | .982 | .896 | .479 |

TABLE 2
Bending Moment Response Matrix—Articulated Blade, $n = 0$

| r/R | $\eta=1$ | $\eta=2$ | $\eta=3$ | $\eta=4$ | $\eta=5$ | $\eta=6$ | $\eta=7$ | $\eta=8$ | $\eta=9$ |
|---|---|---|---|---|---|---|---|---|---|
| 1.00 | 0 | 0 | 0 | 0 | 0 | 0 | 0 | 0 | 0 |
| .90 | .072 | -.005 | -.009 | 0 | 0 | 0 | 0 | 0 | 0 |
| .85 | .115 | -.066 | -.023 | 0 | 0 | 0 | 0 | 0 | 0 |
| .80 | .114 | -.020 | -.057 | -.001 | 0 | 0 | 0 | 0 | 0 |
| .75 | .096 | .028 | -.076 | -.002 | 0 | 0 | 0 | 0 | 0 |
| .70 | .072 | .042 | -.038 | -.006 | -.001 | 0 | 0 | 0 | 0 |
| .65 | .052 | .040 | .007 | -.074 | -.001 | 0 | 0 | 0 | 0 |
| .60 | .039 | .025 | .013 | -.043 | -.005 | -.001 | -.001 | 0 | 0 |
| .55 | .027 | .015 | .011 | -.007 | -.067 | -.001 | -.001 | 0 | 0 |
| .50 | .010 | .009 | .009 | .004 | -.038 | -.004 | -.004 | -.001 | -.001 |
| .45 | .008 | .008 | .007 | .006 | -.006 | -.064 | -.017 | -.004 | -.001 |
| .40 | .009 | .009 | .009 | .009 | .006 | -.040 | -.059 | -.015 | -.004 |
| .35 | .012 | .012 | .012 | .012 | .011 | -.007 | -.096 | -.043 | -.013 |
| .30 | .016 | .016 | .016 | .016 | .015 | .006 | -.073 | -.104 | -.031 |
| .25 | .019 | .019 | .019 | .019 | .018 | .013 | -.031 | -.151 | -.064 |
| .20 | .021 | .021 | .021 | .021 | .021 | .018 | -.009 | -.124 | -.119 |
| .10 | .020 | .020 | .020 | .020 | .020 | .019 | .009 | -.035 | -.176 |
| 0 | 0 | 0 | 0 | 0 | 0 | 0 | 0 | 0 | 0 |

TABLE 3
Bending Moment Response Matrix—Teetering or Articulated Blade, $n = 1$

| r/R | $\eta=1$ | $\eta=2$ | $\eta=3$ | $\eta=4$ | $\eta=5$ | $\eta=6$ | $\eta=7$ | $\eta=8$ | $\eta=9$ |
|---|---|---|---|---|---|---|---|---|---|
| 1.00 | Re 0<br>Im 0 | 0<br>0 | 0<br>0 | 0<br>0 | 0<br>0 | 0<br>0 | 0<br>0 | 0<br>0 | 0<br>0 |
| .90 | .046<br>.005 | -.001<br>.002 | -.017<br>-.001 | -.011<br>-.002 | -.007<br>-.002 | -.007<br>-.002 | -.007<br>-.002 | -.004<br>-.002 | -.002<br>-.001 |
| .85 | .073<br>.007 | -.019<br>.002 | -.032<br>-.001 | -.006<br>-.002 | .005<br>-.003 | .003<br>-.002 | -.008<br>-.002 | -.001<br>-.002 | .001<br>-.001 |
| .80 | .086<br>.010 | -.011<br>.002 | -.037<br>-.002 | -.018<br>-.004 | -.003<br>-.004 | -.004<br>-.004 | -.009<br>-.003 | -.003<br>-.002 | -.001<br>-.002 |
| .75 | .084<br>.010 | 0<br>.003 | -.035<br>-.002 | -.027<br>-.004 | -.012<br>-.005 | -.003<br>-.004 | -.007<br>-.004 | -.004<br>-.003 | -.001<br>-.002 |
| .70 | .066<br>.009 | .009<br>.003 | -.020<br>-.001 | -.025<br>-.003 | -.017<br>-.004 | -.008<br>-.004 | -.005<br>-.004 | -.006<br>-.004 | -.005<br>-.002 |
| .65 | .052<br>.010 | .031<br>.004 | -.013<br>-.001 | -.043<br>-.004 | -.037<br>-.005 | -.012<br>-.005 | .001<br>-.007 | -.005<br>-.003 | -.005<br>-.002 |
| .60 | .027<br>.005 | .020<br>.002 | -.009<br>-.001 | -.025<br>-.002 | -.023<br>-.003 | -.010<br>-.003 | -.00<br>-.004 | -.004<br>-.002 | -.004<br>-.001 |
| .55 | .017<br>.005 | .019<br>.002 | .003<br>-.001 | -.017<br>-.002 | -.025<br>-.002 | -.020<br>-.003 | -.010<br>-.002 | -.002<br>-.002 | .001<br>-.001 |
| .50 | .009<br>.002 | .010<br>.001 | .004<br>0 | -.007<br>-.001 | -.014<br>-.002 | -.015<br>-.002 | -.010<br>-.002 | -.003<br>-.002 | -.001<br>-.001 |
| .45 | .012<br>.004 | .009<br>.002 | .010<br>0 | .001<br>-.001 | -.017<br>-.002 | -.010<br>-.003 | -.026<br>-.001 | -.010<br>-.002 | -.002<br>-.001 |
| .40 | .015<br>.005 | .009<br>.002 | .012<br>0 | .007<br>-.002 | -.013<br>-.003 | -.012<br>-.004 | -.036<br>-.004 | -.013<br>-.003 | -.011<br>-.001 |
| .35 | .018<br>.007 | .010<br>.003 | .014<br>.001 | .012<br>-.002 | -.008<br>-.004 | -.035<br>-.005 | -.050<br>-.005 | -.045<br>-.005 | -.030<br>-.003 |
| .30 | .022<br>.009 | .016<br>.004 | .015<br>.001 | .014<br>-.002 | 0<br>-.005 | -.027<br>-.006 | -.058<br>-.007 | -.07<br>-.00 | -.056<br>-.004 |
| .25 | .024<br>.010 | .022<br>.005 | .013<br>.001 | .014<br>-.002 | .011<br>-.005 | -.011<br>-.007 | -.062<br>-.009 | -.10<br>-.008 | -.084<br>-.005 |
| .20 | .023<br>.010 | .027<br>.005 | .010<br>.001 | .012<br>-.002 | .020<br>-.006 | .006<br>-.008 | -.058<br>-.009 | -.10<br>-.009 | -.105<br>-.005 |
| .10 | .017<br>.009 | .028<br>.004 | .004<br>.001 | .005<br>-.002 | .027<br>-.005 | .026<br>-.007 | -.041<br>-.008 | -.121<br>-.007 | -.109<br>-.005 |
| 0 | 0<br>0 | 0<br>0 | 0<br>0 | 0<br>0 | 0<br>0 | 0<br>0 | 0<br>0 | 0<br>0 | 0<br>0 |

TABLE 4
Bending Moment Response Matrix—Teetering Blade, $n = 2$

| r/R | $\eta=1$ | $\eta=2$ | $\eta=3$ | $\eta=4$ | $\eta=5$ | $\eta=6$ | $\eta=7$ | $\eta=8$ | $\eta=9$ |
|---|---|---|---|---|---|---|---|---|---|
| 1.00 | Re 0<br>Im 0 | 0<br>0 | 0<br>0 | 0<br>0 | 0<br>0 | 0<br>0 | 0<br>0 | 0<br>0 | 0<br>0 |
| .90 | .051<br>.013 | -.012<br>.004 | -.026<br>-.003 | -.006<br>-.008 | -.002<br>-.009 | -.004<br>-.009 | -.003<br>-.006 | -.001<br>-.003 | -.002<br>-.001 |
| .85 | .086<br>.023 | -.018<br>.008 | -.043<br>-.005 | -.014<br>-.013 | 0<br>-.017 | .009<br>-.015 | -.005<br>-.010 | -.008<br>-.005 | -.003<br>-.004 |
| .80 | .105<br>.033 | -.011<br>.010 | -.049<br>-.007 | -.029<br>-.018 | -.013<br>-.022 | -.001<br>-.020 | -.004<br>-.013 | -.005<br>-.007 | -.002<br>-.002 |
| .75 | .108<br>.038 | 0<br>.012 | -.047<br>-.009 | -.042<br>-.021 | -.028<br>-.024 | -.010<br>-.022 | -.001<br>-.016 | -.001<br>-.008 | 0<br>-.003 |
| .70 | .096<br>.039 | .016<br>.011 | -.033<br>-.009 | -.051<br>-.020 | -.044<br>-.023 | -.017<br>-.021 | -.004<br>-.015 | -.002<br>-.008 | -.002<br>-.002 |
| .65 | .051<br>.030 | .027<br>.007 | -.011<br>-.008 | -.047<br>-.015 | -.049<br>-.017 | -.029<br>-.015 | -.005<br>-.010 | .001<br>-.005 | -.002<br>-.002 |
| .60 | .038<br>.025 | .024<br>.007 | -.005<br>-.006 | -.038<br>-.012 | -.043<br>-.013 | -.030<br>-.012 | -.010<br>-.008 | -.001<br>-.006 | .001<br>-.001 |
| .55 | .019<br>.017 | .020<br>.004 | .001<br>-.004 | -.025<br>-.008 | -.031<br>-.009 | -.027<br>-.007 | -.014<br>-.006 | -.005<br>-.004 | -.001<br>-.001 |
| .50 | .010<br>.013 | .015<br>.003 | .004<br>-.003 | -.015<br>-.006 | -.024<br>-.006 | -.026<br>-.006 | -.019<br>-.003 | -.010<br>-.003 | -.004<br>-.001 |
| .45 | .006<br>.012 | .010<br>.003 | .004<br>-.002 | -.008<br>-.004 | -.018<br>-.004 | -.027<br>-.003 | -.026<br>-.002 | -.016<br>-.001 | -.006<br>0 |
| .40 | 0<br>.012 | .003<br>.005 | .004<br>0 | -.002<br>-.002 | -.014<br>-.002 | -.029<br>-.001 | -.034<br>0 | -.023<br>0 | -.009<br>0 |
| .35 | -.015<br>.014 | -.009<br>.009 | 0<br>.006 | .005<br>.006 | -.006<br>.006 | -.028<br>.006 | -.040<br>.004 | -.029<br>.002 | -.012<br>.001 |
| .30 | -.048<br>.013 | -.034<br>.018 | -.009<br>.010 | .013<br>.010 | .010<br>.018 | -.010<br>.014 | -.025<br>.010 | -.021<br>.003 | -.009<br>.002 |
| .25 | -.112<br>.011 | -.074<br>.023 | -.024<br>.045 | .025<br>.048 | .038<br>.047 | .034<br>.033 | .017<br>.022 | .009<br>.010 | .002<br>.004 |
| .20 | -.220<br>.005 | -.138<br>.027 | -.050<br>.081 | .051<br>.094 | .071<br>.085 | .112<br>.075 | .102<br>.044 | .060<br>.020 | .023<br>.007 |
| .10 | -.565<br>-.012 | -.340<br>.134 | -.130<br>.222 | .059<br>.245 | .215<br>.217 | .314<br>.260 | .155<br>.104 | .035<br>.048 | .010<br>.016 |
| 0 | -1.030<br>-.029 | -.616<br>.241 | -.237<br>.404 | .101<br>.448 | .343<br>.396 | .505<br>.292 | .195<br>.148 | .024<br>.086 | .014<br>.029 |

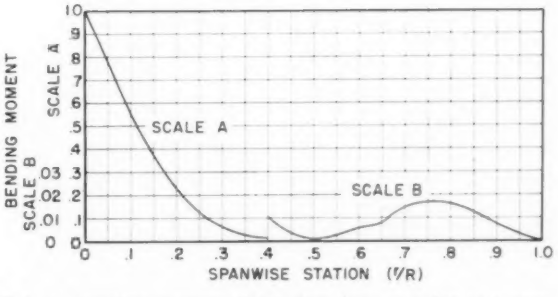


FIG. 2. Bending moment distribution for $n = o$ due to a parabolic load.

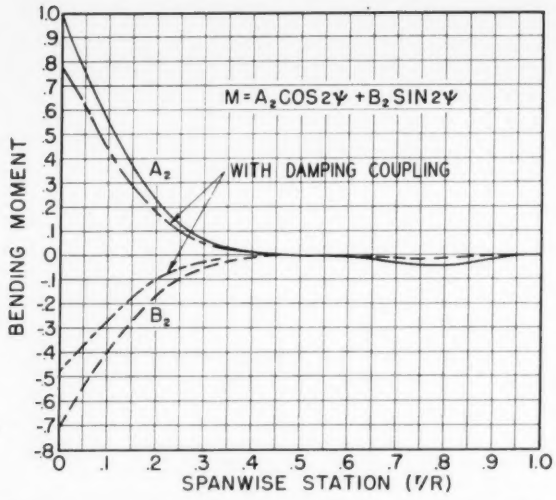


FIG. 3. Second harmonic bending moment distribution due to $r^2 \cos 2\psi$ loading.

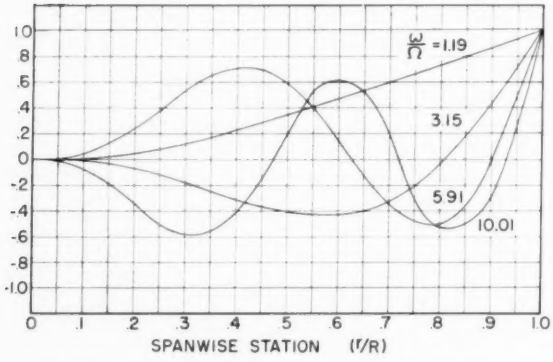


FIG. 4. Symmetric vibratory modes of rotating beam.

TABLE 5

Bending Moment Response Matrix with Damping Coupling—Teetering Blade, $n = 2$

| r/R | ψ =1 | ψ =2 | ψ =3 | ψ =4 | ψ =5 | ψ =6 | ψ =7 | ψ =8 | ψ =9 |
|---|---|---|---|---|---|---|---|---|---|
| 1.00 | Re 0<br>Im 0 | 0<br>0 | 0<br>0 | 0<br>0 | 0<br>0 | 0<br>0 | 0<br>0 | 0<br>0 | 0<br>0 |
| .90 | .040<br>.012 | -.012<br>.004 | -.022<br>-.001 | -.004<br>-.003 | .007<br>-.004 | .007<br>-.003 | -.002<br>-.002 | -.004<br>-.001 | -.003<br>0 |
| .85 | .072<br>.021 | -.018<br>.007 | -.036<br>-.002 | -.009<br>-.006 | .008<br>-.007 | .010<br>-.005 | -.003<br>-.004 | -.006<br>-.002 | -.003<br>-.001 |
| .80 | .095<br>.029 | -.012<br>.010 | -.040<br>-.003 | -.021<br>-.009 | -.002<br>-.010 | .007<br>-.008 | .001<br>-.005 | -.003<br>-.003 | -.001<br>-.001 |
| .75 | .105<br>.033 | -.002<br>.011 | -.037<br>-.004 | -.032<br>-.011 | -.015<br>-.012 | 0<br>-.010 | .003<br>-.006 | .002<br>-.003 | .001<br>-.001 |
| .70 | .097<br>.031 | .012<br>.012 | -.024<br>-.004 | -.039<br>-.012 | -.030<br>-.013 | -.011<br>-.011 | .003<br>-.007 | .005<br>-.004 | .003<br>-.001 |
| .65 | .074<br>.025 | .023<br>.009 | -.006<br>-.003 | -.036<br>-.010 | -.037<br>-.011 | -.020<br>-.010 | .002<br>-.006 | .007<br>-.003 | .004<br>-.001 |
| .60 | .044<br>.020 | .021<br>.008 | -.002<br>-.002 | -.029<br>-.008 | -.033<br>-.009 | -.022<br>-.008 | -.004<br>-.005 | .005<br>-.003 | .002<br>-.001 |
| .55 | .010<br>.014 | .017<br>.006 | -.004<br>-.001 | -.018<br>-.005 | -.025<br>-.007 | -.022<br>-.006 | -.010<br>-.004 | -.003<br>-.002 | -.001<br>-.001 |
| .50 | .005<br>.010 | .012<br>.004 | .005<br>0 | -.009<br>-.004 | -.018<br>-.005 | -.021<br>-.005 | -.015<br>-.004 | -.008<br>-.002 | -.003<br>-.001 |
| .45 | .002<br>.008 | .008<br>.004 | .005<br>0 | -.002<br>-.002 | -.014<br>-.004 | -.022<br>-.004 | -.022<br>-.003 | -.014<br>-.002 | -.005<br>-.001 |
| .40 | -.002<br>.009 | .002<br>.005 | .004<br>.002 | .004<br>0 | -.001<br>-.002 | -.025<br>-.003 | -.031<br>-.003 | -.021<br>-.002 | -.008<br>-.001 |
| .35 | -.012<br>.010 | -.008<br>.009 | .001<br>.007 | .010<br>.004 | -.003<br>.002 | -.024<br>0 | -.037<br>-.001 | -.026<br>-.001 | -.011<br>0 |
| .30 | -.03?<br>.011 | -.027<br>.014 | -.008<br>.015 | .014<br>.014 | .008<br>.012 | -.010<br>.008 | -.027<br>.004 | -.021<br>.002 | -.009<br>.001 |
| .25 | -.079<br>.010 | -.059<br>.027 | -.023<br>.030 | .013<br>.032 | .027<br>.030 | .023<br>.023 | .009<br>.016 | .002<br>.007 | 0<br>.003 |
| .20 | -.155<br>.009 | -.107<br>.034 | -.048<br>.054 | .006<br>.062 | .054<br>.060 | .045<br>.050 | .032<br>.035 | .013<br>.018 | .019<br>.006 |
| .10 | -.397<br>.007 | -.260<br>.075 | -.127<br>.130 | -.019<br>.156 | .139<br>.157 | .273<br>.134 | .306<br>.097 | .201<br>.049 | .078<br>.017 |
| 0 | -.723<br>.006 | -.469<br>.134 | -.233<br>.234 | -.044<br>.284 | .254<br>.287 | .517<br>.246 | .589<br>.180 | .389<br>.091 | .151<br>.032 |

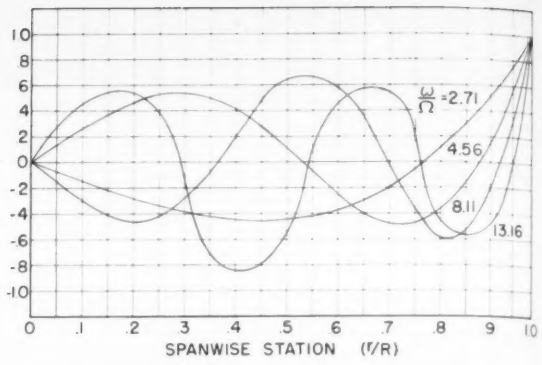


FIG. 5. Antisymmetric vibratory modes of rotating beam.

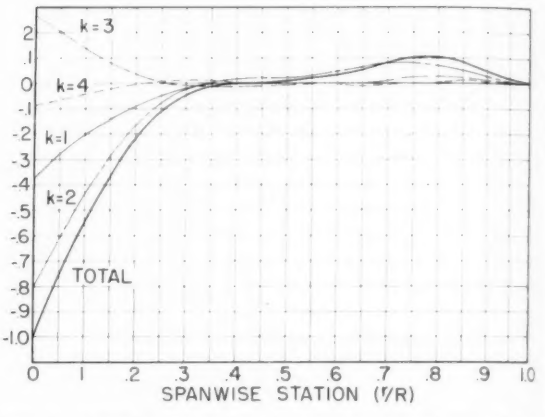


FIG. 6. Contribution of first four modes to real part of first column of $Q_2$.

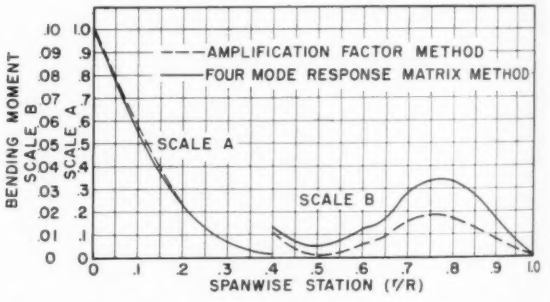


FIG. 7. Amplitude of second harmonic bending moments for $r^2 \cos 2\psi$ loading.

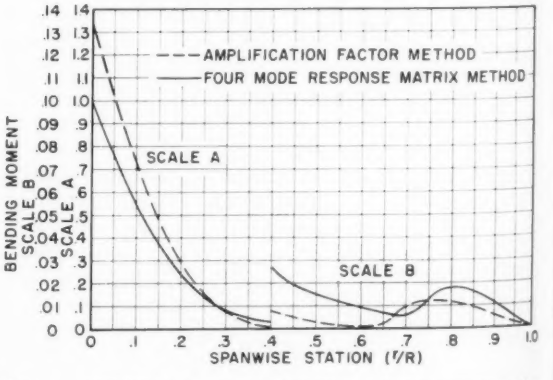


FIG. 8. Amplitude of second harmonic bending moments for $r \cos 2\psi$ loading.

$$\frac{d^2}{dr^2}\left(\frac{EI}{\Omega^2}\frac{d^2Z_{n\eta}}{dr^2}\right) - A\frac{d^2Z_{n\eta}}{dr^2} + mr\frac{dZ_{n\eta}}{dr} - (n^2m - in\Theta)Z_{n\eta} = (1/\Omega^2)\,\lambda_\eta(r) \quad (38)$$

Assuming solutions of form

$$Z_{n\eta} = \sum_{k=1}^{\infty} q_{n\eta k}\phi_k \quad (39)$$

where $q_{n\eta k}$ are complex constants and $\phi_k$ are the rotating modes satisfying Eq. (13), and substituting in Eq. (38), one gets:

$$\sum_{k=1}^{\infty} q_{n\eta k}\left[\frac{d^2}{dr^2}\left(\frac{EI}{\Omega^2}\frac{d^2\phi_k}{dr^2}\right) - A\frac{d^2\phi_k}{dr^2} + mr\frac{d\phi_k}{dr} - (n^2m - in\Theta)\phi_k\right] = \frac{1}{\Omega^2}\lambda_\eta(r) \quad (40)$$

which may be written

$$\sum_{k=1}^{\infty} q_{n\eta k}\left[\mathfrak{L}_0(\phi_k) - (n^2m - in\Theta)\phi_k\right] = \frac{1}{\Omega^2}\lambda_\eta(r) \quad (41)$$

Thus, substituting from Eq. (13), Eq. (41) becomes:

$$\sum_{k=1}^{\infty} q_{n\eta k}\left[\left(\frac{\omega_k}{\Omega}\right)^2 m\phi_k - (n^2m - in\Theta)\phi_k\right] = \frac{1}{\Omega^2}\lambda_\eta(r) \quad (42)$$

By multiplying Eq. (42) by $\phi_l dr$ and integrating from $r = 0$ to $r = R$ and since $\int_0^R m\phi_k\phi_l dr = 0$, $l \neq k$, Eq. (42), after interchanging $l$ and $k$, becomes:

$$q_{n\eta k}\left[\left(\frac{\omega_k}{\Omega}\right)^2 - n^2\right]\int_0^R m\phi_k{}^2 dr + in\sum_{l=1}^{\infty} q_{n\eta l}\int_0^R \Theta\phi_k\phi_l\,dr = \frac{1}{\Omega^2}\int_0^R \lambda_\eta\phi_k dr \quad (43)$$

If, as in reference 1, the damping coupling terms are assumed to be negligibly small—i.e., $\int_0^R \Theta\phi_k\phi_l dr = 0, l \neq k$—the simultaneous equations, Eq. (43), become independent of each other:

$$q_{n\eta k}\left\{\left[\left(\frac{\omega_k}{\Omega}\right)^2 - n^2\right]\int_0^R m\phi_k{}^2 dr + in\int_0^R \Theta\,\phi_k{}^2 dr\right\} = \frac{1}{\Omega^2}\int_0^R \lambda_\eta\phi_k dr \quad (44)$$

Defining

$$\sigma_k = \left(\int_0^R \Theta\phi_k{}^2 dr\right)\Big/\left(\int_0^R m\phi_k{}^2\,dr\right) \quad (45)$$

and multiplying by

$$\left[\left(\frac{\omega_k}{\Omega}\right)^2 - n^2 - in\sigma_k\right]\Big/\int_0^R m\phi_k{}^2 dr$$

Eq. (44) gives for $q_{n\eta k}$:

$$q_{n\eta k} = \left[\left(\int_0^R \lambda_\eta\phi_k dr\right)\Big/\left(\Omega^2\int_0^R m\phi_k{}^2 dr\right)\right]\times\left(\left[\left(\frac{\omega_k}{\Omega}\right)^2 - n^2 - in\sigma_k\right]\Big/\left\{\left[\left(\frac{\omega_k}{\Omega}\right)^2 - n^2\right]^2 + n^2\sigma_k{}^2\right\}\right) \quad (46)$$

Knowing $\phi_k$ and $\omega_k$, all the corresponding $q_{n\eta k}$ may be easily calculated.

Eq. (39) may be written:

$$Z_{n\eta\nu} = \sum_{k=1}^{\infty} q_{n\eta k}\,\phi_{k\nu} \quad (47)$$

and thus, also

$$M_{n\eta\nu} = \sum_{k=1}^{\infty} q_{n\eta k}M_{k\nu} \quad (48)$$

Eqs. (47) and (48) define the elements of $\boldsymbol{P}_n$ and $\boldsymbol{Q}_n$. When these series converge rapidly, good approximations to the response matrices are obtained by using only the first several terms of Eqs. (47) and (48). The results shown in Tables 3 and 4 were obtained using the first four modes only. The convergence of the four terms is shown for one particular column of the $\boldsymbol{Q}_2$ matrix on Fig. 6.

Somewhat more accurate results may be obtained if the coupling terms in Eq. (45) are not assumed to be negligible. In this case, simultaneous solution of Eqs. (43) is required. This was carried out for four modes for $n = 2$. The results are shown in Table 5 and Fig. 3.

It is apparent from Eqs. (46), (47), and (48) that once sufficient modes have been obtained the response matrices for any harmonic are easily calculated. Thus, in accordance with the previous discussion of the response matrices, this method may be used to ascertain how sensitive the blade may be to higher harmonic loading.

## Comparison with Amplification Factor Method

The simplest form of the amplification factor method[1] assumes that the first vibratory mode is predominant under a given load. Thus good results may be expected when the loading is such that this is true. By the same argument the matrices calculated in this paper for $n > 0$ may be expected to give good results when the loading excites primarily the first four modes.

Bending moments have been calculated for both parabolic and triangular cos $2\psi$ loads by the response matrix method and by the amplification factor method. The amplitudes are shown in Figs. 7 and 8. For the parabolic load, which tends to excite the first mode, the agreement is good, especially at the root end. When the triangular load is applied, however, the other modes contribute enough to cause a considerable error in the results of the amplification factor method.

## Conclusions

The method developed in this paper is believed to offer considerable advantages over previous methods. The response matrices, in addition to simplifying calculation of blade response under various loadings, provide general information as to the dynamical properties of the blade. The possible effects of high harmonic loadings and more detailed calculation of loads may be obtained.

(Continued on page 172)

# Heat Transfer to an Incompressible Turbulent Boundary Layer and Estimation of Heat-Transfer Coefficients at Supersonic Nozzle Throats*

MERWIN SIBULKIN†

*California Institute of Technology*

ABSTRACT

An approximate solution is obtained for the heat transfer to an incompressible turbulent boundary layer with arbitrary free-stream-velocity and surface-temperature distributions. The analysis is based on the simultaneous solution of the boundary-layer momentum and energy integral equations and employs several simplifying assumptions, the most important of which is the approximation that the boundary-layer velocity and total-temperature profiles and the skin-friction coefficient are independent of pressure gradient. Solutions are given for two-dimensional and axisymmetric flows.

Although the flow in supersonic nozzles is not incompressible, an adaptation of the aforementioned result, termed the quasi-incompressible solution, is suggested for calculating the heat transfer to such nozzles. In order to estimate rapidly the maximum rate of heat transfer which occurs near the throat of a supersonic nozzle, a throat approximation is developed which involves only the nozzle supply conditions, throat opening, and throat radius of curvature.

The application of these solutions to a sample nozzle gave the following results using the quasi-incompressible analysis: (1) The heat-transfer coefficients based on solution of both the momentum and energy equations were between 0 and 15 per cent lower than the values based on a solution of the momentum equation alone, and (2) the heat-transfer coefficients that included the effects of variable wall temperature were between 0 and 15 per cent lower than the values obtained assuming constant wall temperature. The throat-approximation, heat-transfer coefficients were within 10 per cent of the corresponding quasi-incompressible values.

NOMENCLATURE

$a$ = speed of sound
$A$ = flow area
$B$ = constant defined by assumption (IX)
$c_f$ = local skin-friction coefficient $\equiv 2\tau_w/\rho_1 u_1^2$
$c_p$ = specific heat at constant pressure
$C_1$, $C_2$ = constants
$F$ = defined by Eq. (15)
$G$ = defined by Eq. (30)
$h$ = (1) heat-transfer coefficient $\equiv q_w/(T_e - T_w)$; (2) specific enthalpy
$H$ = $\delta^*/\theta$
$L^*$ = radius of curvature at nozzle throat $\equiv 2/(d^2t/dx^2)^*$ or $1/(d^2r/dx^2)^*$
$m$ = mass flow rate
$M$ = Mach Number
$p$ = static pressure
$p_0$ = nozzle supply pressure
$Pr$ = Prandtl Number
$q$ = heat-transfer rate per unit area (positive toward wall)
$Q$ = heat-transfer rate from fluid
$r$ = (1) radius, distance from surface of axisymmetric nozzle to center line; (2) recovery factor $\equiv (T_e - T_1)/(T_0 - T_1)$
$R$ = gas constant
$St$ = Stanton Number $\equiv h/c_p\bar{\rho}u_1$
$t$ = total height of two-dimensional-flow nozzle $\equiv A/w$
$T$ = static temperature
$T_e$ = equilibrium temperature—i.e., local wall temperature for case of zero heat transfer to wall
$T^0$ = total temperature
$T_0$ = nozzle supply temperature
$u$ = velocity in $x$ direction
$w$ = width of two-dimensional-flow nozzle
$W$ = rate of work done on fluid
$x$ = distance parallel to wall
$y$ = distance perpendicular to wall
$\beta$ = free-stream velocity gradient at nozzle throat
$\gamma$ = ratio of specific heats
$\delta$ = dynamic-boundary-layer thickness
$\delta^*$ = boundary-layer displacement thickness $\equiv \int_0^\infty \left(1 - \frac{\rho u}{\rho_1 u_1}\right) dy$
$\Delta$ = thermal-boundary-layer thickness
$\epsilon$ = eddy diffusivity $\equiv \tau/(\partial u/\partial y)$
$\theta$ = boundary-layer momentum thickness $\equiv \int_0^\infty \frac{\rho u}{\rho_1 u_1}\left(1 - \frac{u}{u_1}\right) dy$
$\kappa$ = eddy conductivity $\equiv -q/(\partial T/\partial y)$
$\mu$ = viscosity
$\nu$ = kinematic viscosity
$\rho$ = static density
$\rho_0$ = nozzle supply density
$\tau$ = shearing stress
$\phi$ = boundary-layer energy thickness $\equiv \int_0^\infty \frac{\rho u}{\rho_1 u_1}\left(\frac{T_0 - T^0}{T_e - T_w}\right) dy$

***Subscripts***

$i$ = corresponding value for incompressible flow
$t$ = value determined by throat-approximation method
$w$ = local value at wall
1 = local value at boundary-layer edge

***Superscripts***

$(\ )^*$ = value at $M = 1$ (except $\delta^*$)
$(\bar{\ })$ = mean value

Received December 3, 1954.

* This paper presents the results of one phase of research carried out at the Jet Propulsion Laboratory, California Institute of Technology, under joint sponsorship of the Department of the Army, Ordnance Corps (under Contract No. DA-04-495-Ord 18), and the Department of the Air Force.

† Research Engineer, Jet Propulsion Laboratory.

## (I) Introduction

Knowledge of the rate of heat transfer to the walls of supersonic nozzles is desirable for the design of rocket nozzles and of hypersonic-wind-tunnel nozzles. The calculation of the heat transfer to such a nozzle is a boundary-layer problem with variable free-stream velocity and, in many cases, variable wall temperature. In this report an approximate solution to this problem will be given for the case of a turbulent boundary layer. The solution employs several simplifications of the problem, including the assumption (in part of the analysis) that the flow is incompressible. This assumption greatly simplifies the analysis and has the advantage of enabling one to integrate the boundary-layer equations for analytic free-stream-velocity distributions. This result will in turn make it possible to visualize more directly the relative importance of changes in various parameters (such as stagnation temperature, radius of curvature at the throat, etc.) on the heat-transfer coefficient.

An attempt will be made to present the analysis in a manner that will facilitate its application to engineering problems. Accordingly, the numbers of equations expressing final results will be placed in brackets, and the assumptions made during the analysis will be designated by Roman numerals.

## (II) Analysis

The analysis is based on the boundary-layer integral equations for axisymmetric flow which include the equations for two-dimensional flow as a special case. The momentum equation is

$$\frac{d\theta}{dx} + \left(\frac{H+2}{u_1}\frac{du_1}{dx} + \frac{1}{r}\frac{dr}{dx} + \frac{1}{\rho_1}\frac{d\rho_1}{dx}\right)\theta = \frac{\tau_w}{\rho_1 u_1^2} \quad (1)$$

and can be obtained in this form by extending the derivation in reference 1 (Cf. pp. 131–134). The energy equation expressed in a similar form [a derivation is given in Appendix (A)] is

$$\frac{d\phi}{dx} + \left(\frac{1}{u_1}\frac{du_1}{dx} + \frac{1}{r}\frac{dr}{dx} + \frac{1}{T_e - T_w}\frac{d(T_e - T_w)}{dx} + \frac{1}{\rho_1}\frac{d\rho_1}{dx}\right)\phi = \frac{q_w}{c_p\rho_1 u_1(T_e - T_w)} \quad (2)$$

where the boundary-layer energy thickness $\phi$ is defined in terms of total temperature as

$$\phi \equiv \int_0^\infty \frac{\rho u}{\rho_1 u_1}\left(\frac{T_0 - T^0}{T_e - T_w}\right) dy$$

In these equations the axis of $x$ is parallel and the axis of $y$ is perpendicular to the wall. When the boundary layer is turbulent, it is to be understood that the equations refer to mean values of the fluctuating variables. In addition to the Prandtl boundary-layer assumptions (Cf. pp. 116–120 of reference 1) made in deriving Eqs. (1) and (2), it has been assumed that

$$c_p = \text{constant} \quad (I)$$

that the flow is adiabatic outside of the boundary layer—i.e.,

$$T^0 = T_0 \text{ (outside of boundary layer)} \quad (II)$$

and that for axisymmetric flow the boundary layer is relatively thin, so that

$$1 + (y/r) \cong 1 \text{ (in boundary layer)} \quad (III)$$

### (A) *Solution of Momentum Equation*

The analysis is now restricted to the case of incompressible flow by assuming that

$$\rho = \bar{\rho} = \text{constant} \quad (IV)$$

although the analysis will be subsequently applied to cases that are not strictly incompressible. Some advantages of this procedure are mentioned in Section (I). Further simplification of the analysis is accomplished by restricting it to cases (in which supersonic nozzles are included) having a pressure gradient in the flow direction which is either favorable or only moderately adverse. Although the pressure gradient in these cases strongly affects the growth of the boundary-layer thickness $\delta$ with $x$, for turbulent boundary layers it does not as greatly affect the local skin-friction relation or the shapes of the boundary-layer profiles. Consequently the following approximations are adopted:

$$c_f = f(u_1\delta/\bar{\nu}), \quad u/u_1 = g(y/\delta) \quad (V)$$

Assumptions (IV) and (V) have the important property of making the solution of the momentum equation independent of the temperature distribution in the boundary layer and thus independent of the solution of the energy equation; the energy equation, however, is still dependent upon the momentum equation.

For the specific form of the first part of assumption (V) an adaptation of the Blasius turbulent-pipe-flow result (Cf. pp. 18–21 of reference 2) is used.

$$\tau_w/(\bar{\rho}u_1^2) = 0.0225\,[\bar{\nu}/(u_1\delta)]^{1/4} \quad (VI)$$

The Blasius law is recommended for turbulent flows having pipe Reynolds Numbers up to $10^5$ which is equivalent to $u_1\delta/\nu < 6 \times 10^4$ (the corresponding flat-plate Reynolds Number $u_1x/\nu$ is $3 \times 10^6$). For the form of the second part of assumption (V) the frequently used power law $u/u_1 = (y/\delta)^n$ is adopted. It can be shown (Cf. pp. 18–21 of reference 2) that there is a connection between $n$ and the exponent in the friction law (VI). For a friction-law exponent of $1/4$, this relation gives

$$u/u_1 = (y/\delta)^{1/7} \quad (VII)$$

Combining assumptions (IV) and (VII) with the definitions of $H$ and $\theta$ gives

$$H = 9/7, \quad \theta/\delta = 7/72 \quad (3)$$

After substituting assumptions (IV) and (VI) and Eq. (3) in Eq. (1) and after algebraic manipulation, the following expression is obtained:

$$(d\delta^{8/4}/dx) + [(d/dx)\ (\ln r^{8/4}u_1^{115/28})]\ \delta^{8/4} = (5/4)(0.231)\ (\bar{\nu}/u_1)^{1/4} \quad (4)$$

which is a linear, first-order equation in $\delta^{8/4}$. Applying the boundary condition

$$\delta = \delta_0,\ u_1 = u_{1_0},\ \text{and}\ r = r_0\ \text{at}\ x = 0 \quad (5)$$

and integrating Eq. (4) gives

$$\delta^{8/4} = \frac{0.289\bar{\nu}^{1/4}}{r^{8/4}u_1^{115/28}} \int_0^x r^{8/4}\, u_1^{27/7}\, dx_1 + \delta_0^{8/4}\left(\frac{r_0}{r}\right)^{8/4}\left(\frac{u_{1_0}}{u_1}\right)^{115/28} \quad [6]$$

The corresponding equation for a cylinder in axial flow or for two-dimensional flow can be obtained by substituting $r$ = constant in Eq. [6].

### (B) *Solution of Energy Equation*

In order to solve the energy equation in a manner comparable to the solution of the momentum equation, it is necessary to find an expression for the heat flux $q_w$ in terms of local boundary-layer conditions and to derive an expression for $\phi$ in terms of assumed velocity and total-temperature profiles.

(1) *Modified Reynolds Analogy for* $\Delta \neq \delta$.—For flow over a flat plate, $q_w$ can be expressed in terms of $\tau_w$ by the Reynolds analogy approach. A possible extension of this approach to the case for which the pressure gradient is variable will be derived.

If for the case of turbulent flow over a flat plate the assumptions are made that the Prandtl Number $Pr = 1$ and the turbulent Prandtl Number $c_p\epsilon/\kappa = 1$ (which are reasonable approximations for gases), it can be shown[3] that $\Delta = \delta$ and

$$(T^0 - T_w)/(T_0 - T_w) = u/u_1$$

If assumption (VII) is made, the total-temperature profile becomes

$$(T^0 - T_w)/(T_0 - T_w) = (y/\Delta)^{1/7} \quad \text{(VIII)}$$

since in this case $\Delta = \delta$. An additional approximation is now made that the total-temperature profile is also given by assumption (VIII) for the case of variable pressure gradient although in this case $\Delta \neq \delta$.

Combining assumptions (VII) and (VIII) gives

$$(\partial T^0/\partial y)/(\partial u/\partial y) = [(T_0 - T_w)/u_1]\ (\delta/\Delta)^{1/7} \quad (7)$$

and using the definitions of $\epsilon$ and $\kappa$ and the assumption $c_p\epsilon/\kappa = 1$ gives

$$(\partial T^0/\partial y)/(\partial u/\partial y) = (1/c_p)\ [(q + \tau u)/\tau] \quad (8)$$

By combining Eqs. (7) and (8) and assuming that the result holds at $y = 0$, the following equation is obtained:

$$q_w/\tau_w = \{[c_p(T_0 - T_w)]/u_1\}\ (\delta/\Delta)^{1/7} \quad (9)$$

which reduces to Reynolds analogy for $\Delta = \delta$. An approximate allowance for $Pr \neq 1$ is now made by modifying Eq. (9) to

$$St \equiv q_w/[\bar{\rho}u_1c_p(T_e - T_w)] = [1/(Pr^m)]\ [\tau_w/(\bar{\rho}u_1^2)]\ (\delta/\Delta)^{1/7} \quad (10)$$

where $m$ is a constant. For the case of a flat plate with constant wall temperature, Rubesin[4] found that $\delta/\Delta = Pr^{7/12}$. By requiring that for this case Eq. (10) reduce to the Colburn relation[5]

$$St = c_f/2(Pr)^{2/3}$$

it is found that $m = 3/4$. Finally, combining assumption (VI) with Eq. (10) and $m = 3/4$ gives

$$St \equiv h/(\bar{\rho}u_1c_p) = [0.0225/(Pr^{3/4})] \times [\bar{\nu}/(u_1\delta)]^{1/4}(\delta/\Delta)^{1/7} \quad (11)$$

(2) *Calculation of the Boundary-Layer Energy Thickness* $\phi$.—The definition of $\phi$ can be rewritten as

$$\phi \equiv \int_0^\Delta \frac{\rho u}{\rho_1 u_1}\left(\frac{T_0 - T^0}{T_0 - T_w}\right)\left(\frac{T_0 - T_w}{T_e - T_w}\right) dy \quad (12)$$

It is now assumed that

$$(T_0 - T_w)/(T_e - T_w) \equiv B = \text{constant} \quad \text{(IX)}$$

noting that when the heat-transfer rate is not zero, $B \to 1$ as $M \to 0$. Substituting assumptions (IV), (VII), (VIII), and (IX) in Eq. (12) and integrating,

$$\phi = (7/72)B\Delta(\Delta/\delta)^{1/7} = (7/72)B\delta(\Delta/\delta)^{8/7} \quad (13)$$

It may be noted that $\phi = \theta$ for $\Delta = \delta$ and $B = 1$.

(3) *Integration of Energy Equation.*—After substituting Eqs. (11) and (13) in Eq. (2) and after algebraic manipulation, one obtains

$$\frac{8}{9}\delta^{8/4}\frac{d}{dx}\left(\frac{\Delta}{\delta}\right)^{9/7} + \left\{\delta^{1/4}\frac{d\delta}{dx} + \left[\frac{1}{u_1}\frac{du_1}{dx} + \frac{1}{r}\frac{dr}{dx} + \frac{1}{T_e - T_w}\frac{d(T_e - T_w)}{dx}\right]\delta^{8/4}\right\}\left(\frac{\Delta}{\delta}\right)^{9/7} = \frac{0.231}{BPr^{2/3}}\left(\frac{\bar{\nu}}{u_1}\right)^{1/4} \quad (14)$$

which describes the variation of $\Delta/\delta$ with $x$ in terms of the variation of $\delta$ with $x$ for the prescribed external conditions given by the terms in the bracket.

Choosing the coordinate system so that

$$\text{at}\ x = 0,\ \text{either}\ \delta\ \text{or}\ u_1\ \text{or}\ r = 0 \quad \text{(X)}$$

Eq. [6] becomes

$$\left.\begin{aligned}\delta^{8/4} &= (5/4)\ [0.231/(r^{8/4}u_1^{27/7})]\ (\bar{\nu}/u_1)^{1/4}\ F(x)\\ \text{where}\qquad F(x) &\equiv \int_0^x r^{8/4}\, u_1^{27/7}\, dx_1\end{aligned}\right\} \quad (15)$$

Then

$$\delta^{1/4}\frac{d\delta}{dx} = 0.231\left(\frac{\bar{\nu}}{u_1}\right)^{1/4}\left[1 - F\left(\frac{115}{28}\frac{1}{r^{8/4}u_1^{84/7}}\frac{du_1}{dx} + \frac{5}{4}\frac{1}{r^{8/4}u_1^{27/7}}\frac{dr}{dx}\right)\right] \quad (16)$$

Substituting Eqs. (15) and (16) in Eq. (14) and noting that $r^{8/4}u_1^{27/7} = dF/dx$, gives

$$\frac{d}{dx}\left(\frac{\Delta}{\delta}\right)^{9/7} + \left\{\frac{d}{dx}\left[\ln \frac{F^{9/10}(T_e - T_w)^{9/8}}{u_1^{18/7}}\right]\right\}\left(\frac{\Delta}{\delta}\right)^{9/7} = \frac{9}{10}\frac{1}{B}\frac{1}{Pr^{2/3}}\frac{r^{5/4}u_1^{27/7}}{F} \quad (17)$$

which is a linear, first-order equation in $(\Delta/\delta)^{9/7}$. As a boundary condition it is assumed that $T_w = T_e$ for $x < x_0$, or

$$\Delta = \Delta/\delta = 0 \qquad \text{at } x = x_0 \quad (18)$$

Integrating Eq. (17) with condition (18) results in

$$\left(\frac{\Delta}{\delta}\right)^{9/7} = \frac{9}{10}\frac{1}{B}\frac{1}{Pr^{2/3}}\frac{u_1^{18/7}}{\left(\int_0^x r^{5/4}u_1^{27/7}\,dx_1\right)^{9/10}(T_e - T_w)^{9/8}} \times \int_{x_0}^x \frac{u_1^{9/7}r^{5/4}(T_e - T_w)^{9/8}}{\left(\int_0^{x_1} r^{5/4}u_1^{27/7}\,dx_2\right)^{1/10}}\,dx_1 \quad [19]$$

For $x_0 = 0$, condition (18) is not appropriate since $\delta = 0$, but it can be shown that Eq. [19] is still valid. The corresponding equation for a cylinder in axial flow or for two-dimensional flow can be obtained by substituting $r$ = constant in Eq. [19].

### (C) *Solutions for $\Delta/\delta$ for Special Cases of $u_1(x)$ and $T(x)$*

Eq. [19] may be integrated for special free-stream velocity and wall-temperature distributions. The following are some solutions that may be of general interest:

(1) *Flat Plate with Varying Wall Temperature.*—Substituting $u_1$ = constant and $r$ = constant in Eq. [19] yields

$$\left(\frac{\Delta}{\delta}\right)^{9/7} = \frac{9}{10}\frac{1}{B}\frac{1}{Pr^{1/3}}\frac{1}{(T_e - T_w)^{9/8}x^{9/10}} \times \int_{x_0}^x \frac{(T_e - T_w)^{9/8}}{x_1^{1/10}}\,dx_1 \quad (20)$$

In the case of a flat plate with a step function in the wall temperature, $(T_e - T_w)$ is constant and different from zero downstream from $x_0$ giving

$$(\Delta/\delta)^{9/7}Pr^{2/3}B = 1 - (x_0/x)^{9/10} \quad (21)$$

which, when combined with Eq. (11) and the result of Eq. [6] for the case of a flat plate with $\delta = 0$ at $x = 0$, yields

$$\left.\begin{aligned} St &= St'(x)\,[1 - (x_0/x)^{9/10}]^{-1/9} \\ &\text{for } x > x_0, \text{ where} \\ St' &\equiv [0.0288\,B^{1/9}/(Pr^{2/3})]\,[\bar{\nu}/(u_1x)]^{1/5} \end{aligned}\right\} \quad (22)$$

is the local value of Stanton Number for a constant-temperature flat plate. (In many cases the value of $B$ will be near 1, and $B^{1/9}$ can be neglected.) This result is similar to that obtained by Rubesin[4] and could be used to find the heat-transfer-coefficient distribution on a flat plate with variable wall temperature in the manner shown in reference 4, instead of using Eqs. (20), [6], and [33].

In the case of a flat plate with constant wall temperature, $x_0 = 0$, and Eq. (21) gives

$$\delta/\Delta = B^{7/9}Pr^{7/12} \quad (23)$$

which, for $B = 1$, was the value used in deriving Eq. (11).

(2) *Two-Dimensional Flow with $u_1 = ax^n$ and $(T_e - T_w) = bx^k$.*—In this case $x_0 = 0$, and Eq. [19] can be integrated as

$$(\Delta/\delta)^{9/7}\,Pr^{2/3}B = [(27/7)n + 1]/[n + 1 + (5/4)k] \quad (24)$$

In the case of two-dimensional flow with $u_1 = ax$ and $(T_e - T_w)$ = constant, which will be used later, $n = 1$ and $k = 0$, thereby reducing Eq. (24) to

$$(\Delta/\delta)^{9/7}Pr^{2/3}B = 17/7 \quad (25)$$

(3) *Initial Variation of $\Delta/\delta$ for Arbitrary $u_1(x)$ and $r$ and for $(T_e - T_w)$ Constant.*—In this case $x_0 = 0$. The velocity distribution is expanded around $x = 0$ as

$$u_1 = u_{1_0}[1 + (ax/u_{1_0}) + \ldots] \quad (26)$$

and only the first two terms are retained. This step limits the approximation to values of $x$ for which

$$(x/2)\,(d^2u_1/dx^2)_0 \ll (du_1/dx)_0 \quad (27)$$

When in addition $x$ is limited to values for which

$$ax/u_{1_0} \ll 1 \quad (28)$$

the result of substituting Eq. (26) in Eq. [19] and retaining only terms of the first order in $ax/u_{1_0}$ is

$$(\Delta/\delta)^{9/7}\,Pr^{2/3}B = 1 + (180/133)\,(ax/u_{1_0}) + \ldots \quad (29)$$

(4) *Preliminary Step for Numerical Integration of Eq. [19].*—For nonanalytic free-stream velocity or wall-temperature distribution, Eq. [19] must be integrated numerically. When the momentum and energy boundary layers start at the same point—i.e., $x_0 = 0$—inspection of the last part of Eq. [19]

$$G(x) \equiv \int_0^x \frac{u_1^{9/7}r^{5/4}(T_e - T_w)^{9/8}}{\left(\int_0^{x_1} r^{5/4}u_1^{27/7}\,dx_2\right)^{1/10}}\,dx_1 \quad (30)$$

shows that, in general, the integrand of $G$ is infinite at $x = 0$. Consequently, numerical methods of integration such as Simpson's rule cannot be applied to Eq. [19] until an estimate of an initial value of $G$ has been made. This estimation can be performed most easily by approximating $u_1$, $r$, and $(T_e - T_w)$ by their value at $x = 0$ which, for sufficiently small values of $x$, gives

$$G(x) = (10/9)\,(u_{1_0})^{9/10}r_0^{9/8}(T_e - T_w)_0^{9/8}x^{9/10} \quad (31)$$

## (III) Practical Application of Analysis

In applying the foregoing analysis to a calculation of heat transfer to the walls of a supersonic nozzle, one assumes that the boundary-layer concept applies—i.e., that the effects of skin friction and heat transfer are confined to a portion of the fluid flowing near the

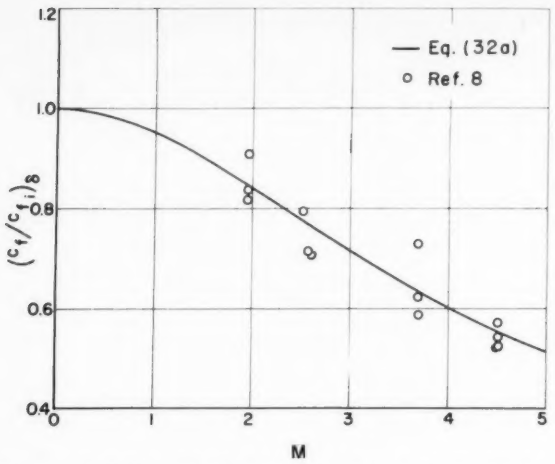


FIG. 1. Variation with Mach Number of the local skin-friction coefficient ratio $c_f/c_{fi}$ where $c_f$ and $c_{fi}$ are evaluated at the same Reynolds Number based on $\delta$.

walls—leaving a core of fluid in the center of the nozzle whose pressure and temperature at each station correspond to an isentropic expansion from supply conditions to the local Mach Number. For a particular nozzle, this assumption can be checked *a posteriori* by calculating the ratio of boundary-layer thickness to nozzle height or radius.

In order to calculate the heat-transfer coefficient $h$ from Eq. (11), it is necessary to select values of $\bar{\rho}$ and $\bar{\nu}$. Although the boundary-layer equations have been integrated using the assumption $\bar{\rho}$ = constant, in applying Eq. (11) better results should be obtained by using local values of density and viscosity. In applying this inconsistent procedure, one takes account of the actual variation of a parameter—e.g., $\rho_1(x)$—whenever it occurs in the equations governing the problem, while formally assuming that the gradient of the parameter—e.g., $d\rho_1/dx$—equals zero wherever it occurs in an equation. The results of this procedure will be termed the quasi-incompressible solution.

For supersonic-wind-tunnel nozzles, values of $\rho_1$, $p_1$, $T_1$, and $u_1$ can generally be calculated with sufficient accuracy in the region between the nozzle entrance and the inflection point by using one-dimensional, isentropic-flow equations. For rocket nozzles having conical diverging sections, one-dimensional flow should be applicable throughout. In addition to its variation with $x$, the temperature and therefore the density and viscosity also vary across the boundary layer at a given $x$ position. The pressure, however, is constant across a boundary layer at a given $x$ position (Cf. p. 120, reference 1), thus reducing the problem of choosing $\bar{\rho}$ and $\bar{\nu}$ to one of choosing $\bar{T}$.

Therefore, to apply Eq. (11), one must choose a particular expression for $\bar{T}$; a reasonable choice is to assume that

$$\bar{T} = (T_1 + T_w)/2 \qquad \text{(XI)}$$

For heat transfer to a plate in low-speed flow, this expression is suggested by Eckert (Cf. pp. 115 and 120, reference 6). Tucker (Cf. Fig. 1, reference 7), has also used assumption (XI) and has shown that it gives a variation of $(c_f/c_{fi})_x$ with $M$ that agrees with theory for the insulated plate case; the subscript $x$ means that $c_f$ and $c_{fi}$ are evaluated at the same Reynolds Number based on $x$. It may be of interest to compare the effect of assumption (XI) with the values measured on an insulated flat plate by Coles;[8] for the present application [Cf. assumption (VI)], interest lies in the variation of $(\tau_w/\tau_{wi})_\delta$ with $\bar{T}$ (the subscript $\delta$ implying evaluation at the same Reynolds Number based on $\delta$). This relation depends to a small extent on the variation of $\mu$ with $T$, but assuming that $\mu \propto T^{3/4}$ and that for $M \geq 0$

$$\tau_w/(\bar{\rho}u_1^2) \propto [\bar{\nu}/(u_1\delta)]^{1/4}$$

results in the relation

$$(c_f/c_{fi})_\delta \equiv (\tau_w/\tau_{wi})_\delta = (\bar{T}/T_1)^{-9/16} \qquad (32)$$

When the heat flux $q$ is small, $T_w \cong T_e$, and substituting assumption (XI) in Eq. (32) gives

$$(c_f/c_{fi})_\delta = \{1 + [r(\gamma - 1)/4]M^2\}^{-9/16} \qquad (32a)$$

where $r$ is the recovery factor. Eq. (32a) was evaluated for $r = 0.9$ and $\gamma = 1.4$, and the results are plotted in Fig. 1, together with the values measured by Coles.[8] For a fixed value of $M$ the measured values of $(c_f/c_{fi})_\delta$ decrease with increasing Reynolds Number based on $\delta$, but for engineering calculations the agreement may be satisfactory.

Eq. (11) can be modified by expressing $\bar{\rho}$ as

$$\bar{\rho} = \rho_1(T_1/\bar{T}) = [p_0/(RT_0)]\,(\rho_1/\rho_0)\,(T_1/\bar{T})$$

and rearranged to give

$$h = 0.0225\,\frac{c_p}{Pr^{2/3}R}\,\frac{p_0}{T_0}\,\frac{\rho_1}{\rho_0}\,\frac{T_1}{\bar{T}} \times u_1^{3/4}\left(\frac{\bar{\nu}}{\delta}\right)^{1/4}\left[\left(\frac{\Delta}{\delta}\right)^{9/7} Pr^{3/4}B\right]^{-1/9} B^{1/9} \qquad [33]$$

In many cases the value of $B$ will be near 1, and $B^{1/9}$ can be neglected.

In evaluating Eq. [6] to find $\delta$, the correct value of $\bar{\nu}$ would be an average value not only across the boundary layer but also between 0 and $x$. However, considering (1) the approximate character of the equations, (2) the fact that only $\delta^{1/4}$ affects the heat transfer, and (3) the relatively greater importance of the higher values of $u_1$ near $x$ in determining the value of the integral in Eq. [6], it is suggested that the local value of $\bar{\nu}$ used in Eq. [33] be used in Eq. [6].

For most nozzle designs it will not be possible to choose a point $x = 0$ at which either $\delta$ or $u_1$ or $r = 0$ as required by assumption (X). However, it can be seen from Eq. [6] that $\delta_0$ (the boundary-layer thickness at $x = 0$) only affects the term

$$\delta_0^{5/4}(r_0/r)^{5/4}(u_{1_0}/u_1)^{115/28}$$

Since $u_{1_0}/u_1$ decreases rapidly near the nozzle throat, the effect of $\delta_0$ on $\delta$ decreases very rapidly. This means,

for most cases, that assuming $\delta_0 = 0$ at some convenient point near the nozzle entrance where the velocity is low (e.g., $M < 0.1$) gives a negligible error in $\delta$ near the nozzle throat.

Since the wall temperature $T_w(x)$ will not in general be known beforehand, and iterative procedure can be used when a more accurate value of $h$ is desired. One iteration should be sufficient, and a possible sequence of steps in calculating the heat transfer to a supersonic nozzle may be summarized as follows:

(1) Knowing $p_0$, $T_0$, and $t(x)$ or $r(x)$ and assuming a particular distribution (or a constant value) for $T_w$, calculate $u_1$, $p_1$, $T_1$, and $\rho_1/\rho_0$ as functions of $x$ from the one-dimensional-flow equations; calculate $\bar{T}(x)$ from assumption (XI); look up $\bar{\nu}(p_1, \bar{T})$ in a table of kinematic viscosity (e.g., reference 9, for air).

(2) Having chosen a coordinate system such that $\delta = 0$ at $x = 0$, calculate $\delta(x)$ from Eq. [6] using the $\bar{\nu}(x)$ found in step (1).

(3) Calculate $(\Delta/\delta)^{9/7} Pr^{3/4} B$ as a function of $x$ from Eq. [19] using assumed $(T_e - T_w)$ distribution; begin numerical integration by applying Eq. (31).

(4) Calculate $h(x)$ from Eq. [33] using $\bar{T}(x)$ and $\bar{\nu}(x)$ found in step (1).

(5) Calculate $T_w(x)$ for the particular nozzle-wall thickness and material and the known (or assumed) coolant-side, heat-transfer coefficient using the $h(x)$ found in step (4) as the gas-side, heat-transfer coefficient; calculate $T_e(x)$ assuming a turbulent-boundary-layer recovery factor (a suggested value is $r = 0.9$); recalculate $\bar{T}(x)$ and $\bar{\nu}(x)$.

(6) Recalculate $(\Delta/\delta)^{9/7} Pr^{3/4} B$ for variable $(T_e - T_w)$ found in step (5).

(7) Recalculate $h$ using $\bar{T}$ and $\bar{\nu}$ found in step (5) and $(\Delta/\delta)^{9/7} Pr^{3/4} B$ found in step (6).

(8) Calculate the heat-transfer rate $q \equiv h(T_e - T_w)$ using $h$ found in step (7) and $(T_e - T_w)$ found in step (5).

For the aforementioned procedure to be consistent, it would be necessary to recalculate $\delta(x)$ for the values of $\bar{\nu}(x)$ found in step (5), but this refinement is not considered to be worth the additional labor.

## (IV) Estimation of Heat-Transfer Coefficients at Supersonic Nozzle Throats

It can be shown (Cf. p. 22 and Fig. 33 of reference 10) that in a supersonic nozzle the maximum value of the heat-transfer coefficient $h$ occurs near the nozzle throat. Consequently a rapid method of estimating the value of $h$ at nozzle throats may be of value (1) in determining the maximum heat-transfer condition in a variable-Mach-Number hypersonic nozzle for different supply conditions and (2) in determining the relative importance of $p_0$, $T_0$, and nozzle geometry on the peak value of $h$.

This throat approximation is based upon the observation, referring to Eq. [6], that for a monotonically increasing $u_1(x)$ the previous history of the boundary layer has a rapidly diminishing effect on downstream values of the boundary-layer thickness. Consequently $u_1(x)$ is approximated by a linear velocity distribution having the same magnitude and gradient as $u_1(x)$ at the nozzle throat; in addition, it is assumed that the boundary layer begins at the point where this hypothetical $u_1$ begins; that is, the following assumptions are made:

$$u_1 = \beta x \tag{XII}$$

$$\delta = x = 0 \qquad \text{at } u_1 = 0 \tag{XIII}$$

It can be shown [Appendix (B)] that for a two-dimensional-flow nozzle, assuming one-dimensional, isentropic flow,

$$\beta \equiv (du_1/dx)^* = \sqrt{\gamma R}[2/(\gamma + 1)] \sqrt{T_0/(t^* L^*)} \tag{34}$$

and since $x^* = a^*/\beta$,

$$x^* = \sqrt{(\gamma + 1)/2} \sqrt{t^* L^*} \tag{34a}$$

For an axisymmetric nozzle, Eqs. (34) and (34a) apply if $t^*$ is replaced by $r^*$.

The two-dimensional- and axisymmetric-flow nozzles are now considered separately.

### (A) *Two-Dimensional-Flow Nozzle*

Substituting Eqs. (34) and (34a) and assumptions (XII) and (XIII) in Eq. [6] gives upon integration

$$\left.\begin{aligned} \delta_t &= C_1 \frac{(\bar{\nu}^*)^{1/5} (t^* L^*)^{2/5}}{T_0^{1/10}} \\ \text{where} \qquad C_1 &\equiv \frac{0.1048}{(\gamma R)^{1/10}} \left(\frac{\gamma + 1}{2}\right)^{1/2} \end{aligned}\right\} \tag{35}$$

For the throat approximation, it is assumed that $(T_e - T_w)$ is constant, a fact that enables one to use a previously derived result [Cf. Eq. (25)] for $[(\Delta/\delta)^{9/7} Pr^{3/4} B]_t$. However, since Eq. [19] contains the factor $u_1^{27/7}$ as compared with Eq. [6] which depends upon $u_1^{27/7}$, the approximation $u_1 = \beta x$ cannot be expected to yield as accurate values of $[(\Delta/\delta)^{9/7} Pr^{3/4} B]_t$ as of $\delta_t$. This fact should not greatly affect $h$, however, since the factor $[(\Delta/\delta)^{9/7} Pr^{3/4} B]_t$ is raised to the $1/9$ power.

Finally, substituting Eqs. [35] and (25) in Eq. [33] gives

$$\left.\begin{aligned} h_t &= C_2 \frac{p_0 (\bar{\nu}^*)^{1/5}}{T_0^{3/5} (t^* L^*)^{1/10}} \left(\frac{T_1}{\bar{T}}\right) \\ \text{where} \qquad C_2 &\equiv 0.0226 \left(\frac{2}{\gamma + 1}\right)^{1/2} \frac{\gamma^{3/5}}{R^{3/5}} \frac{c_p}{Pr^{2/3}} \end{aligned}\right\} \tag{36}$$

Since $\bar{\nu}^*$ is a function of $p_0$, $T_0$, and $T_w$, it may be of interest, when considering the effect of these parameters, to eliminate $\bar{\nu}^*$ from Eq. [36]. Assuming that $\mu \propto T^{3/4}$ and low rates of heat transfer (i.e., $T_w \cong T_e \cong T_1$) gives

$$h_t \propto \frac{p_0^{4/5}}{T_0^{1/4} (t^* L^*)^{1/10}} \tag{37}$$

An interesting result given by Eq. [36] is that changes in the radius of curvature at the throat $L^*$ will have relatively little effect on $h_t$.

### (B) *Axisymmetric-Flow Nozzle*

In order to integrate Eq. [6] for an axisymmetric-flow nozzle, one must, in addition to making assumptions (XII) and (XIII), select a particular nozzle shape in the region $0 > x < x^*$. Approximating the actual nozzle shape $r(x)$ by a parabola having at $x = x^*$ the same radius of curvature $L^*$ as $r(x)$ gives

$$r/r^* = 1 + [(x - x^*)^2/(2r^*L^*)] \qquad \text{(XIV)}$$

Then integrating Eq. [6] numerically gives

$$\delta_t = 1.04C_1 \frac{(\bar{\nu}^*)^{1/5}(r^*L^*)^{2/5}}{T_0^{1/10}} \qquad [35a]$$

Assuming that $(T_e - T_w)$ is constant and using assumptions (XII), (XIII), and (XIV) give upon numerical integration of Eq. [19]

$$[(\Delta/\delta)^{9/7}Pr^{3/4}B]_t = 2.60 \qquad (38)$$

which when raised to the $^1/_9$ power is within 1 per cent of the two-dimensional value given by Eq. (25). Substituting Eqs. [35a] and (38) in Eq. [33] then gives, within 2 per cent,

$$h_t = C_2 \frac{p_0(\bar{\nu}^*)^{1/5}}{T_0^{2/5}(r^*L^*)^{1/10}} \left(\frac{T_1}{\bar{T}}\right)^* \qquad [36a]$$

If one writes $h_t$ in terms of $\beta$, it can be seen that for both the two-dimensional and the axisymmetric cases, Eqs. [36] and [36a] respectively, one obtains

$$h_t = 0.0226 \left(\frac{2}{\gamma + 1}\right)^{3/10} \frac{\gamma^{2/10}}{R^{7/10}} \frac{c_p}{Pr^{2/3}} \frac{p_0(\bar{\nu}^*)^{1/5}\beta^{1/5}}{T_0^{2/10}} \left(\frac{T_1}{\bar{T}}\right)^* \qquad (39)$$

showing that for the same $\beta$ the difference between axisymmetric and two-dimensional flow has a negligible effect on the heat-transfer coefficient at the nozzle throat.

### (C) *Throat Approximation for Air*

When applying Eqs. [35], [36], [35a], and [36a] a consistent set of units must, of course, be used. As a specific example, consider the case of air flowing through a nozzle at temperatures of the order of 500° to 1,000°F. Taking the properties of air as

$c_p$ = 8.0 B.t.u./slug °R.
$R$ = 1718 lb.ft./slug °R. (= ft.$^2$/sec.$^2$ °R.)
$\gamma$ = 1.40
$Pr$ = 0.71

the values of $C_1$ and $C_2$ are

$$C_1 = 0.052 \text{ sec.}^{1/5} \text{ °R.}^{1/10}/\text{ft.}^{1/5}$$

and

$$C_2 = 0.0027 \text{ B.t.u./lb. sec.}^{4/5} \text{ ft.}^{1/5} \text{ °R.}^{2/5}$$

The variables in Eqs. [35] and [36] must then have the dimensions

$p$, lb. per sq.ft.
$T$, °R.
$t$, $r$, $L$, ft.
$\nu$, ft.$^2$ per sec.
$\delta$, ft.
$h$, B.t.u. per sec. sq.ft. °R.

## (V) Consideration of an Example

To illustrate the results of the analysis, a particular example of a supersonic nozzle will be considered in detail. The values of boundary-layer thickness and heat-transfer coefficient given by the quasi-incompressible solution and the throat-approximation solution will be compared, and where possible, comparison will be made to compressible-flow calculations. Unfortunately there are no satisfactory experimental results, to the author's knowledge, with which to compare the various analyses.

The example chosen is the initial portion of a hypothetical, two-dimensional, hypersonic-wind-tunnel nozzle whose wall coordinates are given by the cubic equation

$$t/t^* = -5.35(x - 1.307)^3 + 26.3(x - 1.307)^2 + 1$$

where $t^* = 0.00701$ ft., $L^* = 5.43$ ft., and $x$ is taken along the nozzle center line. The nozzle shape is shown in part a of Fig. 2 where the ordinate $t/2 = 0$ is the nozzle centerline. In the subsequent calculations the difference in distance between two points on the curved nozzle wall and the component of that distance along the nozzle centerline is neglected.

The nondimensional velocity distribution $u_1/a_0$ is shown in part b of Fig. 2. Corresponding Mach Numbers of interest are $M = 0.01$ at $x = 0$, $M = 1$ at $x = 1.307$, and $M = 3$ at $x = 1.671$. Also shown is the linear velocity distribution assumed in the throat-approximation calculation; for this nozzle $x^* = 0.213$ ft. and, assuming that $T_0 = 1{,}000$°F., $\beta = 8{,}020$ sec.$^{-1}$.

### (A) *Comparison of Boundary-Layer Growth with Compressible-Flow Theory*

The distributions of $\delta$ and $\theta$, shown in parts c and d of Fig. 2, were calculated from Eqs. [6] and (3), assuming that $T_w = T_0 = 1{,}000$°F., that $p_0 = 45.6$ atmospheres, and that the boundary layer is turbulent and begins at $x = 0$. It is interesting to note that $d\delta/dx$ was already negative at the end of the first step in the numerical integration ($M = 0.02$, $x = 0.363$). Values of $\delta$ and $\theta$ were also calculated by the method of Tucker[7] for a compressible turbulent boundary layer with $Pr = 1$ and zero heat transfer (i.e., $T_w = T_0$); the value of the exponent in the velocity-power-law profile was chosen as $^1/_7$. The difference between the calculations of quasi-incompressible and compressible flow (Cf. parts c and d of Fig. 2) increased with increasing $M$; at $M = 3.0$ ($x = 1.671$) the quasi-incompressible value of $\delta$ is 27 per cent lower than the compressible value. However, the heat-transfer coefficient

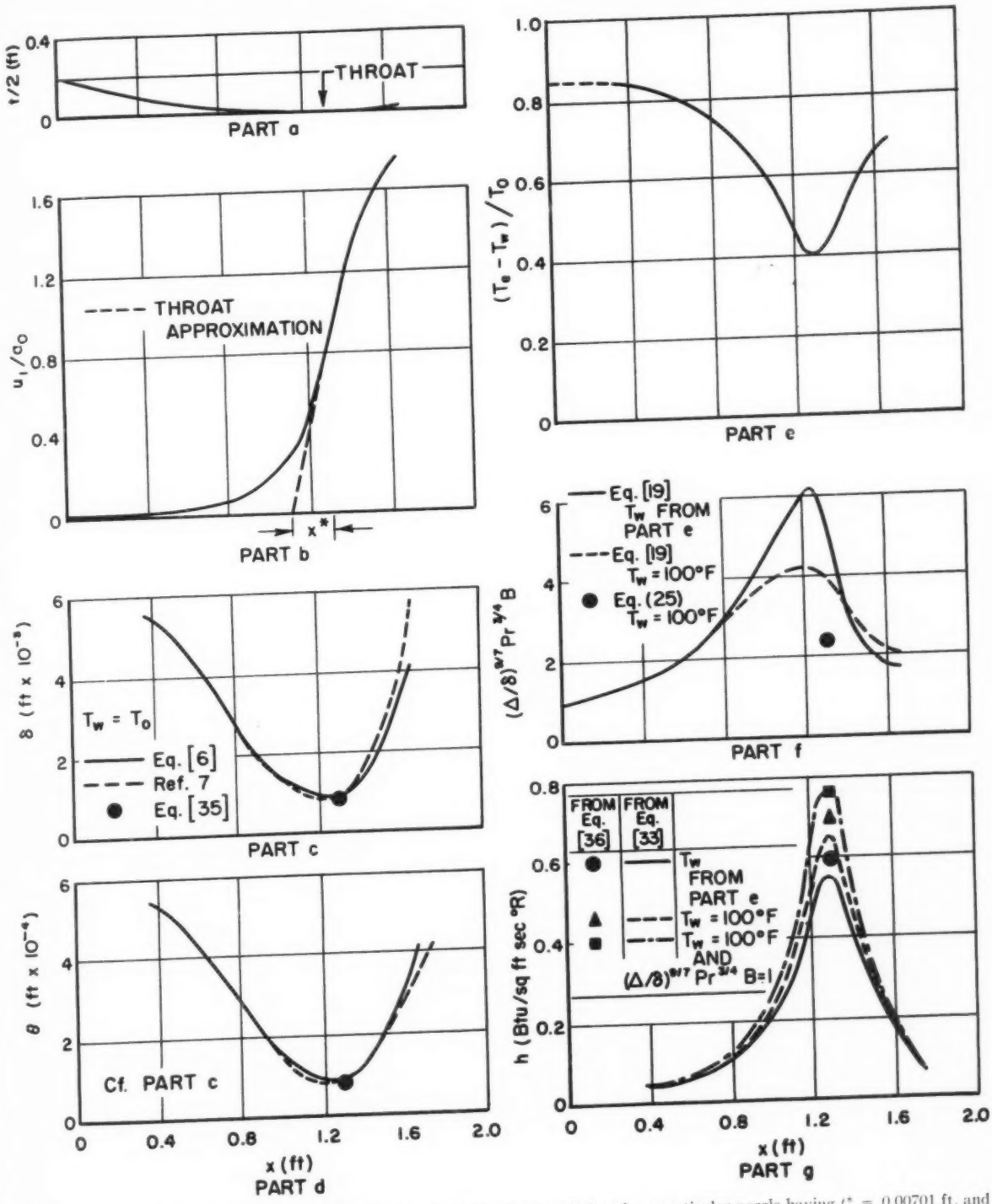


FIG. 2. Sample calculation of boundary-layer growth and heat-transfer coefficient for a particular nozzle having $t^* = 0.00701$ ft. and $L^* = 5.43$ ft. for $p_0 = 45.6$ atmospheres and $T_0 = 1{,}000°F$.

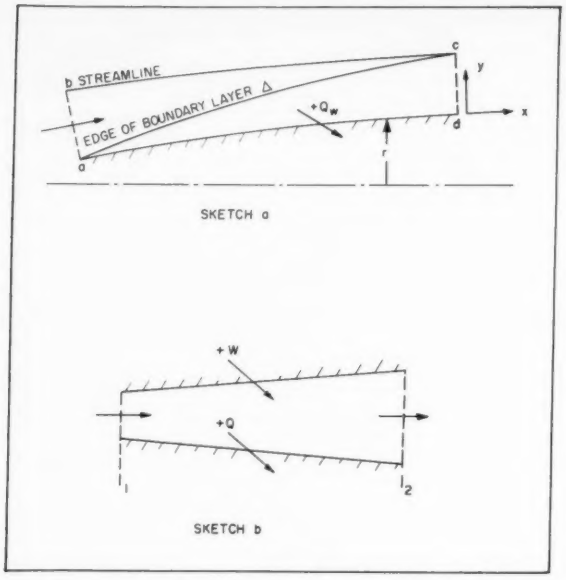


FIG. 3. Control surfaces used in derivation of boundary-layer energy integral equation.

varies as $\delta^{1/4}$; therefore the resulting error in $h$ should be of the order of 6 per cent. At $M = 1$ ($x = 1.307$) the calculations for both $\delta$ and $\theta$ are, apparently by coincidence, in excellent agreement.

### (B) *Results of Solving Energy Equation and of Allowing Wall Temperature To Vary*

A more significant case will now be considered. It is assumed that the walls of the nozzle are cooled by water circulating at a temperature of 100°F. The steps outlined in Section (III) will be applied.

(1) As a first approximation it is assumed that $T_w$ = constant = 100°F.

(2) The distribution of $\delta(x)$ was calculated; the result is similar to that plotted in part c of Fig. 2.

(3) $(\Delta/\delta)^{9/7}Pr^{3/4}B$ was calculated assuming $(T_e - T_w)$ = constant; the result is plotted as the dashed line in part f of Fig. 2.

(4) The corresponding $h(x)$ is plotted as the dashed line in part g of Fig. 2.

(5) It is assumed that the nozzle wall is $^1/_4$-in. copper sheet (thermal conductivity 210 B.t.u. per hr. ft. °F.), that the coolant-side, heat-transfer coefficient is 1 B.t.u. per sq.ft. sec. °F., and that $r = 0.9$. Conduction of heat in the nozzle wall parallel to the surface is neglected. The resulting distribution of $(T_e - T_w)/T_0$ is shown in part e of Fig. 2. For $0 < x < 0.363$, $(T_e - T_w)/T_0$ was assumed constant at its value at $x = 0.363$.

(6) The recalculated value of $(\Delta/\delta)^{9/7}Pr^{3/4}B$ using the variable $(T_e - T_w)$ found in step (5) is plotted as the solid-line curve of part f in Fig. 2.

(7) The recalculated value of $h$ is plotted as the solid-line curve of part g in Fig. 2.

One of the methods which is used in practice to estimate the heat transfer for cases of variable free-stream-velocity distribution is to solve only the momentum equation and then apply the flat-plate analogy $St\ Pr^{2/3} = c_f/2$. This method is equivalent to assuming that $(\Delta/\delta)^{9/7}Pr^{3/4}B = 1$ in Eq. [33]; the result of applying this procedure to the case $T_w = 100$°F. is shown by the uppermost curve of part g in Fig. 2. Considering this procedure as a first approximation, it can be said for this particular case (1) that solving the energy equation lowered the local values of heat-transfer coefficient up to 14 per cent and (2) that including the effect of variable wall temperature further lowered the local heat-transfer coefficients by amounts up to 16 per cent. The effect of variable wall temperature is primarily due to the change in $\bar{T}(x)$ since the change in $(\Delta/\delta)^{9/7}Pr^{3/4}B$, although appreciable, enters the equation for $h$ raised to only the $^1/_9$ power.

### (C) *Throat-Approximation Results*

Values obtained from the throat-approximation equations are also shown in Fig. 2. The values of $\delta$ and $\theta$ (Cf. parts c and d of Fig. 2) are 8 per cent lower than the corresponding quasi-incompressible values. Consequently, when it is assumed that $(\Delta/\delta)^{9/7}Pr^{3/4}B = 1$, the throat approximation for $h$ agrees well with the corresponding quasi-incompressible value of $h$. The value of the throat approximation for $(\Delta/\delta)^{9/7}Pr^{3/4}B$ is about half that of the quasi-incompressible value (Cf. part f of Fig. 2), and this result gives throat-approximation values of $h$ which are 6 and 8 per cent higher, respectively, than the corresponding quasi-incompressible values for the case $T_w = 100$°F. and the case $T_w$ = variable (Cf. part g of Fig. 2).

Since there is no satisfactory solution of the compressible turbulent boundary layer for heat transfer to the walls of a variable-area channel, the effect of compressibility on the values of $h$ is not known. However, since it has been shown that the use of a mean temperature $\bar{T} = (T_1 + T_w)/2$ approximates the effects of compressibility on $c_f$ in the special cases $M = 0$ (reference 6) and $M > 0$, $q = 0$ (Cf. Fig. 1), it may be hoped that the use of this mean temperature will be satisfactory in more general cases. It should be emphasized that the aforementioned comparisons are only between theories of varying degrees of approximation; consequently the adequacy of any of these theories cannot be judged until satisfactory experimental results are available.

### (D) *Examination of Several Assumptions*

To complete the consideration of this example one can check whether or not the numerical results agree with several of the assumptions made in the analysis.

It has been assumed that the boundary-layer concept rather than the pipe-flow concept should be applied. The calculated values of the relative displacement and total thicknesses of the boundary layer at the nozzle throat are

$$2\delta^*/t = 0.046 \text{ and } 2\delta/t = 0.26$$

which agree with that assumption.

The magnitude of the Reynolds Number based on $\delta$ does not vary greatly along most of the nozzle, rising from $6.4 \times 10^4$ at the throat to $7.6 \times 10^4$ at $x = 1.671$. These values are near the upper limit of validity of the Blasius turbulent-pipe-flow friction law used in the analysis and, to the best of the author's knowledge, confirm the assumption that the boundary layer is turbulent.

Finally, the relative magnitude of the heat conducted in the nozzle wall parallel to the surface can be estimated from the curvature of $T_w(x)$. The curvature of $T_w(x)$ is greatest at $x = 1.28$ (Cf. part e of Fig. 2), and at this point

$$\frac{q_{\text{conduction}}}{q_{\text{convection}}} = \frac{kd(d^2T_w/dx^2)}{h(T_e - T_w)} = 0.045$$

where $d$ is the thickness of the nozzle wall. Consequently, the conduction of heat in the nozzle wall should not greatly alter the calculated wall-temperature distribution.

## Appendix (A)

### The Energy Integral Equation for Axisymmetric Flow

The axisymmetric control volume as shown in sketch a of Fig. 3, in which abcda is a typical cross section, and also the simplified control volume shown in sketch b of the same figure are now considered. Assuming that the flow is uniform at stations 1 and 2, one may write the steady-flow energy equation [Cf., e.g., Eq. (6) of reference 11] for sketch b of Fig. 3 as

$$Q - W = m[h_1 + (u_1^2/2)] - m[h_2 + (u_2^2/2)] \equiv m\bar{c}_{p_1} T_1^0 - m\bar{c}_{p_2} T_2^0 \quad \text{(A-1)}$$

In applying Eq. (A-1) to the boundary-layer flow problem of sketch a in Fig. 3, one makes the following assumptions:

(1) At the edge of the boundary layer $\partial u/\partial y = \partial T/\partial y = 0$; in the boundary layer $\partial u/\partial x = \partial T/\partial x \cong 0$ (Prandtl boundary-layer assumptions). (A-I)

(2) Outside the boundary layer the flow is adiabatic, i.e., $T^0 =$ constant $= T_0$. (A-II)

(3) The specific heat $c_p =$ constant. (A-III)

(4) The flow is steady. (A-IV)

Now by assumptions (A-I) and (A-II) there is no transfer of heat $Q$ or work $W$ across the surfaces abcd since the temperature gradient and the velocity gradient vanish on these surfaces. Also there is no transfer of $W$ across surface ad since the velocity is zero at the wall. Since there is no flow of fluid across surfaces bc and ad, the only convection of total enthalpy $c_pT^0$ is across ab and dc. Therefore the energy equation for the control surface of sketch a of Fig. 3 becomes

$$Q_w = m_{ab}c_pT_0 - 2\pi c_p \int_d^c \rho u T^0(r + y)dy \quad \text{(A-2)}$$

But by the conservation-of-mass requirement,

$$m_{ab} = 2\pi \int_d^c \rho u(r + y)dy \quad \text{(A-3)}$$

It is now assumed that the boundary layer is thin; that is,

$$r + y = r[1 + (y/r)] \cong r \quad \text{(A-V)}$$

Combining Eqs. (A-2), (A-3), and (A-V) gives

$$Q_w = 2\pi r c_p \int_0^\infty \rho u(T_0 - T^0)dy \quad \text{(A-4)}$$

Note that the edge of the energy boundary layer could be substituted at the upper limit of the integral since it has been assumed that $T^0 = T_0$ for $y \geq \Delta$.

Eq. (A-4) is now partially nondimensionalized to obtain the form

$$Q_w = 2\pi r c_p \rho_1 u_1 (T_e - T_w)\phi(x) \quad \text{(A-5)}$$

where $$\phi(x) \equiv \int_0^\infty \frac{\rho u}{\rho_1 u_1}\left(\frac{T_0 - T^0}{T_e - T_w}\right) dy$$

noting that $\rho_1 u_1$ is taken at the same $x$ station as $\phi$. The boundary-layer energy integral equation can now be obtained by differentiating Eq. (A-5) with respect to $x$ (note that $dQ_w/dx = 2\pi r q_w$) which gives

$$\frac{q_w}{c_p\rho_1 u_1(T_e - T_w)} = \frac{d\phi}{dx} + \left[\frac{1}{u_1}\frac{du_1}{dx} + \frac{1}{r}\frac{dr}{dx} + \frac{1}{T_e - T_w}\frac{d(T_e - T_w)}{dx} + \frac{1}{\rho_1}\frac{d\rho_1}{dx}\right]\phi \quad \text{(A-6)}$$

Eq. (A-6) can also be obtained by combining the boundary-layer momentum and energy equations to obtain the Busemann form of the energy equation (Cf. p. 612, reference 1) and then integrating this equation across the boundary layer in the manner of von Kármán (Cf. pp. 131–134 and 613–615, reference 1).

## Appendix (B)

### Velocity Gradient at Supersonic Nozzle Throat

The following derivation is based on the equations for one-dimensional, isentropic fluid flow in a varying-area channel. The velocity gradient is first expressed in terms of the local Mach Number as (Cf. p. 108, reference 12)

$$du_1/dx = -\{u_1/[A(1 - M^2)]\}(dA/dx) \quad \text{(B-1)}$$

where $x$ is taken along the nozzle centerline. Since this expression is indeterminate at the nozzle throat, applying l'Hospital's rule gives at the throat

$$(du_1/dx)^* = [u_1^*/(2A^*)][(d^2A/dx^2)^*/(dM/dx)^*] \quad \text{(B-2)}$$

Expressing the Mach Number gradient as

$$dM/dx = (dA/dx)/(dA/dM)$$

which is indeterminate at the throat and again applying l'Hospital's rule,

$$(dM/dx)^* = \sqrt{(d^2A/dx^2)^*/(d^2A/dM^2)^*} \quad \text{(B-3)}$$

The problem thus becomes the evaluation of $(d^2A/dM^2)^*$ and $(d^2A/dx^2)^*$.

The variation of $A$ with $M$ is given by (Cf. p. 115, reference 12)

$$\frac{A}{A^*} = \frac{1}{M}\left(\frac{1 + [(\gamma - 1)/2]M^2}{(\gamma + 1)/2}\right)^{(\gamma+1)/[2(\gamma-1)]} \quad \text{(B-4)}$$

which after differentiating twice gives at the nozzle throat

$$(d^2A/dM^2)^* = 4A^*/(\gamma + 1) \quad \text{(B-5)}$$

For a two-dimensional-flow nozzle

$$(d^2A/dx^2)^* = 2w/L^* \quad \text{(B-6)}$$

and for an axisymmetric-flow nozzle

$$(d^2A/dx^2)^* = 2\pi r^*/L^* \quad \text{(B-7)}$$

Finally, combining Eqs. (B-2), (B-3), (B-4), and either (B-6) or (B-7) and noting that

$$u_1^* = a^* = \sqrt{2/(\gamma + 1)}\ \sqrt{\gamma R T_0}$$

one obtains for a two-dimensional-flow nozzle [using Eq. (B-6)]

$$(du_1/dx)^* = [2/(\gamma + 1)]\ \sqrt{\gamma R}\ \sqrt{T_0/(t^*L^*)} \quad \text{(B-8)}$$

and for an axisymmetrical-flow nozzle [using Eq. (B-7)]

$$(du_1/dx)^* = [2/(\gamma + 1)]\ \sqrt{\gamma R}\ \sqrt{T_0/(r^*L^*)} \quad \text{(B-9)}$$

### References


[1] Goldstein, S., *Modern Developments in Fluid Dynamics*, Oxford University Press, 1938.

[2] Schlichting, H., *Lecture Series "Boundary Layer Theory," Part II—Turbulent Flows*, NACA TM 1218, 1949.

[3] Van Driest, E. R., *Turbulent Boundary Layer in Compressible Fluids*, Journal of the Aeronautical Sciences, Vol. 18, No. 3, pp. 145–160, March, 1951.

[4] Rubesin, M. W., *The Effect of an Arbitrary Surface-Temperature Variation Along a Flat Plate on the Convective Heat Transfer in an Incompressible Turbulent Boundary Layer*, NACA TN 2345, 1951.

[5] Colburn, A. P., *A Method of Correlating Forced Convection Heat Transfer Data and a Comparison with Fluid Friction*, Trans. American Institution of Chemical Engineers, Vol. 29, pp. 174–210, 1933.

[6] Eckert, E. R. G., *Introduction to the Transfer of Heat and Mass;* McGraw-Hill Book Company, Inc., New York, 1950.

[7] Tucker, M., *Approximate Calculation of Turbulent Boundary-Layer Development in Compressible Flow*, NACA TN 2337, 1951.

[8] Coles, D., *Measurements in the Boundary Layer on a Smooth Flat Plate in Supersonic Flow*, Ph.D. Thesis, California Institute of Technology, Pasadena, Calif., May, 1953.

[9] *The NBS-NACA Tables of Thermal Properties of Gases, Table 2.39, Dry Air, Coefficients of Viscosity*, National Bureau of Standards, 1950.

[10] Wegener, P., Lobb, R. K., Winkler, E. M., Sibulkin, M., and Staab, H., *NOL Hypersonic Tunnel No. 4 Results V: Experimental and Theoretical Investigation of a Cooled Hypersonic Wedge Nozzle*, U.S. Naval Ordnance Laboratory, NAVORD Report 2701, 1953.

[11] Keenan, J. H., *Thermodynamics;* John Wiley & Sons, Inc., New York, 1941.

[12] Hall, N., *Thermodynamics of Fluid Flow;* Prentice-Hall, Inc., New York, 1951.


## Response Matrix Method . . .

*(Continued from page 161)*

The calculation of the rotating beam modes and frequencies, of some interest in themselves, is accomplished by a straightforward method not involving trial-and-error or iteration processes, which characterize many of the previous methods.

The particular choice of the loading functions, $\lambda_n$, decreases the numerical work necessary since many of the tabular solutions required are identically zero over large portions of the span.

### References


[1] Flax, A. H., and Goland, L., *Dynamic Effects in Rotor Blade Bending*, Journal of the Aeronautical Sciences, Vol. 18, No. 12, pp. 813–829, December, 1951.

[2] Johnson, W. C., and Mayne, R., *Effect of Second-Harmonic Flapping on the Stresses of a Hinged Rotor Blade*, Goodyear Aircraft Report No. R-107-4, Part III, 1946.

[3] Saibel, E., and Berger, W. J., *On Finding the Characteristic Equation of a Square Matrix*, Technical Report No. 4, Mathematical Analysis of Electrical and Mechanical Systems, Carnegie Institute of Technology, Department of Mathematics, March 2, 1953.

[4] Acrives, Andrew, and Amundson, Neal R., *A Method for Determining the Roots of a Secular Determinant of Order m, by Means of the IBM Model 602-A Calculating Punch*, Technical Newsletter No. 7, IBM Applied Science Division, pp. 44–52, August, 1954.

# Stress Distribution, Instability, and Free Vibration of Beam Grid-Works on Elastic Foundations

HUGH L. COX* AND PAUL H. DENKE†

*Douglas Aircraft Company, Inc.*

SUMMARY

An approximate method for finding the stress distribution, buckling load, and lowest natural frequency for a beam grid-work structure on an elastic foundation is presented. The structure may have variable load distributions, beam and foundation stiffnesses, and boundary conditions. The method of solution can be used effectively in conjunction with electronic digital computors so that the work of the stress analyst is reduced to tabulating a few matrices.

## INTRODUCTION

Oftentimes the aircraft structural engineer must determine the stress distribution, instability, and natural frequencies of flexural vibration for a structure that is composed of an orthogonal network of beams. Such a structure may represent an actual structure or some assumed replacement structure. In an airplane fuselage a network of longitudinal and transverse floor beams supported elastically by struts attached to the fuselage frames is one example of the type of structure under consideration.

This paper presents an approximate method of solution that consists essentially of solving the governing differential equations for a beam grid-work structure by replacing derivatives with finite difference expressions. The method of solving differential equations by finite difference techniques is well known[1, 2]; however, some of the advantages of finite difference solutions in conjunction with electronic digital computation have not been pointed out. The simultaneous algebraic equations, which result from writing the governing differential equation of a beam grid-work structure in difference form, may be written matrically so that a very simple matrix equation expresses the behavior of the structure. For stress distribution problems, it is possible to write a stress matrix so that the stresses at various points along the beams may be computed within an electronic computor; the resulting stresses may be printed out automatically.

Beams that are parallel are assumed to be equally spaced. Each beam in the grid-work may have a variable moment of inertia of the cross section along its length and any nondeflecting boundary conditions for each beam may be treated. Variable load distributions and foundation moduli also may be considered. The torsional rigidity of individual beams is disregarded.

Received June 28, 1954. Revised and received August 9, 1955.

* Strength Engineer, Santa Monica Division.

† Strength Analysis Methods Engineer, Santa Monica Division.

## BASIC EQUATIONS

Consider the structure shown in Fig. 1. The beams are assumed to transmit only shear at their intersection points and one of the principal axes of each beam is assumed to be parallel to the plane of the beam grid-work. The governing differential equation for the structure, when the moment of inertia of the cross section of each beam is constant along the beam length, is

$$EI_x \frac{h_x}{h_y}\frac{d^4w}{dx^4} + EI_y \frac{d^4w}{dy^4} + P_x(y)\frac{h_x}{h_y}\frac{d^2w}{dx^2} + P_y(x)\frac{d^2w}{dy^2} + h_x k(x, y)w = h_x q(x, y) \quad (1)$$

where

$w$ = deflection positive downward
$E$ = modulus of elasticity of beam material
$I_x$ = moment of inertia of beams parallel to the $x$ direction
$I_y$ = moment of inertia of the cross section of beams parallel to the $y$ direction
$h_x$ = spacing of beams parallel to $y$ direction
$h_y$ = spacing of beams parallel to $x$ direction
$P_x$ = axial load on beams parallel to $x$ direction, positive for compression
$P_y$ = axial load on beams parallel to $y$ direction, positive for compression
$k(x, y)$ = distributed spring constant with units of force per length cubed
$q(x, y)$ = lateral pressure, positive acting downward

When the moments of inertia of the beams vary along the beam lengths, Eq. (1) becomes

$$E\frac{h_x}{h_y}\left(I_x\frac{d^4w}{dx^4} + 2\frac{dI_x}{dx}\frac{d^3w}{dx^3} + \frac{d^2I_x}{dx^2}\frac{d^2w}{dx^2}\right) + E\left(I_y\frac{d^4w}{dy^4} + 2\frac{dI_y}{dy}\frac{d^3w}{dy^3} + \frac{d^2I_y}{dy^2}\frac{d^2w}{dy^2}\right) + P_{x(y)}\frac{h_x}{h_y}\frac{d^2w}{dx^2} + P_{y(x)}\frac{d^2w}{dy^2} + h_x\,k(x, y)\,w = h_x\,q(x, y) \quad (2)$$

Since it will be necessary to express Eqs. (1) or (2) in difference form, the following difference patterns[1] for derivatives are needed:

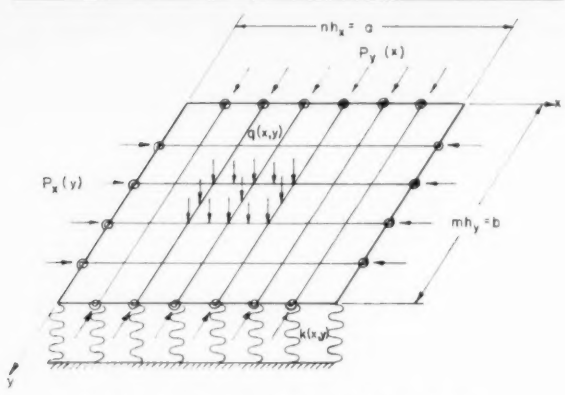


FIG. 1. Beam grid-work on elastic foundation.

$$\left.\begin{aligned}
\frac{df}{d\xi} &= \frac{1}{2h}(-f_{n-1} + f_{n+1}) \\
\frac{d^2f}{d\xi^2} &= \frac{1}{h^2}(f_{n-1} - 2f_n + f_{n+1}) \\
\frac{d^3f}{d\xi^3} &= \frac{1}{2h^3}(-f_{n-2} + 2f_{n-1} - 2f_{n+1} + f_{n+2}) \\
\frac{d^4f}{d\xi^4} &= \frac{1}{h^4}(f_{n-2} - 4f_{n-1} + 6f_n - 4f_{n+1} + f_{n+2})
\end{aligned}\right\} \tag{3}$$

where the derivative of a function $f$ with respect to any variable $\xi$ is given for the point $f_n$ when $h$ is the spacing between grid points.

## Boundary Conditions

For the problem under consideration, the boundary conditions may be written directly into the difference pattern so that the difference equations which replace the governing differential equation automatically satisfy equilibrium, compatibility, and the boundary conditions. It is necessary to establish fictitious points outside of the boundary in order that difference equations may be written for internal points.

A partially restrained boundary refers to a boundary that can develop some moment but not as much moment as a clamped boundary. Physically this type of boundary may be represented as shown in Fig. 2 where the coil spring at the support develops moment as the support rotates. Let

$M$ = moment in coil spring
$R$ = spring constant in unit moment per radian
$\theta$ = slope at support, positive downward to the right

Therefore, at the support,

$$M = R\theta \tag{4}$$

but

$$\theta = \frac{dy}{dx} \cong \frac{1}{2h}(-y_e + y_i) \tag{5}$$

$$M = -EI\frac{d^2y}{dx^2} \cong -\frac{EI}{h^2}(y_e + y_i) \tag{6}$$

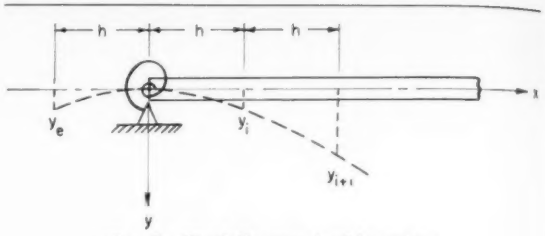


FIG. 2. Partially restrained boundary.

Substitution of Eqs. (5) and (6) into Eq. (4) yields

$$y_e = -y_i\frac{(EI/h) + (R/2)}{(EI/h) - (R/2)} = -\alpha_i y_i \tag{7}$$

where

$$\alpha_i = \frac{(EI/h) + (R/2)}{(EI/h) - (R/2)}$$

Note that when $R = 0$, $y_i = -y_e$ which is the case of a simple support, and when $R = \infty$, $y_i = y_e$ which is the case of a clamped support. Thus, when the rotational spring constant of the support is given, the fictitious point may be written in terms of the first interior point by means of Eq. (7). Usually, the spring constant $R$ is determined experimentally for riveted joints, welded connections, etc.

## Illustrative Example

### *Stress Distribution*

An example will illustrate the general method of solution. Consider the structure shown in Fig. 3. Assume that the lateral loads are distributed as a pressure over the beam grid-work. A thin plate may serve to distribute the loads in this manner. If the lateral loads consist of concentrated loads at the grid-points, or beam intersection points, then the concentrated loads may be replaced with equivalent dis-

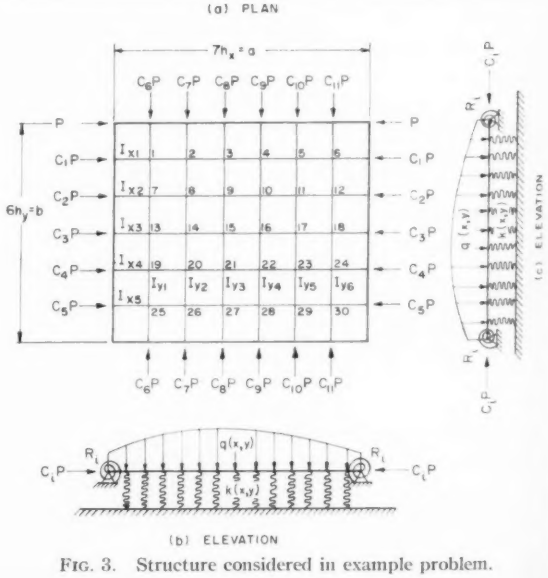


FIG. 3. Structure considered in example problem.

tributed loads over the areas $h_x h_y$. Consider each beam to have a different moment of inertia, axial load, lateral load, and rotational spring constant; but for purposes of illustration assume that the moment of inertia of each beam is constant along its length. The beam intersection points are numbered as shown. By referring to Eqs. (3), one may write Eq. (1) in difference form as follows:

$$EI_{x1}\frac{1}{h_y h_x^3}(\alpha_1 w_1 + 6w_1 - 4w_2 + w_3) + \frac{EI_{y1}}{h_y^4}(\alpha_1 w_1 + 6w_1 - 4w_7 + w_{13}) + \frac{C_1 P}{h_x h_y}(-2w_1 + w_2) + \frac{C_6 P}{h_y^2}(-2w_1 + w_7) + h_x k_1 w_1 = h_x q_1$$

at point (2)

$$EI_{x1}\frac{1}{h_y h_x^3}(-4w_1 + 6w_2 - 4w_3 + w_4) + \frac{EI_{y2}}{h_y^4}(\alpha_1 w_2 + 6w_2 - 4w_8 + w_{14}) + \frac{C_1 P}{h_x h_y}(w_1 - 2w_2 + w_3) + \frac{C_7 P}{h_y^2}(-2w_2 + w_8) + h_x k_2 w_2 = h_x q_2 \qquad \text{etc . . .}$$

at point (15)

$$EI_{x3}\frac{1}{h_y h_x^3}(w_{13} - 4w_{14} + 6w_{15} - 4w_{16} + w_{17}) + \frac{EI_{y3}}{h_y^4}(w_3 - 4w_9 + 6w_{15} - 4w_{21} + w_{27}) + \frac{C_3 P}{h_x h_y}(w_{14} - 2w_{15} + w_{16}) + \frac{C_8 P}{h_y^2}(w_9 - 2w_{15} + w_{21}) + h_x k_{15} w_{15} = h_x q_{15} \qquad \text{etc . . .}$$

The resulting 30 simultaneous algebraic equations may be written matrically as

$$\left(E\frac{1}{h_y h_x^4}J_x G + \frac{E}{h_x h_y^4}J_y B + \frac{P}{h_x^2 h_y}C_x D + \frac{P}{h_x h_y^2}C_y F + K\right)W = Q \tag{8}$$

where $E$, $h_x$, $h_y$, and $P$ are scalars

$J_x$ = diagonal matrix of $I_x$ values where, on the diagonal,
first 6 terms = $I_{x1}$
next 6 terms = $I_{x2}$
next 6 terms = $I_{x3}$
next 6 terms = $I_{x4}$
next 6 terms = $I_{x5}$

$G$ = matrix of coefficients of terms multiplied by $E(1/h_y h_x^4)$

$J_y$ = diagonal matrix of $I_y$ values where, on the diagonal, terms follow the order $C_6$, $C_7$, $C_8$, $C_9$, $C_{10}$, $C_{11}$, $C_6$, $C_7$, $C_8$ . . .

$B$ = matrix of coefficients of terms multiplied by $(E/h_x h_y^4)$

$C_x$ = diagonal matrix of $C$ values where, on the diagonal
first 6 terms = $C_1$
next 6 terms = $C_2$
next 6 terms = $C_3$
next 6 terms = $C_4$
next 6 terms = $C_5$

$D$ = matrix of coefficients of terms multiplied by $(P/h_x^2 h_y)$

$C_y$ = diagonal matrix of $C$ values, where on the diagonal, terms follow the order $C_6$, $C_7$, $C_8$, $C_9$, $C_{10}$, $C_{11}$, $C_6$, $C_7$, $C_8$ . . .

$F$ = matrix of coefficients of terms multiplied by $(P/h_y^2 h_x)$

$K$ = diagonal matrix of $k$ values

$Q$ = column matrix of $q$ values

$W$ = column matrix of unknown deflections

Eq. (8) may be expressed more compactly as

$$(S + P\,N)\,W = Q \tag{9}$$

where $S = (1/h_y h_x^4)J_x G + (E/h_x h_y^4)J_y B + K$

$$N = (1/h_x^2 h_y)C_x D + (1/h_y^2 h_x)C_y F$$

The solution for the deflections of the system from Eq. (9) may be written as

$$W = (S + P\,N)^{-1}Q \tag{10}$$

The extreme fiber stress at any point in any beam parallel to the $x$ direction will be

$$\sigma_{ix} = \frac{C_{ix}P}{A_{ix}} \pm \frac{M_{ix}c_{ix}}{I_{ix}} \tag{11}$$

where

$\sigma_{ix}$ = stress at same point $i$
$c_{ix}$ = distance from neutral axis to extreme fiber
$M_{ix}$ = moment at point $i$

The value of $C_{ix}P$ will be known, and $M_{ix}$ may be computed from the deflections as

$$M_{ix} = -EI_{ix}\frac{d^2 w}{dx^2} \cong -\frac{EI_{ix}}{h_x^2}(w_{i-1} - 2w_i + w_{i+1}) \tag{12}$$

The moments $M_{ix}$ will be slightly in error since the deflection curve is differentiated twice; however, the error will be small when $h_x$ is taken so that several subdivision points along the total beam length are used.

Substitution of Eq. (12) into Eq. (11) gives

$$\sigma_{iz} = \frac{C_{iz}P}{A_{iz}} \mp \frac{Ec_{iz}}{h_x^2}(w_{i-1} - 2w_i + w_{i+1}) \quad (13)$$

The above equation may be written matrically as

$$\sigma_x = PC_xA_x \mp (E/h_x^2)H_xDW \quad (14)$$

Where $P$, $E$, $h_x$ are scalars

$\sigma_x$ is a column matrix of unknown stresses
$C_x$ is defined for Eq. (8)
$D$ is defined for Eq. (8)
$A_x$ is a column matrix of reciprocal areas at points 1 through 30
$H_x$ is a diagonal matrix of distances from neutral axes of beams to extreme fibers for all grid points along the beams. When the minus sign in Eq. (14) is used, $c_i$ is the distance to the top fiber—when the plus sign is used, $c_i$ is the distance to the bottom fiber.

If the value of $W$ from Eq. (10) is substituted into Eq. (14) there results

$$\sigma_x = P\,C_x\,A_x \mp (E/h_x^2)H_xD(S + P\,N)^{-1}\,Q \quad (15)$$

Eq. (15) gives the extreme fiber stresses at points 1 through 30 for the beams in the $x$ direction. Once the matrices $C_x$, $A$, $H$, $D$, $S$, $N$, and $Q$ have been tabulated, Eq. (15) may be solved rapidly on an electronic computor. The engineer will only have to read off the stresses at various points when the results of the calculations are returned to him. Similarly the stresses in the beams in the $y$ direction may be written as

$$\sigma_y = P\,C_yA_y \mp (E/h_y^2)H_yF(S + P\,N)^{-1}\,Q \quad (16)$$

### *Instability*

Consider the instability of the structure shown in Fig. 3. Assume that the elastic foundation is soft—i.e., no buckles will develop between the grid points. The condition for buckling from Eq. (9) is

$$(S + P\,N)\,W = 0 \quad (17)$$

Eq. (17) is in standard eigenvalue form and methods for determining $P_{CR}$ from this equation have been coded for most electronic computors.

### *Lowest Natural Frequency*

When a soft spring support exists, the approximate lowest natural frequency of the system may be determined by rewriting Eq. (9) as

$$[(S + P\,N) - \beta T]\,W = 0 \quad (18)$$

where

$(S + P\,N)$ is defined for Eq. (9)
$T$ = diagonal matrix of $q$ values, where $q$ includes the equivalent distributed weight per unit length squared of the beams plus the weights of the lateral loads that are on the structure when it is vibrating
$\beta = \omega^2/g$
$\omega$ = natural frequency
$g$ = acceleration resulting from gravity

The lowest root of $\beta$ and consequently $\omega$ may be determined from Eq. (18) easily on an electronic computor.

## Concluding Remarks

It is seen that the formulation of the problem is quite simple when expressed matrically. Since variable quantities such as load distribution, moments of inertia and spring constants are treated, the method of solution has practical application to certain aircraft structures. It should be apparent that any parameter may be varied simply by changing the proper matrix—for example, if it is desired to change the stiffness of the beams in the $x$ direction, then it is only necessary to change matrix $J_x$ in Eq. (8).

## References

[1] Jensen, V. P., *Analyses of Skew Slabs*, Engineering Experiment Station Bulletin No. 332, U. of Illinois, September, 1941.

[2] Grinter, L. E., *Numerical Methods of Analysis in Engineering*; Macmillan, New York, 1949.

## Experimental Pressure Distributions . . .

(*Continued from page 124*)

*Axis*, British Aeronautical Research Council Reports and Memoranda No. 1921, Nov., 1938.

[9] Bratt, J. B., and Wight, K. C., *The Effect of Mean Incidence, Amplitude of Oscillation, Profile and Aspect Ratio on Pitching Moment Derivatives*, British Aeronautical Research Council Reports and Memoranda No. 2064, June, 1945.

[10] Silverstein, A., and Joyner, U. T., *Experimental Verification of the Theory of Oscillating Airfoils*, NACA Technical Report 673, 1939.

[11] Reid, E. G., and Vincenti, W., *An Experimental Determination of the Lift of an Oscillating Airfoil*, Journal of the Aeronautical Sciences, Vol. 8, No. 1, Nov., 1940.

[12] Reid, E. G., *Experiments on the Lift of Airfoils in Non-Uniform Motion*, Stanford University Report, July 23, 1942.

[13] Halfman, R. L., *Experimental Aerodynamic Derivatives of a Sinusoidally Oscillating Airfoil in Two-Dimensional Flow*, NACA Report 1108, 1952.

[14] Perls, T. A., *Electrical Noise from Instrument Cables Subjected to Shock and Vibration*, National Bureau of Standards Report 1388, Jan., 1952.

# Readers' Forum

*BRIEF REPORTS of investigations in the aeronautical sciences and discussions of papers published in the JOURNAL are presented in this special department. Entries must be restricted to a maximum of 1,300 words or the equivalent of one JOURNAL page including formulas and illustrations. Publication is completed as soon as possible after receipt of the material. The Editorial Committee does not hold itself responsible for the opinions expressed by the correspondents.*

## Contents


An Experimental Investigation of Flow About Simple Blunt Bodies at a Nominal Mach Number of 5.8 ..... ROBERT EARL OLIVER 177

Thermally Induced Vibrations of Beams . BRUNO A. BOLEY 179

On the Model of the Free, Shock-Separated, Turbulent Boundary Layer ..... ARTUR MAGER 181

Experimental Observation of Laminar Boundary-Layer Oscillations in Supersonic Flow ..... JOHN LAUFER 184

The Normal Shock Properties for Air in Dissociation Equilibrium ..... MARY F. ROMIG 185

Some Results of Linearized Transonic Flow About Slender Airfoils and Bodies of Revolution ..... P. F. MAEDER AND H. U. THOMMEN 187

Heat Flow in a Fluid with Eddying Flow ..... WILLIAM H. DURFEE 188

An Experimental Study of One-Dimensional Shock-Wave Refraction ..... C. A. FORD AND I. I. GLASS 189

Aerodynamic Cross-Coupling Between Side Force and Normal Force on Bodies and Wing-Body Combinations ..... MARTIN ZLOTNICK 192


## An Experimental Investigation of Flow About Simple Blunt Bodies at a Nominal Mach Number of 5.8*


Robert Earl Oliver

*Guggenheim Aeronautical Laboratory, California Institute of Technology, Pasadena, Calif.*



July 22, 1955



SUMMARY

An experimental investigation was conducted in the GALCIT Hypersonic Wind Tunnel to determine flow characteristics for a series of blunt bodies at a nominal Mach Number of 5.8 and free-stream Reynolds Numbers per in. of $0.6 \times 10^6$, $1.2 \times 10^6$, and $2.4 \times 10^6$. The measured values for the pressure coefficient distributions are compared with a modified Newtonian expression. The agreement is very good for the three-dimensional bodies and is fair for the circular cylinder transverse to the free-stream flow direction. A complete report of the investigation is given in a GALCIT Hypersonic Wind Tunnel Memorandum.[1]


SYMBOLS

$C_p$ = $\Delta p/q$ = pressure coefficient

$\gamma$ = ratio of specific heats


* This investigation was a part of a broad hypersonic research program sponsored and supported jointly by U.S. Army Ordnance and Air Force under Contract No. DA-04-495-Ord-19. The advice and guidance of Henry T. Nagamatsu and Prof. Lester Lees in connection with this investigation are gratefully acknowledged.


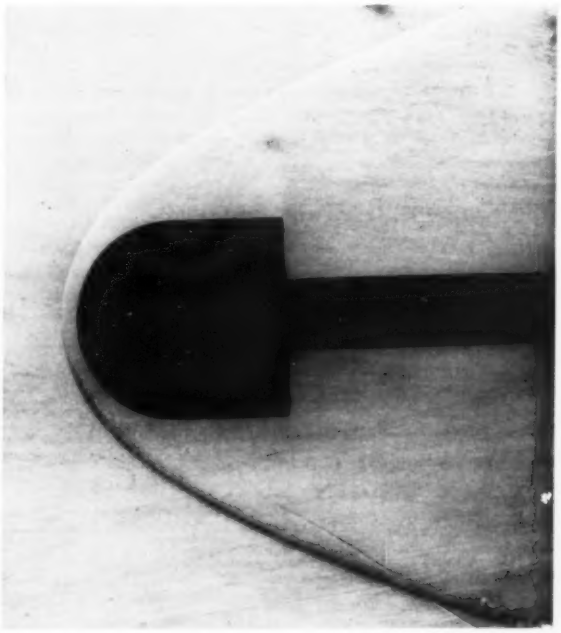

FIG. 1. Hemisphere-cylinder at $M_\infty = 5.8$ and $R_e/\text{in.} = 2.4 \times 10^6$ (schlieren photograph).

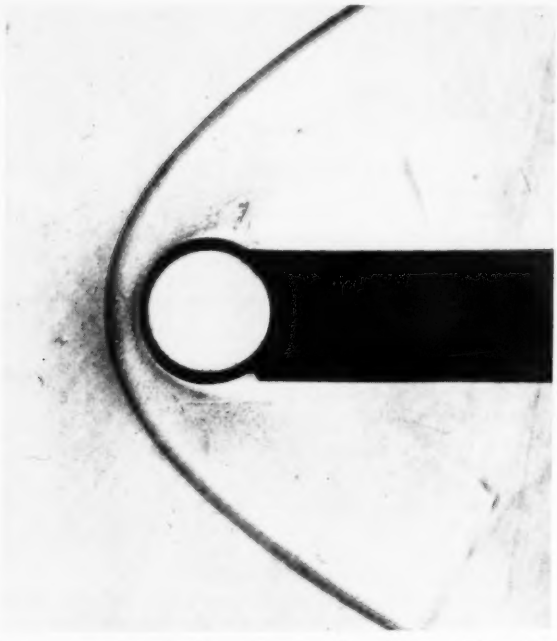

FIG. 2. Circular cylinder transverse to free stream at $M_\infty = 5.8$ and $R_e/\text{in.} = 2.4 \times 10^5$ (Schlieren).

$D$ = characteristic length used in defining Reynolds Number
$\eta$ = angle between the free-stream flow direction and the normal to the body surface element
$\theta$ = central angle of a spherical or cylindrical body measured from the stagnation point
$\mu_\infty$ = absolute viscosity of the fluid in the free stream
$M_\infty$ = free-stream Mach Number
$p_\infty$ = free-stream static pressure
$p_0$ = reservoir pressure
$p_s$ = local static pressure
$\Delta p$ = $p_0 - p_\infty$
$q$ = $(1/2)\rho_\infty U_\infty^2$ = dynamic pressure
$\rho_\infty$ = free-stream mass density
$\rho_2$ = mass density behind a normal shock
$R_e$ = $(\rho_\infty D U_\infty)/\mu_\infty$ = free-stream Reynolds Number
$U_\infty$ = free-stream velocity

## INTRODUCTION

THE PRESENT INVESTIGATION was undertaken in view of the considerable current interest in the hypersonic flow over the forward portion of simple blunt shapes. In cases where a detached shock wave is produced, a complete theoretical analysis of the flow is difficult. However, the nearness of the shock to the body surface suggests the possibility of using the Newtonian theory as an approximation to the pressure distribution on the surface. According to Newton's concept, the pressure coefficient is given by $C_p = 2\cos^2\eta$. For a real gas at a finite but high Mach Number the maximum pressure coefficient $C_{pmax}$ (at the stagnation point) is given by

$$C_{pmax} \cong 2 - \frac{\rho_\infty}{\rho_2} = \frac{\gamma+3}{\gamma+1}\left(1 - \frac{2}{\gamma+3}\,\frac{1}{M_\infty^2}\right)$$

which is less than the value 2.0 predicted by Newton. This result suggests that it might be more revealing to compare the ratio $C_p/C_{pmax}$ with $\cos^2\eta$. This relationship is referred to in this investigation as the "modified Newtonian theory."

## DISCUSSION OF RESULTS

Schlieren photographs show that the detached shock waves lie very close to the surfaces of the bodies of revolution (see Fig. 1) but relatively far from the surface of the circular cylinder transverse to the free-stream flow direction (see Fig. 2). This observation suggests that the modified Newtonian theory should give a closer approximation to the pressure distribution for three-dimensional bodies than for two-dimensional, and the measured pressure distributions (see Figs. 3, 4, and 5) indicate that this is generally true. The pressure distribution for the hemisphere-cylinder (see Fig. 4) shows excellent agreement with the modified Newtonian theory over nearly all of the spherical portion, while the pressure distribution for the cylinder transverse to the flow (see Fig. 5) agrees with the modified Newtonian theory only near the stagnation point. The pressure distribution for the spherical-nosed cone (see Fig. 3) shows that the modified Newtonian theory gives a fair

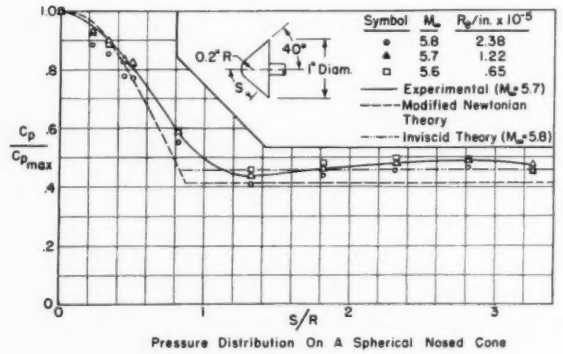


Pressure Distribution On A Spherical Nosed Cone

Fig. 3

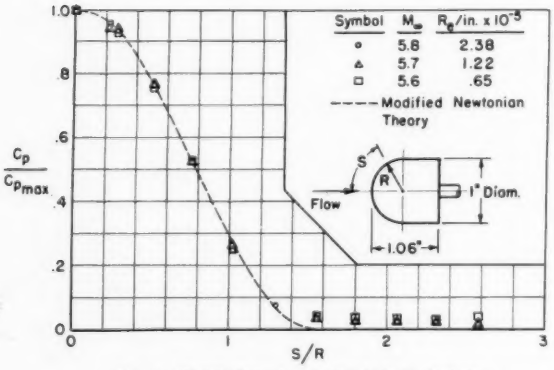


Presure Distribution On A Hemisphere-Cylinder

Fig. 4

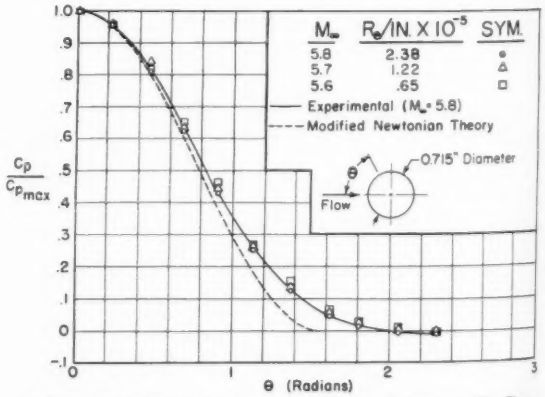


Pressure Distribution On A Circular Cylinder Transverse To Flow

Fig. 5

approximation, but that inviscid theory[2,3] gives a better approximation over the conical portion of the model.

For the Mach Number and Reynolds Number range of this investigation, the modified Newtonian theory provides a good approximation to the pressure distributions for blunt bodies of revolution.

### References


[1] Oliver, Robert E., *An Experimental Investigation of Flow Over Simple Blunt Bodies at a Nominal Mach Number of 5.8*, GALCIT Hypersonic Wind Tunnel Memorandum No. 26, June 1, 1955.

[2] Taylor, G. I., and Maccoll, J. W., *The Air Pressure on a Cone Moving at High Speeds*. Proc. Roy. Soc., Vol. 139, 1933, and Vol. 159, 1937.

[3] Ames Research Staff, *Equations, Tables, and Charts for Compressible Flow*, NACA Report 1135, 1953.


## Thermally Induced Vibrations of Beams*


Bruno A. Boley†

*Institute of Air Flight Structures, Columbia University, New York*


July 26, 1955

### Summary


The behavior of a simply supported rectangular beam, one of whose sides is subjected to a sudden application of heat, is analyzed taking into account the effect of inertia. It is found that the deflections thus calculated oscillate at the lowest natural frequency of the beam about the static ones obtained neglecting the inertia of the beam. A simple equation approximating the maximum deflection is given. It depends upon the parameter $B$ which is directly proportional to the natural frequency of the beam and to the characteristic thermal time ($h^2/\kappa$), $h$ being the height of the beam and $\kappa$ the thermal diffusivity of its material. The effect of inertia is found to be of importance particularly with thin plates.


### Introduction

In thermal stress analysis it is customary to perform the calculations in two distinct phases. In the first of these the (time-dependent) temperature distribution is calculated from the heat equations under the appropriate thermal boundary and initial conditions; in the second the expression for this temperature distribution is substituted in the equations of thermoelasticity (or inelasticity). In general, the inertia of the structure is omitted from the calculations in the second phase, so that the time is here reduced to the role of a parameter.

The procedure just outlined thus neglects any interaction between the heat and stress problems which might affect the temperature distr bution, and disregards any vibrations which may arise in the structure. A solution obtained under the above simplifications will be referred to, in the present paper, as a "static" solution. It is the purpose of the analysis presented here to assess, with the aid of an example, the accuracy of such a solution with regard to the second of the above assumptions; a "dynamic" solution is therefore presented for a particular problem, which is obtained by retaining the inertia terms in the thermoelastic equations. Account is thus taken of the heat-produced oscillations, while the question of improving the temperature distribution is left, for the time being, untouched. The resulting level of accuracy is probably consistent with that obtained (in the example which follows, which is concerned with the behavior of a heated beam) through the elementary Bernoulli-Euler theory of beams; if, however, the calculation of the temperature distribution were to be refined so as to assume a more wave-like character, a corresponding improvement in the solution of the stress problems would have to be introduced, possibly that provided by the Timoshenko theory of beams.[1, 2]


* This investigation was carried out under Contract Nonr-266(20) of the Office of Naval Research, whose support is gratefully acknowledged.


† Associate Professor of Civil Engineering.

### Basic Equations

The curvature $(\partial^2 v/\partial x^2)$ of a uniform beam under the simultaneous action of external forces and of heat is given, according to the Bernoulli-Euler theory of bending,[3, 4, 5] by

$$EI\,(\partial^2 v/\partial x^2) = M + M_T \tag{1}$$

where $M$ is the bending moment produced by the applied forces, and

$$M_T = \iint E\alpha T y\, dA \tag{2}$$

(All unspecified limits of integration are to be taken so as to cover the entire cross-sectional area $A$.) In these equations $v$ is the transverse deflection (in the $y$ direction), $T$ is the temperature (in general dependent on $x$, $y$, and $t$), $\alpha$ the coefficient of thermal expansion, $E$ Young's modulus, $I$ the moment of inertia of the beam cross section, $x$ the distance along the span, and $t$ the time.

It has been shown[3, 6] that the bending moment $M$ is in reality proportional to the curvature, as Eq. (1) implies, only if

$$(\partial^2 M/\partial x^2) = 0 \tag{3}$$

This relation certainly does not hold in problems of beam vibrations (such as the present one), but it is well known that use of Eq. (1) nevertheless yields good practical approximations provided the disturbance does not set up in the beam waves with extremely short wave-lengths.[7, 8]

In a similar manner, the proportionality between curvature and the quantity $M_T$ was shown in reference 4 to hold provided that

$$(\partial^2 T/\partial x^2) = 0 \tag{3a}$$

where the curvature is calculated from the average deflection

$$v_{av} = \frac{1}{A}\iint v\, dA \tag{3b}$$

In the example which follows the temperature is independent of $x$ so that Eq. (3a) is valid,

$$M_T = M_T(t) \tag{3c}$$

and therefore Eq. (1) holds exactly insofar as the temperature terms are concerned. If the temperature varied with $x$ in such a manner that Eq. (3a) were not satisfied, then Eq. (1) would be only approximate in this respect, but reference 4 shows that the error involved is small. Eq. (1) may thus be used, at least as a first approximation, in a great variety of problems of practical interest.

If Eq. (1) is now differentiated twice with respect to $x$, the term $(\partial^2 M/\partial x^2)$, which is proportional to the distributed loading along the beam span, will appear on the right-hand side of the resulting expression. Let the loading consist entirely of the (negative of the) inertia forces; then

$$(\partial^2 M/\partial x^2) = -\rho A(\partial^2 v/\partial t^2) \tag{4}$$

where $\rho$ is the mass density. The governing equation for the deflection then becomes

$$(\partial^4 v/\partial x^4) + k^4\,(\partial^2 v/\partial t^2) = [(\partial^2 M_T/\partial x^2)/(EI)] \tag{5}$$

$$\text{where} \qquad k = [\rho A/(EI)]^{1/4} \tag{5a}$$

The particular case of a simply supported rectangular beam of length $L$ and height $h$ will now be considered. A step heat input $Q$, constant along $x$, is assumed to be applied over the edge $y = (h/2)$, while the edge $y = -(h/2)$ is insulated, so that the temperature distribution is[9]

$$T = \left(\frac{hQ}{K}\right)\left[\tau + \frac{1}{2}\left(\frac{y}{h}+\frac{1}{2}\right)^2 - \frac{1}{6} - \frac{2}{\pi^2}\sum_{j=1}^{\infty}\frac{(-1)^j e^{-j^2\pi^2\tau}}{j^2}\cos j\pi\left(\frac{y}{h}+\frac{1}{2}\right)\right] \tag{6}$$

provided that the beam is initially at $T = 0$. Here $K$ is the thermal conductivity, $\tau$ a nondimensional time parameter defined by

$$\tau = (\kappa t/h^2) \tag{6a}$$

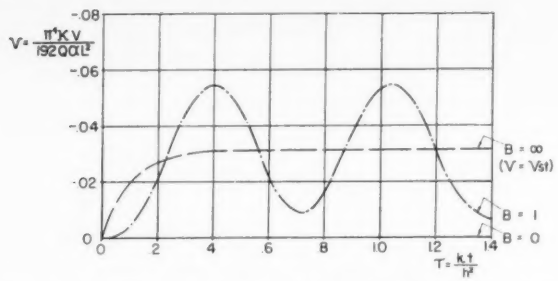


FIG. 1. Nondimensional variation of deflection at $x = (L/2)$ with time for $B = 0, 1, \infty$.

and $\kappa$ the thermal diffusivity. From Eqs. (2) and (6) one obtains

$$m_T(\tau) = \left[\frac{\pi^4 K\ M_T}{(192EIQ\alpha)}\right] = \left(\frac{1}{4}\right)\left[\left(\frac{\pi^4}{96}\right) - \sum_{j=1,3,5}^{\infty} \frac{e^{-j^2\pi^2\tau}}{j^4}\right] \tag{6b}$$

Note that Eq. (3d) holds and that

$$m_T(0) = 0 \tag{6c}$$

in view of the identity

$$\sum_{j=1,3,5}^{\infty} \frac{1}{j^4} = \frac{\pi^4}{96} \tag{6d}$$

Let the following additional nondimensional notation be introduced

$$\left.\begin{aligned} V(\xi, \tau) &= [\pi^4 Kv/(192\ Q\alpha L^2)] \\ \xi &= (x/L) \\ m_T(\xi, \tau) &= [\pi^4 K\ M_T(192EIQ\alpha)] \\ B &= \frac{h}{(kL\sqrt{\kappa})} = \\ &\quad \frac{h}{L}\left[\frac{c\ \sqrt{(I/A)}}{\kappa}\right]^{1/2} = \left(\frac{h}{L}\ \frac{hc}{\kappa}\ \frac{1}{S}\right)^{1/2} \end{aligned}\right\} \tag{7}$$

where $S$ is the slenderness ratio and

$$c = \sqrt{E/\rho} \tag{7a}$$

is the velocity of propagation of longitudinal waves. The physical significance of the parameter $B$ will be discussed later. With the above notation and with Eq. (3d), the basic equation to be solved becomes

$$B^4 V'''' + V'' = 0 \tag{8}$$

The boundary and initial conditions for a beam initially at rest are

$$\left.\begin{aligned} V(0, \tau) = V(1, \tau) = V(\xi, 0) = V'(\xi, 0) = 0 \\ V''(0, \tau) = V''(1, \tau) = m_T \end{aligned}\right\} \tag{8a}$$

Differentiations with respect to $\xi$ and $\tau$ have been denoted by primes and dots, respectively.

## Static Solution

The static solution, denoted by the subscript $st$, is obtained by neglecting the inertia of the beam; thus Eq. (8) becomes:

$$V_{st}'''' = 0 \tag{9}$$

The pertinent solution—namely,

$$V_{st} = [(\xi^2 - \xi)/2]m_T \tag{9a}$$

is obtained by disregarding all conditions at $\tau = 0$ listed in Eqs. (8a). The condition $V_{st}(\xi, 0) = 0$ is nevertheless automatically satisfied because of Eq. (6c). The static solution is independent of the parameter $B$; a plot of Eq. (9a) for the center of the beam ($\xi = 0.5$) is presented in Fig. 1. Note that as time increases the static deflection approaches asymptotically the value

$$V_{st,\ max} = (\xi^2 - \xi)(\pi^4/768) \tag{9b}$$

## Dynamic Solution

The solution of Eq. (8) is conveniently found by setting[10]

$$V = V_{st} + \sum_n X_n(\xi)T_n(\tau) = \sum_n (a_n m_T + T_n) X_n \tag{10}$$

where $V_{st}$ has been expanded in the form

$$V_{st} = \sum_n a_n X_n m_T \tag{10a}$$

Substitution of Eq. (10) into Eq. (8) and separation of variables shows that Eq. (8) will be satisfied if

$$\frac{X_n''''}{X_n} = -\frac{(T_n'' + m_T\ddot{a}_n)}{(B^4 T_n)} = c_n^2 \tag{10b}$$

where $c_n$ is a constant. From Eqs. (8a) it follows that

$$X_n(0) = X_n(1) = X_n''(0) = X_n''(1) = 0 \tag{10c}$$

and, therefore,

$$X_n = \sin n\pi\xi; \qquad c_n = n^2\pi^2 \tag{10d}$$

Eq. (10a) is then simply a Fourier expansion of $V_{st}$, so that one may find without difficulty that

$$a_n = -[4/(n^3\pi^3)]; \qquad n = 1, 3, 5, \ldots \tag{10e}$$

The functions $T_n$ are found by solving the pertinent equation of (10b) under the initial conditions Eq. (8a). The final result for the deflection may be written as follows:

$$V - V_{st} = \sum_{n=1,3,5}^{\infty} \frac{\sin n\pi\ \xi}{n^3\pi^3}\left[\frac{\pi^2}{8B^2n^2}\sin n^2\pi^2B^2\ \tau - \sum_{j=1,3,5}^{\infty} \frac{e^{-j^2\pi^2\tau} + (j/nB)^2 \sin n^2\pi^2B^2\tau - \cos n^2\pi^2B^2\tau}{j^4 + n^4B^4}\right] \tag{11}$$

The bending moment follows by substitution in Eq. (1); in nondimensional form it is

$$m_T = (V - V_{st})'' = -\sum_{n=1,3,5}^{\infty} \frac{\sin n\ \pi\ \xi}{n\pi}\left[\ \right] \tag{11a}$$

where the symbol [ ] indicates the quantity contained in similar brackets in Eq. (11).

Nondimensional plots of deflection and of bending moment against time for $B = 1$ and $\xi = 0.5$ are shown in Figs. 1 and 2, respectively. A plot of the variation with $B$ of the quantity $v_{max}/v_{st,\ max}$, representing the maximum error in the static solution, is given in Fig. 3. These plots are discussed in the next section; a few remarks concerning the numerical evaluation of the series contained in Eqs. (11) and (11a) are collected here.

The index $n$ of the summations in Eqs. (11) and (11a) assumes only odd values, so that the quantity $(n^2 - 1)$ is always divisible by 8; it then follows that the functions $(\cos n^2\pi^2B^2\tau)$ and $(\sin n^2\pi^2B^2\tau)$ will be independent of $n$ if the time $\tau$ is chosen so that the quantity $(8\pi B^2\tau)$ is a multiple of $2\pi$. Table 1 may then

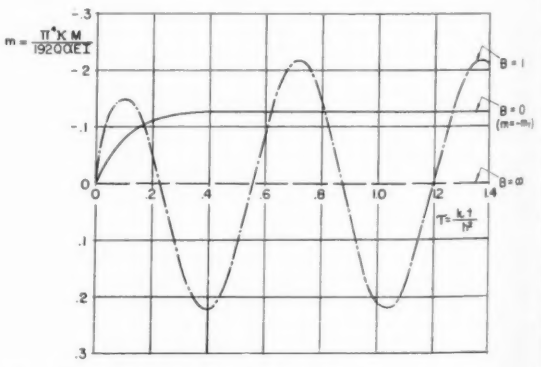


FIG. 2. Nondimensional variation of bending moment at $x = (L/2)$ with time for $B = 0, 1, \infty$.

TABLE 1

| | | | | | | | | | |
|---|---|---|---|---|---|---|---|---|---|
| $\pi B^2\tau$ | 0 | 1/4 | 1/2 | 3/4 | 1 | 5/4 | 3/2 | 7/4 | 2 |
| $\cos n^2\pi^2B^2\tau$ | 1 | $1/\sqrt{2}$ | 0 | $-1/\sqrt{2}$ | $-1$ | $-1/\sqrt{2}$ | 0 | $1/\sqrt{2}$ | 1 |
| $\sin n^2\pi^2B^2\tau$ | 0 | $1/\sqrt{2}$ | 1 | $1/\sqrt{2}$ | 0 | $-1/\sqrt{2}$ | $-1$ | $-1/\sqrt{2}$ | 0 |

be set up (and can of course be extended indefinitely in view of the periodic character of the trigonometric functions).

For these special values of $\tau$, Eq. (11) becomes

$$\pi^4(V - V_{st})_{\text{special }\tau} = B^2 \sin n^2\pi^2B^2\tau \left\{ \sum_{n=1,3,5}^{\infty} \frac{\sin n\pi\xi}{n} \times \sum_{j=1,3,5}^{\infty} \frac{1}{j^2(j^4 + n^4B^4)} \right\} + \cos n^2\pi^2B^2\tau \left\{ \sum_{n=1,3,5}^{\infty} \frac{\sin n\pi\xi}{n^3} \sum_{j=1,3,5}^{\infty} \frac{1}{j^4 + n^4B^4} \right\} - \left\{ \sum_{n=1,3,5}^{\infty} \frac{\sin n\pi\xi}{n^3} \sum_{j=1,3,5}^{\infty} \frac{e^{-j^2\pi^2\tau}}{j^4 + n^4B^4} \right\} \tag{11b}$$

The coefficient of $(\sin n^2\pi^2B^2\tau)$ in this equation has been derived with the aid of the identity

$$\frac{\pi^2}{8} = \sum_{j=1,3,5}^{\infty} \frac{1}{j^2} \tag{11c}$$

The series in Eq. (11b) were evaluated numerically without difficulty. An expression similar to Eq. (11b) was employed for the calculation of the nondimensional bending moment $m$ at the above special values of $\tau$.

## Discussion

The above development and numerical results lead to the following observations.

(1) The basic parameter of the problem is $B$, defined by the last of Eqs. (7), and is the square root of the ratio of the characteristic time $(h^2/\kappa)$ of the heat problem to the characteristic time $k^2L^2$ (proportional to the natural period of the beam) of the vibration problem. Thus $B$ is large for beams with low diffusivity, low density, or high bending rigidity; it is low if the beam is slender or dense. The importance of the inertia effects increases with decreasing $B$, so that for $B = 0$ they in effect prevent the beam from deflecting at any finite time. On the other hand as $B$ increases beyond all bounds, the inertia forces disappear and the static solution results.

(2) A quantitative illustration of the discussion of the previous paragraph may be found in Fig. 3, which can be used to estimate numerically the error committed by adopting the static solution. The error is less than 10 per cent (of the static deflection) if $B$ is larger than about 3.25. It is interesting to see what type of structural member corresponds to such a value of $B$; for this purpose a second abscissa scale (labeled $h$) was provided in Fig. 3. This scale gives, alongside each value of $B$, the thickness of a rectangular aluminum [$\kappa = 0.86$ cm.²/sec. $= 0.1333$ in.²/sec.,[9] $c = 2 \times 10^6$ in./sec.] beam 10 in. long. It may be noticed that all thicknesses indicated are relatively small and that the error will be more than 10 per cent and therefore not negligible for beams less than about 0.135 in. thick. This means that the major portion of Fig. 3 corresponds in reality to thin plates or sheets, and that for such slender members the heat-induced vibrations may be quite large, while for heavier beams they would ordinarily be negligible.

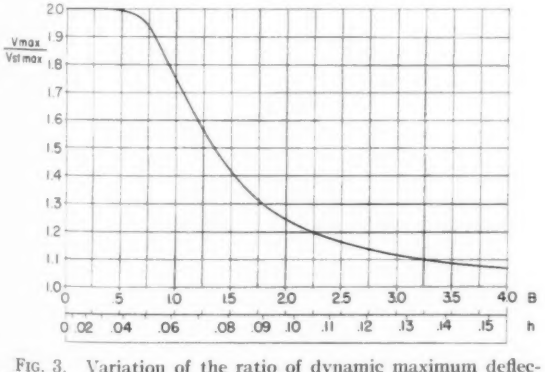


FIG. 3. Variation of the ratio of dynamic maximum deflection to static maximum deflection with the parameter $B$ and with the thickness of a rectangular aluminum beam with $L = 10$ in., at $x = (L/2)$.

(3) It is interesting to note that the ratio of actual to static deflections is closely approximated by the equations

$$\frac{v_{max}}{v_{st,\,max}} = \begin{cases} 1 + 2e^{-B} & \text{for } B \geq \log_e(1/2) = 0.6931 \\ 2 & \text{for } B \leq \log_e(1/2) = 0.6931 \end{cases} \tag{12}$$

(4) Figs. 1 and 2 show that the dynamic solution oscillates about the static one. The period $\tau^*$ of these oscillations is

$$\tau^* = 2/(\pi B^2) \tag{13}$$

while their amplitude may be estimated (for the case of the deflections) with the aid of Eqs. (12) and (9b) to be [for $B \leq \log_e(1/2)$]

$$(V_{max} - V_{st,\,max}) = 2\,V_{st,\,max}\,e^{-B} = (\pi^4/1536)e^{-B} \tag{13a}$$

Eq. (13) shows that the maximum amplitude and therefore the maximum deflection is reached at later and later times as $B$ decreases; at the same time its magnitude increases and approaches, as $B$ approaches zero, the maximum static deflection.

## References


[1] Timoshenko, S., *On The Correction for Shear of the Differential Equations for Transverse Vibrations of Prismatic Bars*, Phil. Mag., Vol. 41, 1921.

[2] Boley, Bruno A., and Chao, Chi-Chang, *Some Solutions of the Timoshenko Beam Equations*, Paper 55-APM-28, Journal of Applied Mechanics.

[3] Timoshenko, S., and Goodier, J. N., *Theory of Elasticity*, 2nd Ed.; McGraw-Hill, N. Y., 1951.

[4] Boley, Bruno A., *The Determination of Temperature, Stresses, and Deflections in Two-Dimensional Thermo-Elastic Problems*, Journal of the Aeronautical Sciences, (to be published): also W.A.D.C. Tech. Rep. 54-424.

[5] Boley, Bruno A., and Mechanic, Harold, *Thermo-Elastic Stresses and Deflections in Beam-Columns*, W.A.D.C. Tech. Rep. 54-425, March, 1954.

[6] von Karman, Th., *Ueber die Grundlagen der Balkentheorie*, Abh. Aerodynam. Inst., Tech. Hochschule Aachen, Vol. 7, p. 3, 1927.

[7] Mindlin, R. D., *Influence of Rotatory Inertia and Shear on Flexural Motions of Isotropic Elastic Plates*, J. of Appl. Mech., Trans. A.S.M.E., Vol. 73, pp. 31–38, 1951.

[8] Boley, Bruno A., *An Approximate Theory of Lateral Impact on Beams*, J. of Appl. Mech., Vol. 22, No. 1, p. 69, March, 1955.

[9] Carslaw, H. S., and Jaeger, J. C., *Conduction of Heat in Solids*; Clarendon Press, Oxford, 1947.

[10] Mindlin, R. D., and Goodman, L. E., *Beam Vibrations with Time-Dependent Boundary Conditions*, J. of Appl. Mech., Vol. 17, p. 377, 1950.


# On the Model of the Free, Shock-Separated, Turbulent Boundary Layer


Artur Mager

*Research Scientist, Marquardt Aircraft Co., Van Nuys, Calif.*


August 3, 1955

## Symbols

| | | |
|---|---|---|
| $A$ | = | area |
| $a$ | = | speed of sound |
| $B,C,D,E,$ | = | points in flow field |
| $K$ | = | constant ( = 0.55) |
| $M$ | = | Mach Number |

$P$ = total pressure
$p$ = static pressure
$u$ = velocity in $\xi$ direction
$\gamma$ = ratio of specific heats
$\delta$ = thickness of separated layer
$\delta^+$ = displacement thickness
$\delta^{++}$ = momentum thickness
$\eta,\xi$ = orthogonal curvilinear coordinates (see Fig. 1)
$\theta$ = deflection
$\kappa$ = curvature of the $\xi$ axis
$\rho$ = density

***Subscripts***

$d$ = discharge
$f$ = final
$i$ = initial
$s$ = separation

***Superscripts***

$^*$ = throat
bar above the value indicates incompressible flow quantity

## Introduction

In general, shock-separated boundary layers may be divided into two main groups; the free and the restricted separated boundary layers. By free shock-separated layers, one means that type of separation where the flow downstream of the separation region is free to adjust to any direction that may result from the shock-boundary-layer interaction process. Such separation occurs ahead of sufficiently large steps or in overexpanded nozzles of sufficiently large divergence.

The name restricted shock-separated boundary layers, on the other hand, is given to all other cases of separation—that is, where the flow downstream of the separation region must adjust not only to the imposed pressure but also to a definite direction. An example of such separation is the case of an oblique (or normal) shock striking the boundary layer and calling for certain pressure and directional adjustment.

As it has been found in various experimental investigations,[1, 2, 3] the shape of the wall pressure distribution in the interaction region permits certain special characteristics (inflection points, peaks, etc.) to be discerned which in turn can be connected to definite changes of flow such as the onset of separation. In this way, for instance, it has been established[2] that the pressure ratio at which the free or the restricted turbulent boundary-layer separation occurs is appreciably smaller than that which exists when the interaction process is complete. Also, in the free shock-separated turbulent boundary layers ahead of steps a certain peak pressure ratio has been observed, and it is felt that the understanding of the mechanism through which this arises may throw a light on the way in which the interaction process takes place. Furthermore, by matching the shape of the pressure distribution curves, it has been shown,[2] at least in some cases, that the interaction process of the restricted shock-separated turbulent boundary layer starts as a free shock-separation.

For these reasons, the understanding of the obviously simpler free shock-separation process, while important in itself, also has undoubtedly a considerable bearing on the more complex restricted shock-separation case.

An analysis of the free shock-separated turbulent boundary layer has been carried out lately by Crocco and Probstein[4] and indeed their results seem to agree very well with experiment.[5] Unfortunately, however, the method used by Crocco and Probstein requires that flow be considered at large distances from the separation region and thus it does not give an indication of the process through which the adjustment in flow occurs. Free shock-separation has also been investigated by Reshotko and Tucker;[6] however, these investigators have not recognized the experimentally observed difference[2] between the separation and final pressures. This failure, to note that separation occurs at pressure lower than that which is ultimately reached, forces an adjustment in the "separation parameter" of reference 6, depending on the mode in which the separation is produced—e.g., a different parameter is used for separation ahead of steps and that ahead of wedges. This of course is not plausible, since it is unlikely that the turbulent boundary layer "knows," when it separates, that the pressure gradient causing the separation is due to a wedge, a step, or what have you. It will in fact be demonstrated in this paper that the difference between the separation pressure and final pressure can be accounted for analytically and consequently the more or less arbitrary adjustments in the "separation parameter" as suggested in reference 6 are incorrect.

A restricted shock-separation has been analyzed by Gadd;[3] however the various assumptions used and certain discrepancies in the experimental data[7] (from which the semiempirical information was obtained) throw some doubt on his results.

In what follows, first a detailed model of the free shock-separated turbulent boundary layer is postulated, and next the pressure rise following from this model is estimated and compared with experiment. Finally, the results are applied to the prediction of separation in an overexpanding nozzle.

## Analysis

It is postulated that free shock-separation of turbulent boundary layer occurs whenever the layer finds itself at a certain pressure ratio $p_f/p_i$, which is different from the separation ratio $p_s/p_i$ and is primarily a function of the local Mach Number $M_i$. It is furthermore postulated that under these conditions the following flow situation develops (see Fig. 1): (a) corresponding to the separation pressure ratio $p_s/p_i$ a wave ($B$–$C$) forms in the boundary layer, so that upon crossing this wave the boundary layer separates, deflecting away from the surface; (b) due to this deflection a transverse pressure gradient $\Delta p$ establishes itself in the boundary layer so as to balance the centrifugal forces; (c) once separated, the boundary layer transforms in character to jet-like—that is, at some point $E$ it has the same pressure $p_f$ and direction $\theta_f$ as the flow outside the layer; (d) the flow outside the boundary layer adjusts to the pressure $p_f$ and the direction $\theta_f$ by means of an oblique shock ($C$–$D$) emanating from the edge of the boundary layer.

It should be noted that although the separation wave $B$–$C$ is *not* identical with the shock $C$–$D$, it still may be considered as the start of the shock's bifurcation through which the turning and additional rise in pressure occurs.

As it has been shown analytically by the author[8] and argued heuristically by Schuh[9], the separation of the compressible turbulent boundary layer in absence of surface friction can be predicted by use of the well-known semiempirical relations for the behavior of turbulent boundary layer when these are transformed to their compressible-flow equivalents. This results in a relation between the Mach Numbers[8]

$$M_s^2 = KM_i^2 \tag{1}$$

which can then, together with the oblique shock approximation, be used to determine the pressure ratio across the separation wave $B$–$C$,

$$p_s/p_i = 1 + \frac{\gamma M_i^2}{2}\,\frac{(1-K)}{1+[(\gamma-1)/2]M_i^2} \tag{2}$$

It should be noted here that since, as is well known, the boundary layer cannot stand a very large pressure ratio without separation, the conditions across the wave $B$–$C$ must be similar to those across a Mach wave—that is, the use of the oblique shock approximation is essential to the determination of the correct pressure ratio $p_s/p_i$. This point has not been made quite clear in reference 8 and consequently the authors of reference 6 were apparently misled into an incompatible comparison with experiment and an incorrect conclusion about the accuracy of the results of reference 8.

The existence of such an essentially straight separation wave $B$–$C$ in the boundary layer is justified by the fact that the separation causes a disturbance at the wall which propagates into the layer, and by the fact that the turbulent boundary layer—which

surface friction had no time to distort—is predominantly a high-speed layer.

Since the separation pressure $p_s$ may thus be computed from Eq. (2), it is next necessary to estimate the transverse pressure rise $\Delta p$. This can be done by imagining that the boundary layer flows along a curved surface of the coordinate $\xi$ (see Fig. 1), so that from the momentum equation in the $\eta$ direction

$$\partial p/\partial \eta = \kappa \rho u^2 \tag{3}$$

where $\kappa = -d\theta/d\xi$ is the local curvature of the $\xi$ axis and the velocity $u$ is in the $\xi$ direction. Assuming that the pressure in this transition region may be represented approximately as

$$p = p_s + \Delta p F(\eta/\delta) \tag{4}$$

with $F(0) = 1$ and $F(\delta) = 0$. Eq. (3) may be integrated to

$$-\Delta p = \kappa \int_0^\delta \rho u^2 d\eta \tag{5}$$

It should be noted here that the meaning of $\delta$ refers to the thickness of the separated layer measured along the $\eta$ coordinate, and that $\Delta p = p - p_s$ is a function of $\xi$ only, varying from 0 to $(\Delta p)_f = p_f - p_s$. It is now convenient to change the right-hand side of Eq. (5) to the incompressible form according to the modified Dorodnietzyn-Stewartson transformation.[10] After some manipulation this results in

$$\left.\begin{aligned} \int_0^\delta \frac{\rho u^2}{\rho_s u_s^2}\, d\eta &= \bar{\delta} \frac{\rho_f t_0}{\rho_s t_s} \left[1 - \frac{\bar{\delta}^+}{\bar{\delta}} - \frac{\bar{\delta}^{++}}{\bar{\delta}}\right] \\ \frac{\Delta p}{p_s} &= \frac{\gamma M_s^2}{1 + [(\gamma-1)/2] M_s^2} \frac{\bar{\delta}}{d\xi}\, d\theta \left[1 - \frac{\bar{\delta}^+}{\bar{\delta}} - \frac{\bar{\delta}^{++}}{\bar{\delta}}\right] \end{aligned}\right\} \tag{6}$$

In view of the small changes involved and the approximate nature of this computation, one replaces the differentials by finite differences, $d\theta \backsimeq \Delta\theta$, $d\bar{\xi} \backsimeq \Delta\bar{\xi}$ and in this form attempts to evaluate Eq. (6) at point $E$— that is, when the transition to jet-like flow is complete. The quantity in brackets can thus be obtained from incompressible data for jets, and in particular using the well-known Tollmien's distribution[11] one finds that $[1 - (\bar{\delta}^+/\bar{\delta}) - (\bar{\delta}^{++}/\bar{\delta})] \backsimeq 0.328$.

Furthermore, at point $E$, $\Delta\theta = \theta_f$, so that the only quantity which remains to be established is $\bar{\delta}/\Delta\bar{\xi}$. Now $\bar{\delta}/\Delta\bar{\xi}$, for incompressible separating boundary layer must be of the order of magnitude of unity, and an examination of some unpublished data indicates a value of 1.03 (?). This means that the transformation to jet-like flow for incompressible layer seems to occur in slightly less than one boundary-layer thickness and this appears in agreement with the remarks of Crocco and Lees[12] so that $\bar{\delta}/\Delta\bar{\xi} = 1.0$ has been used in this computation. It should be noted that this quantity is *not* the same as the "adjustment distance" used by Crocco and Probstein[4] and which does not enter the determination of $p_f/p_i$. Using the above values one thus

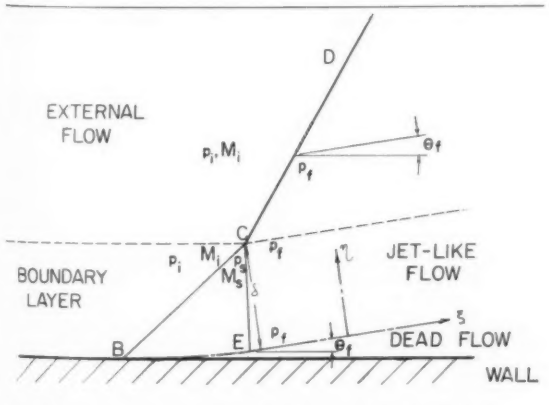


FIG. 1. MODEL OF THE FREE, SHOCK-SEPARATED TURBULENT BOUNDARY LAYER

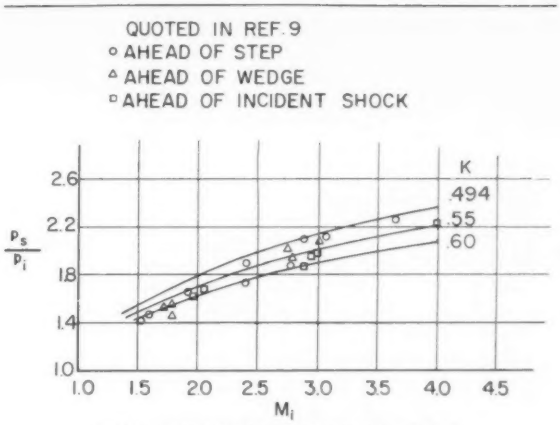


FIG. 2. SEPARATION PRESSURE RATIO

obtains from Eq. (6)

$$\frac{p_f}{p_s} = 1 + 0.328 \frac{\gamma M_s^2 \theta_f}{1 + [(\gamma-1)/2] M_s^2} \tag{7}$$

or

$$\frac{p_f}{p_i} = \frac{p_f}{p_s}\frac{p_s}{p_i} = \frac{p_s}{p_i}\left\{1 + 0.328 \frac{\gamma K M_i^2 \theta_f}{1 + [(\gamma-1)/2] K M_i^2}\right\} \tag{7a}$$

Eqs. (7a) and (2) furnish a relation which exists at any $M_i$ between $p_f/p_i$ and $\theta_f$. Another such relation is, of course, given by the flow outside the boundary layer which adjusts by means of a shock wave ($C$–$D$) to the same pressure and direction.

Eliminating $\theta_f$ between these two permits the determination of the particular value of $p_f/p_i$ which occurs in cases of free shock-separated turbulent boundary layer.

To carry this out, the following procedure was used: the value of $\theta_f$ across the shock $C$–$D$ was first approximated by

$$\theta_f \backsimeq \left(\sqrt{M_i^2 - 1}/\gamma M_i^2\right)[(p_f/p_i) - 1] \tag{8}$$

and the substitution of this into Eq. (7a) gave

$$\frac{p_f}{p_i} \doteq \frac{p_s}{p_i}\left(\frac{1+G}{1 + (p_s/p_i)G}\right) \tag{9}$$

$$\text{with} \qquad G \equiv -0.328 \frac{K\sqrt{M_i^2 - 1}}{1 + (\gamma - 1/2) K M_i^2} \tag{10}$$

It should be noted that for small values of $Gp_s/p_i$ Eq. (9) can be further reduced to

$$p_f/p_i \backsimeq (p_s/p_i)\left\{1 + G[1 - (p_s/p_i)]\right\} \tag{9a}$$

and this amounts to a replacement of $\theta_f$ in Eq. (7a) by $\theta_s$.

Next, using the value of $p_f/p_i$ from Eq. (9), a new value of $\theta_f$ was obtained from the oblique shock relation and this new value was used in Eq. (7a) to obtain a better approximation to $p_f/p_i$. In view of the rather rough nature of this estimate, only one adjustment is really justifiable.

Reference 8 suggested that $K = 0.494$. This value was obtained from the semiempirical relation of Gruschwitz and the values of the boundary-layer form factor at separation. Although this value appeared to fit the experiments quoted in reference 1, it has been noted by Schuh[9] that in these experiments the separation was not directly determined. Because of the semiempirical nature of $K$ it is plausible to adjust its value so that it fits the greatest amount of data where the separation point was either directly measured or its position established through the characteristic point of the pressure distribution curve. The data quoted by Schuh[9] seem to indicate that a value of 0.55 appears to agree somewhat better with experiment. This is shown in Fig. 2, and consequently $K = 0.55$ has been used in subsequent computation.

The solution of Eq. (9) with $\gamma = 1.4$, together with the experimental data obtained by various investigators ahead of large steps[1, 2, 5] and the analytical results of Crocco and Probstein[4] is

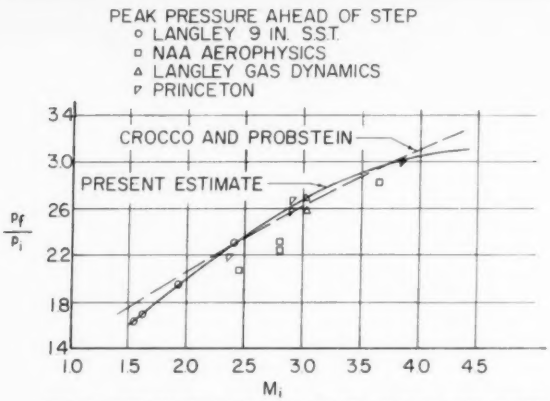


FIG. 3. PRESSURE RATIO OF FREE, SHOCK-SEPARATED TURBULENT BOUNDARY LAYER ($\gamma = 1.4$, PLANE SHOCK)

shown in Fig. 3. It may be seen that in spite of the rather approximate nature of this estimate, fair agreement has been obtained with the experiment as well as with the analysis of Crocco and Probstein. On the basis of this agreement it is concluded that the postulated model of the free-shock separated turbulent boundary layer represents a reasonably accurate picture of the flow.

It should be noted here that the pressure ratio $p_f/p_i$ shown in Fig. 3 is applicable only to cases of plane shock and $\gamma = 1.4$. For other conditions a different value of $p_f/p_i$, computed, say, from conical shock relations, will be applicable.

### Separation in Nozzles

In an overexpanding nozzle the ambient discharge pressure $p_d$ is much higher than the local wall pressure $p_i$ at the nozzle outlet. If the ratio of the discharge pressure to the local wall pressure is larger than $p_f/p_i$ at the corresponding $M_i$, then a free shock-separation of the turbulent boundary layer will occur. Since, however, the pressure in the separated region must equal the ambient discharge pressure, the separation point is free to move upstream until the ratio $p_d/p_i$ just equals the appropriate value of $p_f/p_i$ at the corresponding wall Mach Number $M_i$. In other words, in order to determine the separation point in an overexpanded nozzle, one simply plots $p_d/p_i$ vs. $M_i$ on Fig. 3. The intersection of the two curves determines the conditions at which the separation will occur.

To furnish a comparison with this experiment, $p_i$ and $M_i$ were computed for conditions of McKenney's[13] investigation, by assuming one-dimensional isentropic flow up to the separation point. McKenney's data have been used because his nozzle was two-dimensional and thus the shock was plane, and because McKenney used dry nitrogen for which $\gamma = 1.4$. Proceeding as outlined above, the area ratio at which the separation will occur could thus be determined. This result together with actual experimental points is shown in Fig. 4. It may be seen that in spite of the rather crude method of obtaining $p_i$ and $M_i$, the prediction shows a fair agreement with experiment.

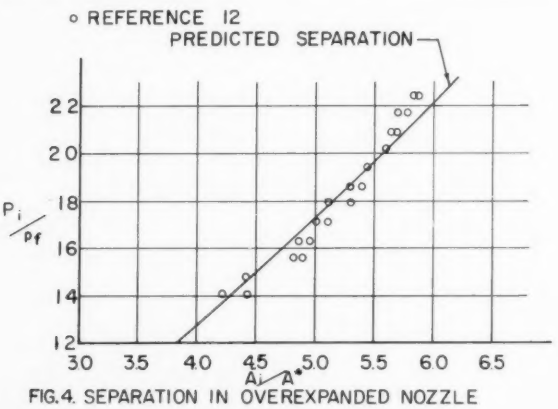


FIG. 4. SEPARATION IN OVEREXPANDED NOZZLE ($\gamma = 1.4$)

### References


[1] Lange, R. H., *Present Status of Information Relative to the Prediction of Shock-Induced Boundary-Layer Separation*, NACA TN 3605, February, 1954.

[2] Bogdonoff, S. M., and Kepler, E. C., *The Separation of a Supersonic Turbulent Boundary Layer*, Journal of the Aeronautical Sciences, Vol. 22, No. 5, pp. 414–424, June, 1955.

[3] Gadd, G. E., *Interactions Between Wholly Laminar and Wholly Turbulent Boundary Layers and Shock Waves Strong Enough to Cause Separation*, Journal of the Aeronautical Sciences, Vol. 20, No. 11, pp. 729–739, November, 1953.

[4] Crocco, L., and Probstein, R. F., *The Peak Pressure Rise Across an Oblique Shock Emerging from a Turbulent Boundary Layer Over a Plane Surface*, Princeton U. Report 254, March, 1954.

[5] Bogdonoff, S. M., *Some Experimental Studies of the Separation of Supersonic Turbulent Boundary Layers*, Proc. of the 1955 Heat Transfer and Fluid Mechanics Inst., U. of Calif., June, 1955.

[6] Reshotko, E., and Tucker, M., *Effect of a Discontinuity on Turbulent Boundary-Layer-Thickness Parameters with Application to Shock-Induced Separation*, NACA TN 3454, May, 1955.

[7] Bogdonoff, S. M., *Remarks on Interaction Between Wholly Laminar or Wholly Turbulent Boundary Layers and Shock Waves Strong Enough to Cause Separation*, Journal of the Aeronautical Sciences, Vol. 21, No. 2, pp. 138–193, February, 1954. See also reply by Gadd and Holder in *Journal of the Aeronautical Sciences*, Vol. 21, No. 8, pp. 571–572, August, 1954.

[8] Mager, A., *Prediction of Shock-Induced Turbulent Boundary-Layer Separation*, Journal of the Aeronautical Sciences, Vol. 22, No. 3, pp. 201–202, March, 1955.

[9] Schuh, H., *On Determining Turbulent Boundary-Layer Separation in Incompressible and Compressible Flow*, Journal of the Aeronautical Sciences, Vol. 22, No. 5, pp. 343–345, May, 1955.

[10] Van Lee, Nguyen, *Transformation Between Compressible and Incompressible Boundary-Layer Equations*, Journal of the Aeronautical Sciences, Vol. 20, No. 8, pp. 583–584, August, 1953.

[11] Pai, Shih-I., *Fluid Dynamics of Jets*; D. Van Nostrand Co. Inc., New York.

[12] Crocco, L., and Lees, L., *A Mixing Theory for the Interaction Between Dissipative Flows and Nearly Isentropic Streams*, Journal of the Aeronautical Sciences, Vol. 19, No. 10, pp. 649–676, October, 1952.

[13] Summerfield, M., Foster, C. R., and Swan, W. C., *Flow Separation in Overexpanded Supersonic Exhaust Nozzles*, Jet Propulsion, Vol. 24, No. 5, pp. 319–321, September–October, 1954.


## Experimental Observation of Laminar Boundary-Layer Oscillations in Supersonic Flow*


John Laufer

*Research Specialist, Jet Propulsion Laboratory, California Institute of Technology, Pasadena, Calif.*


August 3, 1955

THIS NOTE gives a short description of exploratory experiments carried out recently in an attempt to detect oscillations in a supersonic laminar boundary layer as predicted by theory.[1] It is known theoretically that the laminar boundary layer selectively amplifies or damps fluctuations present in a narrow frequency band of a disturbance spectrum introduced into the layer. This behavior has been quantitatively confirmed in the incompressible case;[2] however, no such experiments have been reported in supersonic flows.

An available flat plate[3] was installed in the 18 by 20 in. supersonic wind tunnel of the Jet Propulsion Laboratory. A small plastic plug containing hot-wire prongs could be placed at stations

* This paper presents the results of one phase of research carried out at the Jet Propulsion Laboratory, California Institute of Technology, under joint sponsorship of the Department of the Army, Ordnance Corps (under Contract No. DA-04-495-Ord 18), and the Department of the Air Force.

of either 5.5 or 13 in. from the leading edge, as shown in Fig. 1. The prongs (approximately 0.005 in. in diameter) protruded from the surface by about 0.020 in., and they were 0.020 in. apart. A platinum-rhodium (90–10 per cent) wire of 0.00005-in. diameter was stretched between these prongs at a distance of about 0.003 to 0.004 in. from the surface. This distance was of the order of one-tenth of the laminar boundary-layer thickness.

Most of the preliminary experiments were carried out at Mach Number 2.15. The measuring procedure consisted of obtaining the spectra (or the peaks in a spectrum) of the hot-wire signal at various tunnel pressures using a Sierra wave analyzer. An example of such a spectrum taken at a tunnel Reynolds Number per in. of about 200,000 is shown in Fig. 2. Note a small peak corresponding to the second harmonic.

After a critical examination of the presence of the energy peaks in the spectrum, it has been concluded that they are due to laminar boundary-layer oscillations. Visual observation of the hot-wire signal on the oscilloscope did not indicate the oscillations as clearly as seen by Schubauer and Skramstad.[2] This is due to the high relative noise level present in the signal inherently present in supersonic hot-wire measurements. However, if transition occurred a short distance downstream from the wire, periodic oscillation could clearly be observed.

The frequency values corresponding to the energy peaks were reduced in the conventional form, as shown in Fig. 3. There $\beta = 2\pi f$, where $f$ is the oscillation frequency, $\nu$ the kinematic viscosity, $V_0$ the free stream velocity, and $R_\theta$ the Reynolds Number based on momentum thickness calculated from laminar boundary-layer theory. This figure also indicates the theoretical maximum amplification curves for $M = 0.7$ and 1.3. These values were calculated by Lester Lees (private communication) and were obtained for a given $R_\theta$ by assuming a flat disturbance spectrum along the first branch of the neutral curve and integrating the amplification coefficients along constant frequency lines from the first branch of the neutral curve to $R_\theta$.

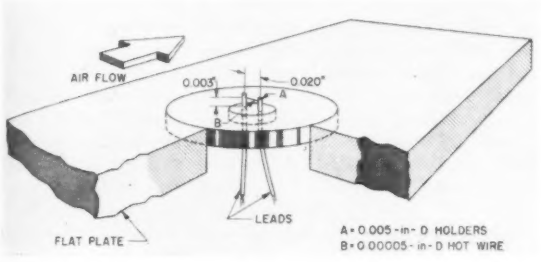


FIG. 1

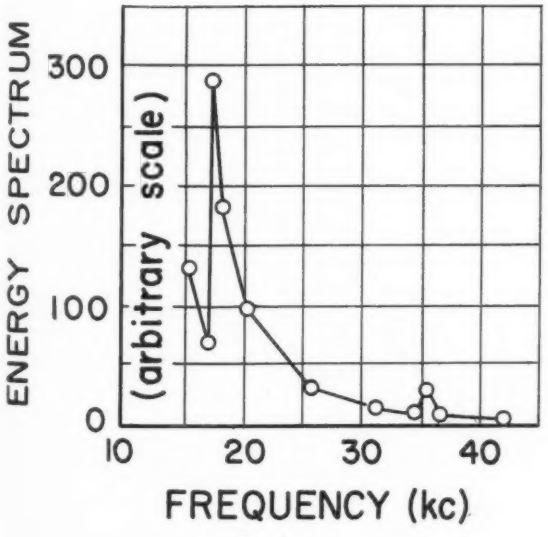


FIG. 2

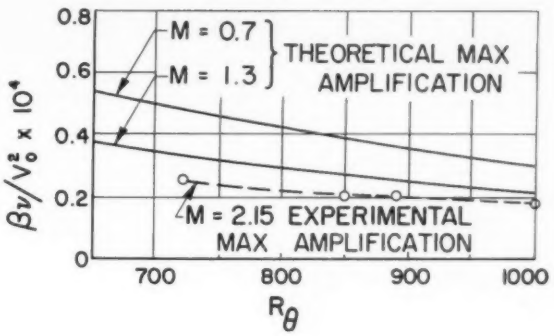


FIG. 3.

## REFERENCES

[1] Lees, L., and Lin, C. C., *Investigation of the Stability of the Laminar Boundary Layer in a Compressible Fluid*, NACA TN 1115, 1946.

[2] Schubauer, G. B., and Skramstad, H. K., *Laminar Boundary Layer Oscillations and Transition on a Flat Plate*, NACA TR 909, 1948.

[3] Coles, Donald, *Measurements of Turbulent Friction on a Smooth Flat Plate in Supersonic Flow*, Journal of the Aeronautical Sciences, Vol. 21, No. 7, pp. 434–448, July, 1954.

## The Normal Shock Properties for Air in Dissociation Equilibrium

Mary F. Romig
*Aerodynamics Engineer, Convair, A Division of General Dynamics Corporation, San Diego, Calif.*

August 15, 1955

### INTRODUCTION

THE PURPOSE of this note is to present the normal shock parameters using the most recent thermodynamic properties of air in dissociation equilibrium.

### SYMBOLS

$E$ = internal energy
$M$ = Mach Number
$p$ = static pressure
$R$ = universal gas constant
$T$ = static temperature

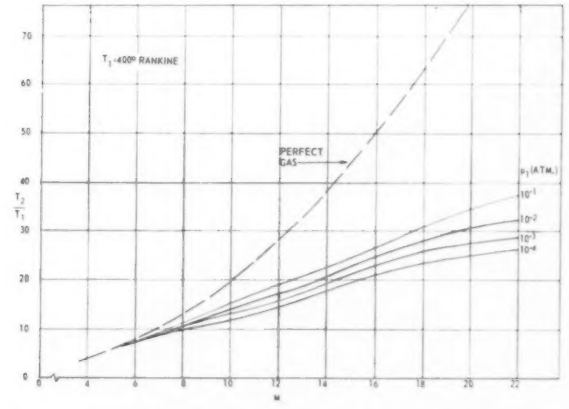


FIG. 1. Normal shock static temperature ratio for air in dissociation equilibrium.

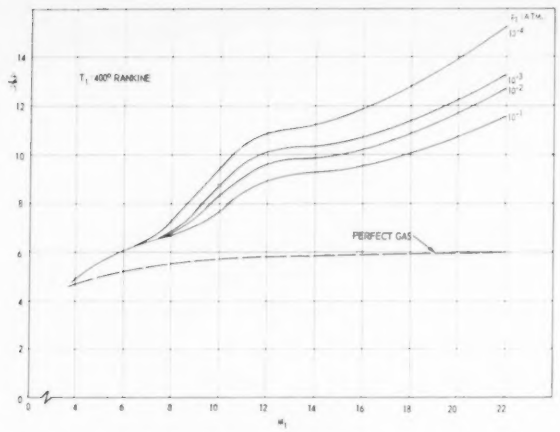


FIG. 2. Normal shock density ratio for air in dissociation equilibrium.

$U$ = velocity
$Z$ = factor used to modify the perfect gas law [see Eq. (3)]
$\gamma$ = ratio of specific heats
$\epsilon$ = dissociation energy of nitrogen ($N_2$)
$\rho$ = density

## DISCUSSION

A recent revision of the dissociation energy of nitrogen has rendered all previous air properties obsolete above 5,000° Rankine, where they reflect prematurely the dissociation of nitrogen. The corrected thermodynamic air properties, based on $\epsilon$ = 9.758 e.v. rather than 7.373 e.v., have been published by the National Bureau of Standards,[1] and were used here to solve the normal shock equations for a variety of free-stream conditions. The air behind the shock was assumed to be in dissociation equilibrium.

The equations of energy, momentum, and continuity, which relate conditions before (1) and after (2) a normal shock, are combined to give

$$(1/2)(p_1 + p_2)[(1/\rho_1) - (1/\rho_2)] = E_2 - E_1 \qquad (1)$$

$$U_1^2 = (\rho_2/\rho_1)[(p_2 - p_1)/(\rho_2 - \rho_1)] \qquad (2)$$

Tabulated in reference 1 for given temperatures and densities are $E$, the internal energy, and $Z$, a factor which is inserted in the perfect gas law

$$p = Z\rho RT \qquad (3)$$

to account for the change in molecular weight due to dissociation.

For a given set of initial conditions ($p_1$ and $T_1$) the simplest solution of Eqs. (1) and (2) is to choose $T_2$, solve Eq. (1) by iteration and accept whatever velocity Eq. (2) gives. The results,

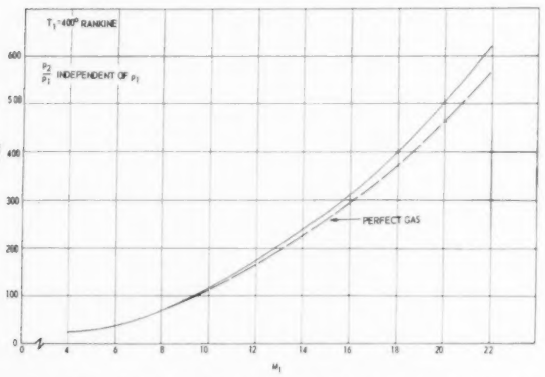


FIG. 3. Normal shock static pressure ratio for air in dissociation equilibrium.

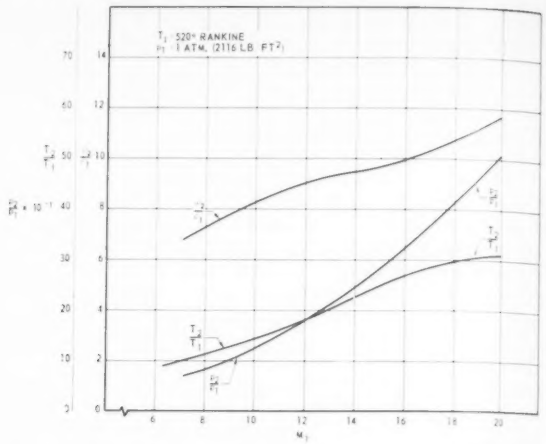


FIG. 4. Normal shock properties for standard sea level free-stream conditions.

$p_2/p_1$, $\rho_2/\rho_1$ and $T_2/T_1$ are plotted versus free-stream Mach Number in Figs. 1, 2, and 3, for the initial conditions of $T_1$ = 400° Rankine and $p_1 = 10^{-1}$, $10^{-2}$, $10^{-3}$, and $10^{-4}$ atmospheres, corresponding to flight in or near the isothermal altitudes. Fig. 4 presents the same parameters for standard sea level conditions, corresponding to the static region in a shock tube. Also shown in these figures, for comparative purposes, are the perfect gas solutions, with $\gamma = 1.4$.

It is of interest to see what effects the change in the dissociation energy of nitrogen have on conditions behind the shock. Fig. 5 gives the normal shock temperature ratio for three values of $\epsilon$; the perfect gas ($\epsilon = \infty$), the present solution ($\epsilon$ = 9.758 e.v.), and a solution based on the air properties of Krieger and White[2] ($\epsilon$ = 7.373 e.v.). Raising the dissociation energy of nitrogen to its present value causes about 18 per cent increase in temperature. From Fig. 3 it can be seen that even an infinite change in $\epsilon$ has little effect on the pressure ratio. The density, which is roughly inversely proportional to the temperature (since $1.0 \leq Z \leq 1.5$) is lower for the present solution by about 20 per cent.

## REFERENCES

[1] Hilsenrath, Joseph, and Beckett, Charles W., *Thermodynamic Properties of Argon-Free Air (0.78847$N_2$, 0.21153$O_2$) to 15,000°K.*, National Bureau of Standards Report 3991, April, 1955.

[2] Krieger, F. J., and White, W. B., *Composition and Thermodynamic Properties of Air*, RAND Corporation Report R-149, April, 1949.

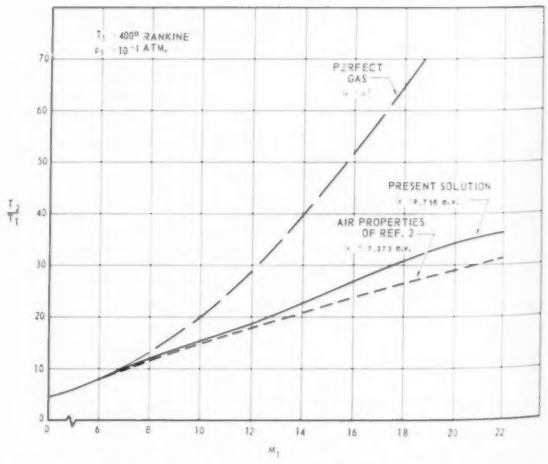


FIG. 5. Normal shock temperature ratio for three dissociation energies of nitrogen.

## Some Results of Linearized Transonic Flow About Slender Airfoils and Bodies of Revolution*

P. F. Maeder and H. U. Thommen
*Division of Engineering, Brown University, Providence, R.I.*
August 8, 1955

IF THE EQUATION for the velocity potential of a compressible nonviscous fluid is linearized in the conventional manner—i.e., by neglecting all second and higher order terms, then it changes its character abruptly from elliptic to hyperbolic as the speed of sound is passed. In particular, it degenerates at the speed of sound very much as the equation for the vibration of a rotating shaft degenerates at the critical speed, if no damping is assumed. It was found, therefore, that for transonic flows a nonlinear or damping term had to be retained in the equation. This term then essentially takes account of the fact that the speed of sound in the medium changes due to the perturbation velocities themselves. It describes the interference between the signals originating from various points of the body or airfoil.

K. Oswatitsch,[1] in a recent paper, determined the flow about a half-body of revolution at the speed of sound by assuming part of the nonlinear term, the derivative of $u$ in $x$-direction, constant and thus linearizing the transonic equation without omitting the damping or interference term altogether. He made the further assumption that no disturbances shall travel upstream of the nose of the body. The result obtained in this special case agreed surprisingly well with experiments.

A perusal of the situation now shows that the first assumption by Oswatitsch is far closer to the actual behavior of the fluid at all speeds than originally suspected, while the second one does not have to be made. In particular, if employed in conjunction with modern methods of operational calculus, as applied by Ward[2] to linear supersonic and by Sears[3] to linear subsonic flows about slender bodies, this approach allows the calculation of transonic flows in an easy and explicit manner. It is also no longer necessary to have information about the Mach cone, as, for example, was supposed by Ward in order to be able to use Laplace transforms. Rather, it is sufficient to apply the usual boundary conditions at infinity and to use exponential Fourier transform at all speeds. Conventional linearized subsonic and supersonic flows are then obtained merely as special cases of this more complete linear transonic treatment. The choice of $\partial u/\partial x$ as positive or negative in the approximate transonic term determines the direction of the supersonic and transonic flow.

It is naturally beyond the scope of this note to discuss all the implications of this theory. This will have to be deferred to a later more complete paper. It will be sufficient to mention here that all solutions of slender body and airfoil theory, as well as wing-body combinations, which have been obtained by using the equations of linearized subsonic or supersonic flow can be incorporated in this more general treatment, which yields results throughout the transonic regime also. Furthermore the well-known transonic similarity laws follow explicitly from this theory.

In the following paragraphs some theoretical results shall be given for the symmetrical airfoil and the body of revolution at zero angle of attack, and a comparison of the theory with experiment shall be presented.

In the transonic equation for the perturbation potential

$$\varphi_{yy} + \varphi_{zz} = (M_\infty^2 - 1)\,\varphi_{xx} + (\gamma + 1)M_\infty^2\varphi_x\varphi_{xx} \qquad (1)$$

we put

$$(\gamma + 1)M_\infty^2\varphi_{xx} = K = \text{constant} \qquad (2)$$

in the second term on the right-hand side. The boundary conditions are

at infinity:

$$\varphi(x,y) \to 0 \qquad (3)$$

at two-dimensional airfoils:

$$\left.\begin{aligned} y \to 0 \qquad \varphi_y(x,y) &= (\tau/2)F'(x) \\ \text{at bodies of revolution:} \qquad & \\ r \to 0 \qquad r\varphi_r(x,r) &= (\tau/2\pi)F'(x) \end{aligned}\right\} \qquad (4)$$

In these equations $\tau F'(x)$ is the derivative of the cross-sectional area distribution of an obstacle extending from $x = 0$ to $x = 1$ (and of unit span in the two-dimensional case), and $\tau$ is the thickness ratio.

If the exponential Fourier transform is used to solve Eq. (1) with the assumption Eq. (2) and the boundary conditions Eqs. (3) and (4), the velocity potential becomes

For Symmetrical airfoils

$$\varphi(x,y) = -\frac{\tau}{2\pi}\,Re\left\{\int_0^1 F'(\xi)e^{\alpha s}\,\frac{K_0[\alpha(s^2 + \beta^2y^2)^{1/2}]}{\beta}\,d\xi\right\} \qquad (5)$$

For bodies of revolution

$$\left.\begin{aligned} \varphi(x,r) &= -\frac{\tau}{4\pi}\int_0^1 F'(\xi)e^{\alpha s}\,\frac{\exp\{-\alpha(s^2 + \beta^2r^2)^{1/2}\}}{(s^2 + \beta^2r^2)^{1/2}}\,d\xi \qquad M_\infty \le 1 \\ \varphi(x,r) &= -\frac{\tau}{2\pi}\int_0^{x-rm} F'(\xi)e^{\alpha s}\times \\ &\qquad \frac{\cosh[\alpha(s^2 - m^2r^2)^{1/2}]}{(s^2 - m^2r^2)^{1/2}}\,d\xi \qquad M_\infty \ge 1 \end{aligned}\right\} \qquad (6)$$

where $\quad s = x - \xi \qquad \beta^2 = 1 - M_\infty^2 = -m^2$

$$\alpha = K/2\beta^2$$

*Re* denotes the real part and $K_0$ is the modified Bessel function of the second kind.

If the contour of the body or airfoil is given as a power series in $x$, the integration can be carried out.

It remains to assign a value of $K$ which represents a significant mean value for $\partial u/\partial x$. It is suggested to choose $K = (\gamma + 1)M_\infty^2\bar{\varphi}_{xx}$ where $\bar{\varphi}_{xx}$ is the value of $\varphi_{xx}$ on the axis at the point of

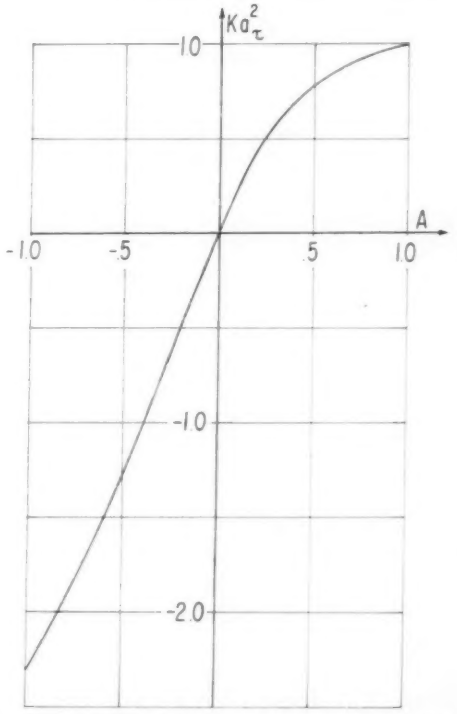


FIG. 1. Karman Number vs. transonic parameter $A$ for a biconvex airfoil $y = 2\tau(x - x^2)$.

* This research was sponsored by OSR of the ARDC, USAF, under Contract AF 18(600)-664.

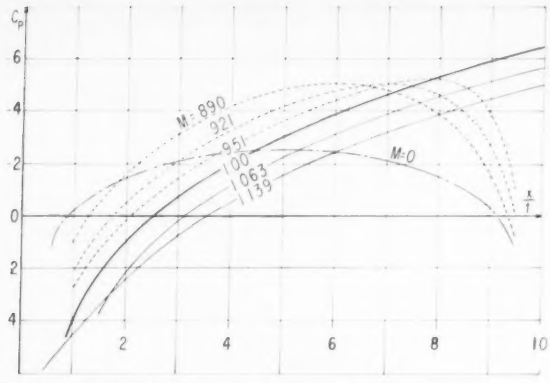


FIG. 2. Theoretical pressure distribution on biconvex airfoil with thickness ratio $\tau = 0.10$.

maximum velocity in the incompressible case. $K$ can then be evaluated from Eq. (5) and (6).

Carrying out the integration for a biconvex airfoil

$$y = 2\tau(x - x^2) \qquad 0 \leq x \leq 1$$

with thickness ratio $\tau$, one obtains for the pressure coefficient

$$C_p(x) = -\frac{8\tau}{\pi} Re \left\{ \frac{e^{\frac{x-\xi}{A}}}{\beta} \left[ \left( \frac{1}{2} - x \right) K_0\left( \frac{x-\xi}{A} \right) - (x - \xi) K_1 \left( \frac{x-\xi}{A} \right) \right] \right\}_{\xi=0}^{\xi=1} \quad (7)$$

where $A = 2\beta^2/K$

For $M = 1$ and $\gamma = 1.40$ Eq. (7) reduces to

$$C_p(x) = \tau^{2/3} \frac{1 - 4x}{\sqrt{x}} \quad (7a)$$

In Fig. 1 the Karman Number with respect to the thickness ratio

$$Ka_\tau = \beta \{ [(\gamma + 1)/2] M_\infty^2 \tau \}^{-1/3} \quad (8)$$

is plotted as a function of the transonic-parameter $A$ for this case.

Fig. 2 shows the calculated pressure distribution over the airfoil for different Mach Numbers, and in Fig. 3 the local Mach Numbers are compared with measurements of reference 4 for $M \leq 1$.

The present theory naturally does not permit the existence of shock waves. However, the rapid pressure increase at the rear portion of the airfoil seems to simulate their effect in the lower transonic regime. It can be seen that the theoretical and experimental results are in fair agreement.

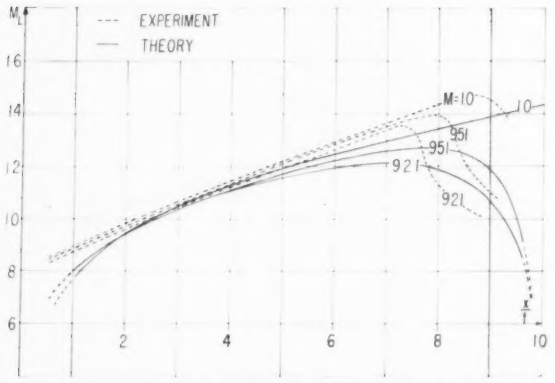


FIG. 3. Distribution of the local Mach Number on biconvex airfoil with thickness ratio $\tau = 0.10$.

For pointed bodies of revolution the theory yields the interesting result that the drag coefficient obtained at Mach Number one is half as large as if it were extrapolated from the conventional linearized supersonic theory. This result has been found by Oswatitsch for the special case of a half-body of revolution.

Additional work on this method as well as its extension to other cases is in progress.

### REFERENCES


[1] Oswatitsch, K., *Flow Around Bodies of Revolution at Mach Number One*. Paper presented at the Brooklyn Polytechnic's Conference on High-Speed Aeronautics, January 20–22, 1955.

[2] Ward, G. N., *Supersonic Flow Past Slender Pointed Bodies*, Quart. Jour. Mech. & Appl. Math., Vol. 2, pp. 75–97, 1949.

[3] Adams, Mac C., and Sears, W. R., *Slender-Body Theory—Review and Extension*, Journal of the Aeronautical Sciences, Vol. 20, No. 2, pp. 85–98, February, 1953.

[4] Michel, R., Marchaud, F. et LeGallo, T., Etude des écoulements Transoniques autour des profils lenticulaires, à incidence nulle, ONERA, publication No. 65, 1953.


## Heat Flow in a Fluid with Eddying Flow*


William H. Durfee

*Department of Mathematics, Mount Holyoke College, South Hadley, Mass.*


August 26, 1955

IN STUDYING THE flow of heat in a fluid flowing with eddying flow in a pipe, Latzko,[1] after making several simplifying assumptions, derived the following equation for the temperature distribution in a circular pipe when turbulence is fully established—

$$\frac{\partial}{\partial r}\left[ r \left( \frac{R^2 - r^2}{2R} \right)^{6/7} \frac{\partial t}{\partial r} \right] = Kr \left( 1 - \frac{r^2}{R^2} \right)^{1/7} \frac{\partial t}{\partial z} \quad (1)$$

where $t$ is the temperature of the fluid at the point with cylindrical coordinates $r$, $z$ (axial symmetry has been assumed), $R$ the radius of the pipe, and $K$ a combination of physical constants. The boundary conditions are $t = 0$ for $r = R$, $(\partial t/\partial r) = 0$ for $r = 0$. In addition, the radial temperature distribution for $z = 0$ must be given.

If a solution of the form $t = e^{-mz} f(r)$, is tried, the equation for $f(r)$ is

$$\frac{d}{dr}\left[ r \left( \frac{R^2 - r^2}{2R} \right)^{6/7} f'(r) \right] = -Kmrf(r) (1 - r^2/R^2)^{1/7}$$

Setting

$$x = (1 - r^2/R^2)^{1/7}$$

this becomes

$$(d/dx) [(1 - x^7)y'(x)] = -wx^7 y(x) \quad (2)$$

where $y(x) = f(r)$ and $w = 49\, Km(R/2)^{8/7}$. The boundary conditions become $y(0) = 0$ and $|y'(1)| < \infty$.

Since the general solution of Eq. (2) can be expressed in the form

$$y = A \sum_0^\infty a_i (x - 1)^i + B \log (x - 1) \sum_0^\infty b_i (x - 1)^i$$

the effect of the second boundary condition is to require $B = 0$. The constant $A$, then, has no essential effect on the solution and

*This work was done while the author was a member of the staff of the Computation Laboratory of the National Bureau of Standards. The computations were performed on the SEAC, a digital computer there. He wishes to express his thanks to Mrs. Ethel Marden for her help with the coding and machine work.

TABLE 1

| $n$ | $w_n$ | $n$ | $w_n$ |
|---|---|---|---|
| 0 | 8.72747 | 5 | 2110 |
| 1 | 152.423 | 6 | 2944 |
| 2 | 435.06 | 7 | $392 \times 10^1$ |
| 3 | 855.68 | 8 | $503 \times 10^1$ |
| 4 | 1414.1 | | |

can be chosen without loss of generality so that $y(1) = 1$. The problem thus reduces to finding values of $w$ and corresponding solutions $y(x)$ such that $y(0) = 0$.

Latzko found an approximate solution by expressing $y(x)$ as a linear combination of the first three Legendre polynomials of odd order and obtained as values of the first three eigenvalues $w_0 = 8.712$, $w_1 = 164.36$, and $w_2 = 1700.40$.

The author using purely numerical methods has computed the first nine eigenvalues together with the tabulated values and first derivatives of the corresponding functions in the interval $0 \leqq x \leqq 1$. It was found that the first eigenvalue agreed closely with Latzko's figure, the second differed slightly, while the third was so far from Latzko's result as to represent a considerable improvement. (See Table 1.)

The values of the last two eigenvalues are only approximate. While the method employed is capable of computing them or succeeding ones to any desired degree of accuracy, the computation time required is considerable. As these later values are not so important as the earlier ones, we have given only their approximate values.

The method of computation was essentially one of trial and error. The interval $0 \leqq x \leqq 1$ was divided into $n$ equal parts (initially 20). Using a trial value of $w$, Taylor's series was used to evaluate the function $y(x)$ successively at the points of the subdivision, starting with $x = 1$, until $x = 0$ was reached. This was repeated for other values of $w$ until one was found for which $y(0) = 0$. The number of subintervals was then successively doubled and the process each time repeated until further subdivisions did not affect the value of $w$ within the limits of accuracy imposed. This value of $w$ was accepted as the correct one.

### REFERENCES


[1] Latzko, H., *Wärmeübergang an einen turbulenten Flüssigkeits-oder Gasstrom*, Zeitschrift für Angewandte Mathematik und Mechanik, Vol. 1, pp. 268–290, 1921.

[2] Jakob, M., *Heat Transfer*, pp. 476–478; John Wiley and Sons, 1949.

[3] Durand, W. F., (Ed.), *Aerodynamic Theory*, Vol. VI, pp. 238–244; California Institute of Technology, 1943.


## An Experimental Study of One-Dimensional Shock-Wave Refraction*


C. A. Ford† and I. I. Glass‡

*Institute of Aerophysics, University of Toronto, Toronto, Canada*


August 21, 1955

A THEORETICAL ANALYSIS for the one-dimensional refraction of a shock wave at a contact surface may be found in reference 1. The predicted wave systems are shown in Fig. 1. If the internal energy ratio across the contact surface [$E_{15} = (e_1/e_5)$] exceeds a certain critical value ($E_{\text{crit.}}$), then a transmitted shock wave and a reflected rarefaction wave, separated by a contact surface, results after the interaction of the incident shock with the contact surface (Fig. 1a). If the internal energy ratio is

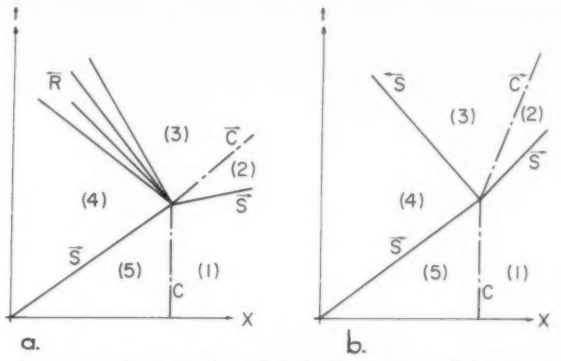


FIG. 1. Interaction of a plane shock wave with a stationary contact surface. $S$ = shock wave, $C$ = contact surface, $R$ = rarefaction wave.

below $E_{\text{crit.}}$, then a transmitted shock and a reflected shock, separated by a contact surface, are formed (Fig. 1b). In the limit, when the internal energy ratio is identical with $E_{\text{crit.}}$, then the reflected wave is a Mach line or a sound wave and the incident shock wave is transmitted unchanged.

The critical energy ratio is expressed by the relation

$$E_{\text{crit.}} = (\alpha_1 + P_{54})/(\alpha_5 + P_{54}) \tag{1}$$

where $\alpha = (\gamma + 1)/(\gamma - 1)$, and $\gamma$ is the specific heat ratio which is assumed constant and $P_{54} = p_5/p_4$, the pressure ratio across the incident shock wave.

The case of the reflected rarefaction wave ($P_{54}$) is given by the equation

$$P_{54}^{\beta_5} + f(P_{54} - P_{54}) \sqrt{\frac{\beta_5 E_{15}}{\alpha_1 P_{54} + P_{54}}} - g - 1 = 0 \tag{2}$$

where

$$\begin{aligned} f &= [(\alpha_5 + P_{54})/(\alpha_5 P_{54} + 1)]^{1/2} \\ g &= (1 - P_{54})\,[\beta_5/(\alpha_5 P_{54} + 1)]^{1/2} \\ e &= \text{internal energy per unit mass} \\ E_{15} &= e_1/e_5 \\ E_{15} &> E_{\text{crit.}} \\ \beta &= (\gamma - 1)/2\gamma \end{aligned}$$

Eq. (2) makes it possible to determine the waves and states following the interaction in terms of the initial conditions and the fact that

$$P_{21}/P_{45} = P_{54} \tag{3}$$

Similarly, the case of the reflected shock wave is described by the

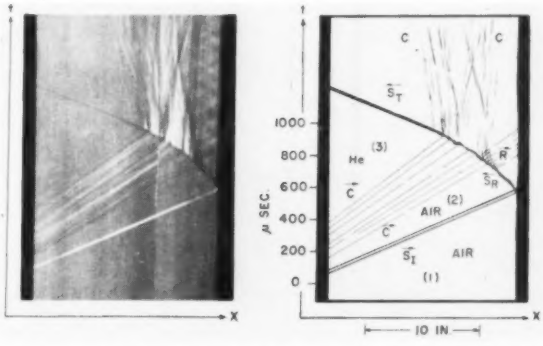


PLATE 1. Refraction of a shock wave at a contact region generated in a shock tube by bursting a diaphragm. (A) Composite photograph of two $(x,t)$-plane schlieren records. (B) Explanatory line diagram of (A). $S_I$ = incident shock wave $S_R$ = normally reflected shock wave, $S_T$ = refracted shock wave, $C$ = contact region, $R$ = reflected rarefaction wave, Mach Number of incident shock ($S_I$) = 2.25, $p_1$ = 65 mm. Hg, $t_1$ = 24.1°C.

* This investigation was made under a grant from the Defence Research Board of Canada.

† Formerly, Research Assistant, Institute of Aerophysics, University of Toronto. Now, Aerodynamicist, Avro (Aircraft), Malton, Ont.

‡ Research Associate and Assistant Professor of Aeronautical Engineering.

PLATE 2a. Composite photograph of two $(x,t)$-plane schlieren records showing the double refraction of a plane shock wave at a helium layer and subsequent overtaking of two similarly-facing shock waves. Case: Air || He || Air. Microfilm method.

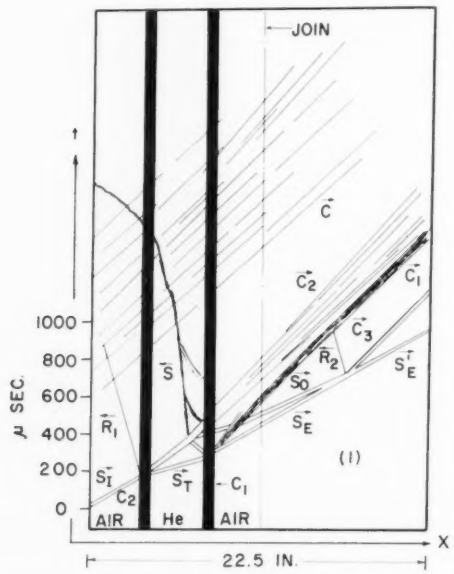


PLATE 2b. Explanatory line diagram of (a). Air || He || Air initially at rest. $p_1$ = 747 mm. Hg, $a_1$ = 1,130 ft./sec., Mach Number of emergent shock wave $(S_E)$ = 1.65, Mach Number of overtaking shock wave $(S_O)$ = 1.23, Mach Number of shock-amplified wave $(S'_E)$ = 1.69, speed of head of reflected rarefaction wave $(R_2)$ = 0.28 (pressure ratio across $R_2$ = 0.97), speed of contact front $(C_3)$ = 0.90 (all velocities referred to sound speed in air), $C_1$, $C_2$ = microfilm contact surfaces, $S_T$ = refracted shock wave at $C_2$, $S$ = Reflected shock wave at $C_1$, $C$ = contact region generated in the shock tube by the ruptured diaphragm, $R_1$ = reflected rarefaction wave at $C_2$.

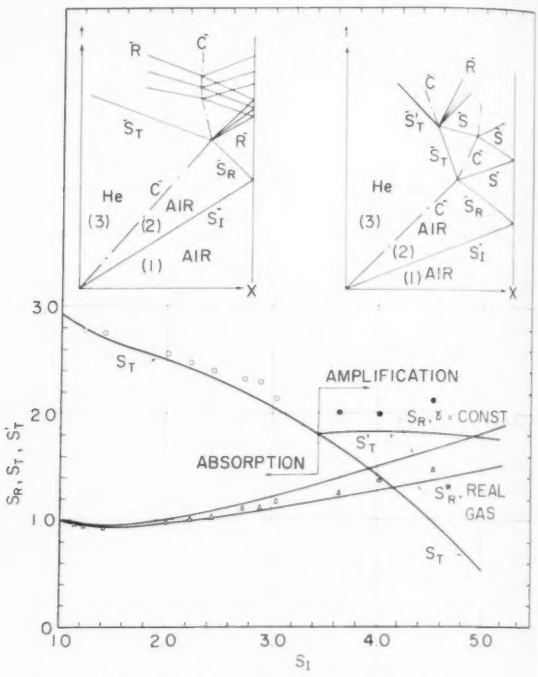


FIG. 2. Variation of the reflected shock Mach Number $(S_R)$, the refracted shock Mach Number $(S_T)$, and the shock-amplified Mach Number $(S'_T)$, with the incident shock Mach Number $(S_I)$—all referred to the speed of sound in air. (The experimental points are averages of a number of runs.) Case: Air || He.

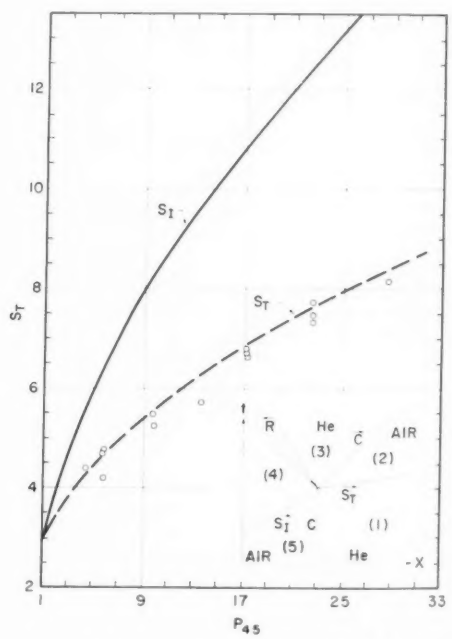


FIG. 3. Variation of the refracted shock Mach Number $(S_T)$ (referred to the speed of sound in air) with the pressure ratio $(P_{45})$ across the incident shock wave. $S_I$ = Mach Number of the incident wave. Case: Air || He.

following relation;

$$E_{15} = \frac{\alpha_1 + P_{54}P_{43}}{(1 - P_{54}P_{43})^2} \quad h \left[ k\sqrt{P_{43}} + \frac{P_{43} - 1}{\sqrt{\alpha_5 + P_{43}}} \right]^2 \quad (4)$$

where

$$h = (\alpha_5 P_{54} + 1)/(\alpha_5 + P_{54})$$
$$k = (1 - P_{54})/\sqrt{\alpha_5 P_{54} + 1}$$
$$E_{15} < E_{crit.}$$

The more difficult problem of two-dimensional shock-wave refraction has been treated theoretically[2] and checked experimentally.[3, 4]

The one-dimensional theory was tested in the 3 × 3 in. UTIA wave interaction tube,[5] by employing the following techniques:[6]

(a) The shock wave generated by rupturing a diaphragm separating helium and air was reflected from the end of the channel and then refracted at the moving natural air-to-helium contact region. A typical $(x, t)$-plane schlieren record of this interaction appears on Plate 1.

(b) A single mechanical slide was used to separate air from helium in the channel. When the correct initial conditions were obtained, the slide was withdrawn and the shock formed by breaking a diaphragm was allowed to refract at the stationary contact front. Schlieren records were taken of the transmitted shock wave in the $(x, t)$-plane.

(c) A double mechanical slide was utilized to separate a layer of helium from the rest of the shock-tube channel. Shock waves of known strength were fired through the layer and recorded as described in (b) above, in order to check the double refraction theory presented in reference 1.

(d) The double refraction wave system was substantiated by taking $(x, t)$-plane schlieren records. In this case, nitrate dope microfilms (1,500 to 3,300 Å thick) were used as artificial contact surfaces in order to obtain a well defined interaction. A typical record appears on Plate 2. It will be noted that the double refraction also leads to the overtaking of similarly facing shock waves.[7]

The experimental wave speeds which were obtained from the $(x, t)$-plane schlieren records in (a), (b), and (c) above are summarized on Figs. 2–5, inclusive.

Fig. 2 shows the shock refraction obtained at the natural air-to-helium contact surface produced in a shock tube. The normal reflected shock wave $S_R$ is seen to approach the thermal equilibrium wave speeds $S_R^*$ for the higher strength initial shocks $S_I$. The normal reflected shock then strikes the contact region and refracts. For weak waves the energy ratio across the contact region ($E_{32}$) is greater than $E_{crit.}$ and a reflected rarefaction wave results. As a result the transmitted wave is weaker than the incident wave (case of shock absorption or attenuation). $E_{crit.}$ is reached when the initial incident shock Mach Number ($S_I$) is

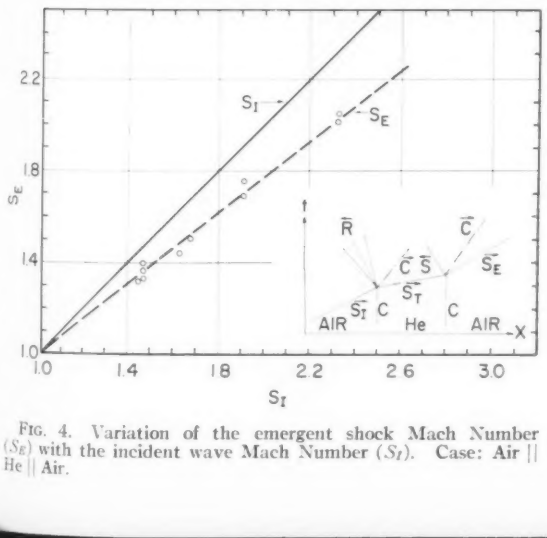


FIG. 4. Variation of the emergent shock Mach Number ($S_E$) with the incident wave Mach Number ($S_I$). Case: Air || He || Air.

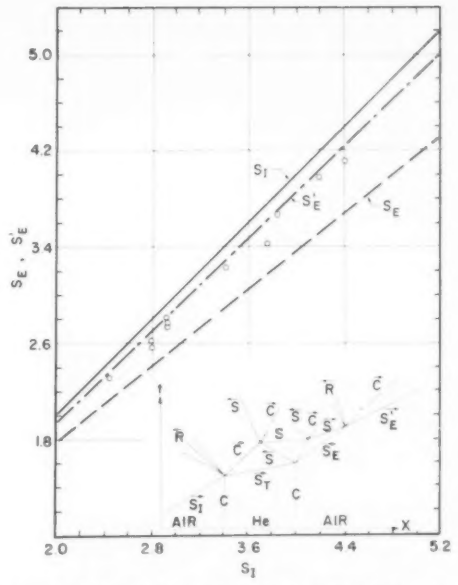


FIG. 5. Variation of the emergent shock Mach Number ($S_E$) and shock-amplified Mach Number ($S'_E$) with the incident shock Mach Number ($S_I$). [Experimental points are for the shock-amplified wave ($S'_E$)]. Case: Air || He || Air.

about 3.4, and beyond that point the reflected wave at refraction is a shock wave. The transmitted shock wave is stronger than the incident wave (case of shock amplification).

It should be noted that it is necessary to take account of the overtaking shock waves. If one such interaction is introduced into the calculations, then the agreement with the new theoretical wave speed ($S_T'$) is much improved. The consistently higher values of the refracted wave speed also may be attributed to a lower particle velocity and a higher temperature in state (3) than predicted by the idealized theory.

Fig. 3 indicates that the agreement between theory and experiment for a single refraction at an air-to-helium contact surface is very satisfactory. Therefore, it may be concluded that it is possible to obtain very significant shock-wave attenuation by employing a single refraction into a gas such as helium (or hydrogen).

Fig. 4 shows reasonable agreement for the double refraction at a layer of helium for incident waves up to a Mach Number of about 2.3. Beyond this value, the effects of the overtaking shock waves resulting from this interaction are very rapid and must be taken into account as shown on Fig. 5. It may be concluded, therefore, that a helium layer does not provide a means of attenuating a shock wave, owing to the amplification produced by the subsequent weaker overtaking shock waves. These bring the emergent shock wave back to almost the original incident wave strength.

Further details of this entire problem may be found in reference 6.

## REFERENCES

[1] Bitondo, D., Glass, I. I., and Patterson, G. N., *One-Dimensional Theory of Absorption and Amplification of a Plane Shock Wave by a Gaseous Layer*, UTIA Report No. 5, 1950.

[2] Polachek, H., and Seeger, R. J., *Refraction of Shock Waves at a Gaseous Interface*, NOLM 9971, 1949.

[3] Peckham, D. C., and Stoner, R. G., *Interferometric Studies of Shock Refraction*, Penn. State College TR Nos. 312-3 and 312-4, 1955.

[4] Jahn, R. G., *The Refraction of Shock Waves at a Gaseous Interface*, Princeton U. Tech. Reports II-16, II-18, II-19, 1954–1955.

[5] Glass, I. I., Martin, W. A., and Patterson, G. N., *A Theoretical and Experimental Study of the Shock Tube*, UTIA Report No. 2, 1953.

[6] Ford, C. A., and Glass, I. I., *An Experimental Study of Shock-Wave Refraction*, UTIA Report No. 29, 1954.

[7] Bull, G. V., Fowell, L. R., and Henshaw, D. H., *The Interaction of Two Similarly-Facing Shock Waves*, UTIA Report No. 25, 1953.

## Aerodynamic Cross-Coupling Between Side Force and Normal Force on Bodies and Wing-Body Combinations

Martin Zlotnick
*Principal Aerodynamicist, Aerophysics Section, Aerodynamics Department, Republic Aviation Corp.*
September 8, 1955

IT MAY BE WORTHWHILE to remark that a consequence of the nonlinear relation between the normal force on a body of revolution and its angle of attack[1, 2] will be a variation of the static *directional* stability derivatives with *angle of attack* (or a variation of static longitudinal stability derivatives with angle of sideslip). This effect will be substantial for slender bodies where the nonlinear component of the loading is dominant even at relatively low angles of attack. It may therefore be important on missile and airplane configurations where the body plays a major role in the stability of the aircraft.

If $\theta = \sqrt{\alpha^2 + \beta^2}$ is the angle of the body with the free stream, the resultant force coefficient $C_{F_R}$ may be expressed according to reference 1 as

$$C_{F_R} = C_{F_1}\theta + C_{F_2}\theta^2$$

The side force coefficient, $C_Y$, is then

$$C_Y = C_{F_R}(\beta/\sqrt{\alpha^2 + \beta^2})$$

and the side force derivative $C_{Y_\beta}$ is

$$C_{Y_\beta} = C_{F_1} + C_{F_2}\alpha\left[\frac{1 + 2(\beta^2/\alpha^2)}{\sqrt{1 + (\beta^2/\alpha^2)}}\right]$$

so that $(C_{Y_\beta})_{\beta=0}$ varies linearly with angle of attack. Similarly $(C_{Y_\alpha})$ is given as

$$C_{Y_\alpha} = C_{F_2}\beta\left[\frac{1}{\sqrt{1 + (\beta^2/\alpha^2)}}\right]$$

The normal force derivatives $C_{N_\alpha}$ and $C_{N_\beta}$ are of course the same, respectively, as $C_{Y_\beta}$ and $C_{Y_\alpha}$ except that $\alpha$ and $\beta$ are interchanged in the equations.

The magnitude of the aerodynamic cross-coupling effect on airplane stability depends entirely on the cross-flow drag which determines $C_{F_2}$ and the corresponding moment coefficient $C_{M_2}$. Whereas $C_{F_2}\theta^2$ is fairly large even at moderate angles, the moment $C_{M_2}\theta^2$ about the airplane c.g. is usually small at all practical values of $\theta$. This is because the center of pressure of the force due to cross-flow drag almost always falls near the airplane c.g.

The center of pressure of the force due to cross-flow drag need not always be near the c.g., however, and can to some extent be controlled by the designer. For example if the portion of an ogive cylinder body aft of the c.g. were extended, or changed to a square cross-section, a substantial increase in directional stability at high angle of attack (or longitudinal stability at a high angle of sideslip) might be obtained. With respect to airplane configurations it must be realized, however, that the reduction of the flow angle on the afterbody due to the wing downwash could reduce the effect of a change in cross-section on the portion of the afterbody strongly affected by the downwash.

### References

[1] Allen, H. Julian, and Perkins, Edward W., *A Study of Effects of Viscosity on Slender Inclined Bodies of Revolution*, NACA TR 1048, 1951.

[2] Kelly, Howard R., *The Estimation of Normal-Force, Drag, and Pitching-Moment Coefficients for Blunt-Based Bodies of Revolution at Large Angles of Attack*, Journal of the Aeronautical Sciences, pp. 549–555, Vol. 21, No. 8, August, 1954.

## Transition Studies and Skin-Friction Measurements . . .

(*Continued from page 107*)

[17] Stalder, J. R., and Slack, E. G., *The Use of a Luminescent Lacquer for the Visual Indication of Boundary Layer Transition*, NACA TN 2263, January, 1951.

[18] Schaevitz, H., *The Linear Variable Differential Transformer*, Proceedings of the Society for Experimental Stress Analysis, Vol. 4, No. 2, 1947.

[19] DeLauer, R. D., *Experimental Heat Transfer at Hypersonic Mach Number*, GALCIT, Ph.D. Thesis, June, 1953; also Hypersonic Wind Tunnel Memorandum No. 14, California Institute of Technology.

[20] Charters, A. C., Jr., *Transition between Laminar and Turbulent Flow by Transverse Contamination*, NACA TN 881, March, 1943.

[21] Liepmann, H. W., Roshko, A., and Dhawan, S., *On the Reflection of Shock Waves from Boundary Layers*, NACA TN 2334, April, 1951, p. 23 and Fig. 18.

[22] Pai, S. I., *Two-Dimensional Jet Mixing of a Compressible Fluid*, Journal of the Aeronautical Sciences, Vol. 16, No. 8, pp. 463–469, August, 1949.

[23] Corrsin, S., and Uberoi, M. S., *Further Experiments on the Flow and Heat Transfer in a Heated Turbulent Jet*, NACA TR 998, 1950; also NACA TN 1865, 1949.

[24] Fage, A., and Sargent, R. F., *An Air-Injection Method of Fixing Transition from Laminar to Turbulent Flow in a Boundary Layer*, British ARC, R & M 2106, June, 1944.

[25] von Kármán, Th., and Tsien, H. S., *Boundary Layer in Compressible Fluids*, Journal of the Aeronautical Sciences, Vol. 5, No. 6, pp. 227–232, April, 1938.

[26] Van Driest, E. R., *Investigation of Laminar Boundary Layer in Compressible Fluids Using the Crocco Method*, NACA TN 2597, January, 1952.

[27] Young, G. B. W., and Janssen, E., *The Compressible Boundary Layer*, Journal of the Aeronautical Sciences, Vol. 19, No. 4, pp. 229–236, 288, April, 1952.

[28] von Mises, R., and von Karman, Th., "Advances in Applied Mechanics," Vol. 2, Academic Press Inc., 1951.

[29] Wegener, P. P., Winkler, E. M., and Sibulkin, M., *A Measurement of Turbulent Boundary-Layer Profiles and Heat-Transfer Coefficient at $M = 7$*, Readers' Forum, Journal of the Aeronautical Sciences, Vol. 20, No. 3, March, 1953.

[30] Coles, D., *The Law of the Wall in Turbulent Shear Flow*, California Institute of Technology, Pasadena, California, May 5, 1954.

[31] Tucker, M., *Approximate Calculation of Turbulent Boundary Layer Development in Compressible Flow*, NACA TN 2337, April, 1951.

[32] Rubesin, M. W., Maydew, R. C., and Varga, S. A., *An Analytical and Experimental Investigation of the Skin Friction of the Boundary Layer on a Flat Plate at Supersonic Speeds*, NACA TN 2305, February, 1951.

[33] Laufer, J., *Factors Affecting Transition Reynolds Numbers on Models in Supersonic Wind Tunnels*, Readers' Forum, Journal of the Aeronautical Sciences, Vol. 21, No. 7, July, 1954.

[34] von Kármán, Th., *Turbulence and Skin Friction*, Journal of the Aeronautical Sciences, Vol. 1, No. 1, 1934.

[35] Crocco, L., *The Laminar Boundary Layer in Gases*, North American Aviation, Inc., APL/CF-1038, Report AL-684, July, 1948 (translation).

[36] Coles, Donald, *Measurements of Turbulent Friction on a Smooth Flat Plate in Supersonic Flow*, Journal of the Aeronautical Sciences, Vol. 21, No. 7, July, 1954.

[37] Lobb, R. K., Winkler, E., and Persh, J., *Experimental Investigation of Turbulent Boundary Layers in Hypersonic Flow*, paper presented at the 22nd Annual Meeting of the IAS, Jan. 25–29, 1954, IAS Preprint No. 452.